Czech Technical University in Prague
Faculty of Nuclear Sciences and Physical Engineering

DOCTORAL THESIS

Modelling of non local energy transport in laser plasma

Praha 2022 Ing. Jan Nikl

■ Bibliografický záznam

Autor:	Ing. Jan Nikl České vysoké učení technické v Praze Fakulta jaderná a fyzikálně inženýrská Katedra fyzikální elektroniky
Název práce:	Modelování nelokálního transportu energie v plazmatu
Studijní program:	(D4CS) Aplikace přírodních věd
Studijní obor:	(3901V012) Fyzikální inženýrství
Školitel:	doc. Ing. Milan Kuchařík, Ph.D. České vysoké učení technické v Praze Fakulta jaderná a fyzikálně inženýrská Katedra fyzikální elektroniky
Školitel specialista:	Dr. Stefan Andreas Weber Akademie věd ČR Fyzikální ústav ELI Beamlines
Akademický rok:	2021/22
Počet stran:	181
Klíčová slova:	nelokální transport, laserové plazma, kinetické modelování, rezistivní magnetohydrodynamika, lagrangeovská hydrodynamika, transport tepla, absorpce laseru, radiační transport

■ Bibliographic entry

Author:	Ing. Jan Nikl Czech Technical University in Prague Faculty of Nuclear Sciences and Physical Engineering Department of Physical Electronics
Title of dissertation:	Modelling of non local energy transport in laser plasma
Degree Programme:	(D4CS) Applications of Natural Sciences
Field of Study:	(3901V012) Physical engineering
Supervisor:	doc. Ing. Milan Kuchařík, Ph.D. Czech Technical University in Prague Faculty of Nuclear Sciences and Physical Engineering Department of Physical Electronics
Supervisor specialist:	Dr. Stefan Andreas Weber Czech Academy of Sciences Institute of Physics ELI Beamlines Centre
Academic year:	2021/22
Number of Pages:	181
Keywords:	non-local transport, laser plasma, kinetic modelling, resistive magnetohydrodynamics, Lagrangian hydrodynamics, heat transport, laser absorption, radiation transport

Prohlášení

Prohlašuji, že jsem předloženou práci vypracoval samostatně a že jsem uvedl veškerou použitou literaturu.

V Praze dne 17. května 2022 Ing. Jan Nikl

Acknowledgements

This work and all the research leading to its compilation would not be possible without the sincere boundless support, scientific guidance and countless hours spent on revisions of the manuscripts by my supervisor doc. M. Kuchařík. My deepest gratitude belongs to him and it is not an overstatement that this work would not exist in this form without him. At this place, I would like to thank also to my supervisor specialist Dr. S. Weber for stimulating inputs and management of my scientific efforts. I would like to also acknowledge my collaborator M. Holec, Ph.D. for the common work on the methods of non-local transport and bringing me to this interesting topic. Finally, I want to thank my family for their patience with me while writing this work over days and nights.

Ing. Jan Nikl

■ Abstrakt

Interakce laseru s pevným terčem je složitý jev, který zahrnuje různé mechanismy transportu energie. Numerické modelování transportních dějů v plazmatu typicky následuje klasickou difúzní teorii. Existuje však rozpor mezi výsledky simulací a experimentálními daty v případě intezivních laserových impulzů, jelikož energetické elektrony a fotony pronikají hluboko do terče. Musí být proto modelována tato nelokalita transportu, což má zásadní důležitost pro aplikace jako je inerciální fúze, předpulzy laserů o ultravysoké intenzitě, magneticky držená fúze nebo studie teplé husté hmoty. Tato práce shrnuje podkladovou teorii a příspěvky autora k výzkumu tohoto komplexního jevu. Je následováno několik přístupů k modelování interakce laseru s terčem, jmenovitě kinetické simulace problému v rámci Vlasov–Fokker–Planck–Maxwell modelu. Zadruhé je to magnetohydrodynamická Lagrangeovská tekutinová metoda opatřená doplňujícími modely pro absorpci laseru a difúzní nebo nelokální transport elektronového tepla a radiace. Jsou vyvinuty vícedimenzionální numerické metody založené na konečných prvcích vysokého řádu, které jsou ověřeny na relevantních testovacích problémech a dalších realistických simulacích, které demonstrují jejich aplikovatelnost na simulace interakce laseru s terčem.

■ Abstract

Interaction of a laser with a solid target is a complex phenomenon, involving various energy transport mechanisms. Numerical modelling of these processes in laser plasma follows the classical diffusion theory typically. However, a discrepancy between the simulation results and the experimental measurements exists in the case of intense laser pulses, since the energetic electrons and photons penetrate deep into the target. Hence, non-locality of the transport must be modelled, which holds a significant importance for applications like inertial confinement fusion, prepulses of ultra-high intensity lasers, magnetic confinement fusion or warm dense matter studies. This work summarizes the background theory and author's contributions to the research of this complex phenomenon. Multiple approaches to modelling of the laser–target interaction are followed, namely the kinetic treatment of the problem in terms of the Vlasov–Fokker–Planck–Maxwell simulations. Secondly, it is the magneto-hydrodynamic Lagrangian fluid method equipped with additional models for the laser absorption and the electron heat and radiation diffusive or non-local transport. Multi-dimensional numerical methods based on high-order finite elements are developed, which are then validated on relevant test problems and further realistic simulations, demonstrating their applicability on the simulations of the laser–target interaction.

Contents

Introduction

Plasma, the fourth state of matter, is the primordial origin of all matter, as the quark–gluon plasma dominated the early stage of our universe, and maybe its ultimate end at the same time, when trapped on the accretion disk of a black hole. Plasma also accompanied our kind from its very beginning, as our civilization would not exist probably, when fire, a form of plasma, was not discovered. And it may also shape its future, as it provides a nearly unlimited source of energy thanks to the process of thermonuclear fusion. Hence, its mysterious nature has attracted attention of scientists for long time.

Unless being absolutely still and homogeneous, plasma exhibits transport processes. Therefore, their understanding is a cardinal discipline of the plasma research from its beginning. Actually, it can be tracked even before its foundation to the studies about neutral gases. It was as early as 1905, when Lorentz described the transport processes in metals in a simple collisional manner by what is hence known as the Lorentz gas [1]. Another landmark is then the formulation of the theory of gases by Chapman in 1916 [2]. However, plasma is not a neutral gas, even though it behaves similarly in certain aspects. An important difference are the involved long range forces in contrast to the close encounters in a gas. A fundamental, yet incomplete, description was then given by Landau for the Coulombic interaction [3]. Later, the notion of dynamic friction, stemming from the astrophysical context originally, was formulated by Chandrasekhar [4], but its statistical basis predetermined the model to be generalized to other fields. However, the effect of electron–electron collisions was not clear and a strong belief existed that the theory of gases should be simply extended to plasma, as envisioned by Cowling [5]. The influential paper of Cohen, Spitzer and Routly then described the collisions in a consistent manner as the dynamic friction and diffusion [6]. The theory was then further refined in the work of Spitzer and Härm [7], which defines what is known today as the classical diffusion theory of plasma. In the context of magnetized plasmas, it was rather the work of Braginskii [8] based on the earlier formulation of Landau, which presents the cornerstone of the description. However, the models relied only on the small anisotropy approximations, limiting their physical accuracy. A systematic formulation was later provided by Rosenbluth [9].

In parallel, the research of lasers started. However, it was recognized with their increasing power [10] that the diffusion theory does not reflect the phenomenon of heat flux saturation for steep gradients in plasma and the heat flux limiting technique was proposed for the numerical modelling [11]. The physical findings were later confirmed by dedicated experiments [12]. Also kinetic simulations suggested that there may exist such a limitation [13, 14], but it was believed that the diffusion description can be simply corrected. The flux limiting techniques could solve with a partial success the problem of the excessive heat flow, but they could not describe the pre-heating effect occurring in the downstream of the temperature gradient. Various empirical methods were proposed [15, 16], delocalizing the electron heat flux and introducing the notion of non-locality to the hydrodynamic simulations in a simplified manner. However, the ground-shaking mathematical analysis of the problem showed such numerical treatment may produce severe non-physical effects [17]. From that time, various models

of non-local transport have been proposed [18, 19, 20], but all possessing their own fundamental advantages and disadvantages.

This defines the starting point of our research, which focuses on the phenomenon of non-local energy transport in plasma. The complex nature of the non-local energy transport is given by the fact that it originates from the microscopic phenomena in the plasma, but becomes manifested on the macroscopic level. Therefore, also the numerical modelling must be reformed to reflect this multi-scale problem adequately. This text addresses several aspects of the non-local transport in the context of laser–target interaction, which cannot be attributed to the electrons solely as discussed so far, but also to the radiative transfer, where energetic photons may penetrate deep into the target. Moreover, the laser absorption methods are deeply connected to both phenomena, when an intense laser beam irradiates a solid target and its power drives both effects. Finally, it is the hydrodynamic modelling which provides the vessel for integration of all mentioned methods together and simulation of plasma formation and expansion, which must be also improved to accommodate the new models and follow the shift of paradigm in the modelled detail.

The field computational fluid dynamics is dominated by the two major approaches, cell-centered and staggered methods for Lagrangian hydrodynamics [21, 22]. While the former collocates the discrete quantities, the latter separates the thermodynamic potentials and kinematic vectors spatially. The compatible staggered approach has the indisputable advantage of the local conservation property, meaning the local update of internal energy is truly given by the work of the forces at the volume boundary [23, 24]. On the other hand, the evaluation of the Riemann invariants requires an additional interpolation, in contrast to the cell-centered methods. In this work, we build on the high-order curvilinear finite element hydrodynamics, which can be seen as a generalization of the staggered method for high-order representation of the quantities [25]. Still, the appealing properties of the approach are retained, like mass, momentum and total energy (local) conservation [26]. On top of that, the high-order treatment provides an unprecedented detail of the plasma profiles. The curvilinear shape of the elements then perfectly matches the framework of Lagrangian hydrodynamics, where the computational mesh follows the flow of the fluid, which is advantageous for modelling of the rapidly expanding laser plasma.

The topic of non-local energy transport has a great importance for multiple fields of applications like the inertial confinement fusion (ICF) research [27], pre-pulse physics of ultra-high intensity lasers [28], magnetic confinement fusion (MCF) [29] or warm dense matter research [30]. In the context of ICF, the non-local species can penetrate deeper to the target, preheating the non-compressed material. The compression ratio for the shock wave is then decreased and the ignition conditions are jeopardised [31, 32]. On the other hand, more energy can be delivered to the shock wave, increasing the efficient ablative pressure [33]. The non-locality can be important also for the pre-pulse physics, where ultra-relativistic laser pulses have unavoidable intense pre-pulses or pedestals, which are far beyond the plasma formation threshold and the produced pre-plasma can filament the main pulse [34, 35]. The sensitivity of the process then requires to take into account the non-local species. Significantly different physical conditions appear in MCF, but the fundamental principle remains the same. The non-

local or even run-away electrons non-classically contribute to the heat flux towards the tokamak walls [29], hazarding stability of the plasma conditions and integrity of the divertors. Finally, the warm dense matter research investigates behaviour of matter under a strong compression and simultaneous heating, which is the case for laser-driven shock waves. Exact measurements of the propagating shock then reveal contribution from the non-local species [30] with implications for the aforementioned ICF research or laboratory astrophysics [36].

The aim of this work is investigation of the models for description of the non-local transport and development of numerical methods to increase the overall physical realism of the laser plasma simulations and enable transition from the classical treatment towards the high-order multi-scale modelling. The performance of the methods is to be benchmarked on numerical tests and physically-relevant problems. Finally, conclusions from the achieved results are to be drawn and the directions of the possible future improvements outlined.

The text is organized to three main parts. The first part concentrates on the physical theory. An introduction to the basic kinetic theory is given in chapter 1, which is reduced to the hydrodynamic description in chapter 2. However, the hydrodynamic model is incomplete as it misses exactly the transport processes we are mostly interested in. This is addressed by chapter 3, which describes the phenomenon of heat transport, followed by chapter 4 dedicated to the radiative transfer. Finally, a brief overview of the methods for laser absorption is given in chapter 5.

The second part is dedicated to the numerical methods developed for modelling of the physical phenomena. Since the finite element method is predominantly used, chapter 6 presents an overview of its fundamentals. The rest of the outline follows the first part, starting from the kinetic model of reduced Vlasov–Fokker–Planck–Maxwell in chapter 7. However, the the most significant contribution is the multi-physics magneto-hydrodynamic code, where its basis is described in chapter 8. The heat and radiation closure models are approximated by the diffusion model, as summarized in chapter 9. Alternatively, the non-local electron heat or radiation closure models can be applied, which are subjects of chapter 10. Finally, the methods for tracking of the laser propagation and absorption are described in chapter 11.

In the third part, simulations of laser–target interaction are performed. The single-dimensional ones in chapter 12 concentrate on the comparison of the diffusive and non-local transport within radiative transfer and thermal transport. Chapter 13 then extends the modelling to 2D, where the problems involving geometric effects are investigated, like laser absorption and spontaneous magnetic field generation. A demonstrative example of the capabilities in 3D is then presented in chapter 14.

Part I
Physical models

1 Kinetic theory

Kinetic description of plasma originates from the statistical picture, where the exact population of species is replaced by the distribution function through the averaging process. It is assumed that there exists sufficiently high number of species on every observable scale, so the statistics of such ensemble converge to the average values and the continuous description is valid in turn. The distribution function $f_\alpha = f_\alpha(\vec{x}, \vec{v}, t)$ is then function of the phase space coordinates and describes the number of particles α in the differential volume $\mathrm{d}\vec{x}$, $\mathrm{d}\vec{v}$, where $\vec{x}$ is the spatial coordinate, $\vec{v}$ is the velocity space coordinate and t is time. Following Liouville's theorem, the total derivative $\frac{\mathrm{d}f_\alpha}{\mathrm{d}t}$ can be expanded to form the Boltzmann equation:

$$\frac{\partial f_\alpha}{\partial t} + \vec{v} \cdot \nabla_{\vec{x}} f_\alpha - \frac{\vec{F}_\alpha}{m_\alpha} \cdot \nabla_{\vec{v}} f_\alpha = \left(\frac{\partial f_\alpha}{\partial t} \right)_{\mathrm{coll}} . \tag{1}$$

The symbol $\vec{F} = F(\vec{x}, \vec{v}, t)$ represents the generalized force exerted on the α species and m_α is their mass. The term on the right-hand-side represents the collision operator, where it is assumed that the collisions involve only strongly localized transient fields. Therefore, they can be separated in the averaging process and $\vec{F}$ does not include these microscopic contributions.

In the context of plasma dynamics, the (free) electron distribution f_e is of a significant interest as it is responsible for the most transport phenomena described in later chapters. Because its frequent occurrence in the text, the lower index is omitted henceforth. The collective behaviour of the plasma is intermediated by the macroscopic electric field $\vec{E} = \vec{E}(\vec{x}, t)$ and magnetic field $\vec{B} = \vec{B}(\vec{x}, t)$ acting on the electrons through the Lorenz force. Inserting it to (1), the kinetic equation is obtained:

$$\frac{\partial f}{\partial t} + \vec{v} \cdot \nabla_{\vec{x}} f - \frac{e}{m_e} (\vec{E} + \vec{v} \times \vec{B}) \cdot \nabla_{\vec{v}} f = \left(\frac{\partial f}{\partial t} \right)_{\mathrm{coll}} , \tag{2}$$

where e is the elementary charge.

The description is complemented by the Maxwell's equations for the macroscopic fields, which are composed of Ampère's law and Faraday's law taking the following forms respectively:

$$-\frac{1}{c^2} \frac{\partial \vec{E}}{\partial t} + \nabla \times \vec{B} = \mu_0 \vec{j}, \tag{3}$$

$$\frac{\partial \vec{B}}{\partial t} + \nabla \times \vec{E} = 0. \tag{4}$$

The quantity $\vec{j} = \vec{j}(\vec{x}, t)$ is the electric current and its relation to the distribution function is defined in chapter 1.2. The symbol μ_0 represents the vacuum permeability and c is the speed of light in vacuum.

1.1 Collision operator

The kinetic description cannot be complete without a particular definition of the collision operator operating on the right-hand-side of the kinetic equation (2). In the simplest case, when the plasma is ideal in the sense that the collective phenomena completely dominate over the close range interactions, it can be modelled as nearly collision-less and the collision operator is set $(\partial f/\partial)_{\text{coll}} \equiv 0$. This form of the equation is known as the Vlasov equation.

However, the collisions cannot be neglected in the applications of the primary interest here. In order to reduce complexity of the collision term, it is expanded to the BBGKY hierarchy in the number of interacting particles [37, 38]. This expansion is then truncated after the first term, i.e., the binary interaction between the species. This approximation is related to the Debye-Hückel theory of shielding, where potential of a single particle over the distances longer than the Debye length λ_{De} is effectively shielded and decays exponentially. Therefore, even in the case of long range inverse square forces like the Coulomb interaction between the particles, only the close range interaction on the distances $< \lambda_{De}$ must be modelled within the collision term and the long range interaction is intermediated by the macroscopic fields. The collisions then present local fluctuations and do not contribute to the mean values of the fields. This kind of wavelength splitting is applicable only when the electrons are weakly coupled, i.e. the kinetic energy of the species is significantly higher than the potential energy.

1.1.1 Fokker–Planck operator

In order to simplify the collision operator, several additional assumptions are made. First, the observed time scales are relatively short compared to the collision time, which can be defined as the time taken by an average particle to be deflected to the perpendicular direction. However, the number of single events is high per that time in collisionally-dominant plasma, implying that the deflection can be considered as a series of small angle collisions. It is in an agreement with the fact the plasma parameter $N_D = \frac{4\pi}{3} n_e \lambda_{De}^3 \gg 1$, so there is a high number of particles in the Debye sphere and the statistical treatment on this scale is meaningful. Moreover, the binary collisions are also elastic, conserving the relative velocity during the encounter. Finally, they can be superposed within the Debye sphere (i.e. distances $\leq \lambda_{De}$), as they are not correlated, and form a Markovian chain, where the event can be modelled by the probability ψ. In particular, the probability $\psi = \psi(\vec{v}, \Delta\vec{v})$ is introduced for the transition of the distribution function from velocity $\vec{v}$ to $\vec{v} + \Delta\vec{v}$. The distribution function then can be expressed as [39]:

$$f(\vec{x}, \vec{v}, t) = \int \psi(\vec{v} - \Delta\vec{v}, \Delta\vec{v}) f(\vec{x}, \vec{v} - \Delta\vec{v}, t - \Delta t)\, \mathrm{d}\Delta\vec{v}. \tag{5}$$

These considerations enable to expand the collision term to the Taylor series in the velocity increments. When this procedure is ceased after the second term following

the assumption on short time increment Δt, the Fokker–Planck operator is obtained:

$$\left(\frac{\partial f}{\partial t}\right)_{\text{coll}} = -\nabla_{\vec{v}} \cdot \left\{ f \left\langle \frac{\Delta \vec{v}}{\Delta t} \right\rangle \right\} + \frac{1}{2} \nabla_{\vec{v}} \nabla_{\vec{v}} : \left\{ f \left\langle \frac{\Delta \vec{v} \Delta \vec{v}}{\Delta t} \right\rangle \right\}. \tag{6}$$

The physical meaning of the terms can be identified. The first term is known as the dynamic friction and describes the process of slowing down, while the second term of diffusion is responsible for spreading of the distribution function and increase of entropy. The averaged collision coefficients appearing in (6) are defined as follows [9]:

$$\left\langle \frac{\Delta \vec{v}}{\Delta t} \right\rangle = \frac{1}{\Delta t} \int \psi(\vec{v}, \Delta \vec{v}) \Delta \vec{v} \, \mathrm{d}\vec{v}, \tag{7}$$

$$\left\langle \frac{\Delta \vec{v} \Delta \vec{v}}{\Delta t} \right\rangle = \frac{1}{\Delta t} \int \psi(\vec{v}, \Delta \vec{v}) \Delta \vec{v} \Delta \vec{v} \, \mathrm{d}\Delta v. \tag{8}$$

Then, transition to the center-of-mass system for the colliding particles α and β is performed, where the relative velocity $\vec{g} = \vec{v}_\beta - \vec{v}_\alpha$ is introduced ($g = |\vec{g}|$). For an interaction with the differential cross-section σ, the probability is given by the volume of the collision cylinder $\psi \, \mathrm{d}\Delta \vec{v} = \Delta t f_\beta g \sigma \, \mathrm{d}\vec{v}_\beta$. Substitution to (7–8) yields [40]:

$$\left\langle \frac{\Delta \vec{v}}{\Delta t} \right\rangle = \sum_\beta \frac{m_\beta}{m_\alpha + m_\beta} \int \Delta \vec{g} g f_\beta \sigma \, \mathrm{d}\vec{v}_\beta, \tag{9}$$

$$\left\langle \frac{\Delta \vec{v} \Delta \vec{v}}{\Delta t} \right\rangle = \sum_\beta \left(\frac{m_\beta}{m_\alpha + m_\beta} \right)^2 \int \Delta \vec{g} \Delta \vec{g} g f_\beta \sigma \, \mathrm{d}\vec{v}_\beta. \tag{10}$$

The derivation is continued by insertion of the Coulomb cross-section, which takes the form [39]:

$$\sigma(\chi, \theta) = \frac{b_0^2}{4 \sin^4 \frac{\chi}{2}}, \qquad b_0 = \frac{q_\alpha^2 q_\beta^2}{4 \pi \varepsilon_0 \mu_{\alpha\beta} g^2}, \qquad \mu_{\alpha\beta} = \frac{m_\alpha m_\beta}{m_\alpha + m_\beta}, \tag{11}$$

where χ is the deflection angle, θ azimuthal angle, ε_0 vacuum permittivity, q_α charge of the α species and $\mu_{\alpha\beta}$ reduced mass in the center-of-mass system. The integration is elaborated, while the divergence of the collision integral is overcome by limiting the impact parameter of the collisions to only the Debye length $\lambda_{D\alpha}$ following the aforementioned assumptions [41]. Finally, the form with the Rosenbluth potentials is obtained after some manipulations:

$$\left\langle \frac{\Delta \vec{v}}{\Delta t} \right\rangle = \sum_\beta \frac{m_\beta}{m_\alpha + m_\beta} Y_{\alpha\beta} \nabla_{\vec{v}_\alpha} \cdot H_{\alpha\beta}, \tag{12}$$

$$\left\langle \frac{\Delta \vec{v} \Delta \vec{v}}{\Delta t} \right\rangle = \sum_\beta \left(\frac{m_\beta}{m_\alpha + m_\beta} \right)^2 Y_{\alpha\beta} \nabla_{\vec{v}_\alpha} \nabla_{\vec{v}_\alpha} : G_{\alpha\beta}, \tag{13}$$

where the potentials themselves are defined as:

$$H_{\alpha\beta} = \int f_\beta \left|\vec{v}_\alpha - \vec{v}_\beta\right|^{-1} \mathrm{d}\vec{v}_\beta, \tag{14}$$

$$G_{\alpha\beta} = \int f_\beta \left|\vec{v}_\alpha - \vec{v}_\beta\right| \mathrm{d}\vec{v}_\beta. \tag{15}$$

The name potentials stems from the fact that they satisfy the Poisson equation in the form:

$$\nabla^2_{\vec{v}} H_{\alpha\beta} = -4\pi f_\beta, \qquad \nabla^2_{\vec{v}} G_{\alpha\beta} = 2H_{\alpha\beta}. \tag{16}$$

In the previous, it is assumed that $Y_{\alpha\beta}$ is slowly spatially variable and is given by:

$$Y_{\alpha\beta} = \frac{q_\alpha^2 q_\beta^2}{4\pi\varepsilon_0^2 \mu_{\alpha\beta}^2} \ln\Lambda_{\alpha\beta}, \qquad \Lambda_{\alpha\beta} = \frac{\lambda_{D\alpha}}{b_0}, \tag{17}$$

The term $\ln\Lambda_{\alpha\beta}$ is known as the Coulomb logarithm. The relative velocity g in the definition of the impact parameter b_0 (11) is approximated by the thermal velocity of the species usually. It is worth noting that $\Lambda_{\alpha\beta} \sim N_D$, so the Coulomb logarithm attains high values in ideal plasma, where $N_D \gg 1$. This correlates again with the fact that the small angle deflections are more frequent in the plasma, where it can be shown that the ratio between the contribution from subsequent small deflections and a single $\pi/2$ scattering is $\sim \ln\Lambda$ [42].

The Coulomb logarithm can be interpreted as a ratio between the maximal impact parameter b_{max} and "minimal" impact parameter b_{min}. The maximum cut-off is given by the Debye length, conforming with the assumptions made. The "minimal" value is given by b_0, which can be interpreted as the impact parameter of the $\pi/2$ deflection. However, this parameter does not present a true cut-off in the physical sense. It can be viewed as a mere convenient approximation of a more exact treatment [43]. Moreover, the definition is usually modified in the case of dense plasmas, where electrons undergo partial degeneracy [44]. In the first approximation, the quantum treatment of highly energetic encounters can be reduced to limiting the value by the reduced thermal de Broglie wavelength $\lambda_\hbar$ [39]. The impact parameters are then defined as:

$$b_{max} = \lambda_{De} = \sqrt{\frac{\varepsilon_0 k_B T_e}{n_e e^2}}, \qquad b_{min} = \max(b_0, \lambda_\hbar), \qquad \lambda_\hbar = \frac{\hbar}{\sqrt{m_e k_B T_e}}, \tag{18}$$

where k_B is the Boltzmann constant, $\hbar$ reduced Planck constant, n_e electron density, T_e electron kinetic temperature.

In addition to the Rosenbluth formalism used here, there exists a different approach based on the work of Landau [3], which treats the collisions as an anisotropic diffusion process in phase space. However, both formulations are equivalent and the Landau form of the operator can be derived from (6) by application of the differential identity $\nabla_{\vec{v}_\alpha}\nabla_{\vec{v}_\alpha} g = \underline{\underline{I}}/g - \vec{g}\vec{g}/g^3$, where $\underline{\underline{I}}$ is the identity tensor. After some manipu-

lations, the Landau form of the Fokker–Planck operator is obtained:

$$\left(\frac{\partial f_\alpha}{\partial t}\right)_{coll} = \sum_\beta \frac{1}{2} Y_{\alpha\beta} \frac{\mu_{\alpha\beta}^2}{m_\alpha} \nabla_{\vec{v}_\alpha} \cdot \int \frac{g^2 \underline{\underline{I}} - \vec{g}\vec{g}}{g^3} \cdot \left(\nabla_{\vec{v}_\alpha} \frac{f_\alpha}{m_\alpha} f_\beta - f_\alpha \nabla_{\vec{v}_\beta} \frac{f_\beta}{m_\beta} \right) \mathrm{d}\vec{v}_\beta. \tag{19}$$

The operator holds many convenient properties like full symmetry of the integral part in the index of the species and other, which are further explored in the subsequent chapters.

It is also of an interest to investigate the limit $m_\alpha \ll m_\beta$, which will be the case for the electron–ion scattering for example. Under these conditions, the second term in the Fokker–Planck–Landau operator (19) can be neglected compared to the first one. Furthermore, approximation of the relative velocities as $\vec{g} \approx \vec{v}_\alpha$ for nearly static scatterers yields the simplified form of the operator:

$$\left(\frac{\partial f_\alpha}{\partial t}\right)_{coll} = \sum_\beta \frac{1}{2} Y_{\alpha\beta} \frac{\mu_{\alpha\beta}^2}{m_\alpha^2} n_\beta \nabla_{\vec{v}_\alpha} \cdot \left(\frac{\vec{v}_\alpha^2 \underline{\underline{I}} - \vec{v}_\alpha \vec{v}_\alpha}{v_\alpha^3} \cdot \nabla_{\vec{v}_\alpha} f_\alpha \right), \tag{20}$$

where $n_\beta = \int f_\beta \, \mathrm{d}\vec{v}_\beta$ is the density of the β species.

1.1.2 Albritton–Williams–Bernstein–Swartz operator

The Fokker-Planck operator presented in chapter 1.1.1 has inherently non-linear structure. Consequently, numerical solution of the collisional processes is computationally demanding. However, when the physical system is close to the collisional equilibrium, even only a linearized form can be sufficient for the description of the relaxation processes. In order to simplify its form even further, an additional assumption is made that we are mostly interested in the behaviour of the high-velocity electrons ($v_e \gg v_{Te} = \sqrt{k_B T_e / m_e}$), which are responsible for most of the transport phenomena. However, the high-velocity limit of the Landau operator (20) exhibits the rapid $\sim v_e^{-3}$ decrease. Thus, even electrons with $v_e / v_{Te} \gtrsim 3$ have very low collision rate and are governed by the limit behaviour approximately. Under these conditions, the Fokker–Planck operator reduces to the form of the Fisch operator [45]:

$$\left(\frac{\partial f}{\partial t}\right)_{coll} = \bar{\nu}_{ee} n_e \left(\frac{1}{v^2} \frac{\partial}{\partial v} \left(\frac{v_{Te}^2}{v} \frac{\partial f}{\partial v} + f \right) + \frac{1 - v_{Te}^2/(2v^2)}{2v^3} \frac{\partial^2}{\partial \hat{\vec{v}}^2} f \right), \tag{21}$$

where $\bar{\nu}_{ee} = 1/4 Y_{ee}$. In this notation, the vector velocity $\vec{v}_e$ is replaced by the scalar velocity $v = |v_e|$ and the direction vector $\hat{\vec{v}} = \vec{v}_e / v$. The first term is then responsible for frictional deceleration of the electrons and their equilibration, while the second represents angular diffusion due to their scattering.

It can be noticed that the first term in (21) is proportional to $(v_{Te}/v)^2$, so it can be neglected in the first approximation for the high-velocity species. However, its importance is in equilibration of the distribution for the thermal species especially, so it is desired to retain it in the formula. When we consider only the relaxation near the equilibrium distribution f_M, the distribution function can be replaced by f_M in this

term directly. Furthermore, the second part of the angular diffusion operator can be omitted as it is of the second order as well. The formula (21) then reduces to the form of the operator proposed by Albritton, Williams, Bernstein and Swartz (AWBS) [46]:

$$\left(\frac{\partial f}{\partial t}\right)_{coll} = \bar{\nu}_{ee} n_e \left(\frac{1}{v^2}\frac{\partial}{\partial v}\left(f - f_M\right) + \frac{1}{2v^3}\frac{\partial^2}{\partial \hat{\vec{v}}^2} f\right). \tag{22}$$

An apparent problem of this definition is the requirement on an a priori known equilibrium distribution function, which is the Maxwell–Boltzmann distribution as long as pure collisions are considered. Its form can be deduced from (21), where the first term is zero for any $f \sim \exp(-v^2/(2v_{Te}^2))$ and the second for any isotropic function, but it is derived more rigorously from the original Landau operator in the next chapter (1.1.3). On the other hand, the operator still conserves the number of particles (second velocity moment, see 1.3) and is derived from the first principles directly.

1.1.3 Bhatnagar–Gross–Krook operator

The AWBS operator presented in chapter 1.1.2 greatly simplified the Landau operator (19). Though, derivatives in the velocity magnitudes and angles were still present, which complicate its application. When only the phenomenology of the processes is of an interest, the derivatives can be dropped all together. A linear operator of this kind was constructed by Bhatnagar, Gross and Krook [47]. It can be written as:

$$\left(\frac{\partial f_\alpha}{\partial t}\right)_{coll} = -\sum_\beta \nu_{\alpha\beta}(f_\alpha - f_{\beta 0}), \tag{23}$$

where $\nu_{\alpha\beta}$ is the collision frequency between α and β species. This kind of operator is called empirical, as the a priori known equilibrium distribution functions $f_{\beta 0}$ appear in the definition. In addition, an apparent drawback of this approach is violation of the conservation laws. Unless the collision frequency is independent of velocity, it does not conserve neither of mass, momentum nor energy [48]. On the other hand, convergence to the equilibrium is guaranteed and the distribution function remains positive.

This can be compared to the Fokker–Planck operator from chapter 1.1.1, which conserves all three mentioned collisional invariants as shown in chapter 1.2. Moreover, it satisfies the H-theorem, so the entropy $S = -\int f \log f \,\mathrm{d}\vec{v}$ increases in time. In order to prove this, (19) is simplified to the single specie case and rewritten as:

$$\left(\frac{\partial f_\alpha}{\partial t}\right)_{coll} \sim \nabla \cdot \int \frac{g^2 \underline{\underline{I}} - \vec{g}\vec{g}}{g^3} \cdot f f' \left(\nabla \log f - \nabla' \log f'\right) \mathrm{d}\vec{v}', \tag{24}$$

where $f' = f(\vec{x}, \vec{v}', t)$ and ∇' is the velocity derivative with respect to $\vec{v}'$ analogously. The Fokker–Planck–Landau operator in this form is multiplied by $-(1 + \log f)$ and integrated to obtain:

$$\frac{\partial S}{\partial t} \sim \int\int f f' \frac{g^2 \underline{\underline{I}} - \vec{g}\vec{g}}{g^3} : \left(\nabla \log f - \nabla' \log f'\right)\left(\nabla \log f - \nabla' \log f'\right) \mathrm{d}\vec{v}\,\mathrm{d}\vec{v}', \tag{25}$$

where Green's theorem was applied, assuming that f vanishes when $|\vec{v}| \to \infty$, and symmetry of the inner part of the operator was utilized. Due to symmetry and positivity of the expression for any $f > 0$, it can be concluded that $\partial S/\partial t \geq 0$ and a unique maximum exists. The maximum of entropy is attained when the distribution function reaches the Maxwell–Boltzmann distribution, which takes the following form for electrons:

$$f_M(\vec{x}, \vec{v}, t) = f_M(n_e, \vec{u}, T_e, \vec{v}) = n_e \left(\frac{m_e}{2\pi k_B T_e} \right)^{3/2} \exp\left(-\frac{m_e |\vec{v} - \vec{u}|^2}{2 k_B T_e} \right), \tag{26}$$

where $\vec{u}$ is the mean velocity. This provides the sought equilibrium solution, as it also zeros the collision operator itself. This function is then inserted to the Bhatnagar–Gross–Krook (BGK) operator (23) usually [47].

As a final remark, it should be noted that a conserving form of the BGK operator exists, where the parameters of density and temperature are unknown functions [49]. In order to determine them, a system of coupled integral equation must be solved, so the method its convenient tractability.

1.2 Velocity moments

The kinetic description of plasma presented so far used functions defined in the phase space. However, macroscopic measurable quantities like electron density or electric current appear in the configuration space only. The link between the two is provided by the velocity moments of the distribution function.

Proceeding further, elastic binary collisions are considered, following chapter 1.1. Under these conditions, mass, momentum and energy are conserved during the scattering event. In particular, they present special cases of summation invariants. In other words, the sum of the quantities before and after (denoted by prime) the collision is equal:

$$\phi_\alpha + \phi_\beta = \phi'_\alpha + \phi'_\beta, \tag{27}$$

where $\phi_\alpha \in \{m_\alpha, m_\alpha \vec{v}_\alpha, \frac{1}{2} m_\alpha |\vec{v}_\alpha|^2\}$.

The conservation properties for a continuous collision operator can be proved as well. Restricting ourself to the single specie case again, the Fokker–Planck–Landau operator in the form (24) is taken and multiplied by one of the summation invariants ϕ, which we consider as functions of velocity now. Integration over the velocity space is performed and the expression is rearranged in a similar manner to (25) to obtain:

$$\int \phi \left(\frac{\partial f_\alpha}{\partial t} \right)_{coll} \mathrm{d}\vec{v} \sim \int\int \left(\nabla\phi - \nabla'\phi' \right) \cdot \frac{g^2 \underline{\underline{I}} - \vec{g}\vec{g}}{g^3} . f f' \left(\nabla \log f - \nabla' \log f' \right) \mathrm{d}\vec{v}\, \mathrm{d}\vec{v}'. \tag{28}$$

This formulation shows that mass, momentum and energy are collisional invariants of the Fokker–Planck operator or any linear combination of 1, $\vec{v}$ and $|\vec{v}|^2$ is conserved more generally. Note that the property of the central tensor was used here, that its product with a vector collinear with $\vec{g}$ is zero.

The governing equations for the velocity moments of the distribution function are

obtained using the mean value operator defined as follows for functions $X = X(\vec{v})$:

$$\langle X \rangle_\alpha = \frac{\int X(\vec{v}_\alpha) f_\alpha(\vec{v}_\alpha)\,\mathrm{d}\vec{v}_\alpha}{\int f_\alpha(\vec{v}_\alpha)\,\mathrm{d}\vec{v}_\alpha}. \tag{29}$$

Multiplication of the kinetic equation (1) by ϕ_α and integration over the velocity space yields the moment equation:

$$\frac{\partial}{\partial t}\langle n_\alpha \phi_\alpha \rangle_\alpha + \nabla_{\vec{x}} \cdot \langle n_\alpha \vec{v}_\alpha \phi_\alpha \rangle_\alpha - \frac{q_\alpha}{m_\alpha} \langle n_\alpha (\vec{E} + \vec{v}_\alpha \times \vec{B}) \cdot \nabla_{\vec{v}} \phi_\alpha \rangle_\alpha = \int \phi_\alpha \sum_{\beta \neq \alpha} \left(\tfrac{\partial f_\alpha}{\partial t} \right)^\beta_{coll} \mathrm{d}\vec{v}_\alpha, \tag{30}$$

where the Lorenz force was inserted. The collision operator on the right-hand-side is expanded to the contributions from different species, where the contribution from the identical species α vanishes, since ϕ_α are collisional invariants. Due to the symmetry of the Fokker–Planck operator (19), it can be recognized that the sum of the kinetic equations gives on the right-hand-side:

$$\int \sum_\alpha \sum_\beta \phi_\alpha \left(\frac{\partial f_\alpha}{\partial t} \right)^\beta_{coll} \mathrm{d}\vec{v}_\alpha = 0, \tag{31}$$

so the total mass, momentum and energy are conserved by collisions.

1.2.1 Mass equation

The first invariant $\phi_\alpha = m_\alpha$ represents the zeroth velocity moment of the kinetic equation. Insertion of ϕ_α to the moment equation (30) yields:

$$\frac{\partial}{\partial t}(m_\alpha n_\alpha) + \nabla \cdot (m_\alpha n_\alpha \vec{u}_\alpha) = 0, \tag{32}$$

where we restricted ourselves only to the single specie case, so the collisional contributions to the equation are zero due to the collisional invariance. This simplification is applied even for other velocity moments for brevity.

In the previous, the definitions of the integral and mean quantities of the particle density and mean velocity were used respectively:

$$n_\alpha = \int f_\alpha \,\mathrm{d}\vec{v}, \qquad \vec{u}_\alpha = \langle \vec{v}_\alpha \rangle_\alpha = \frac{1}{n_e} \int \vec{v} f_\alpha \,\mathrm{d}\vec{v}. \tag{33}$$

It can be recognized from the form of (32) that it represents the law of mass conservation, since integration over the whole volume Ω of the configuration space yields:

$$\frac{\mathrm{d}M_\alpha}{\mathrm{d}t} = -\oint_\Gamma \rho_\alpha \vec{u}_\alpha \cdot \vec{n}\,\mathrm{d}\Gamma, \tag{34}$$

where $\rho_\alpha = m_\alpha n_\alpha$ is the mass density, $M_\alpha = \int_\Omega \rho_\alpha \,\mathrm{d}\vec{x}$ the total mass and $\vec{n}$ the outer unit normal defined on the boundary $\Gamma = \partial\Omega$. Provided that the system is closed, i.e. there is no exchange of particles over the boundaries, the total mass is conserved.

A closely related phenomenon to the mass conservation is the law of charge conservation. Taking divergence of the Ampère's law (3) and Faraday's law (4) yields:

$$\frac{\partial}{\partial t}\nabla\cdot\vec{E} = -\frac{1}{\varepsilon_0}\nabla\cdot\vec{j}_\alpha, \tag{35}$$

$$\frac{\partial}{\partial t}\nabla\cdot\vec{B} = 0, \tag{36}$$

where $\vec{j}_\alpha = q_\alpha n_\alpha u_\alpha$ is the electric current. Assume that Gauss's law for the electric field and magnetic field holds at the beginning of the reference time in the form:

$$\nabla\cdot\vec{E} = \frac{\rho_\alpha^q}{\varepsilon_0}, \qquad \nabla\cdot\vec{B} = 0, \tag{37}$$

where the charge density is defined as $\rho_\alpha^q = q_\alpha n_\alpha$. Substitution back to (35) and (36) yields the law of non-existence of magnetic monopoles (also known as magnetic Gauss's law) and the continuity equation for electric charge:

$$\frac{\partial}{\partial t}\rho_\alpha^q + \nabla\cdot\vec{j}_\alpha = 0. \tag{38}$$

Similarly to (34), the total charge $Q_\alpha = \int_\Omega q_\alpha n_e \,\mathrm{d}\vec{x}$ is conserved when the electric currents through boundaries are zero. Therefore, the electrodynamic theory behaves consistently with the kinetic theory for the collisional invariant $\phi_\alpha = q_\alpha$.

1.2.2 Momentum equation

The first velocity moment of the kinetic equation (1) governs the momentum $\rho_\alpha\vec{u}_\alpha$. It is obtained from (30) by choosing the invariant $\phi_\alpha = m_\alpha\vec{v}_\alpha$:

$$\frac{\partial}{\partial t}(\rho_\alpha\vec{u}_\alpha) + \nabla\cdot(\rho_\alpha\vec{u}_\alpha\vec{u}_\alpha + \rho_\alpha\langle\vec{w}_\alpha\vec{w}_\alpha\rangle_\alpha) = \rho_\alpha^q\vec{E} + \vec{j}_\alpha\times\vec{B}, \tag{39}$$

where $\vec{w}_\alpha = \vec{v}_\alpha - \vec{u}_\alpha$ is the chaotic part of the velocity. The two components of the stress tensor appearing in the divergence can be identified as the dynamic pressure and kinetic/thermal pressure:

$$\underline{\underline{D}}^\alpha = \rho_\alpha\vec{u}_\alpha\vec{u}_\alpha = m_\alpha\int\vec{u}_\alpha\vec{u}_\alpha f_\alpha\,\mathrm{d}\vec{v}, \tag{40}$$

$$\underline{\underline{P}}^\alpha = \rho_\alpha\langle\vec{w}_\alpha\vec{w}_\alpha\rangle_\alpha = m_\alpha\int(\vec{v}-\vec{u}_\alpha)(\vec{v}-\vec{u}_\alpha)f_\alpha\,\mathrm{d}\vec{v}, \tag{41}$$

Similarly to the continuity equation (32), the integral over the domain gives rise to the law of momentum conservation:

$$\frac{\mathrm{d}\vec{P}_\alpha}{\mathrm{d}t} = -\oint_\Gamma(\underline{\underline{D}}^\alpha + \underline{\underline{P}}^\alpha)\cdot\vec{n}\,\mathrm{d}\Gamma + \int_\Omega\rho_\alpha^q\vec{E} + \vec{j}_\alpha\times\vec{B}\,\mathrm{d}\vec{x}, \tag{42}$$

where the total momentum of α species is defined as $\vec{P}_\alpha = \int_\Omega\rho_\alpha\vec{u}_\alpha\,\mathrm{d}\vec{x}$. The contribution

to the boundary integral from $\underline{\underline{D}}^{\alpha}$ is zero, when the system is closed, since $\vec{u}_\alpha \cdot \vec{n} = 0$. The pressure part can be interpreted as the macroscopic normal and tangential forces acting at the boundary and becomes zero for an isolated system. However, the Lorenz force action does not vanish in general, since the momentum is exchanged with the fields as illustrated further.

The field counterpart of the momentum equation is obtained by vector multiplication of (3) and (4) by $\vec{B}$ and $\vec{E}$ respectively:

$$\frac{\partial \vec{E}}{\partial t} \times \vec{B} - c^2(\nabla \times \vec{B}) \times \vec{B} = -\frac{1}{\varepsilon_0}\vec{j} \times \vec{B}, \tag{43}$$

$$\vec{E} \times \frac{\partial \vec{B}}{\partial t} + (\nabla \times \vec{E}) \times \vec{E} = 0. \tag{44}$$

The antisymmetric products are reduced to a symmetric tensor through the differential identity:

$$(\nabla \times \vec{A}) \times \vec{A} = (\vec{A}\nabla)\vec{A} - \frac{1}{2}\nabla|\vec{A}|^2 = \nabla \cdot \left(\vec{A}\vec{A} - \frac{1}{2}|\vec{A}|^2 \underline{\underline{I}}\right) - (\nabla \cdot \vec{A})\vec{A}. \tag{45}$$

When applied to the system (43–44) considering the Gauss's law (37), the sum of the equations results in the equation of electromagnetic momentum:

$$\frac{\partial}{\partial t}\vec{\gamma}_{EM} - \nabla \cdot \left(\underline{\underline{T}}^{E} + \underline{\underline{T}}^{B}\right) = -\rho_\alpha^q \vec{E} - \vec{j}_\alpha \times \vec{B}, \tag{46}$$

where $\vec{\gamma}_{EM} = \varepsilon_0 \vec{E} \times \vec{B}$ is the electromagnetic momentum vector and $\underline{\underline{T}}^{E}$,$\underline{\underline{T}}^{B}$ are the electric and magnetic parts of the Maxwell's stress tensor:

$$\underline{\underline{T}}^{E} = \varepsilon_0 \left(\vec{E}\vec{E} - \frac{1}{2}|\vec{E}|^2 \underline{\underline{I}}\right), \qquad \underline{\underline{T}}^{B} = \mu_0^{-1} \left(\vec{B}\vec{B} - \frac{1}{2}|\vec{B}|^2 \underline{\underline{I}}\right). \tag{47}$$

Integration of (46) over the configuration space yields the law of electrodynamic momentum conservation:

$$\frac{\mathrm{d}\vec{P}_{EM}}{\mathrm{d}t} = \oint_\Gamma (\underline{\underline{T}}^{E} + \underline{\underline{T}}^{B}) \cdot \vec{n}\,\mathrm{d}\Gamma - \int_\Omega \rho_\alpha^q \vec{E} + \vec{j}_\alpha \times \vec{B}\,\mathrm{d}\vec{x}. \tag{48}$$

The boundary term is obviously zero for the normal components of the fields and the second term is again the interaction part or the action of Lorentz force in other words, which appeared in (42). Together, they form the sought law of total momentum conservation for $\vec{P}_\alpha + \vec{P}_{EM}$.

1.2.3 Energy equation

The last, but not least, collisional invariant is the kinetic energy $\phi_\alpha = \frac{1}{2}m_e|\vec{v}|^2$ and the corresponding second velocity moment of the kinetic equation (1). Insertion to the

moment equation (30) yields:

$$\frac{\partial}{\partial t}\left(\frac{1}{2}\rho_\alpha u_\alpha^2+\frac{1}{2}\rho_\alpha\langle w_\alpha^2\rangle_\alpha\right)+\nabla\cdot\rho_\alpha\left(\frac{1}{2}u_\alpha^2\vec{u}_\alpha+\frac{1}{2}\langle w_\alpha^2\rangle_\alpha\vec{u}_\alpha+\right.$$
$$\left.+\langle\vec{w}_\alpha\vec{w}_\alpha\rangle_\alpha\cdot\vec{u}_\alpha+\frac{1}{2}\langle w_\alpha^2\vec{w}_\alpha\rangle_\alpha\right)=\vec{j}_\alpha\cdot\vec{E},\quad(49)$$

where identification with the kinetic pressure tensor (41), kinetic energy density $\epsilon_\alpha^k = 1/2\rho_\alpha u_\alpha^2$, internal energy density ϵ_α^i and heat flux $\vec{q}_\alpha$ can be made. The latter are defined as:

$$\epsilon_\alpha^i=\frac{1}{2}\rho_\alpha\langle w_\alpha^2\rangle_\alpha=\frac{1}{2}m_\alpha\int|\vec{v}-\vec{u}_\alpha|^2\,f_\alpha\,\mathrm{d}\vec{v},\quad(50)$$
$$\vec{q}_\alpha=\frac{1}{2}\rho_\alpha\langle w_\alpha^2\vec{w}_\alpha\rangle_\alpha=\frac{1}{2}m_\alpha\int|\vec{v}-\vec{u}_\alpha|^2\,(\vec{v}-\vec{u}_\alpha)f_\alpha\,\mathrm{d}\vec{v}.\quad(51)$$

After the substitution, the equation of energy reads:

$$\frac{\partial}{\partial t}\left(\epsilon_\alpha^k+\epsilon_\alpha^i\right)+\nabla\cdot\left(\epsilon_\alpha^k\vec{u}_\alpha+\epsilon_\alpha^i\vec{u}_\alpha+\underline{\underline{P}}^\alpha\cdot\vec{u}_\alpha+\vec{q}_\alpha\right)=\vec{j}_\alpha\cdot\vec{E}.\quad(52)$$

Integration of (52) over space provides the law of energy conservation for the total energy of α species $E_\alpha=\int_\Omega\epsilon_\alpha^k+\epsilon_\alpha^i\,\mathrm{d}\vec{x}$, which takes the form:

$$\frac{\mathrm{d}E_\alpha}{\mathrm{d}t}=-\oint_\Gamma\left((\epsilon_\alpha^i+\epsilon_\alpha^k)\vec{u}_\alpha\cdot\vec{n}+\underline{\underline{P}}^\alpha:\vec{u}_\alpha\vec{n}+\vec{q}_\alpha\cdot\vec{n}\right)\mathrm{d}\Gamma+\int_\Omega\vec{j}_\alpha\cdot\vec{E}\,\mathrm{d}\vec{x}.\quad(53)$$

The first boundary term is convective and is zero when there is no mass flow over the boundaries. The pressure part describes the action of the boundary forces and becomes zero together with the normal heat flux for an isolated system. The last part describes the total amount of Joule heating, which presents an interaction term between the α particles and electromagnetic fields.

The field counterpart of the energy equation is obtained from (3) and (4) when multiplied by $\vec{E}$ and $\vec{B}$ respectively. The system then takes the form:

$$\frac{1}{2}\frac{\partial}{\partial t}|\vec{E}|^2-c^2\nabla\times\vec{B}\cdot\vec{E}=-\frac{1}{\varepsilon_0}\vec{j}_\alpha\cdot\vec{E},\quad(54)$$
$$\frac{1}{2}\frac{\partial}{\partial t}|\vec{B}|^2+\nabla\times\vec{E}\cdot\vec{B}=0.\quad(55)$$

A linear combination of the equation then gives the energy equation for electromagnetic field after some manipulations:

$$\frac{\partial}{\partial t}\epsilon_{EM}+\nabla\cdot\vec{S}=\vec{j}_\alpha\cdot\vec{E},\quad(56)$$

where the density of electromagnetic energy and Poynting vector are defined as follows:

$$\epsilon_{EM} = \frac{1}{2}\varepsilon_0|\vec{E}|^2 + \frac{1}{2}\mu_0^{-1}|\vec{B}|^2, \qquad \vec{S} = \mu_0^{-1}\vec{E}\times\vec{B} = \frac{\vec{\gamma}_{EM}}{c^2}. \tag{57}$$

The law of electromagnetic energy conservation can be derived from (56) by integration over space:

$$\frac{\mathrm{d}E_{EM}}{\mathrm{d}t} = -\oint_\Gamma \vec{S}\cdot\vec{n}\,\mathrm{d}\Gamma - \int_\Omega \vec{j}_\alpha\cdot\vec{E}\,\mathrm{d}\vec{x}. \tag{58}$$

Provided that the Poynting vector $\vec{S}$ is zero at the boundary, the electromagnetic energy is conserved except the action on particles through the Joule heating term $\vec{j}_\alpha\cdot\vec{E}$. However, comparison of (58) with (53) reveals that the total energy $E_\alpha + E_{EM}$ is conserved.

1.3 Cartesian tensor expansion

The kinetic theory described the distribution function $f = f(\vec{x},\vec{v},t)$ in 7 dimensions of the phase space essentially. Consequently, solution of the kinetic equation (1) is cumbersome, when a non-linear collision operator like the one presented in chapter 1.1.1 is applied especially. For this reason, it is desirable to expand the distribution function and solve only a finite set of equations in a lower number of dimensions. Expansions in spherical harmonics or Cartesian tensors belong to the most frequently used. The rationale of this choice can be seen in the fact that spherical harmonics present eigenvectors of the diffusion operator, greatly simplifying the structure of the Fokker–Planck collision operator. Moreover, the Maxwell–Boltzmann distribution (26) is modelled by the zeroth mode already and higher modes present only anisotropic corrections to it. Alternatively, an expansion in Cartesian tensors can be made, which is also pursued here, but the two approaches are formally equivalent [50].

In the following, the distribution function f is expanded in Cartesian tensors as:

$$f(\vec{x},\vec{v},t) = f(\vec{x},\hat{\vec{v}},v,t) = f_0(\vec{x},v,t) + \vec{f}_1(\vec{x},v,t)\cdot\hat{\vec{v}} + \underline{\underline{f_2}}(\vec{x},v,t) : \hat{\vec{v}}\hat{\vec{v}} + \ldots, \tag{59}$$

where $v = |\vec{v}|$ and $\hat{\vec{v}} = \vec{v}/v$. The term f_0 is the isotropic part of the distribution function, $\vec{f}_1$ the first order tensor (i.e. vector) anisotropic correction and $\underline{\underline{f_2}}$ is the second order tensor anisotropic correction, etc. Note that the series is infinite, but it is truncated after several terms typically, as mainly electron–ion collisions isotropize the electron distribution function due to the high mass ratio of the species, which leads to a high momentum exchange during an encounter. However, the energy exchange is significantly slower due to this ratio, so rather the direction of momentum is affected. In a typical collisional plasma, the ordering $f_0 \gg |\vec{f}_1| \gg |\vec{f}_2|$ holds consequently.

The velocity moments of the distribution function, which were defined in chapter

1.2, then take the form:

$$n_e = 4\pi \int_0^{+\infty} f_0 v^2 \,\mathrm{d}v, \qquad \vec{u}_e = \frac{1}{n_e}\frac{4\pi}{3}\int_0^{+\infty} \vec{f}_1 v^3 \,\mathrm{d}v, \tag{60}$$

$$\epsilon_e^T = \frac{1}{2} m_e 4\pi \int_0^{+\infty} f_0 v^4 \,\mathrm{d}v, \qquad \vec{q}_e^T = \frac{1}{2} m_e \frac{4\pi}{3}\int_0^{+\infty} \vec{f}_1 v^5 \,\mathrm{d}v, \tag{61}$$

while the pressure tensors are obtained in the form:

$$\underline{\underline{D}}^e + \underline{\underline{P}}^e = \frac{4\pi}{3} m_e \left(\int_0^{+\infty} f_0 v^4 \,\mathrm{d}v \right) \underline{\underline{I}} + \frac{8\pi}{15} m_e \int_0^{+\infty} \underline{\underline{f_2}} v^4 \,\mathrm{d}v. \tag{62}$$

It must be noted that ϵ_e^T and $\vec{q}_e^T$ are rather the total quantities related to (50), (51) by the following relations:

$$\epsilon_e^T = \epsilon_e^k + \epsilon_e^i, \qquad \vec{q}_e^T = \vec{q}_e + \epsilon_e^T \vec{u}_e + \underline{\underline{P}}^e \cdot \vec{u}_e. \tag{63}$$

It is enlightening and also serves for the purposes of later reference to derive the splitting of the pressure tensor $\underline{\underline{P}}^e = p_e \underline{\underline{I}} + \Pi$ to the scalar pressure p_e and the anisotropic part Π responsible for viscous effects:

$$p_e = \frac{4\pi}{3} m_e \left(\int_0^{+\infty} f_0 v^4 \,\mathrm{d}v \right) - \frac{1}{3}\rho_e u_e^2, \qquad \underline{\underline{\Pi}}^e = \frac{8\pi}{15} m_e \int_0^{+\infty} \underline{\underline{f_2}} v^4 \,\mathrm{d}v + \frac{1}{3}\rho_e u_e^2 - \rho_e \vec{u}_e \vec{u}_e. \tag{64}$$

From the given expression, it is clear that f_0 contributes to the scalar pressure and $\underline{\underline{f_2}}$ to the anisotropic part only.

To proceed further, the expansion (59) is inserted to the kinetic equation (2), where the equations for the first two contributions parts of the distribution function give:

$$\frac{\partial f_0}{\partial t} + \frac{v}{3}\nabla \cdot \vec{f}_1 - \frac{e}{m_e}\frac{1}{3v^2}\frac{\partial}{\partial v}\left(v^2 \vec{E} \cdot \vec{f}_1 \right) = C_0, \tag{65}$$

$$\frac{\partial \vec{f}_1}{\partial t} + v\nabla f_0 - \frac{e}{m_e}\frac{\partial f_0}{\partial v}\vec{E} - \frac{e}{m_e}\vec{B} \times \vec{f}_1 + \\ + \frac{2}{5} v \nabla \cdot \underline{\underline{f_2}} - \frac{2e}{5 m_e v^3}\frac{\partial}{\partial v}\left(v^3 \vec{E} \cdot \underline{\underline{f_2}} \right) = C_1. \tag{66}$$

The equations for higher anisotropic corrections can be found in the literature and are not detailed here [50]. The tensor $\underline{\underline{f_2}}$ is assumed to be given by a closure relation, which is a function of f_0 and $\vec{f}_1$. When $\underline{\underline{f_2}}$ is the zero tensor, the classical P1 model is obtained. Other choices are discussed in chapter 3.2.

The symbols C_0 and C_1 represent the tensor expansion of the collision operator on the right-hand-side. Their complete prescription for the Fokker–Planck operator can be found in the literature [39]. However, we are particularly interested in a simplified

form of the collision operator for a two-specie plasma:

$$\left(\frac{\partial f}{\partial t}\right)_{coll} = C_{ee} + C_{ei} = C_{ee} + \frac{\nu_{ei}}{2}\frac{\partial^2}{\partial \hat{\vec{v}}^2} f = \\ = C_{ee} + \frac{\nu_{ei}}{2}\left(\frac{1}{\sin\varphi}\frac{\partial}{\partial\varphi}\left(\sin\varphi\frac{\partial}{\partial\varphi} f\right) + \frac{1}{\sin^2\varphi}\frac{\partial^2}{\partial\theta^2} f\right), \quad (67)$$

where ϕ is the polar angle and θ the azimuthal angle of the velocity vector in spherical coordinates. The symbol C_{ee} represents the Fokker–Planck operator for electron–electron collisions following the definition (6) and C_{ei} is the electron–ion collision operator in the approximation (20). The simplification made here is that electron–ion collisions lead to pure scattering of the electrons on a static background of ions. This procedure assumes that the thermal velocities of ions are significantly lower than that of electrons, i.e. $v_{Ti} \ll v_{Te}$ ($v_{T\alpha}^2 = k_B T_\alpha / m_\alpha$). Moreover, the system is observed for notably shorter times than the thermal relaxation time $1/\nu_{ei}^{\epsilon} \sim m_i/(m_e\nu_{ei})$. Due to the high mass ratio between the ions and electrons typically, the approximation is justified. The collisional terms C_0 and C_1 then take the form:

$$C_0 = \frac{\bar{\nu}_{ee}}{v^2}\frac{\partial}{\partial v}\left(C(f_0)f_0 + D(f_0)\frac{\partial f_0}{\partial v}\right) + C_{11}(\vec{f_1}, \vec{f_1}), \quad (68)$$

$$C_1 = -\nu_{ei}\vec{f_1} + C_{01}(f_0, \vec{f_1}), \quad (69)$$

where the Rosenbluth potentials of friction C and diffusion D are defined as:

$$C(f_0) = 4\pi\int_0^v f_0(v')v'^2 dv', \quad (70)$$

$$D(f_0) = \frac{4\pi}{v}\int_0^v v'^2\int_{v'}^{+\infty} f_0(v'')v''dv''dv'. \quad (71)$$

It is evident from the form of (68–69) that the tensor expansion separates the maxwellization process mediated by C_0 and isotropization process mediated by C_1. The angular diffusion operator (also known as Laplace–Beltrami) from (67) simplifies substantially, manifesting the convenient construction of the expansion basis, where spherical harmonics are eigenvectors of this operator. It can be immediately recognized that the basis function $\cos\varphi$ coincides with the scalar product of $\hat{\vec{v}}$. The collision term C_{01} is responsible for the electron–electron scattering and holds main importance for low-Z plasmas, otherwise electron–ion collisions dominate due to favourable charge and mass ratio. In the Lorentz approximation (for $Z \to \infty$), this term is neglected completely. Finally, the term C_{11} describes growth of f_0 due to electron–electron scattering, but it presents a second-order effect $\sim |\vec{f_1}|^2$ and can be neglected usually (assuming $|\vec{f_1}| \ll f_0$). Definitions of both can be found in the literature and it is not detailed due to their complex formulation [39].

For completeness, the formulae for the collision frequencies read:

$$\nu_{ee}(v) = \bar{\nu}_{ee} n_e v^{-3} = \frac{n_e e^4}{4\pi\varepsilon_0^2 m_e^2} v^{-3} \log\Lambda_{ee}, \tag{72}$$

$$\nu_{ei}(v) = \frac{Z^2 n_i e^4}{4\pi\varepsilon_0^2 m_e^2} v^{-3} \log\Lambda_{ei}, \tag{73}$$

where Z is the mean ionization. The expressions can be derived from the Fokker–Planck operator (6) after substitution of the Maxwell–Boltzmann distribution (26) as the target distribution f_β, which linearises the operator effectively. It can be shown that a solution exists in the form of Chandrasekhar function [51], which behaves as $\sim v^{-3}$ in the high velocity limit and yields the sought formulae when the approximation $m_e/m_i \approx 0$ is made.

2 Magnetohydrodynamics

The fluid model describes plasma as a continuum governed by the equations for macroscopic quantities. The single-specie model was derived in chapter 1.2 from the kinetic theory through velocity moments of the kinetic equation (1). In particular, it is comprised of the mass equation (32), momentum equation (39) and energy equation (52). These macroscopic quantities then parametrize the shifted Maxwell–Boltzmann distribution (26), which presents the assumed solution of the kinetic problem within the fluid description. Only infinitesimal perturbations are considered classically, in order to model the transport processes as described in chapter 3. This procedure is valid only for well thermalized plasma ($t \gg \nu_{\alpha\alpha}^{-1}$), isotropized ($t \gg \nu_{\alpha}^{-1}$), where ν_α is the total scattering frequency and dominated by kinetic phenomena ($\epsilon_\alpha^i \gg \epsilon_{EM}$). Under these conditions, the solution attains the near (collisional) equilibrium limit.

2.1 Multi-specie fluid model

The single-specie model derived in chapter 1.2 can be then extended to the multi-specie case by adding the inter-specie interaction according to (30):

$$\frac{\partial \rho_\alpha}{\partial t} + \nabla \cdot (\rho_\alpha \vec{u}_\alpha) = 0, \tag{74}$$

$$\frac{\partial \rho_\alpha \vec{u}_\alpha}{\partial t} + \nabla \cdot (\rho_\alpha \vec{u}_\alpha \vec{u}_\alpha) = -\nabla \cdot \underline{\underline{P}}^\alpha + \rho_\alpha^q \vec{E} + \vec{j}_\alpha \times \vec{B} + \vec{g}_{\alpha\beta}, \tag{75}$$

$$\frac{\partial \rho_\alpha \varepsilon_\alpha^T}{\partial t} + \nabla \cdot \left(\rho_\alpha \varepsilon_\alpha^T \vec{u}_\alpha\right) = -\nabla \cdot (\underline{\underline{P}}^\alpha \cdot \vec{u}_\alpha) - \nabla \cdot \vec{q}_\alpha + \vec{j}_\alpha \cdot \vec{E} + g_{\alpha\beta}, \tag{76}$$

where $\varepsilon_\alpha^T = \epsilon_\alpha^T / \rho_\alpha$ is the total specific energy of α species. The collisional coupling between the species is mediated by the exchange terms:

$$\vec{g}_{\alpha\beta} = \int m_\alpha \vec{v}_\alpha \sum_{\beta \neq \alpha} \left(\frac{\partial f_\alpha}{\partial t}\right)_{coll}^{\beta} \mathrm{d}\vec{v}_\alpha, \tag{77}$$

$$g_{\alpha\beta} = \int \frac{1}{2} m_\alpha |\vec{v}_\alpha|^2 \sum_{\beta \neq \alpha} \left(\frac{\partial f_\alpha}{\partial t}\right)_{coll}^{\beta} \mathrm{d}\vec{v}_\alpha. \tag{78}$$

The multi-specie model (74–76) considers only momentum and energy transfers between the species based on the form of the collision operator (19), where contribution to the zeroth velocity moment is always zero. In other words, the processes resulting in exchange of particles like ionization or recombination are not modelled dynamically, but left for the stationary closure model described later in chapter 2.4.

2.2 One-fluid magneto-hydrodynamic model

The multi-specie model of chapter 2.1 offers a complete fluid description of the plasma when the self-consistent fields are obtained from the electromagnetic closure, i.e. the Maxwell's equations (3–4). However, the model represents a non-linear problem, ex-

pensive to solve on long time scales. Therefore, the model is reduced to the one-fluid description, provided that a quasi-static electric field develops between the species and couples them together effectively ($t \gg \omega_{p\alpha}^{-1}$). Hence, the electrically charged particles of different species are separated only on distances of the Debye length $\lambda_{D\alpha}$ and the plasma can be considered quasi-neutral ($\sum_\alpha \rho_\alpha^q \approx 0$). The flows of the particles do not need to be modelled separately as their profiles are inter-dependent. Consequently, the plasma is described with the one-fluid quantities like the mass density ρ, center of mass velocity $\vec{u}$ and specific internal energy ε:

$$\rho = \sum_\alpha \int m_\alpha f_\alpha \,\mathrm{d}\vec{v}_\alpha, \tag{79}$$

$$\vec{u} = \frac{\sum_\alpha \int m_\alpha \vec{v}_\alpha f_\alpha \,\mathrm{d}\vec{v}_\alpha}{\sum_\alpha \int m_\alpha f_\alpha \,\mathrm{d}\vec{v}_\alpha}, \tag{80}$$

$$\varepsilon = \frac{\sum_\alpha \int \frac{1}{2} m_\alpha |\vec{v}_\alpha - \vec{u}_\alpha|^2 f_\alpha \,\mathrm{d}\vec{v}_\alpha}{\sum_\alpha \int m_\alpha f_\alpha \,\mathrm{d}\vec{v}_\alpha}. \tag{81}$$

In particular, the velocities are $\vec{u} \approx \vec{u}_e \approx \vec{u}_i$ and densities are $n_e = Z n_i$ for electron–ion plasma, where Z is the mean ionization. Finally, the one-fluid model is obtained by summing over the α index the system (74–76):

$$\frac{\partial}{\partial t}\,\rho + \nabla \cdot (\rho \vec{u}) = 0, \tag{82}$$

$$\frac{\partial}{\partial t}\,(\rho \vec{u}) + \nabla \cdot (\rho \vec{u}\vec{u}) = -\nabla \cdot \underline{\underline{P}} - \nabla \cdot \underline{\underline{P}}^B, \tag{83}$$

$$\frac{\partial}{\partial t}\,(\rho(\tfrac{1}{2}u^2 + \varepsilon)) + \nabla \cdot (\rho(\tfrac{1}{2}u^2 + \varepsilon)\vec{u}) = -\nabla \cdot (\underline{\underline{P}} \cdot \vec{u}) - \nabla \cdot \vec{q} + \vec{j} \cdot \vec{E}, \tag{84}$$

where $\vec{j} = \sum_\alpha \vec{j}_\alpha$ is the electric current, $\vec{q} = \sum_\alpha \vec{q}_\alpha$ heat flux, $\underline{\underline{P}} = \sum_\alpha \underline{\underline{P}}_\alpha$ and $\underline{\underline{P}}^B = -\underline{\underline{T}}^B$ is the magnetic pressure tensor. The contributions from the collisional momentum and energy exchange terms cancel out according to (31) and the Lorenz force densities vanish due to the quasineutrality condition. However, solenoidal currents can exist even under the quasi-neutrality requirement, because the continuity equation (38) only restricts the potential (or divergent) part. In magnetohydrodynamics, where the interplay with a magnetic field is modelled, the solenoidal currents are given by the electrostatic Ampère's law $\vec{j} = \mu_0^{-1} \nabla \times \vec{B}$. Their substitution to the Hall term $\vec{j} \times \vec{B}$ yields the magnetic pressure term $-\nabla \cdot \underline{\underline{P}}^B$. Although, the term is proportional to the magnetic energy $1/(2\mu_0)|\vec{B}|^2$ according to the definition (47) and the kinetic pressure tensor $\underline{\underline{P}}$ to the internal energy $\rho\varepsilon$, so it can be neglected in ideal hydrodynamics, where the assumption $\epsilon_{EM} \ll \rho\varepsilon$ is enforced strictly.

The expression for the electric field can be obtained from the momentum equations (75) when multiplied by ρ/ρ_α and summed over the α index, while the velocities are considered equal already. This procedure can be seen as relative temporal variations of the contributions to the total momentum and the electric field is constructed

in such way to zero them all. Finally, the expression for the electric field is obtained:

$$\vec{E} = -\vec{u} \times \vec{B} + \sigma^{-1}\vec{j} + \left(\sum_\alpha \frac{q_\alpha}{m_\alpha}\right)^{-1} \sum_\alpha \frac{1}{\rho_\alpha} \nabla \cdot \underline{\underline{P}}^\alpha, \tag{85}$$

where σ is the total electric conductivity originating from the collisional terms $\vec{g}_{\alpha\beta}$, where a collisional friction between the species exists. A more detailed analysis of the collisional effects yields (115) presented in chapter 3.1.1. In the case of electron–ion plasma, the situation simplifies notably, because the mass and charge ratio favours the electron pressure contribution $-\nabla \cdot \underline{\underline{P}}^e/(en_e)$ in the last part.

The procedure leading to the one-fluid model (82–84) assumed that there exists a single equilibrium distribution for all species. However, the electron–ion energy exchange time is related to the electron–electron thermalization time as $(\nu^\epsilon_{ei})^{-1} \sim m_i/m_e Z^{-2}\nu^{-1}_{ee}$, so the condition $t \gg \nu^{-1}_{ee}$ can be satisfied securely, but $t \gg (\nu^\epsilon_{ei})^{-1}$ may not. In other words, the thermal equilibrium is reached significantly earlier for electrons separately than the common equilibrium between the species. It is then possible to retain the separate energy equations for electrons and ions instead of the common one (84). This approach is known as the two-temperature one-fluid model. The energy equations then read:

$$\begin{aligned}\frac{\partial}{\partial t}\left(\rho_e(\tfrac{1}{2}u^2 + \varepsilon_e)\right) + \nabla \cdot \left(\rho_e(\tfrac{1}{2}u^2 + \varepsilon_e)\vec{u}\right) &= -\nabla \cdot (\underline{\underline{P}}^e \cdot \vec{u}) - \nabla \cdot \vec{q}_e + \vec{j}_e \cdot \vec{E} + \\ &\quad + G_{ei}(T_i - T_e), \end{aligned} \tag{86}$$

$$\begin{aligned}\frac{\partial}{\partial t}\left(\rho_i(\tfrac{1}{2}u^2 + \varepsilon_i)\right) + \nabla \cdot \left(\rho_i(\tfrac{1}{2}u^2 + \varepsilon_i)\vec{u}\right) &= -\nabla \cdot (\underline{\underline{P}}^i \cdot \vec{u}) - \nabla \cdot \vec{q}_i + \vec{j}_i \cdot \vec{E} + \\ &\quad + G_{ie}(T_e - T_i), \end{aligned} \tag{87}$$

where most of the terms cancel out as in (84), because the quasi-neutrality still holds, but G_{ei}, G_{ie} are the heat exchange coefficients for the linearized heat transfer approximating g_{ei}, g_{ie} terms respectively. It is applicable only for gentle deviations from the common equilibrium, i.e. $G_{ei}|T_e - T_i|\Delta t \ll 1$ holds ideally (Δt is a typical resolved time scale). Moreover, the symmetry $G_{ei} = G_{ie}$ is required to satisfy energy conservation.

2.3 Lagrangian magnetohydrodynamics

The fluid model presented in chapter 2.2 used the Eulerian description, where the reference frame is fixed (the laboratory frame typically). However, ablative processes during laser–target interaction lead to enormous expansion of the matter, where the Lagrangian description is preferable.

The hydrodynamics is modelled within the reference frame co-moving with the fluid. Only the Galilean transformations of the coordinate system are used, respecting the assumption of non-relativistic motion of the fluid. It is convenient to define the differential operator of substantial (or material) derivative:

$$\frac{\mathrm{D}\vec{h}}{\mathrm{D}t} = \frac{\partial \vec{h}}{\partial t} + (\vec{u}\nabla)\vec{h}, \tag{88}$$

for a vector function $\vec{h}$ (or for a scalar function analogously).

Equipped with the substantial derivative, the one-fluid model (82–84) can be rewritten as:

$$\frac{\mathrm{D}}{\mathrm{D}t}\rho = -\rho\nabla\cdot\vec{u}, \tag{89}$$

$$\rho\frac{\mathrm{D}}{\mathrm{D}t}\vec{u} = -\nabla\cdot\underline{\underline{P}} - \nabla\cdot\underline{\underline{P}}^B, \tag{90}$$

$$\rho\frac{\mathrm{D}}{\mathrm{D}t}\varepsilon = -\underline{\underline{P}} : \nabla\vec{u} - \nabla\cdot\vec{q} + \vec{j}\cdot\vec{E}, \tag{91}$$

where the lower velocity moment equations were substituted to simplify the formulation.

The next step is transformation of the coordinate system itself. The hydrodynamic equations (82–84) are primarily hyperbolic, so the quantities $\rho, \rho\vec{u}, 1/2\rho u^2 + \rho\varepsilon$ are advected along the characteristics. Therefore, the time-dependent flux $\vec{\psi}_t : \vec{X} \to \vec{x}$ of the equations can be defined, which assigns the coordinate of an infinitesimal volume of the solution at time t to its initial (or material) coordinate X, so it ideally holds $\rho(\vec{\psi}_t(X), t) = \rho(X, 0)$, etc. Provided that this assignment is bijective and difeomorphic, so the characteristics do not intersect and no singularities exist, a well-defined invertible transformation of the coordinates $(\vec{X}, t) \to (\vec{x}, t)$ can be defined. The pair of the space-time coordinates $(\vec{X}, t)$ is called the Lagrangian coordinates. A function $\tilde{h} = \tilde{h}(\vec{X}, t)$, defined in the Lagrangian coordinates and corresponding to the function $h = h(\vec{x}, t)$ in the Eulerian coordinates, is then differentiated as follows:

$$\left.\frac{\partial\tilde{h}}{\partial t}\right|_{\vec{X},t} = \left.\frac{\partial h}{\partial t}\right|_{\vec{\psi}_t(\vec{X}),t} = \left.\frac{\partial h}{\partial t}\right|_{\vec{\psi}_t(\vec{X}),t} + \frac{\partial\vec{\psi}_t}{\partial t}\cdot\left.\frac{\partial h}{\partial\vec{x}}\right|_{\vec{\psi}_t(\vec{X}),t} = \left.\frac{\mathrm{D}h}{\mathrm{D}t}\right|_{\vec{\psi}_t(\vec{X}),t}, \tag{92}$$

where the fact was utilized that the slope of the characteristics $\partial\vec{\psi}_t/\partial t$ is equal to the velocity of the convection $\vec{u}$.

In addition to the time derivative, the divergence operator is needed. It can be transformed as follows:

$$\nabla_{\vec{X}}\cdot\tilde{h}|_{\vec{X},t} = \left|\frac{\mathrm{d}\vec{\psi}_t}{\mathrm{d}\vec{X}}\right|_{\vec{X}} \nabla_{\vec{x}}\cdot h|_{\vec{\psi}_t(\vec{X}),t} = \frac{\rho_0(\vec{X})}{\rho(\vec{\psi}_t, t)}\,\nabla_{\vec{x}}\cdot h|_{\vec{\psi}_t(\vec{X}),t}\,, \tag{93}$$

where $\rho_0(\vec{x}) = \rho(\vec{x}, 0)$ is the initial density. This fact already reflects that $\rho|J|$ is an invariant of the flow, i.e. $\mathrm{D}\rho|J|/\mathrm{D}t = 0$, where $J = \mathrm{d}\vec{\psi}_t/\mathrm{d}\vec{X}$ is the Jacoby matrix. This can be seen as a consequence of the mass conservation law (89), provided the relation $\mathrm{D}|J|/\mathrm{D}t = \nabla\cdot\vec{u}|J|$ holds, as can be verified from the definition [52]. The continuity equation then gives:

$$0 = \frac{\mathrm{D}\rho}{\mathrm{D}t} + \rho\nabla\cdot\vec{u} = \frac{\mathrm{D}\rho}{\mathrm{D}t} + \rho|J|^{-1}\frac{\mathrm{D}|J|}{\mathrm{D}t} = |J|^{-1}\frac{\mathrm{D}\rho|J|}{\mathrm{D}t} \tag{94}$$

Following these considerations, the system (90–91) can be transformed to the

following form:

$$\rho_0 \frac{\partial}{\partial t} \tilde{\vec{u}} = -\nabla_{\vec{X}} \cdot \tilde{\underline{\underline{P}}} - \nabla_{\vec{X}} \cdot \tilde{\underline{\underline{P}}}^B, \tag{95}$$

$$\rho_0 \frac{\partial}{\partial t} \tilde{\varepsilon} = -\tilde{\underline{\underline{P}}} : \nabla_{\vec{X}} \tilde{\vec{u}} - \nabla_{\vec{X}} \cdot \tilde{\vec{q}} + \frac{\rho_0}{\tilde{\rho}} \tilde{\vec{j}} \cdot \tilde{\vec{E}}. \tag{96}$$

where the functions in the Lagrangian coordinates are denoted by the upper tilde.

Finally, it must be explained how the Maxwell's equations (3–4) are transformed. The procedure is not as straightforward as in the case of the hydrodynamic part. The fields must be transferred to the Lagrangian frame by the proper Lorentz transformations in the low velocity limit. In the simplest case of Lagrangian magnetohydrodynamics, the local electric force can be identified with the classical local Lorentz force, giving the expression for the electric field [53]:

$$\tilde{\vec{E}}(\vec{\psi}_t^{-1}(\vec{x}), t) = \vec{E}(\vec{x}, t) + \vec{u}(\vec{x}, t) \times \vec{B}(\vec{x}, t). \tag{97}$$

This transformation can be absorbed in the definition of the substantial derivative for (partially) solenoidal fields, which becomes [54]:

$$\frac{\mathrm{D}\vec{h}}{\mathrm{D}t} = \frac{\partial \vec{h}}{\partial t} + (\nabla \cdot \vec{h})\vec{u} + \nabla \times (\vec{h} \times \vec{u}). \tag{98}$$

Note that no distinction from the (88) is made in the notation, because the meaning is given from the context. The Faraday's law (4) can be then rewritten as:

$$\frac{\mathrm{D}\vec{B}}{\mathrm{D}t} = -\nabla \times \vec{E}', \tag{99}$$

where $\vec{E}'$ is the fluid-frame electric field ($\vec{E}'(\vec{\psi}_t(\vec{X}), t) = \tilde{\vec{E}}(\vec{X}, t)$).

Proceeding to the Lagrangian coordinates, the Faraday's law (4) maintains its form even in the moving frame and becomes:

$$\frac{\partial}{\partial t} \tilde{\vec{B}} = -\nabla \times \tilde{\vec{E}}, \tag{100}$$

where the differential operator in Eulerian coordinates is retained, because the formula (93) cannot be applied here and the final expression is more complex. It should be noted that (100) together with the definition of the electric field (97) and (85) can be interpreted in such way that the convection of the magnetic field was eliminated by the change of the reference frames similarly to the rest of the quantities.

2.4 Equation of state

The (magneto-)hydrodynamic equations (89–91) together with the equations for the electric field (85) and magnetic field (4) eventually still do not pose a closed system of differential equations. The prescriptions of the pressure tensor and heat flux are

missing in the hydrodynamic picture. The reason is that both are given by higher velocity moments than those appearing in the hydrodynamic system, as in the case of the heat flux according to the definition (51), or multi-directional correlations rather than the scalar in the case of the pressure (41). Discussion of the former is left for the dedicated chapter about the heat transport processes 3, while the latter is the subject of this chapter.

2.4.1 Ideal gas

Based on the kinetic theory, it was recognized after the Cartesian tensor expansion (64) (and also the definition (41)) that the higher order tensors contribute to the anisotropic part of the tensor only. The scalar part was obtained directly from the isotropic part of the distribution function. Considering the equilibrium distribution (26) used throughout the macroscopic model, the scalar pressure (64) can be related to the internal energy of the plasma:

$$p = (\gamma - 1)\rho\varepsilon. \tag{101}$$

This can be recognized as the ideal gas equation of state, where γ is the Poisson constant. As the degrees-of-freedom of the species motion were not restrained anyhow, the constant attains the adiabatic value $\gamma = 5/3$ in the kinetic model of chapter 1. Because the reduced hydrodynamic description does not self-consistently provide this value, it can be varied depending on the given physical problem, so the value $\gamma = 7/5$ can be used for simple diatomic molecules for example. The ionization is not provided by the model and is assumed constant for the ideal gas.

2.4.2 Quotidian Equation of State

The Quotidian Equation of State (QEOS) [55] is one of the most popular models in hydrodynamic simulations of plasma. It provides the analytic formulae for a wide range of temperatures and densities in the one-temperature or even two-temperature model. Conceptually, it is based on the formulation in terms of the Helmholtz free energy:

$$F_{tot}(\rho, T_e, T_i) = F_i(\rho, T_i) + F_e(\rho, T_e) + F_b(\rho, T_e), \tag{102}$$

where F_i is the ion contribution, F_e electron contribution and F_b bounding correction. The ion part is approximated by the solid and liquid scaling laws and by the Cowan model [56]. The term F_b supplements the model by semi-empirical bonding corrections, which serve to decrease the total pressure for solid material and give correct bulk modulus [57]. The bulk modulus of solid and solid density are externally entered parameters in this model. Finally, the electron term is based on the Thomas–Fermi theory [58].

The basic assumptions behind the Thomas–Fermi theory are such that electrons move in the electrostatic field of a point-like ion. As the model originates from the statistical description in the continuum limit, there should be statistically representative number of electrons at any distance from the nucleus, so the model is fully valid only

for infinitely ionized atoms strictly speaking. In essence, the total energy of electrons is given by:

$$E_{TF} = C_{TF}^{kin} \int n^{5/3}(\vec{x})\,\mathrm{d}\vec{x} - \int n(\vec{x}) \frac{Ze^2}{|\vec{x}|}\,\mathrm{d}\vec{x} + \frac{1}{2}e^2 \int\int \frac{n(\vec{x})n(\vec{x}')}{|\vec{x}-\vec{x}'|}\,\mathrm{d}\vec{x}\,\mathrm{d}\vec{x}', \tag{103}$$

the symbol C_{TF}^{kin} is a positive constant. The first term is the kinetic energy of the electrons distributed to Fermi spheres in the phase space, i.e. the volume of phase space occupied by fermionic matter in ground state. The second term is the potential in the field of the ion, which is calculated from the classical solution of the Poisson equation in an agreement with the assumptions already stated. The last term is the expulsion potential of point-like electrons. This energy is then minimized through variations of the density profile for the given total number of electrons. From the form of the equation, it is clear that the resulting solution is only function of the radius, so no higher spherical modes are present and no notion of electron orbitals exists, except the spherically symmetric ones, but no quantization exists either. On the other hand, the solution scales with the ionization Z, so it can be precomputed once and applied on all ions. Another drawback of the theory is the absence of a proper electron energy exchange term, which would respect Pauli exclusion principle. An answer to this deficiency is given by the Thomas–Fermi–Dirac theory, but the model shares the other inaccuracies and the solution cannot be scaled directly, which presents a notable practical inconvenience. Therefore, the classical Thomas–Fermi approach is applied usually.

The convenient simplicity and versatility of the QEOS model stemmed development of many equations of state originating from it. The model was later adopted in the library MPQeos [59] and further extended in FEOS package. It provides in addition to the basic QEOS model proper treatment of mixtures, where the properties of the modelled atoms do not need to be averaged a priori. There are also improvements of the cold curve and the region of liquid–vapour coexistence is treated rigorously [60].

2.4.3 Other equations of state

The Thomas–Fermi model used in the plain QEOS disregarded shell structure of the atoms, making the model applicable only for high-Z materials approximately. This crude simplification of the atomic description was addressed by many other authors. One of the more advanced models is the BADGER library [61]. The ion model is essentially the same as in the one used in QEOS. However, the correction for the atomic bounds do not use the empirical parameters, but a model based on scaled binding energies (SBE) instead. The ionization model is then separated from the electron equation of state and can be switched independently. The model based on the Thomas–Fermi model described in the previous chapter is one of the options, but the continuum treatment predetermines it only for high-Z materials as already stated. On the other hand, the screened hydrogenic model with l-splitting (SHM) can be used instead, where the notion of the atomic structure in the approximation of the principal and azimuthal quantum numbers is present. Another option is the individual electron accounting model (IEM) model, where the electrons in the approximation of discrete

particles are part of the quantum system of the ion. Finally, the electron equation of state models not only the free electrons, but also the bound electrons, which were disregarded in the QEOS(-like) models, using the already mentioned SHM model. All species then interact through the Coulombic forces and partial charge screening is also present between them.

In addition to the analytic models presented so far, there is another wide group of empirical models. One of the major members of the family is the SESAME library [62, 63, 64]. The experimentally measured values of quantities like pressure or ionization are tabulated for various temperatures and densities. Interpolation of the data is then necessary between the discrete point of the thermodynamic space.

2.4.4 Interpolation of equations of state

The interpolation routines are part of HerEOS (Hermite-interpolated Equation of State) [65, 66]. The library provides thermodynamically consistent interpolation of the quantities rather than direct interpolation between the given values of pressure and other measured quantities. In particular, all thermodynamic potentials are calculated from the Helmholtz free energy $F = F(\rho, T)$, where the temperature is the common one for one-temperature models, electron or ion, depending on the given equation of state. For example, the specific internal energy and pressure are calculated as follows:

$$\varepsilon(\rho, T) = F - T\left(\frac{\partial f}{\partial T}\right)_{\rho}, \qquad p(\rho, T) = \rho^2\left(\frac{\partial F}{\partial \rho}\right)_{T}, \tag{104}$$

where the thermodynamic notation of derivatives is used, so the lower index denotes the quantity constant during the process. This approach guarantees that the derived quantities are true potentials as in the theory of thermodynamics. The potentiality is not self-provided for interpolated functions as inconsistencies arise between the discretely approximated quantities, which may lead to violation of the thermodynamic laws. In contrast, the calculation from F gives fully consistent results provided that the interpolated function F is smooth enough. This is achieved by high-order Hermite polynomials used for the interpolation.

Another merit of the interpolation in general is the acceleration of the computation, where the analytic model does not need to be evaluated at the points of the thermodynamic space repeatedly during the numerical simulation.

3 Heat transport

The term heat refers to the energy confined in the chaotic motion of the plasma species. Collisional processes thermalize the plasma and lead to establishing of the collisional equilibrium as explained in chapter 1. However, the physical system rarely attains the full global thermal equilibrium (TE). Due to the presence of strong energy sources like an impinging laser beam (see chapter 5), the physical system is deviated from the global equilibrium and only local thermal equilibrium (LTE) is attained. The heat transport process then emerge, equalizing the thermodynamic conditions.

The kinetic theory provided a description of the heat transfer implicitly together with the rest of the velocity moments of the distribution function (see chapter 1.2). However, the reduction of the kinetic model to the fluid description of chapter 2 truncated the velocity moments expansion yet after the energy moment. Principally, the expansion can be extended further, but higher velocity moments are not invariants of the collision operator according to chapter 1.2. Consequently, they are not governed by conservation laws resembling those of the lower ones. Therefore, heat flux corresponding to the third velocity moment is not provided by the classical fluid model and must be supplied externally. This is circumvented by construction of a closure model for the heat flux, relying on the lower moments only. Various approaches to this problem are subjects of this chapter.

3.1 Diffusion transport

The diffusion treatment of the heat transport is the most frequently adopted one due to its simplicity. Moreover, it is also positivity of the diffusion operator, which guarantees monotonous increase of the entropy in an agreement with the Onsager relations of irreversible processes. Fundamentally, it is based on the linear perturbation theory, so its predictions are valid only for small deviations from the equilibrium. In particular, it will be shown that the perturbation of the Maxwell–Boltzmann distribution (26) scales with mean free path of the electrons λ_e. Therefore, the assumption $\lambda_e \ll L$ is made, where L is the characteristic length scale of the plasma profile (it is $L_T = T_e/|\nabla T_e|$ for the temperature and $L_n = n_e/|\nabla n_e|$ for the density approximately).

Under the conditions stated above, the distribution function f can be formally expanded using the Hilbert expansion in a small parameter λ combined with the expansion in Legendre polynomials in the directional cosine $\mu = \cos\varphi$ of the polar angle φ [67]:

$$f = \sum_{i=0}^{\infty} \lambda^i \sum_{j=0}^{\infty} f_{ij} P_j(\mu) = f_{00} + f_{01}\mu + f_{10}\lambda + f_{11}\lambda\mu + O(\lambda^2, \mu^2). \tag{105}$$

The Chapman–Enskog approach then defines the methodology how to successively solve such a parametric expansion, where the procedure should start with the unperturbed coefficients neglecting the corrections [2, 68, 69]. However, it is clear from chapter 1.1 that the solution is the Maxwell–Boltzmann distribution (26) for collisionally dominant plasma so it can be identified that $f_{00} = f_M$ and $f_{01} = 0$, as it is isotropic. Then, the first order correction are sought, but f_{10} correction can be neglected compared to f_M for the linear theory, so only f_{11} remains to be solved. When the higher order terms

are neglected, this truncated expansion exactly coincides with the Cartesian tensor expansion in chapter 1.3. For convenience and brevity, the equations are not derived again for the expansion (110), but the discussion continues with the the equivalent tensor formulation (59).

The solution of the kinetic problem has an analytic formulation only for the Lorentz approximation [1]. In this limit, the electron–electron collisions are neglected compared to the electron–ion ones. Moreover, the sought solution should be stationary to depend only on the thermodynamic potentials, so the transient term is $\partial \vec{f_1}/\partial t \approx 0$. Finally, we restrict ourselves to the case without a magnetic field for the moment. The equation for $\vec{f_1}$ (66) gives the solution:

$$\vec{f_1} = -\lambda_{ei} \left(\nabla f_M - \frac{e}{m_e v} \frac{\partial f_0}{\partial v} \vec{E} \right), \tag{106}$$

where $\lambda_{ei} = v/\nu_{ei}$ is the electron–ion scattering mean free path. Using only the definition of the equilibrium distribution (26), the gradient term can be evaluated as:

$$\nabla f_M = \left(\frac{\nabla n_e}{n_e} + \left(\frac{m_e v^2}{2 k_B T_e} - \frac{3}{2} \right) \frac{\nabla T_e}{T_e} \right) f_M. \tag{107}$$

The expression for the stationary self-consistent electric field can be directly derived under the condition of quasi-neutrality. Essentially, it implies, based on the continuity equation (38), that the electric current must be zero for a single-directional perturbation of the distribution function, so the definition (60) gives the condition:

$$\int_0^{+\infty} \vec{f_1} v^3 \, \mathrm{d}v = 0. \tag{108}$$

Inserting the solution of $\vec{f_1}$ (106) to (108), the diffusion electric fields is obtained:

$$\vec{E} = -\frac{k_B T_e}{e} \left(\frac{\nabla n_e}{n_e} + \xi^1 \frac{\nabla T_e}{T_e} \right), \tag{109}$$

where the factor $\xi^1 = 5/2$ for the Lorentz gas.

Finally, the electric field (109) is inserted to the $\vec{f_1}$ formula (106) and the full distribution function is constructed from the expanded form (59) yielding:

$$f = n_e \left(\frac{m_e}{2\pi k_B T_e} \right)^{3/2} \exp\left(-\frac{m_e v^2}{2 k_B T_e} \right) \left(1 - D\left(\frac{m_e v^2}{2 k_B T_e}, \vec{\Omega} \right) \right), \tag{110}$$

where D is the transport function taking the form:

$$D(\zeta, \vec{\Omega}) = \xi^0 \lambda_{ei} (\zeta - 4) \vec{\Omega} \cdot \frac{\nabla T_e}{T_e}, \tag{111}$$

The notation with the transport function D follows the work of Spitzer and Härm [6, 7]

and agrees with the classical results for the Lorentz gas [1]. Considering also electron–electron collisions throughout the derivation is non-trivial and the system must be solved numerically. The results obtained with an expansion in Legendre polynomials were tabulated in the influential paper [7]. The findings were later fitted by analytic formulae giving the correction factors [70]:

$$\xi^0(Z) = \frac{Z + 0.24}{Z + 4.2}, \qquad \xi^1(Z) = 1 + \frac{3}{2}\frac{Z + 0.477}{Z + 2.15}. \tag{112}$$

Finally, the diffusion heat flux reads according to the definition (61):

$$\vec{q}_{SH} = \frac{4\pi}{3}\int_0^{+\infty} \frac{1}{2} m_e v^5 \vec{f}_1 \,\mathrm{d}v = -\frac{128}{3\pi}\xi^0 \lambda_{SH} v_{Te} n_e k_B \nabla T_e, \tag{113}$$

where the Spitzer–Härm mean free path is defined as:

$$\lambda_{SH} = \frac{v_{Te}}{\nu_{SH}} = \frac{3 v_{Te}^4 m_e}{4\sqrt{2\pi} Z e^4 \ln \Lambda_{ei}}. \tag{114}$$

To conclude, the diffusion approximation for a small perturbation of the equilibrium distribution resulted in the Fourier's law for heat diffusion $\vec{q}_{SH} = -\kappa_{SH}\nabla T_e$. The electric field had a significant role in eliminating the dependency on the density gradient, which is only true if both gradients are aligned as was tactfully assumed. In the opposite case the solution is more complex and kinetic simulations are needed [71]. The electric field also reduced the heat flux significantly as the electrons cannot free stream in a single direction, but a return current balancing the flow is formed when the quasi-neutrality condition is enforced. Actually, the main contribution to the heat flux is not provided by the electrons with the thermal velocity v_{Te}, but super-thermal species with velocities about $v \approx 3.7 v_{Te}$, since heat flux is a higher velocity moment than electric current and is dominated by higher velocity species in turn [72]. The spectral distributions of the fluxes are shown in Figure 1. These high-velocity species are significantly less collisional (due to $\sim v^{-3}$ dependency of the collision frequency (73)), which leads to violation of the criterion on the mean free path ($\lambda_e \ll L$). This point leads to construction the flux-limiting techniques (chapter 3.1.2) and non-local transport models described in subsequent chapters. Lastly, the dependency on the electron–electron collisions manifests that the electron–electron collisions make the transport less efficient, but the densities are lower for low-Z plasmas typically, outweighing the effect by the value of the mean free path.

3.1.1 Diffusion transport in magnetic field

The diffusion model presented in this chapter did not assume presence of a magnetic field. The theory considering also this effect was summarized by Braginskii [8]. Instead

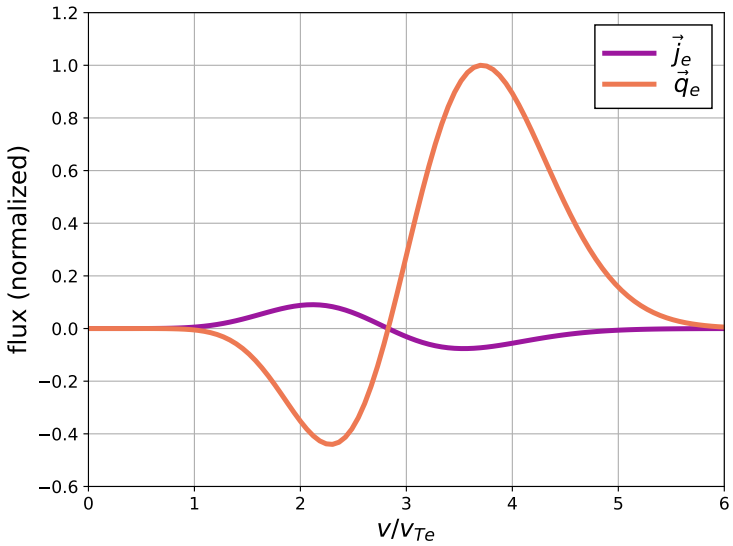

Figure 1: Spectral distributions of the electron electric current ($\vec{j}_e$) and heat flux ($\vec{q}_e$) in the diffusion approximation. The values are normalized and the quantities are functions of the velocity v normalized to the thermal velocity v_{Te}.

of the simple Fourier's law, the following expressions are given:

$$\vec{E} = -\frac{\nabla p_e}{n_e e} + \frac{\vec{j} \times \vec{B}}{n_e e} + \underline{\underline{\alpha}} \cdot \vec{j} - \underline{\underline{\beta}} \cdot \nabla T_e, \tag{115}$$

$$\vec{q} = -\underline{\underline{\kappa}} \cdot \nabla T_e - T_e \underline{\underline{\beta}} \cdot \vec{j}, \tag{116}$$

where $\underline{\underline{\alpha}}$ is the resistivity coefficient, $\underline{\underline{\beta}}$ thermoelectric coefficient, $\underline{\underline{\kappa}}$ heat conductivity coefficient. All coefficients are tensors depending on the magnetization of the plasma. In essence, their structure is following when applied on a vector $\vec{r}$:

$$\underline{\underline{A}} \cdot \vec{r} = A_\parallel (\vec{b} \cdot \vec{r}) \vec{b} + A_\perp \vec{b} \times (\vec{r} \times \vec{b}) \pm A_\wedge \vec{b} \times \vec{r}, \tag{117}$$

where $\vec{b} = \vec{B}/|\vec{B}|$ is the unit vector in the direction of the magnetic field and $A_\parallel, A_\perp, A_\wedge$ are transport coefficients parallel, perpendicular and cross-component contributions respectively (the minus sign appears only for $\underline{\underline{\alpha}}$). The parallel terms are not affected by the magnetic field classically and the values are identical with the findings of Spitzer and Härm [7]. However, the perpendicular coefficients are strongly dependent on the magnetization and the heat flow is limited across the field lines, while the resistivity grows. The most interesting term is the one proportional to the temperature gradient, which is responsible for the Nernst effect in the case of the thermoelectric term $\underline{\underline{\beta}} \cdot \nabla T_e$ and Righi–Leduc effect in the case of the anisotropic heat conduction term $\underline{\underline{\kappa}} \cdot \nabla T_e$. It means that an electric field and heat flux perpendicular to the both gradients, of the temperature and magnetic field, is generated. These terms then become non-local when the Knudsen number of electrons $Kn_e = \lambda_e / L$ grows [73].

Also the first term in (115) is worth a note, it generates a magnetic field through Faraday's law (4), unlike the mostly gradient Nernst term $\underline{\underline{\beta}} \cdot \nabla T_e$. The resulting magnetic field is proportional to $\nabla \ln n_e \times \nabla T_e$, appearing whenever the gradients of the density and temperature are crossed. It shows that a magnetic field can be generated even in a quasi-neutral plasma without significant electric currents. This is effect is known as the Biermann battery was originally studied in the context of proto-stellar seed fields [74] or proto-galactic formation processes [75], but it can generate strong magnetic fields in the cases of laser–target interaction [76] or ICF [77], affecting the thermal transport in turn [78].

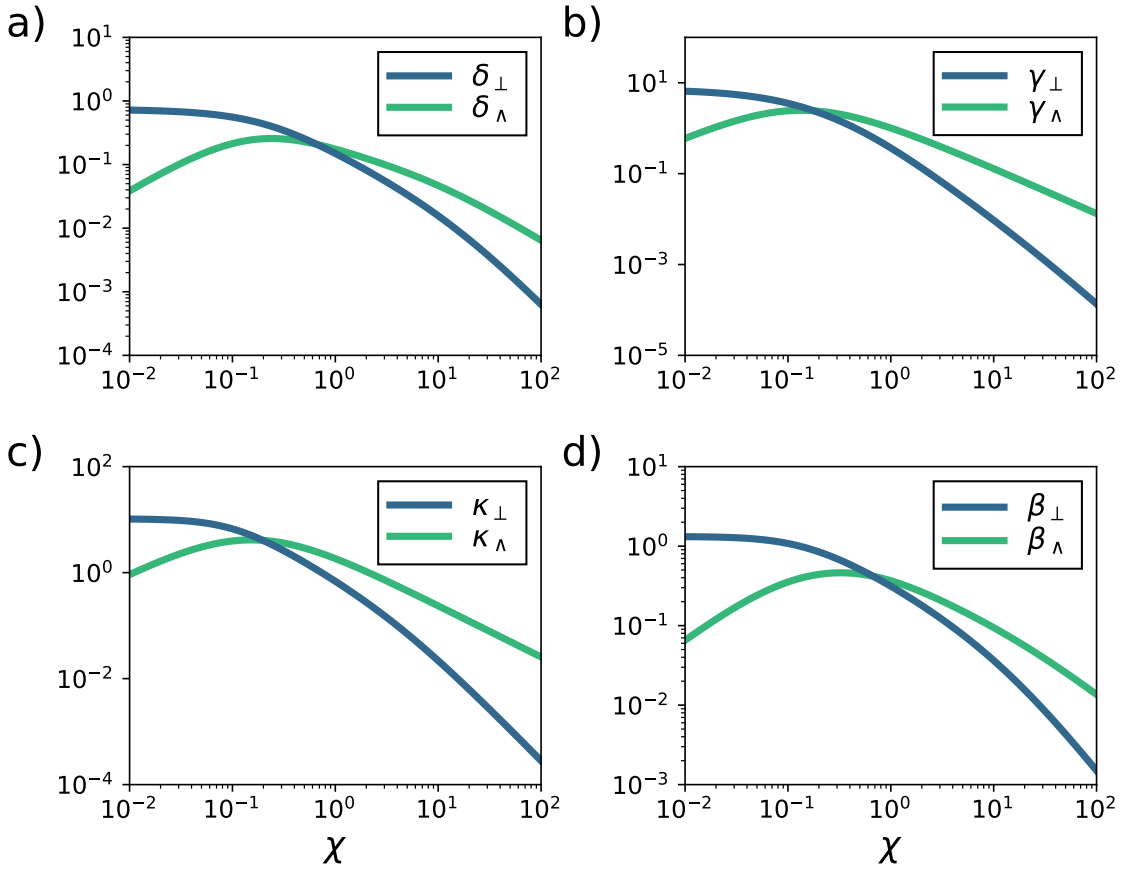

Figure 2: The transport coefficients in a magnetic field (with magnetization χ): a) the Hall coefficients $\delta_\perp, \delta_\wedge$, b) Nernst coefficients $\gamma_\perp, \gamma_\wedge$, c) heat conductivities $\kappa_\perp, \kappa_\wedge$, d) thermoelectric coefficients $\beta_\perp, \beta_\wedge$. The values are normalized according to [79]. The mean ionization is $Z = 13$.

Yet another formulation of the anisotropic current transport can be derived according to [80], giving a better insight to the processes. The vector identity $\vec{j} =$

$(\vec{j}\cdot\vec{b})\vec{b}+\vec{b}\times(\vec{j}\times\vec{b})$ is applied. The electric field then reads:

$$\vec{E}=-\vec{u}_B\times\vec{B}+\alpha_\parallel\vec{j}-\frac{\nabla p_e}{n_e e}-\beta_\parallel\nabla T_e, \tag{118}$$

$$\vec{u}_B=\vec{u}-(1+\delta_\perp)\vec{j}+\delta_\wedge\vec{j}\times\vec{b}-\gamma_\perp\nabla T_e+\gamma_\wedge\nabla T_e\times\vec{b}. \tag{119}$$

It can be observed that the the anisotropic transport can be interpreted as mere convection with the velocity $\vec{u}_B$ and the classical isotropic contribution. The newly appearing transport coefficients are defined as $\delta_\perp=\alpha_\wedge/|\vec{B}|$, $\delta_\wedge=(\alpha_\perp-\alpha_\parallel)/|\vec{B}|$, $\gamma_\perp=\beta_\wedge/|\vec{B}|$ and $\gamma_\wedge=(\beta_\parallel-\beta_\perp)/|\vec{B}|$. This reformulation reveals that the original coefficients are not important by themselves, but rather their differences. Therefore, the coefficients should not be interpolated in their original form [81], but in this symmetrical one [79].

The transport coefficients are plotted as functions of the magnetization $\chi=e|\vec{B}|/(m_e\nu_{SH})$ in Figure 2. The overall decreasing trend of the transport across the field lines is apparent. Note the transport along the field lines is unaffected and coincides with the transversal coefficients in absence of magnetic field, e.g. $\kappa_\parallel=\kappa_\perp(\chi=0)$. In contrast, the exchange between the transversal components is strongest for $\chi\sim 1$. This can be explained in simple terms by matching mean free path of the electrons and their Larmor radius under these conditions. For low ionizations, there exists the additional effect of electron–electron collision with scaling $\sim 1/\sqrt{Z}$.

3.1.2 Heat flux limiting

The heat diffusion model is widely used for plasma simulations for the reasons already mentioned in the introduction of this chapter about the diffusion transport. However, it was recognized based on experimental data that the predictions of the diffusion theory significantly overestimate the heat flux in the upstream of a steep front and underestimate in the downstream [11]. It was proposed to use the heat flux limiting techniques to cure this problem crudely. The heat flux is limited to a fraction of the free streaming value $q_{fs}=n_e m_e v_{Te}^3$, which is the absolutely highest value the heat flux can attain when all electrons propagate in a single direction. The heat flux is then limited by one of the formulae typically [82]:

$$\vec{q}=\min(1,f^{lim}q_{fs}/|\vec{q}_{SH}|)\vec{q}_{SH},\qquad\text{or}\qquad\vec{q}=\frac{\vec{q}_{SH}}{1+|\vec{q}_{SH}|/(f^{lim}q_{fs})}, \tag{120}$$

where f^{lim} is a factor between 0.02 and 0.15 based on experimental data and Fokker–Planck simulations [83, 84]. However, the redefinition of the flux using the local values of the temperature changes the structure of the diffusion equation, which becomes hyperbolic instead of parabolic locally. This can have unforeseen consequences as the entropy may not increase and non-physical artifacts may appear in the simulations [82]. Therefore, limitation of the conductivity is preferred, which does not guarantee that the flux is lower than the given value, but maintains the parabolic structure of the

equation, so the behaviour remains purely diffusive. They are defined as follows:

$$\kappa = \min(1, f^{lim} q_{fs}/|\vec{q}_{SH}|)\kappa_{SH}, \qquad \text{or} \qquad \kappa = \frac{\kappa_{SH}}{1 + |\vec{q}_{SH}|/(f^{lim} q_{fs})}. \tag{121}$$

Apparently, the limiting processes would have to be repeated multiple times until convergence is reached. Unfortunately, the iterations involve computation of the heat fluxes, which makes the process expensive. Therefore, only a single iteration is performed typically.

The main problem associated with the flux limiting techniques is given by the fact that the value q_{fs} depends on the local temperature and density without any notion of the actually transported species. Consequently, the limiter fraction f^{lim} is temporally, spatially and physical problem dependent factor, which can be accurately estimated only on the basis of fully kinetic simulations [85, 86, 87]. This problem led to the development of semi-empirical methods, designed to feasibly cure this loss of predictive capabilities of the hydrodynamic simulations.

3.1.3 Convolution extension

One of the major representatives of the semi-empirical methods is the method of Luciani, Mora and Virmont (LMV) [15]. The idea was to propose a convolution of the classical diffusion results to take into account the emerging non-locality. The heat flux is then calculated as:

$$\vec{q} = \int_\Omega K(\vec{x}, \vec{x}')\vec{q}_{SH}\,\mathrm{d}\vec{x}', \tag{122}$$

where K is the convolution kernel defined in 1D as follows:

$$K(x, x') = \frac{1}{2\lambda_{LMV}(x')} \exp\left(-\left|\frac{\int_x^{x'} n_e(x'')\,\mathrm{d}x''}{\lambda_{LMV}(x')n_e(x')}\right|\right), \tag{123}$$

where λ_{LMV} is a function defined in the reference [15]. The convolution introduces the notion of non-locality, where the flux is dislocated on the length scale comparable with λ_{LMV}. However, a shortcoming of the theory is the asymmetric convolution kernel, where only an ad hoc density correction is present in the form of a path integral. The kernel functions were improved based on a simplified kinetic equation in the model of Albritton, Williams, Bernstein and Swartz [46]. In any case, it was revealed later in an influential paper that negative entropy is generated and non-physical instabilities may arise for any simple convolutional model [17, 88].

A multi-dimensional extension of the method based on less empirical foundation was proposed by Schurtz, Nicolaï and Busquet (SNB) [18], which remains the most widely used non-local transport model probably and has been implemented in large ICF codes [89, 27]. The generalization is made by reformulation of the problem in multiple dimensions in terms of the equivalent linear stationary transport equation:

$$\vec{\Omega} \cdot \nabla\vec{q} = \frac{1}{\lambda_{SNB}}\left(\frac{3}{4\pi}\vec{\Omega} \cdot \vec{q}_{SH} - \vec{q}\right). \tag{124}$$

It can be recognized that the integral solution of the linear transport equation (124) in 1D is the Fredholm equation of the second kind, which nearly coincides with (122), but the kernel is symmetric. The transport equation can be solved by the discrete ordinates method or by angular moments as in the case of radiation transport described in chapter 4. The authors also propose a multi-group extension of the method, so non-locality of the species varying with their velocity can be taken into account approximately. However, one of the most cumbersome simplifications of the model is the non-existence of a self-consistent electric field. Instead, the mean free path is merely limited by the local value of the Spitzer-Härm electric field (109) based on the work of Bendib, Luciani and Matte (BLM) [16]:

$$\frac{1}{\lambda_{SNB}} = \frac{1}{a\lambda_{SH}} + \frac{|e\vec{E}_{SH}|}{k_B T_e}, \tag{125}$$

where a is a problem-dependent positive constant. It is apparent that the configuration of the electric field and non-local fluxes can significantly more complicated in multiple dimensions unlike the 1D case considered by BLM and the local diffusion field is not representative of the actual non-local transport conditions. An effort was then made to reformulate the method with self-consistent electric and magnetic fields [90]. Also the electron–electron collision operator used for theoretical foundation of the model, which was originally approximated by the BGK operator of chapter 1.1.3, was replaced by the more accurate AWBS operator from chapter 1.1.2.

3.2 P1/M1 model of non-local transport

The chapter about the diffusion transport 3.1 revealed that the problem of heat transport becomes non-trivial when steep gradients of the length scale L comparable or smaller than the mean free path of the species λ are present in the plasma. In particular, the condition was specified to $\lambda_{ei}/L \ll 0.06/\sqrt{Z}$ for electrons [91]. This shows that the non-locality emerge very early and a discrepancy between the diffusion predictions and more accurate kinetic simulations arise [85]. The extensions of the diffusion model in chapter 3.1.3 approached the problem empirically or semi-empirically, but did not possess a solid theoretical foundation and empirical factors had to be adjusted for the given physical scenario, limiting the predictive capabilities of the models. However, solution of the full kinetic problem was and still is prohibitively computationally expensive on the hydrodynamic scales. Therefore, simplified non-local transport models were proposed.

A simplified model directly originating from the kinetic theory is the P1 and M1 method using the terminology of radiation transport (see chapter 4.2). They are based on the angular moments technique, formally equivalent to the Cartesian tensor expansion of chapter 1.3, which is truncated after the first term. The collision operators on the right-hand-side of the system (65–66) do not involve the full non-linear collision

operator, but they are simplified in the work of Del Sorbo et al. as follows [19, 92]:

$$C_0 = \nu_{ee} v \frac{\partial}{\partial v} (f_0 - f_M), \tag{126}$$

$$C_1 = \nu_{ee} v \frac{\partial}{\partial v} \vec{f_1} - (\nu_{ee} + \nu_{ei}) \vec{f_1}. \tag{127}$$

The Fokker–Planck operator for electron–electron collisions uses the linear AWBS approximation from chapter 1.1.2, which is valid for high-velocity species near the equilibrium. However, it has an apparent advantage over the BGK operator described in chapter 1.1.3 in the aspect of conserving mass, but it is still rather an empirical operator as the equilibrium distribution function must be entered explicitly.

The P1 and M1 models then differ in the definition of the closure relation replacing the $\underline{\underline{f_2}}$ contributions to the system of equations (65–66). Setting $\underline{\underline{f_2}} = 0$ yields the P1 model, which is applicable only for very small anisotropy $|\vec{f_1}| \ll f_0$. It must be noted that form of the closure appearing in the reference is different. The reason is that formally equivalent technique of angular moments is followed there instead of the tensor expansion (59).

In contrast to the P1 model, M1 method is designed to approximately treat strongly anisotropic media. The idea is that $\underline{\underline{f_2}}$ should maximize the entropy as random scatterings do in long term. The procedure is not detailed here as it is essentially identical with the one performed in the case of radiative transport in chapter 4.2. The system is solved in the stationary limit, i.e. $\partial f_0/\partial t = 0, \partial \vec{f_1}/\partial t = 0$. The electric field is also calculated as stationary, where the solution can be derived immediately from (66) in the Lorenz limit for the zero current condition (108) in the form:

$$\vec{E} = -\frac{m_e}{6e} \frac{\int_0^{+\infty} \nabla f_0 v^7 \, \mathrm{d}v}{\int_0^{+\infty} f_0 v^5 \, \mathrm{d}v}. \tag{128}$$

This formula gives the Spitzer–Härm electric field (109) for the Maxwell–Boltzmann distribution (26). The electron–electron collisions in (127) are taken into account through a correction factor. The whole procedure of solution is performed iteratively until quasi-neutrality is achieved [19].

3.3 BGK model of non-local transport

A problem of the P1/M1 methods is given by their originally kinetic nature, which requires to solve the global system of equations for tens or hundreds of velocity bins as in the case of VFP codes, making it expensive to compute. The reason can be seen in the fact that the equilibrium distribution function is described as any other distribution function, without recognizing its privileged role in the macroscopic heat transfer. Secondly, the anisotropy of the distribution function is strongly limited by the truncated Cartesian expansion. It was assumed that $|\vec{f_1}| \ll f_0$ and when this condition is not fulfilled, a strong flux of electrons in one direction causes negativity

of the distribution function in the opposite direction as both directions are artificially connected though the $\vec{f_1}$ vector. In addition, the entropy maximizing closure leads to an excessively diffusive system even for nearly coherent electron fluxes [93].

These drawbacks led us to construction of a model based on the first-principles, similar by its nature to the discrete ordinates method used in radiative transport of chapter 4.3. The primary quantity in the description is the electron specific heat flux intensity $I_e^v = I_e^v(\vec{x}, \vec{\Omega}, v, t)$ [20, 94, 82]. Essentially, it determines the differential amount of energy $\mathrm{d}E_e$ transported by the electrons with velocities in the interval $(v, v + \mathrm{d}v)$ along the unit vector $\vec{\Omega}$ in time $\mathrm{d}t$ across an infinitesimal oriented surface $\mathrm{d}\vec{S}$ into the solid angle $\mathrm{d}\vec{\Omega}$:

$$\mathrm{d}E_e = I_e^v(\vec{x}, \vec{\Omega}, v, t)\vec{\Omega} \cdot \mathrm{d}\vec{S}\,\mathrm{d}\vec{\Omega}\,\mathrm{d}v\,\mathrm{d}t. \tag{129}$$

Taking the phase space volume expressed in the spherical coordinates similarly to chapter 1.3, the intensity is defined as follows:

$$I_e^v(\vec{x}, \vec{\Omega}, v, t)\,\mathrm{d}\vec{x}\,\mathrm{d}\vec{\Omega}\,\mathrm{d}v = \frac{1}{2}m_e|\vec{v}|^3 f_e(\vec{x}, \vec{x}, t)\,\mathrm{d}\vec{x}\,\mathrm{d}\vec{v} = \frac{1}{2}m_e v^5 f_e(\vec{x}, \vec{\Omega}, v, t)\,\mathrm{d}\vec{x}\,\mathrm{d}\vec{\Omega}\,\mathrm{d}v. \tag{130}$$

The connection to the definition of the heat flux (61) is immediate and the heat flux becomes then:

$$\vec{q_e^T} = \int_0^{+\infty}\int_{4\pi} I_e^v\vec{\Omega}\,\mathrm{d}\vec{\Omega}\,\mathrm{d}v = \int_{4\pi} I_e\vec{\Omega}\,\mathrm{d}\vec{\Omega}. \tag{131}$$

This expression also defines the total electron intensity I_e, which is the velocity integral of I_e^v.

The BGK non-local electron heat transport model is based on the kinetic equation (2) in the stationary limit (considering long times compared to the collision time ν_e^{-1}) equipped with the BGK operator (23):

$$\vec{\Omega} \cdot \nabla f - \frac{e}{m_e v}\frac{\partial f}{\partial v}\vec{\Omega} \cdot \vec{E} = -\frac{\nu_e}{v}(f - f_M), \tag{132}$$

where presence of a magnetic field is not considered. Next, the averaging operator is defined for a function of velocity h as follows:

$$\langle h \rangle^I = \int_0^{+\infty}\frac{1}{2}m_e v^5 h\,\mathrm{d}v. \tag{133}$$

Application of this operator on the kinetic equation (132) yields:

$$\vec{\Omega} \cdot \nabla I_e + \frac{4e}{m_e}\left\langle\frac{f}{v^2}\right\rangle^I \vec{\Omega} \cdot \vec{E} = \left\langle\frac{f_M}{\lambda_e}\right\rangle^I - \left\langle\frac{f}{\lambda_e}\right\rangle^I, \tag{134}$$

where $\lambda_e = v/\nu_e$ is the electron mean free path. Approximating the unknown distribution function by a Maxwellian, the averaging can be performed to obtain:

$$\vec{\Omega} \cdot \nabla I_e = -\frac{e}{k_B T_e}I_e\vec{\Omega} \cdot \vec{E} + \frac{1}{\alpha\lambda_{SH}}\left(\frac{\sqrt{2}}{\pi^{3/2}}n_e v_{Te}^3 - I_e\right). \tag{135}$$

Following this approach, a problem arises in the case of the electric field term, where the zero current condition (108) is related to a different velocity moment of the distribution function. Approximation of the third velocity moment of the angular distribution function by the fifth, i.e. by the intensity, would only non-physically shift the equilibrium intensity and the mean free path. Therefore, the electric field is approximated only by the corrective factor α of the mean free path, which is adjusted to give an agreement of the method with the diffusion heat flux (113) in that limit. The calculation shows that it has the value [20]:

$$\alpha(Z) = \frac{64}{3\sqrt{2\pi}}\xi^0(Z) \doteq 8.51\xi^0(Z). \tag{136}$$

The main benefits of the method can be seen in an arbitrary anisotropy of the transport, which depends only on the numerical quadrature used for the solution of the steady state transport (135). It is also the tractable formulation making the calculation inexpensive and solvable by various numerical methods, while the intensity-based formulation guarantees that the method is always conservative. It can be also extended to an arbitrary number of velocity groups by performing only partial integration in the averaging operator (133). However, the main drawback of the method is the absence of a self-consistent non-local electric field. It is this field that limits the heat transport in the non-local limit and couples the energy groups together, which makes it difficult to stabilize the transport in the non-local limit without it. Still, the method provides good results when the mean free path is known experimentally, as for example in [30].

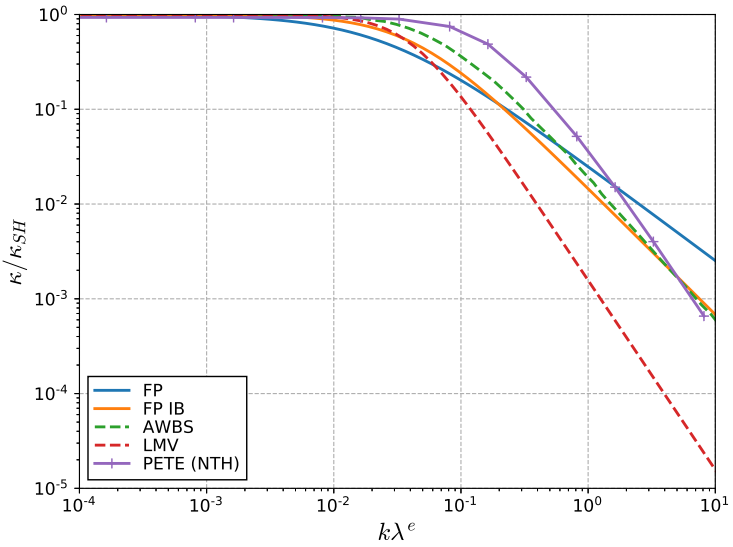

Figure 3: Dependency of the heat conductivity (normalized to the Spitzer–Härm conductivity) on the Knudsen number. The legend designates the non-local transport models: Fokker–Planck simulations without/with the modification of the distribution due to the inverse Bremsstrahlung (FP/FP IB), AWBS model, LMV model, and the BGK model (PETE (NTH)). Adopted from [95] with the underlying data from [70].

Different models on the non-local electron heat transport are compared in Figure 3. The heat flux for infinitesimal harmonic perturbations of the temperature with the wave number k is evaluated and compared to the diffusive heat flux. This ratio is proportional to the hypothetical non-local heat conductivity κ normalized to the Spitzer–Härm conductivity κ_{SH}. Variation of the wave number changes then the non-locality of the transport with the Knudsen number $Kn_e \sim k\bar{\lambda}_e$. This kind of test is known as the Short–Epperlein problem [70, 96]. The details about the setting of the test can be found in [20]. The results show the heat flux inhibition in the non-local regime for all models. Though, no non-local transport model is able to recover the dependency $\sim Kn_e^{-1}$ of the Fokker–Planck simulations. All models based on a linear transport equation exhibit the wrong dependency $\sim Kn_e^{-2}$ in the non-local limit, as can be proved by a Fourier analysis [70]. A slightly better curve corresponds to the AWBS model with the more complex propagators [46], but the desired shape is still not attained. Although the non-local limit dependency is wrong, it might not have severe implications for real simulations of laser plasma, since most of the interaction occurs under the mildly non-local conditions [20]. The classical Fokker–Planck simulations show a very early onset of the flux inhibition, but their correction with the modification of the distribution function due to the action of the laser shows already comparable values to the other models.

4 Radiation transport

The description of the transport processes in plasma in chapters 2, 3 was limited to only convection, i.e. transport by means of an ordered motion, or conduction, i.e. by a chaotic motion, of massive particles. However, strong changes of momenta of the charged particles lead to emission of the thermal radiation, which presents the third mean of energy transport. There exist two fundamental approaches to derivation of the equation of radiative transport similarly to the light itself possessing the wave and particle descriptions.

Considering its wave nature, it can be modelled as an electromagnetic wave propagating through space following the Maxwell's equations (3–4). This methodology is applied in chapter 5 for description of the coherent radiation of a laser, but it is not feasible for the thermal radiation having a broad frequency spectrum. However, the short wavelengths allow to treat the radiation as an energy continuum described by the radiometric quantities, where the final model coincides with the particle approach followed here.

The particle description is chosen to support the analogy between the radiative and heat transport of chapter 3, which is most pronounced in the case of the non-local transport and led us to formulation of the model of chapter 3.3. Within the framework of the particle theory, the radiation can be seen as an ensemble of photons, quanta of electromagnetic force. Similarly to chapter 1, they can be described by the photon distribution function $f_R = f_R(\vec{x}, \vec{\Omega}, \nu, t)$ [97]. It determines the number of photons with frequencies in the interval $(\nu, \nu+\mathrm{d}\nu)$ in the volume $\mathrm{d}\vec{x}$ propagating along the unit vector $\vec{\Omega}$ at position $\vec{x}$ and time t. The distinction of the formalism is given by the presence of the frequency ν instead of the velocity, which was related to the non-relativistic kinetic energy of the species, but becomes meaningless for the massless particles. The correspondence can be recovered through the relation $\vec{p}^{\nu} = (h\nu/c)\vec{\Omega}$ for the momentum of a photon.

Considerations about the fundamental processes in the medium like absorption and scattering lead to reformulation of the Boltzmann equation (1) for the photons distribution [98]:

$$\frac{\partial f_R}{\partial t} + c\vec{\Omega}\cdot\nabla f_R = q^{\nu} - ck^{\nu} f_R + c\int_0^{+\infty}\int_{4\pi} \sigma_s^{\nu}(\nu', \nu, \vec{\Omega}'\cdot\vec{\Omega}) f_R(\nu', \vec{\Omega}') - \\ - \sigma_s^{\nu}(\nu, \nu', \vec{\Omega}\cdot\vec{\Omega}') f_R(\nu, \vec{\Omega})\,\mathrm{d}\vec{\Omega}'\,\mathrm{d}\nu'. \quad (137)$$

The isotropic emission is modelled through the emission function $q^{\nu} = q^{\nu}(\nu, \vec{x}, t)$ and absorption by the absorption coefficient $k^{\nu} = k^{\nu}(\nu, \vec{x}, t)$. The scattering processes are treated by the Bolzmann collision operator with the isotropic differential scattering coefficient $\sigma_s^{\nu}(\nu, \nu', \vec{\Omega}\cdot\vec{\Omega}') = \sigma_s^{\nu}(\nu, \nu', \vec{\Omega}\cdot\vec{\Omega}', \vec{x}, t)$, such that the the probability of scattering from ν to ν' and from $\vec{\Omega}$ to $\vec{\Omega}'$ in time $\mathrm{d}t$ and spectral interval $(\nu, \nu+\mathrm{d}\nu)$ is given by $c\sigma_s^{\nu}(\nu, \nu', \vec{\Omega}\cdot\vec{\Omega}')\,\mathrm{d}\nu\,\mathrm{d}\vec{\Omega}\,\mathrm{d}t$.

Similarly to chapter 3.3, the specific radiation intensity $I_R^{\nu} = I_R^{\nu}(\vec{x}, \vec{\Omega}, \nu, t)$ can be defined, which describes the infinitesimal amount of energy $\mathrm{d}E_R$ transported by radiation with the frequency in the interval $(\nu, \nu + \mathrm{d}\nu)$ along the unit vector $\vec{\Omega}$ at

position $\vec{x}$ and time t across an infinitesimal oriented surface $\mathrm{d}\vec{S}$ in time $\mathrm{d}t$ and solid angle $\mathrm{d}\vec{\Omega}$:

$$\mathrm{d}E_R = I_R^\nu(\vec{x},\vec{\Omega},\nu,t)\vec{\Omega}\cdot\mathrm{d}\vec{S}\,\mathrm{d}\vec{\Omega}\,\mathrm{d}\nu\,\mathrm{d}t. \tag{138}$$

The relation between the distribution function and the specific intensity can be found by transforming the phase space volume to the spherical coordinates. Realizing also that the energy of a photon is $h\nu$, the formula reads:

$$I_R^\nu(\vec{x},\vec{\Omega},\nu,t)\,\mathrm{d}\vec{x}\,\mathrm{d}\vec{\Omega}\,\mathrm{d}\nu = h\nu c f_R(\vec{x},\vec{p}^{\,\nu},t)\,\mathrm{d}\vec{x}\,\mathrm{d}\vec{p}^{\,\nu} = \frac{h^4\nu^3}{c^2} f_R(\vec{x},\vec{\Omega},\nu,t)\,\mathrm{d}\vec{x}\,\mathrm{d}\vec{\Omega}\,\mathrm{d}\nu. \tag{139}$$

Equipped with these relations, the Boltzmann equation of radiation (137) can be rewritten for the intensity. The Boltzmann integral is further simplified for nearly isotropic media by approximation of the BGK operator of chapter 1.1.3, but the relaxation is made towards the implicitly defined angular mean of the intensity $\bar{I}_R^\nu = 1/(4\pi)\int_{4\pi} I_R^\nu\,\mathrm{d}\vec{\Omega}$. This choice guarantees that the radiation energy is conserved as shown later. The equation of radiation transfer then reads in the form most commonly found in the literature [97]:

$$\frac{1}{c}\frac{\partial I_R^\nu}{\partial t} + \vec{\Omega}\cdot\nabla I_R^\nu = j^\nu - k^\nu I_R^\nu + \sigma^\nu(\bar{I}_R^\nu - I_R^\nu) = -\chi^\nu I_R^\nu + j^\nu + \sigma^\nu \bar{I}_R^\nu, \tag{140}$$

where $j^\nu = h^4\nu^3/c^3 q^\nu$ is the (spectral) emissivity, σ^ν the scattering coefficient and $\chi^\nu = k^\nu + \sigma^\nu$ the total extinction coefficient.

Following this notation, the spectral radiation energy density ϵ_R^ν, radiation flux $\vec{q}_R^{\,\nu}$ and radiation pressure $\underline{\underline{P}}^{R,\nu}$ present angular moments of the intensity:

$$\epsilon_R^\nu = \frac{1}{c}\int_{4\pi} I_R^\nu\,\mathrm{d}\vec{\Omega}, \qquad \vec{q}_R^{\,\nu} = \int_{4\pi} I_R^\nu\vec{\Omega}\,\mathrm{d}\vec{\Omega}, \qquad \underline{\underline{P}}^{R,\nu} = \frac{1}{c}\int_{4\pi} I_R^\nu\vec{\Omega}\vec{\Omega}\,\mathrm{d}\vec{\Omega}. \tag{141}$$

An analogy can be seen here with the velocity moments of the distribution function elaborated in chapter 1.2. The difference is given by the fact that the velocity of propagation is assumed to be constant. Practically, it can be reasoned that the refractive index in the X-ray range, which is mostly spectrally occupied by the high-temperature laser plasma [99], is close to the vacuum values in the coronal region. In contrast, the transport is dominated by many subsequent absorptions and reemissions in the dense regions rather than the behaviour of a single photon [100]. Therefore, the velocity of photons and the related transient term in the radiation transfer equation (140) are of an lesser importance here. Furthermore, the transition to the fluid reference frame is not performed as the mean velocities in the hydrodynamics were assumed non-relativistic, i.e. $|\vec{u}| \ll c$.

Integration of (140) over all solid angles yields the zeroth angular moment equation for the radiation energy:

$$\frac{\partial \epsilon_R^\nu}{\partial t} + \nabla\cdot\vec{q}_R^{\,\nu} = 4\pi j^\nu - ck^\nu\epsilon_R^\nu = -g_R^\nu. \tag{142}$$

Similarly to the energy conservation equation for massive particles (76), it has form of

a conservation law, where an interaction term appears on the right hand side of the equation. Consistently with other species, this term provides coupling with the electron distribution function, where the emission and absorption processes symmetrically exchange the energy, so the total energy is conserved. Analogously, the first angular moment of (140) provides the equation for the radiation flux in the form:

$$\frac{1}{c^2}\frac{\partial \vec{q}_R^{\,\nu}}{\partial t} + \nabla \cdot \underline{\underline{P}}^{R,\nu} = -\frac{\chi}{c}\vec{q}_R^{\,\nu} = -\vec{g}_R^{\,\nu}, \tag{143}$$

where the momentum exchange term appears on the right-hand-side for coupling with the equation of electron momentum (75).

In order to simplify the equation of radiative transfer (140) even further, the source spectrum is approximated by the gray body emission, i.e. the black body emission reduced by the opacity of the medium. This is a great simplification, because the matter is not in an equilibrium with the radiation in general and the source function $S^\nu = j^\nu/k^\nu$ is not known a priori [97]. However, following this approximation under the assumption that the physical system is not far from the LTE regime, the gray body radiative transfer equation for the total quantities becomes:

$$\frac{1}{c}\frac{\partial I_R}{\partial t} + \vec{\Omega}\cdot\nabla I_R = \rho\kappa_P\left(\frac{\sigma_{SB}}{\pi}T_e^4 - I_R\right) + \sigma_P\left(\bar{I}_R - I_R\right), \tag{144}$$

where σ_{SB} is the Stefan–Boltzmann constant, $I_R = \int_0^{+\infty} I_R^\nu \,\mathrm{d}\nu$ is the (total) radiation intensity, κ_P the Planck specific opacity and σ_P the (total) scattering coefficient. Here, the mean opacities were used, which are defined as follows:

$$\rho\kappa_P = S_B^{-1}\int_0^{+\infty} k^\nu S_B^\nu \,\mathrm{d}\nu, \qquad \sigma_P = S_B^{-1}\int_0^{+\infty} \sigma^\nu S_B^\nu \,\mathrm{d}\nu, \tag{145}$$

where $S_B^\nu = S_B^\nu(\nu)$ represents the Planck's law of radiation and $S_B = \sigma_{SB}/\pi T_e^4$ the Stefan–Boltzmann law for the total emission.

As shown in the chapter dedicated to the radiation diffusion 4.1, the averaging procedure (145) is not the only one. Essentially, it depends on the regime of transport how the averaging should be performed. In the optically thin limit, $k^\nu L \ll 1$ holds as it takes a photon a long distance to get absorbed. The gradient term on the left hand side of (140) dominates over the right hand side and the intensity is only weakly attenuated like $\sim \exp(-k^\nu s)$, where s is the path integral. The Planck averaging is then justified. However, the diffusion limit $k^\nu L \gg 1$ leads to a strong coupling between the emission and absorption and the Rosseland averaging of chapter 4.1 will be more appropriate. This problem is tackled by splitting the transport to more energy groups, which is known as the multi-group transport, or definition of an averaging process dependent on the transport conditions [101].

4.1 Radiation diffusion

Similarly to the velocity moments of the electron distribution function, the system (142–143) is not closed. There are still three unknowns ϵ_R^ν, $\vec{q}_R^{\,\nu}$ and $\underline{\underline{P}}^{R,\nu}$ for all spectral

frequencies. It remains also here to define an appropriate closure relation. In the diffusion limit $k^\nu L \gg 1$, the photons perform only close random walks in the medium and the radiation can be considered nearly isotropic. In an analogy to chapter 3.1, the intensity is expanded in the Legendre polynomials and the small parameter $(k^\nu)^{-1}$ to the first term:

$$I_R^\nu = I_0^\nu + \mu(k^\nu)^{-1} I_1^\nu, \tag{146}$$

where $\mu = \cos(\varphi)$ is the directional cosine for the polar angle φ from the z axis. The solution for I_0^ν is found from the transport equation (140) immediately, since all terms multiplied by the small parameter can be neglected and only the source function remains [102]. Having the zeroth approximation, the first one is obtained when I_0^ν is inserted instead of the unknown intensity, so the solution reads:

$$I_0^\nu = S^\nu, \qquad I_1^\nu = -\frac{\partial}{\partial z} S^\nu. \tag{147}$$

Substitution of the solution to the definitions of the angular moments (141) gives:

$$\epsilon_R^\nu = \frac{4\pi}{c} S^\nu, \qquad \vec{q}_R^\nu = -\frac{4\pi}{3\chi^\nu} \nabla S^\nu, \qquad \underline{\underline{P}}^{R,\nu} = \frac{4\pi}{3c} S^\nu \underline{\underline{I}} = \frac{1}{3} \epsilon_R^\nu \underline{\underline{I}}. \tag{148}$$

The procedure led to the Eddington's approximation of the transport, where the radiation pressure tensor is isotropic and given by the value of the energy density.

The equation of diffusion is obtained by insertion of the flux (148) to the energy equation (142), which yields:

$$\frac{\partial \epsilon_R^\nu}{\partial t} - \nabla \cdot \left(f_R^{lim} \frac{c}{3\chi^\nu} \nabla \epsilon_R \right) = 4\pi j^\nu - c k^\nu \epsilon_R^\nu. \tag{149}$$

The factor $f_R^{lim} = f_R^{lim}(Kn_R)$ is the flux limiter depending on the radiation Knudsen number $Kn_R = |\nabla \epsilon_R|/(k^\nu \epsilon_R)$ [95]. In the diffusion limit $Kn_R \to 0$, it must converge to the unity. However, it should attain values of $3/Kn_R$ in the free streaming limit, i.e. $Kn_R \to +\infty$. The reason is that this value eliminates the gradient term in the diffusion operator of (149) and changes the whole equation to a hyperbolic wave equation for ϵ_R^ν. Conceptually, this is a similar approach to the flux limiting performed in chapter 3.1.2. There exist numerous formulae in the literature for the definition of the limiter. As the most common can be considered the "sum" flux limiter, the limiter of Larsen [103], Levermore and Pomraning [104] or Minerbo [105], which are defined as follows respectively:

$$f_R^{\text{sum}} = 1/(1 + Kn_R/3), \qquad f_R^{\text{Larsen}} = (1 + (Kn_R/3)^n)^{-1/n} \qquad n \in \mathbb{R}^+, \tag{150}$$

$$f_R^{\text{LP}} = \frac{2 + Kn_R}{2 + Kn_R + Kn_R^2/3}, \qquad f_R^{\text{Minerbo}} = \begin{cases} \frac{2}{1+\sqrt{1+\frac{4}{3}Kn_R^2}} & Kn_R \leq 3/2 \\ \frac{3}{1+Kn_R+\sqrt{1+2Kn_R}} & Kn_R > 3/2 \end{cases}, \tag{151}$$

All of them are based on different assumptions and their description is beyond the scope of this text. A better insight is provided in chapter 4.2 by relating them to a

different method, the variable Eddington factor. However, the variety of the formulations already shows the inconsistency of the diffusion model, which cannot model the non-local, optically thin regime correctly.

Finally, the diffusion equation (149) can be simplified to the gray body approximation by integration over the frequencies:

$$\frac{\partial \epsilon_R}{\partial t} - \nabla \cdot \left(f_R^{lim} \frac{c}{3\rho\kappa_R} \nabla \epsilon_R \right) = c\rho\kappa_P (a_R T_e^4 - \epsilon_R), \tag{152}$$

where $a_R = 4\sigma_{SB}/c$ presents the radiation constant. The scattering opacity can be included in principle, but laser plasmas are typically dominated by the absorption processes [106, 100]. The Rosseland opacity κ_R is calculated as:

$$(\rho\kappa_R)^{-1} = \left(\frac{\partial S_B}{\partial T_e} \right)^{-1} \int_0^{+\infty} (k^\nu)^{-1} \frac{\partial S_B^\nu}{\partial T_e} \, \mathrm{d}\nu. \tag{153}$$

This kind of averaging procedure originates from the equilibrium diffusion approximation, where the temperatures of the radiation and matter are approximately the same, i.e. $T_R \approx T_e$, where the radiation temperature is defined as $\epsilon_R = a_R T_R^4$. The diffusion flux (148) is then given only by the gradient of the source, so the intensity reads [98]:

$$I_R^\nu = S^\nu - \frac{1}{\chi^\nu} \frac{\partial S^\nu}{\partial T_e} \vec{\Omega} \cdot \nabla T_e. \tag{154}$$

The gray body approximation crudely simplifies the transport, but provides the first quantitative estimate for many radiation-hydrodynamic codes [107] and solution of the coupled non-linear radiation–diffusion problem (152),(76) is non-trivial numerically [108, 95]. Radiative shocks may propagate in the medium and exactly the intermediate regime of transport is attained [106].

4.2 Angular moments method

A problem of the diffusion treatment of the radiate transfer was inability to described optically thin regime self-consistently, which led many authors to proposition of various flux limiters to at least crudely approximate the non-locality of the transport. However, the diffusion equations still possesses the infinite signal velocity of the radiation and parabolic nature of the differential operators.

The basic improvement of the model is generalization of the derivation of the diffusion theory performed in the previous chapter. The Legendre expansion method is followed until the closure relation for the pressure tensor is obtained in (148). Rather than taking the definition of the radiation flux directly, only the closure relation is

inserted to the system (142–141), which yields:

$$\frac{\partial \epsilon_R^\nu}{\partial t} + \nabla \cdot \vec{q}_R^\nu = ck^\nu \left(\frac{4\pi}{c} S^\nu - \epsilon_R^\nu \right), \tag{155}$$

$$\frac{1}{c} \frac{\partial \vec{q}_R^\nu}{\partial t} + c\nabla(f_E \epsilon^\nu) = -\chi \vec{q}_R^\nu, \tag{156}$$

where $f_E = |\underline{\underline{P}}^{R,\nu}|/\epsilon^\nu$ is the variable Eddington factor, which reflects anisotropy of the transport. The formulation of the closure is identical with the formula (148) for the value $f_E = 1/3$ defining the method known as P1 approximation [103]. This provides already the simplest non-local model of radiative transfer, as the system is hyperbolic and combination of the equations gives a single wave equation for one of the quantities, ignoring the right hand side for the moment. However, it is apparent that the velocity of propagation is $c/\sqrt{3} \doteq 0.58c$, which is far from the correct speed of light. A simple improvement is scaling the velocity in the first term of (156) by one third as well, which gives the correct velocity of the transport, but leads to excessive attenuation in the optically thin limit [109]. In principle, the value of f_E should be within the interval $(1/3, 1)$ and numerous interpolating formulas were proposed [103]. For example, a simple yet popular expression is $f_E = 1/3 + 2/3(|\vec{q}_R|/(c\epsilon_R))^2$ [110].

It cannot remain unnoticed that there exists a relation between the flux-limiters and the variable Eddigton factor [111]. Based on fundamental properties of the pressure tensor and existence of symmetries due to numerical construction of the schemes for example, an improved prescription of the pressure tensor is given (for the total radiation for simplicity):

$$\underline{\underline{P}}^R = \left(\frac{1}{2}(1 - f_E)\underline{\underline{I}} + \frac{1}{2}(3f_E - 1)\frac{\nabla\epsilon_R \nabla\epsilon_R}{|\nabla\epsilon_R|^2} \right) \epsilon_R. \tag{157}$$

The flux limiter and the Eddington factor are related based on implicit constraints between $\vec{q}_R$ and $\underline{\underline{P}}^R$ by:

$$f_E = \frac{f_R^{lim}}{3} + \frac{(f_R^{lim})^2}{9} Kn_R^2. \tag{158}$$

A method of particular interest is the one proposed by Minerbo [105]. The idea was that the ensemble is close to the Maxwell–Boltzmann distribution and entropy is maximized. It must be noted that this concept is applicable on both, fermionic and bosonic, species, which attain Maxwell–Boltzmann statistics in the high velocity limit, so this method was also applied in the electron heat transport in chapter 3.2. The Eddington factor then reads:

$$f_E^{\text{Minerbo}} = \begin{cases} \frac{1}{3} & 0 \leq \frac{|\vec{q}_R|}{c\epsilon_R} \leq \frac{1}{3} \\ \frac{1}{2}\left(1 - \left(\frac{|\vec{q}_R|}{c\epsilon_R}\right)\right)^2 + \left(\frac{|\vec{q}_R|}{c\epsilon_R}\right)^2 & \frac{1}{3} < \frac{|\vec{q}_R|}{c\epsilon_R} \leq 1 \end{cases}, \tag{159}$$

where a cut-off for low anisotropies is made, since it was believed that the value should not be lower than 1/3, but other authors suggest that this is not a true physical

requirement [103].

As a final remark, it should be noted that the angular moments method can be extended to an arbitrary order, which is known as the P_N method. However, there exist multiple variants depending on the closure relation for the last angular moment [98].

4.3 Discrete ordinates method

In addition to the angular moments method presented in chapter 4.2, there exists another large family of methods known as the discrete ordinates method or S_N method. Unlike the P_N methods, where a series of coupled equations for the Cartesian tensors of an increasing order, the S_N methods give freedom in the choice of the angular discretization and the structure of the solved equations remains identical. They are based on the work of Chadrasekhar [112], but became widely used later due to Pomraning [98].

In essence, the method is based on the approximation of the angular integral over the unit sphere as follows:

$$\frac{1}{4\pi}\int_{4\pi} I_R^\nu(\vec{\Omega}) \approx \sum_i \Psi_i I_R^\nu(\vec{\Omega}_i) = \sum_i \Psi_i (\mathbf{I}_R^\nu)_i, \tag{160}$$

where Ψ_i are weights of the quadrature, $\vec{\Omega}_i$ are their abscissae and $(\mathbf{I}_R^\nu)_i$ are values of the intensity along the discrete directions (ordinates). The weights must satisfy at least the conditions of partitioning of the unity and symmetry, i.e. $\sum_i \Psi_i = 1$ and $\sum_i \Psi_i \vec{\Omega}_i = 0$. The equation of radiative transfer (140) after the substitution splits to the series of equations:

$$\frac{1}{c}\frac{\partial}{\partial t}(\mathbf{I}_R^\nu)_i + \vec{\Omega}_i \cdot \nabla(\mathbf{I}_R^\nu)_i = j^\nu + \sigma_s^\nu \bar{\mathbf{I}}_R^\nu - \chi^\nu (\mathbf{I}_R^\nu)_i. \tag{161}$$

The function $\bar{\mathbf{I}}_R^\nu = \sum_i \Psi_i (\mathbf{I}_R^\nu)_i$ is the discrete angular mean of the intensity.

The linear system of equations is solved numerically in an explicit manner classically, where the domain is swept by the discrete rays, i.e. the characteristics of the hyperbolic equation (161). However, a problem arises for the laser plasma, where the spatial scales are minuscule and the radiation crosses the domain quickly. Rather than the transient transport, the steady state transfer is modelled, but strong coupling with the matter may exist. Therefore, it was proposed in [113] to solve an implicit set of equations for the radiation and matter, where the source function is expanded to the Taylor series in temperature $S_R^\nu = S_A^\nu T_e + S_b^\nu$, which enables the implicit coupling.

Another problem of the classical models was the locking phenomenon, where the methods were unable to treat the diffusive regime correctly and infeasible number of cells was needed to resolve the mean free path of photons $\lambda_R = (\rho\kappa_P)^{-1}$ [114]. This remedy was solved with the advent of the high-order discontinuous Galerkin (DG) methods effectively [115, 113, 94].

Finally, the method traditionally suffered from the ray effects, i.e. artificial effects originating from the fact that preferred directions of the quadrature exist in space [116, 117]. An answer to this issue can be application of the angular finite element method, which enables the local refinement techniques to be employed straightforwardly [118].

5 Laser absorption

Laser absorption has a major role in the laser plasma modelling as it presents the main driving force. Similarly to the kinetic theory of chapter 1, the interaction of the laser radiation with plasma can be divided to the collisional and collective effects [43]. The former originates from an interaction of a single particle of the medium with the incoming radiation, while the latter is given by a resonant excitation of the collective fields. For dense plasmas and moderate intensities of the laser and/or rather short wavelength of the laser, the dominant mechanism of the laser–plasma interaction is the collisional absorption. More specifically, the limit is about the value $I_L\lambda_L^2 < 1{\cdot}10^{15}\,\mathrm{W/cm^2}\mu\mathrm{m}^2$, where I_L is the intensity of the laser and λ_L its wavelength [119]. For higher intensities or longer wavelengths than the given value, the resonance absorption is dominant and other collective effects may contribute significantly like parametric instabilities or Landau damping.

In order to understand the collisional absorption for moderate intensities of the laser, the linear model of the plasma response is sufficient as the distribution function is not distorted significantly. Essentially, the description of motion of a single particle provides the full picture of interaction as already stated. For this purpose, the equation of motion for a single electron in the electric field of the laser $\vec{E}$ is considered in the form:

$$m_e\frac{\mathrm{d}\vec{v}_e}{\mathrm{d}t} = -e\vec{E} - m_e\bar{\nu}_{ei}\vec{v}_e. \tag{162}$$

The linear dumping of the oscillations, through the BGK operator with the mean electron–ion collision frequency $\bar{\lambda}_{ei}$, is applied. The ions are considered relatively cold, so their thermal velocity v_{Ti} is negligible compared to the velocity of the oscillating electrons $\vec{v}_e$. Also non-relativistic intensities of the laser are considered, so the effect of the magnetic field can be neglected in the first approximation.

The electromagnetic field of the laser is governed by the Maxwell's equations (3–4). For the purposes of the derivation, the laser radiation is approximated as a monochromatic planar wave with the angular frequency ω_L and wave vector $\vec{k}$, which has the harmonic amplitude $\sim \exp(i\vec{k}\cdot\vec{x} - i\omega_L t)$. It is also assumed that the electron is only weakly dumped and its quiver velocity is synchronous with the driving field. Insertion of the harmonic profile to (3–4) and (162) then yields:

$$i\omega_L\vec{v}_e = \frac{e}{m_e}\vec{E} + \bar{\nu}_{ei}\vec{v}_e, \tag{163}$$

$$i\vec{k}\times\vec{E} = i\omega_L\vec{B}, \tag{164}$$

$$i\vec{k}\times\vec{B} = -\frac{1}{c^2}i\omega_L\vec{E} - \mu_0 n_e e\vec{v}_e, \tag{165}$$

where the current $\vec{j} = -en_e\vec{v}_e$ is inserted simply averaging the process over an ensemble of particles provided that the interaction is linear as already stated. Multiplication of (164) by $\times\vec{k}$ and subsequent substitution of (163) and (165) gives the stationary wave

equation for the electric field:

$$(\vec{k}\cdot\vec{E})\vec{k} - \left(\vec{k}\cdot\vec{k} - \frac{\omega_L^2}{c^2} + \frac{\omega_{pe}^2}{c^2(1+i\bar{\nu}_{ei}/\omega_L)}\right)\vec{E} = 0. \tag{166}$$

The electron plasma frequency is defined classically as $\omega_{pe}^2 = e^2 n_e/(\varepsilon_0 m_e)$. The wave equation gives the dispersion relation of the transverse electromagnetic waves ($\vec{k}\cdot\vec{E} = 0$) and the definition of the complex relative refractive index $\hat{n}$ as well as the dielectric constant $\hat{\varepsilon}$:

$$\hat{\varepsilon} = \hat{n}^2 = 1 - \frac{\omega_{pe}^2}{\omega_L(\omega_L + i\bar{\nu}_{ei})}, \tag{167}$$

where the relation $|\vec{k}| = \hat{n}\omega_L/c = \hat{n}k_0$ holds. It is evident from the expression that a resonance occurs when $\omega_L = \omega_{pe}$ (despite the fact that this phenomenon is not modelled correctly by the formula due to the assumptions made). In other words, the density must be smaller than the critical density:

$$n_c = \frac{m_e\varepsilon_0}{e^2}\omega_L^2 = 4\pi^2 c^2 \frac{m_e\varepsilon_0}{e^2\lambda_L^2}, \tag{168}$$

where $\lambda_L = 2\pi c/\omega_L$ is the vacuum wavelength. Beyond the critical surface where $n_e = n_c$, only evanescent field exists there, exponentially decaying on distances comparable with the penetration depth $\delta_{pen} = \lambda_L/(2\pi \mathrm{Im}\ \hat{n})$.

The resonance absorption mechanism is caused by a p-polarized laser, which has a longitudinal component of the electric field. This causes stimulation of the plasma waves near the caustic of the beam, which reach the resonance conditions at the critical plane. To see this, the dielectric approximation can be applied using the dielectric function (167). The macroscopic Gauss's law then gives the equation for the longitudinal waves:

$$0 = \nabla\cdot(\hat{\varepsilon}\vec{E}) = \hat{\varepsilon}\nabla\cdot\vec{E} + \nabla\hat{\varepsilon}\cdot\vec{E}. \tag{169}$$

It was observed that $\hat{\varepsilon}$ has a resonance at the critical point, so once the plasma waves and the corresponding longitudinal oscillations with $\nabla\cdot\vec{E} \neq 0$ are generated, the dielectric function having the values $\mathrm{Re}\ \hat{\varepsilon} \to 0$ close to the critical plane causes their resonant excitation and absorption due to the collisions (correlating with the non-zero imaginary part).

When the main absorption mechanisms are understood, the modelling within the framework of the kinetic and hydrodynamic models must be explained. As already mentioned in the chapter about the radiative transfer 4, the small dimensions of the plasma justify stationary treatment also of the laser radiation on the hydrodynamic time scales. The equation of energy conservation for the electromagnetic field (56) then misses the inertial term and only the convective and interaction parts are present. Substitution of the latter in the energy equation of the particles (52) results in the usual form of the equation, where $\partial\epsilon_\alpha^T/\partial t \sim -\nabla\cdot\vec{S}$. The contribution to the momentum equation (39) is neglected normally, since the assumption $\epsilon_{EM} \ll \epsilon_\alpha^i$ was made to guarantee dominance of the collisional effects. However, mild effects of the ponderomotive

force can be included even within the hydrodynamic description [43]. The content of the following chapters is then to present the basic methods giving the closure model for the Poynting vector $\vec{S}$.

5.1 Ray-tracing models

Modelling of laser absorption in the context of the hydrodynamic models like the one-fluid model of chapter 2.2 limits the response frequencies of the medium strongly. Unlike electrons, ions cannot swiftly react on the changes of the local field due to their higher inertia and the center of mass system of the one-fluid model is tightly coupled with them due to their the $m_i/m_e \gg 1$ mass ratio. Moreover, the laser is typically modelled within the hydrodynamic description as only a source of energy, so its dynamic effects are limited. Therefore, the frequency splitting between the slowly evolving envelope and high frequency carrying wave can be made, which correlates with the condition $L \gg \lambda_L$. The electric field is then described as:

$$\vec{E} = \hat{E}(\vec{x}, t) \exp(i\Phi(\vec{x}, t)), \tag{170}$$

where $\hat{E} = \hat{E}(\vec{x}, t)$ is the aforementioned amplitude and $\Phi = \Phi(\vec{x}, t)$ is the phase. Further, the analysis of the of propagation of transverse electromagnetic waves in the plasma made in the introduction this chapter is used. Following the derivation of the system (163–165), the stationary wave equation for the transverse waves reads:

$$\nabla \times \nabla \times \vec{E} - k_0^2 \hat{n}^2 \vec{E} = 0. \tag{171}$$

Inserting the expression (170) to (171) yields:

$$(\nabla\Phi)^2 \vec{E} - (\vec{E} \cdot \nabla\Phi)\nabla\Phi - k_0^2 \hat{n}^2 \vec{E} = 0. \tag{172}$$

Considering that $\vec{k} = \nabla\Phi$ essentially, the central term is zero for the transverse waves and the eikonal equation is obtained:

$$(\nabla\Phi)^2 = k_0^2 \hat{n}^2. \tag{173}$$

This procedure separated the phase from the amplitude and shows that the rays in the geometric approximation follow the gradient of the phase. The phase can be also seen as a potential, where the Fermat's principle minimizes the (optical) path integral and defines the unique metric of the space [120]. The widely used ray equation can be obtained by differentiation along the path element $\mathrm{d}s$:

$$\frac{\mathrm{d}\vec{k}}{\mathrm{d}s} = \frac{1}{|\vec{k}|}(\vec{k}\nabla)\vec{k} = \frac{1}{2|\vec{k}|}\nabla|\vec{k}|^2 - \frac{\vec{k}}{|\vec{k}|} \times \nabla \times \vec{k} = \frac{1}{2|\vec{k}|}\nabla|\vec{k}|^2 - \frac{\vec{k}}{|\vec{k}|} \times \nabla \times \nabla\Phi. \tag{174}$$

The second term is evidently zero and the ray equation reads:

$$\frac{\mathrm{d}\vec{k}}{\mathrm{d}s} = k_0 \nabla\hat{n}. \tag{175}$$

Another common formulation is known as the equation of motion of the rays and can be readily obtained from the definition of the group velocity $v_g = \partial\omega/\partial|\vec{k}| = c|\nabla\Phi|/k_0$, which gives [121]:

$$\frac{\mathrm{d}^2\vec{x}_{RT}}{\mathrm{d}t^2} = \frac{\mathrm{d}\vec{v}_{RT}}{\mathrm{d}t} = \frac{c}{k_0}\frac{\mathrm{d}\nabla\Phi}{\mathrm{d}t} = \frac{c}{k_0}(\vec{v}_{RT}\cdot\nabla)\nabla\Phi = \\ = \frac{c^2}{k_0^2}(\nabla\Phi\cdot\nabla)(\nabla\Phi) = \frac{c^2}{2k_0^2}\nabla|\nabla\Phi|^2 = \frac{c^2}{2}\nabla\hat{n}^2, \quad (176)$$

where $\vec{x}_{RT}$ is the trajectory of the ray and $\vec{v}_{RT}$ its (group) velocity vector. This can be also seen as the Hamilton's equations [122]:

$$\frac{\mathrm{d}\vec{x}_{RT}}{\mathrm{d}t} = \vec{v}_{RT}, \qquad \frac{\mathrm{d}\vec{v}_{RT}}{\mathrm{d}t} = \frac{c^2}{2}\nabla\hat{n}^2, \qquad H = \frac{1}{2}((\vec{v}_{RT})^2 - c^2\hat{n}^2), \quad (177)$$

where $H = H(\vec{x}_{RT}, \vec{v}_{RT}, t)$ is the Hamiltonian of the system.

Either way, the incoming radiation is modelled as a bundle of independent rays following the density gradients, since Re $\hat{n}^2 \sim 1 - n_e/n_c$ as can be recognized from the definition (167). The common approach is then to simply replace the dielectric function by the normalized density n_e/n_c [123]. The geometric optics is then limited to the cases where Im $\hat{\varepsilon} \ll$ Re $\hat{\varepsilon}$. However, it is also possible to solve the equation (175) or (176) in the complex domain, which is known as the complex geometrical optics (CGO) [124]. It has the advantage of being able to solve the (171) behind the caustics. A fundamental problem of the methods is the missing diffraction, where a high number of the rays must be used, but artificial effects can be still noticed as the ray models the behaviour of the wave only on its axis. This led to formulation of numerous paraxial methods [125] (and the references therein). A recent method method of this kind is the paraxial complex geometrical optics (PCGO), which expands the eikonal equation (173) around the central ray in a Taylor series to describe the curvature of the wave front [122]. This results in an additional Riccati type ordinary differential equation, which must be solved along the ray, but reduces the number of rays greatly. Rather then a simple average, the energy deposition is calculated from a mesh-less interpolation of the Gaussian beamlets [93]. Another successful approach are inverse ray-tracing codes, which rather than interpolation of the beam quantities at random points distribute the points optimally in space. By variation of the initial positions of the rays, these points are reached and a smooth interpolation can be performed afterwards even with reconstruction of the wave-front eventually [126]. The piece of information about the phase is then essential for calculation of the cross-beam energy transfer, which is detrimental for the laser–target coupling in the case of multiple overlapping laser beams [127].

Finally, the absorption rate must be specified. The phase Φ is integrated along the characteristics $\vec{x}_{RT} = \int \vec{v}_{RT}\,\mathrm{d}t$ provided they are known already:

$$\Phi(\vec{x}, t) = \pm\int_{\vec{x}_0}^{\vec{x}} \vec{k}\,\mathrm{d}\vec{x}' - \omega t = \pm k_0\int_{s_0}^{s}\hat{n}\,\mathrm{d}s - \omega t. \quad (178)$$

The Wentzel–Kramers–Brillouin (WKB) solution for the Helmholtz equation (171) is obtained in the form [43]:

$$\vec{E} = \left(\frac{Q(s_0)}{\hat{n}(s)Q(s)}\right)^{1/2} \left(\hat{E}_+ \exp\left(ik_0 \int_{s_0}^{s} \hat{n}\,\mathrm{d}s\right) + \hat{E}_- \exp\left(-ik_0 \int_{s_0}^{s} \hat{n}\,\mathrm{d}s\right)\right) \exp\left(-i\omega t\right), \tag{179}$$

where $Q = Q(s)$ is the "cross-section" of the beam (a function of the path). Substitution to (171) reveals that $\mathrm{d}Q/\,\mathrm{d}s = 0$, i.e. the beam is not attenuated by gradual reflections, when the second derivatives are neglected compared to the first. The conditions are precisely:

$$\frac{\mathrm{d}^2\hat{E}}{\mathrm{d}s^2} \ll k_0\hat{E}\,\frac{\mathrm{d}\hat{n}}{\mathrm{d}s}\,, \qquad \frac{\mathrm{d}^2\hat{E}}{\mathrm{d}s^2} \ll k_0\hat{n}\,\frac{\mathrm{d}\hat{E}}{\mathrm{d}s}\,, \quad \Rightarrow \quad \frac{\mathrm{d}\hat{E}}{\mathrm{d}s} \ll \hat{n}\hat{E}, \tag{180}$$

where $\hat{E}(s) = (Q(s_0)/(\hat{n}(s)Q(s)))^{1/2}$. This relation can be translated to the refractive indices as $|\,\mathrm{d}\hat{n}/\,\mathrm{d}s| \ll |\hat{n}|^2$. However, this criterion cannot be satisfied near the critical plane, where rather the opposite is true. Hence, WKB approximation can never self-consistently describe the interaction in the vicinity of the critical density [119].

The intensity of the ray is taken as the average magnitude of the Poynting vector, which gives after substitution of (179) the relation:

$$I_L(s) = \frac{1}{\mu_0}\overline{|\vec{E}\times\vec{B}|} = \frac{1}{2}\varepsilon_0 c\hat{n}_r\hat{E}\hat{E}^* \exp(-2k_0\int_{s_0}^{s}\hat{n}_i\,\mathrm{d}s') = I(s_0)\exp(-\int_{s_0}^{s}\alpha_L\,\mathrm{d}s'), \tag{181}$$

where $\hat{n}_r = \mathrm{Re}\ \hat{n}$, $\hat{n}_i = \mathrm{Im}\ \hat{n}$ and the upper line means averaging over a period and the asterisk denotes the complex conjugate. Finally, the absorption coefficient is $\alpha_L = -2k_0\mathrm{Im}\ \hat{n}$. In other words, the intensity of the ray follows the differential Beer–Lambert law in the form:

$$\frac{\mathrm{d}I_L}{\mathrm{d}s} = \nabla\cdot\overline{\vec{S}} = -\alpha_L I_L. \tag{182}$$

This means that the intensity carried by a ray is linearly attenuated along its path.

This chapter presented only attenuation of the laser radiation. However, the identical formalism can be applied to a gain medium. In essence, the factor of weak attenuation $-\alpha_L$ can be replaced by the gain coefficient α_G, giving the gain equation for the medium. This is the case of plasma X-ray sources, which were studied by the advised student M. Šach in his academic works in collaboration with the PALS facility [128, 129]. The state of population inversion is achieved by a specifically tuned excitation laser. The spontaneous emission or a seed beam preferably is then amplified by a single pass through the pre-formed plasma medium. As the highest gain factors for the X-ray range can be found in the vicinity of the critical plane (with respect to the plasma-forming laser), the refractive effects can be important. Therefore, a ray-tracing code has been developed for this purpose, where the gain coefficients are calculated in an atomic code, solving the rate equations for electron population of the relevant atomic energy levels.

5.2 Stationary Maxwell's equations

It was recognized in chapter 5.1 that the optical approximation is mostly valid in the coronal region, where the densities of the plasma are low and vary slowly compared to the wavelength of the laser. However, it is unable to self-consistenly model the vicinity of the critical plane, where $|\nabla\hat{\varepsilon}|/|\hat{\varepsilon}| \gg k_0\hat{n}_r$ always holds. The problem is circumvented by formulation of an empirical factor for reflection and absorption at the critical density typically [130]. An alternative approach presents the wave optics, which relies on the fundamental principles of electrodynamics without resorting to strongly simplifying assumptions of the geometrical optics. On the other hand, the differential treatment of the stationary wave equation (171) is prohibited by the requirement on the spatial step, where a single wavelength $\lambda_L/\hat{n}_r$ must be resolved classically. Moreover, the microscopic conditions for the electromagnetic fields are not known and only the period averaged value of the Poynting vector enters the hydrodynamic model. Therefore, the phase of the field is not involved in the model and can be considered as an independent unknown.

These considerations led to development of the approach based on the stationary Maxwell's equations (SME) [131, 132]. Rather than solving the Helmholtz equation (171) directly, the method relies on the Maxwell's equations (3–4) rewritten for the harmonic waves (following the introduction of chapter 5) in 1D:

$$H' + ik_0\hat{n}^2 E = 0 \ , \tag{183}$$

$$E' + ik_0 H = 0 \ , \tag{184}$$

where the prime denotes the spatial derivative. It must be noted that the Gaussian system of units is used here in accordance with the references [131, 132]. The key idea of the method is then decomposition of the field to the incoming wave $P = P(x)$ (from the left hand side without the loss of generality) and outgoing (reflected) wave $R = R(x)$:

$$E = P + R, \qquad H = \hat{n}(R - P). \tag{185}$$

Substitution to the system (183–184) yields the governing equations for both waves:

$$P' = +ik_0\hat{n}P - \frac{\hat{n}'}{2\hat{n}}(P - R) \ , \tag{186}$$

$$R' = -ik_0\hat{n}R + \frac{\hat{n}'}{2\hat{n}}(P - R). \tag{187}$$

The next step is definition of the (complex) reflection coefficient $V(x) = R(x)/P(x)$. This procedure implicitly assumes that the incoming wave P does not vanish, but we are interested only in such solutions. Reformulation of the coupled system (186–187) to the new primary variables P and V yields:

$$V' = -2ik_0\hat{n}V + \frac{\hat{n}'}{2\hat{n}}(1 - V^2) \ , \tag{188}$$

$$P' = +ik_0\hat{n}P - \frac{\hat{n}'}{2\hat{n}}P(1 - V). \tag{189}$$

The solution of the given system is equivalent with the wave solution in terms of E and B as back substitution can be made. However, the complex amplitude of the incoming wave P can be reduced to the real function A proportional to the magnitude of the incoming wave $\sim |\tilde{P}|^2 = PP^*$. The governing equation then reads:

$$A' = -2k_0\hat{n}_i A - \mathrm{Re}\left(\frac{\hat{n}'}{\hat{n}}(1-V)\right)A. \tag{190}$$

The new formulation in terms of A and V is no longer equivalent to the original system as the piece of information about the phase is lost in the case of A. However, the solution fully suffices for the purposes of the hydrodynamic simulations, where only the Poynting vector $|\vec{S}| \sim A$ is needed. In particular, the expression for the Poynting vector reads [132]:

$$|\vec{S}| = A(k_0\hat{n}(|\tilde{V}|^2 - 1) - 2k_0\hat{n}_i \mathrm{Im}\ V). \tag{191}$$

It can be recognized that the Beer–Lambert law (181) is obtained in the limit $|\hat{n}'/\hat{n}| \ll k_0|\hat{n}|$. Therefore, the theory is fully consistent with the WKB approximation, but the additional terms represent the exact gradual reflections of the wave and the theory then holds even in the vicinity of the critical plane. As the derivative of the refractive index goes to infinity, the reflection coefficient V closes to the unity, i.e. the wave is completely reflected at the critical point.

The cornerstone of the method is the observation that the equation for the reflection coefficient (188) is decoupled from P or A and can be solved independently. After the solution for V is known, the complementary equation for A or P can be solved. Unlike the classical methods for the Maxwell's equations, the boundary conditions are known even in the macroscopic description, since the reflection coefficient can be set $V \approx 0$ several penetration depths δ_{pen} behind the critical plane. The other boundary condition is given by the known magnitude of the intensity of the laser outside the domain, i.e. $|\vec{S}| = I_L$ at the outer boundary.

Another important advantage of the method is the fact that it can be directly reformulated for an oblique incidence of the of the laser. The structure of the equations remains nearly the same and the refractive index is replaced by the effective value [133]. As the approach is fully wave-based, the resonance absorption in the dielectric approximation is naturally included in the solution, but it is not modelled directly as only the perpendicular components are simulated.

The equation for the reflection coefficient (188) presents a non-linear ordinary differential equation of the Riccati type. We proposed two possible approaches to its solution in [132]. The first one is semi-analytic, where the equation is integrated over a computational cell, where the density profile is approximated by a piecewise constant profile [134, 135, 82] or later extended to arbitrary profile as we proposed in [132]. The advantage of the semi-analytic treatment is the fact it is not principally limited by the constraint on resolution of the wavelength $\lambda_L/\hat{n}_r$, so it can be readily applied even in the coronal plasma. However, the solution itself is still oscillatory, so aliasing effects may be encountered, but strongly rarefied coronal plasma can be considered nearly transparent and a cut-off can be applied [82]. Another fundamental approach is the differential solution of the equation or an equivalent set of linear first order

equations not asimilar to the system (188–189). We proposed to use the high-order finite element method for this purpose, where an arbitrary order of convergence can be attained depending on the choice of the basis only [132]. This is in a contrast with the semi-analytic method, where only the second order convergence is attained.

Concluding the chapter of laser absorption, the methods of geometrical optics and wave optics can be seen as mutually complementary. The former is ideally suited for modelling of the absorption in the far coronal plasma, where the dynamics of the plasma involves remarkably longer length scales that the wavelength of the laser, i.e. $L \gg \lambda_L/\hat{n}_r$. On the other hand, it fails to describe the vicinity of the critical plane, where abrupt heating of the plasma occurs and highly non-local electrons are produced [136, 137]. The coupling of the laser and non-local transport of these is crucial for the fusion research for example [33]. The wave optics provides an answer to this problem by modelling the processes self-consistently, but its inherent complexity makes full simulations of the wave propagation for multi-dimensional hydrodynamic codes infeasible. The method based on the stationary Maxwell's equations then presents an attractive option for solution near the critical point. A combination of the geometrical and wave approach was then proposed in the literature [138], but remains a topic of the future work to accommodate for the SME method, where its benefits could be utilized.

Part II
Numerical methods

6 Finite element method

The finite element method (FEM) is one of the foremost numerical formalisms. From its origins in civil engineering [139] (chapter 1 and the references therein), it has developed to a widely general approach suitable for numerical description of virtually any linear partial differential equation. Moreover, the generality of the formalism allows to unify differential schemes with different orders of polynomial interpolation and infer high-order schemes almost effortlessly. The high-order interpolation offers high orders of convergence and more precise results even for the same number of degrees of freedom, attaining higher computational efficiency this way. Also the geometry of the elements is not restricted, enabling topologically non-uniform meshes, which combine differently shaped elements. This kind of configuration may appear in adaptive h-refinement methods, where resolution of the mesh is locally increased based on a posteriori error evaluation. Furthermore, the seamless description of the elements of different orders allows to refine the polynomial orders of the elements, which is known as the p-refinement [140]. However, it is already the Lagrangian nature of the hydrodynamic description reviewed in chapter 2.3, which leads to an automatically increased resolution in the compressed areas, like shock fronts, for example. The aim of this chapter is to lay out the common framework for the following chapters about particular finite element schemes.

In general, the physical problem is assumed to be solved on a Lipschitz domain Ω (similarly to chapter 1). This allows us to define the outer normal vector $\vec{n} = \vec{n}(\vec{x}, t)$ at (almost) all points of the boundary. The domain is assumed to be simply-connected to simplify the discussion, though it is not principally required for most methods. A physical quantity $\Psi = \Psi(\vec{x}, t)$ is approximated by a function from a given functional space on Ω. The most common choices are Sobolev spaces built from the $L_2(\Omega)$ space of square-integrable functions on Ω. The definitions of the common ones are following:

$$H^1(\Omega) = \{g \in L_2(\Omega) \mid \partial^\alpha g \in L_2(\Omega)\ \forall |\alpha| \leq 1\}, \tag{192}$$

$$H_{curl}(\Omega) = \{\vec{g} \in (L_2(\Omega))^d \mid \nabla \times \vec{g} \in (L_2(\Omega))^{2d-3}\}, \tag{193}$$

$$H_{div}(\Omega) = \{\vec{g} \in (L_2(\Omega))^d \mid \nabla \cdot \vec{g} \in L_2(\Omega)\}, \tag{194}$$

where α is a multi-index for the mixed partial derivative ∂^α. The symbol d represents the dimension of the physical space, where the space of curl-equipped functions H_{curl} is limited only to 2D and 3D. The function Ψ is then considered to be a part of one of the spaces denoted as $V(\Omega)$ ($\Psi \in V(\Omega)$). Henceforth, the notation is slightly abused and no distinction between original quantity and its approximation is made for brevity.

It must be noted that the functional spaces (192–194) are internally related. There exist exact sequences of operations traversing between the spaces, where the resulting function after the operation identically appears in the next space. These are also known as the de Rham complex [141]. In 3D, it takes the form:

$$L_2(\Omega) \xleftarrow{\nabla\cdot} H_{div}(\Omega) \xleftarrow{\nabla\times} H_{curl}(\Omega) \xleftarrow{\nabla} H^1(\Omega). \tag{195}$$

The operation connecting the spaces is noted above the arrow. In 2D, two separate

complexes exist, which can be written as:

$$L_2(\Omega) \xleftarrow{\nabla_\perp \times} H_{curl}(\Omega) \xleftarrow{\nabla} H^1(\Omega), \tag{196}$$

$$L_2(\Omega) \xleftarrow{\nabla \cdot} H_{div}(\Omega) \xleftarrow{\nabla_\parallel \times} H^1(\Omega). \tag{197}$$

Note the subscript of the curl operators denotes the destination transversal ($\perp$) or coplanar ($\parallel$) component. Finally, the 1D de Rham complex is trivial, having the form:

$$L_2(\Omega) \xleftarrow{\nabla} H^1(\Omega). \tag{198}$$

Practically, it is desired to follow the exact sequences, which avoid reinterpolation errors. For this purpose, the mathematical model is rewritten in the weak form typically. Illustratively, consider the governing equation:

$$A\Psi = b, \qquad A : V(\Omega) \mapsto V'(\Omega), b \in V'(\Omega). \tag{199}$$

First, the governing equation is multiplied by a test function from the space $V'(\Omega)$. In the case of the Galerkin methodology, the trial and test spaces are chosen identical in principal. Variations are then performed for all test functions from $V'(\Omega)$ with the inner product induced by the chosen space:

$$(A\Psi, \psi) = (b, \psi) \qquad \forall \psi \in V'(\Omega). \tag{200}$$

The integral formulation allows to apply outer calculus and manipulate the terms to obtain the weak formulation. However, it must be realized that the weak solution may not be contained in the originally searched sub-space used by the differential formulation. This points to another advantage of FEM, where even discontinuous solutions can be obtained directly and without a loss of precision, for example.

It is then convenient to rewrite the equation in terms of (bi-)linear forms, i.e. $(\cdot,\cdot)_A : V(\Omega) \times V'(\Omega) \mapsto \mathbb{R}$ and $(\cdot)_b : V'(\Omega) \mapsto \mathbb{R}$. Existence of a solution for $(\Psi, \psi)_A = (\psi)_b$ and invertibility of the underlying operator A are matter of functional and variational analysis, but a spacial role is played by self-adjoint operators and the associated symmetric forms. These arise from the mass terms in parabolic and hyperbolic equations, i.e. the identity operators multiplied by a lower bounded positive scalar or symmetric positively-definite tensor coefficient. Alternatively, they appear in elliptic equations as the stiffness terms. Provided they satisfy coercivity and boundedness, the Lax–Milgrem lemma can be applied and an unique solution exists.

The next step is tessellation of the domain, which is broken down to the elements Σ_h, covering the domain $\bigcup_{\forall \Omega_e \in \Sigma_h} \overline{\Omega_e} \supset \overline{\Omega_h}$ while not overlapping $\Omega_e \cap \Omega_{e'} = \emptyset \; \forall \Omega_e, \Omega_{e'} \in \Sigma_h, e \neq e'$ (the upper line designates the closure). It must be noted Ω_h is not identical with the original domain Ω strictly speaking, pointing to a possible geometrical error. However, this type of error is not considered any further and it is assumed the domain is perfectly aligned with the edges of the elements for simplicity. This is usually the case for flat solid targets.

An essential part of the construction is then choice of the bases functions. In

the case of conforming methods, the functional space $V(\Omega)$ is replaced by the finite-dimensional sub-space $V_h(\Omega) \subset V(\Omega)$. The functions are expanded to the basis functions:

$$\Psi(\vec{x},t) \approx \Psi_h(\vec{x},t) = \sum_{i=1}^{N_{DOF}} \mathbf{\Psi}_i(t)\psi_i(\vec{x}), \qquad V_h(\Omega) = \mathrm{span}(\{\psi_i, 1 \leq i \leq N_{DOF}\}), \quad (201)$$

where the total number of degrees of freedom is $N_{DOF} = \dim(V_h)$.

Insertion of the expansion to the weak form yields the linear system:

$$\mathbb{A}\mathbf{\Psi} = \mathbf{b}, \qquad \mathbb{A}_{ij} = (\Psi_i, \Psi_j)_A, \mathbf{b}_i = (\Psi_i)_b, \qquad \forall i,j \in \{1, \dots N_{DOF}\}. \quad (202)$$

The system is solved numerically, where the properties of the system matrix $\mathbb{A}$ are closely tight to the underlying bilinear form. The aforementioned self-adjoint operators lead to positively-definite (square) matrices (with appropriate boundary conditions), which are invertible and stable numerical algorithms can be applied. Although in more involved cases, one of the main aims of the finite element theory is then to prove convergence of the discrete solution Ψ_h to Ψ for decreasing maximal diameter of the elements.

A special category of the finite elements are curvilinear elements. These perfectly fit the Lagrangian framework by going beyond the classical affine transformation of the elements, better modelling propagating discontinuities and boundaries. In essence, the basis functions do not have to be constant, but may vary in time. In the case of Lagrangian methods, it is rather their dependency on the Lagrangian coordinates. Following the notation of chapter 2.3, the basis functions can be rewritten as $\psi_i(\vec{x},t) = \tilde{\psi}_i(\vec{\psi}_t^{-1}(\vec{x}))$. Typically, the isoparametric finite elements are used, where the identical polynomial space for interpolation of the values is also used for the mapping [140]. However, inversion of the flow $\vec{\psi}_t$ is not necessary in practice, since integration of the (bi-)linear forms is performed in the reference space, which can be assumed to coincide with the Lagrangian coordinates for simplicity. The time-evolving mapping is then only manifested by a time-dependent Jacoby matrix $J = J(\vec{X},t)$. The transformation rules are applied to perform all differential operations in the reference space, giving various combinations of the Jacoby matrices. Though, the integration is written only in the physical space here for brevity.

The outlined assembly process of the matrices and vectors from the mathematically defined (bi-)linear forms is demanding from the algebraic and computational point of view. For this reason, the construction of the discrete system and actual implementation of the numerical methods relies on the MFEM library [142, 143], which bestows the codes scalability, flexibility and high performance. It offers a large variety of finite elements including the curvilinear, like the aforementioned isoparametric or others. Also it provides the functionality of the mesh refinement mentioned in the introduction and other means of adaptivity. Likewise, it aggregates a large collection of different linear solvers from other libraries. Prominently, it integrates the Hypre library [144] and its construction, preconditioners and solvers for parallel sparse matrices. The recent development goes even further and accelerates the computation on

graphic cards and other architectures, which paves the way towards the exascale computing. However, changes on the side of the code are necessary and dedicated solvers must be used instead of the traditional ones, where the range of choices is limited, but grows steadily. Still, implementation of the presented methods on these architectures remain a topic of the future work.

Also visualization of the results of obtained with high-order finite elements is nontrivial. The support for these modern methods slowly finds its way to the visualization tools, but the best interoperability of MFEM is achieved with the sister project GLVis [145]. It is a lightweight, yet powerful tool for visualization in multiple dimensions, which also offers the possibility of the online regime of operation, when the solution is visualized during the computation directly.

7 Kinetic models

The kinetic modelling reviewed in chapter 1 presented one of the most accurate descriptions of plasma. However, numerical simulations in the full phase space are enormously demanding in multiple dimensions. For this reason, chapter 1.3 expanded the electron distribution function f to the Cartesian tensors $f_0, \vec{f}_1, \underline{f_2}, \ldots$ for increasingly more anisotropic corrections. A truncated series of the tensors for mildly anisotropic electron transport already represents a tractable system of equations in up to three spatial dimensions, a single velocity (magnitude) dimension and time. Our paper [146] presents a new reduced Vlasov–Fokker–Planck–Maxwell code based on the P1 approximation, i.e. solving (65–66) for the first two tensors ($\underline{f_2} = \underline{0}$). In essence, the structure then resembles the non-local heat transport model from chapter 3.2, but it keeps the full non-linear Fokker–Planck operator for f_0 and the Maxwell's equations to model the time-evolving electric and magnetic fields. Unlike traditional codes, it is based on high-order finite elements, giving practically an arbitrary order of convergence in space. Moreover, the temporal discretization is implicit, not requiring to perform time steps significantly shorter than the plasma frequency ω_{pe}. The plasma frequency can be extremely short in a dense plasma due to the dependency $\omega_{pe} \sim \sqrt{n_e}$ and represents a characteristic frequency for the electrodynamic coupling between Vlasov and the Maxwell's equations, as already recognized in the context of the collisional laser absorption in chapter 5. It poses a stringent limit for convergence of explicit schemes, while the implicit scheme remains robust and invulnerable to local inhomogeneities of the plasma. Finally, the scheme is designed to conserve mass, charge and energy, providing a long-term stability to the simulations.

7.1 Weak formulation

The construction of the finite element scheme in space (following the methodology of chapter 6) relies on the following functional spaces:

$$\mathcal{F}_0 = L_2(\Omega) \tag{203}$$

$$\mathcal{F}_1 = \{\vec{\psi} \in H_{div}(\Omega) \,\big|\, \vec{\psi}(\vec{x}) \cdot \vec{n} = 0 \quad \forall \vec{x} \in \Gamma_{\text{isol}}\}, \tag{204}$$

$$\mathcal{E} = \{\vec{\xi} \in H_{div}(\Omega) \,\big|\, \vec{\xi}(\vec{x}) \cdot \vec{n} = E_{\vec{n}}(\vec{x}) \quad \forall \vec{x} \in \Gamma_{\vec{E}_{\vec{n}}}\}. \tag{205}$$

These definitions can be used in 2D or 3D. The 1D case is not detailed, but it is completely analogous, only replacing $H_{div}(\Omega)$ space by $H^1(\Omega)$. The only formal difference between the 2D and 3D models is in the definition of the space for magnetic field. In 2D, only the transversal component of the field is modelled, which can be induced by the electric currents in the plane of simulation. The corresponding space is defined as:

$$\mathcal{B} = \{\omega \in H^1(\Omega) \,\big|\, \omega(\vec{x}) = B_\tau(\vec{x}) \quad \forall \vec{x} \in \Gamma_{\vec{B}_\tau}\}. \tag{206}$$

In contrast, all components of the magnetic field are modelled in 3D with the space defined as:

$$\mathcal{B} = \{\vec{\omega} \in H_{curl}(\Omega) \,\big|\, (\vec{\omega}(\vec{x}) \times \vec{n}) \times \vec{n} = \vec{B}_\tau(\vec{x}) \;\; \forall \vec{x} \in \Gamma_{\vec{B}_\tau}\}. \tag{207}$$

The definitions include the essential boundary conditions (i.e. enforced through the definitions of the spaces, typically corresponding to Dirichlet boundary conditions for the primary variables). Namely, it is the isolating boundary condition on $\Gamma_{\text{isol}} \subset \partial\Omega$ for the anisotropic part of the distribution function $\vec{f_1} \in \mathcal{F}_1$, which is responsible for the fluxes (see chapter 1.3). Secondly, it is the boundary condition for the normal electric field $E_{\vec{n}}$ on $\Gamma_{E_{\vec{n}}} \subset \partial\Omega$ and tangential magnetic field $\vec{B}_\tau$ on $\Gamma_{B_{\vec{\tau}}} \subset \partial\Omega$.

The choices of the functional spaces have a central role for the numerical scheme. The combination of the discontinuous isotropic part of the distribution $f_0 \in \mathcal{F}_0$ and divergence-equipped $\vec{f_1} \in \mathcal{F}_1$ ideally fits the classical thermodynamics, where the thermodynamic potentials originating from f_0 are conserved over an arbitrary volume and only transported by fluxes corresponding to $\vec{f_1}$ (consult chapter 9). This property of local conservation is mimicked through the de Rham complex (195) and (197) and will be preserved on the discrete level. Similarly, coincidence of the electric field $\vec{E} \in \mathcal{E}$ and $\vec{f_1} \in \mathcal{F}_1$ respects consistency of the electric charge $\sim \nabla \cdot \vec{E}$ (according to (37)) and electron density $\sim \nabla \cdot \vec{f_1} \sim f_0$. Finally, the combination of the electric field $\vec{E} \in \mathcal{E}$ and magnetic field $\vec{B} \in \mathcal{B}$ follows the de Rham complex (195) and (196), which is widely utilized in electromagnetism [147]. However, the opposite configuration is more common, where H_{div} space for magnetic field would respect the magnetic Gauss's law (37). Consequently, the conforming discrete scheme does not maintain divergence-free magnetic field, but the violation was found to be minimal [146].

The weak formulation of the system (65–66) in the P1 approximation complemented by the Maxwell's equations (3–4) can be written as ($\forall \varphi \in \mathcal{F}_0', \vec{\psi} \in \mathcal{F}_1', \vec{\xi} \in \mathcal{E}', \vec{B} \in \mathcal{B}'$):

$$\left(\frac{\partial}{\partial t} f_0, \varphi\right)_{\mathcal{F}_0\mathcal{F}_0} + \frac{v}{3}\left(\nabla \cdot \vec{f_1}, \varphi\right)_{\mathcal{F}_1\mathcal{F}_0} - \frac{e}{m_e}\frac{1}{3v^2}\left(\frac{\partial}{\partial v}(v^2\vec{f_1}), \vec{E}, \varphi\right)_{\mathcal{F}_1\mathcal{E}\mathcal{F}_0} = \left(\bar{C}_{ee}[f_0]f_0, \varphi\right)_{\mathcal{F}_0\mathcal{F}_0}, \tag{208}$$

$$\left(\frac{\partial}{\partial t}\vec{f_1}, \vec{\psi}\right)_{\mathcal{F}_1\mathcal{F}_1} - v\left(\nabla \cdot \vec{\psi}, f_0\right)_{\mathcal{F}_1\mathcal{F}_0} - \frac{e}{m_e}\left(\vec{\psi}, \vec{E}, \frac{\partial}{\partial v} f_0\right)_{\mathcal{F}_1\mathcal{E}\mathcal{F}_0} + \\ + \frac{e}{m_e}\left(\vec{f_1}, \vec{B}, \vec{\psi}\right)_{\mathcal{F}_1\mathcal{B}\mathcal{F}_1} = -\left(\nu_s\vec{f_1}, \vec{\psi}\right)_{\mathcal{F}_1\mathcal{F}_1} - v\left\langle \mathrm{T}_{\mathcal{F}_0} f_0, \vec{\psi}\right\rangle_{\mathcal{F}_0\mathcal{F}_1}^{\Gamma_{\text{free}}}, \tag{209}$$

$$-\frac{1}{c^2}\left(\frac{\partial}{\partial t}\vec{E}, \vec{\xi}\right)_{\mathcal{E}\mathcal{E}} + \left(\nabla \times \vec{B}, \vec{\xi}\right)_{\mathcal{B}\mathcal{E}} = \mu_0\left(\vec{j}, \vec{\xi}\right)_{\mathcal{F}_1\mathcal{E}}, \tag{210}$$

$$\left(\frac{\partial}{\partial t}\vec{B}, \vec{\omega}\right)_{\mathcal{B}\mathcal{B}} + \left(\nabla \times \vec{\omega}, \vec{E}\right)_{\mathcal{B}\mathcal{E}} = -\left\langle \vec{E}_\tau, \vec{\omega}\right\rangle_{\mathcal{B}}^{\Gamma_{\vec{E}_\tau}}, \tag{211}$$

where the subscript denotes the spaces on which the (tri-/bi-)linear forms operate. They represent L_2 products with the additional operators as indicated. The usage of the trilinear forms is problematic from the theoretical standpoint, since their integrability is not guaranteed. Though, it is assumed that f_0 and $\vec{f_1}$ are uniformly bounded functions, which is reasonable physically. The bilinear forms designated with $\langle \cdot, \cdot \rangle$ represent the surface integrals over the parts of the domain denoted in the superscript. The symbol $\mathrm{T}_{\mathcal{F}_0}$ stands for the trace of the function from $\mathcal{F}_0$ on the boundary. The newly appearing natural boundary condition (i.e. enforced by an additional term, typically corresponding to Neumann boundary conditon for the primary variables) on Γ_{free} sets $\partial f_0 / \partial \vec{n} = 0$. Finally, the factor $\bar{C}_{ee}[f_0]$ represents the linearized Fokker–Planck operator, which still strongly depends on f_0. The definition follows (68), but is not detailed for brevity. Instead of the full operator C_{01}, the scattering frequency ν_s is calculated from ν_{ei}, but includes the correction for electron–electron collisions according to chapter 3.1. This simplification maintains consistency with the diffusion model, but looses its theoretical foundation with increasing non-locality and becomes rather empirical.

7.2 Discrete model

Moving towards the discrete model, the finite elements are chosen from conforming spaces, i.e. sub-spaces of the functional spaces (208–207). Discontinuous polynomial finite elements are used for discretization of f_0. Since f_0 is a positive quantity fundamentally, the positive basis of Bernstein polynomials is chosen. The (normally-continuous) Raviart–Thomas H_{div}-conforming elements are used for $\vec{f_1}$ and $\vec{E}$ [148, 149]. The magnetic field $\vec{B}$ utilizes the continuous nodal finite elements in 2D and the (tangentially-continuous) Nédélec H_{curl}-conforming finite elements are used in 3D [149]. The details are omitted for brevity, but the spatial layout of the degrees of freedom (DOFs) on elements is visualized in Figure 4. It must be noted the polynomial order p appears in the definitions only as a parameter, where schemes of an arbitrary order can be constructed in principal.

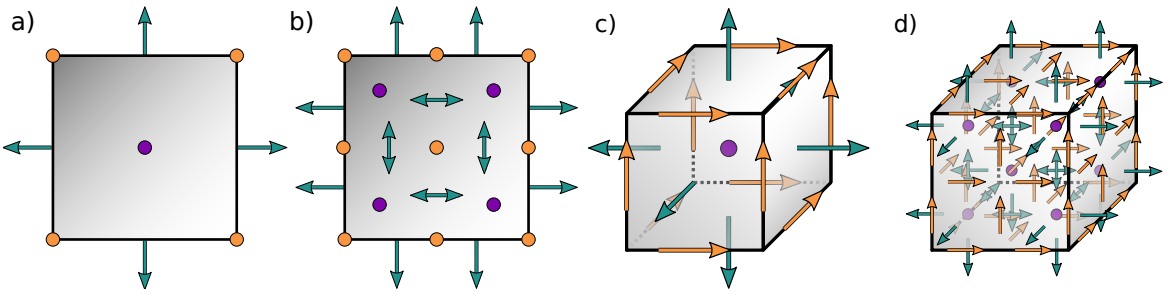

Figure 4: The spatial configuration of the reduced Vlasov–Fokker–Planck–Maxwell finite elements in 2D (a,b) and 3D (c,d) with the polynomial orders $p = 1$ (a,c) and $p = 2$ (b,d). (purple - f_0 DOFs, cyan - $\vec{f_1}$ / $\vec{E}$ DOFs, orange - $\vec{B}$ DOFs).

The discretization in the velocity dimension applies the staggered differences. The reason for this choice is the complex structure of the Fokker–Planck operator

(68). In order to conserve energy, an internal symmetry of the operator (including the Rosenbluth potentials) is required [150, 151]. Thus, application of the finite elements is highly non-trivial and remains a topic of the future work. Still, the scheme is conservative as already mentioned and attains the second order convergence in velocity [146]. In particular, the velocity domain spans from $v_0 = 0$ to $v_{N_g} = v_{max}$, where the maximal velocity v_{max} is chosen as a multiple of the expected maximal electron thermal velocity. The boundary condition $\vec{f_1}(v_{max}) = 0$ is applied, which indicates problems with the choice of v_{max}. Too low values inevitably lead to boundary effects, while too high values poorly resolve the thermal species. For that reason, new adaptive methods are being developed [152]. In any case, the anisotropic part of the distribution function $\vec{f_1}$ occupies the velocity levels with integer indices, while f_0 has the half-integer indices in between $v_{1/2}, \dots v_{N_g-1/2}$. Essentially, the layout is not asimilar to the combination of H^1 and L_2 encountered before and lead to a consistent and conserving discretization. The velocity steps are $\Delta v_g = v_{g+1/2} - v_{g-1/2} = (v_{g+1} - v_{g-1})/2$ for $g \in \{1 \dots N_g - 1\}$ and $\Delta v_{g+1/2} = (v_{g+1}^3 - v_g^3)/(3v_{g+1/2}^2)$ for $g \in \{0 \dots N_g - 1\}$. The latter formula stems from the momentum-conserving differencing [150], although momentum is not conserved by the physical model (65–66) already. The momentum of electrons is lost by scattering on static ions without their reaction to conserve the total balance of momentum between both species. Ultimately, the velocity differences have the form:

$$D_{v_g}[A] = \frac{A_{g+1/2} - A_{g-1/2}}{\Delta v_g}, \qquad D_{v_{g+1/2}}[A] = \frac{A_{g+1} - A_g}{\Delta v_{g+1/2}}. \tag{212}$$

The time integration is fully implicit in the Vlasov part, relying on the backward Euler scheme, which is L-stable and provides robustness to the scheme [153]. This feature becomes important when approaching the plasma frequency ω_{pe}, where problems with convergence of a semi-implicit and only A-stable differencing may appear [154]. In contrast, the Maxwell part is discretized with the semi-implicit Crank–Nicolson scheme, which presents a symplectic integrator [155]. This choice is related to conservation of the electromagnetic energy ϵ_{EM} (57), where both parts, electric and magnetic, are squares of the field intensities, which are not conserved by classical methods. However, the equations posses a Hamilton–Jacobi structure and the symplectic integration leads to the conservation of energy [146]. The notation of the time levels uses integers from 0 to N_t as the upper index and a constant time step Δt. The differences are denoted as:

$$D_t[A] = \frac{A^{n+1} - A^n}{\Delta t}. \tag{213}$$

After the discretization in space, velocity and time, the governing equations (208–

211) can be written for the time level n and velocity level g as:

$$\mathbb{M}^{f_0} D_t[\mathbf{f}_{0\,g+1/2}] + \frac{1}{3}\mathbb{D}\{v\mathbf{f}_1{}^{n+1}\}_{g+1/2} - \frac{1}{3v_{g+1/2}^2} D_{v_{g+1/2}}[v^2 \mathbb{M}^{\vec{f}_1\cdot\vec{E}}]\mathbf{E}^{n+1/2} = +\mathbf{q}_{g+1/2}^{f_0}, \tag{214}$$

$$\mathbb{M}^{\vec{f}_1} D_t[\mathbf{f}_{1\,g}] + (\mathbb{B}_{\text{free}}^{\vec{f}_1} - \mathbb{D}^T)\{v\mathbf{f}_0{}^{n+1}\}_g - D_{v_g}[\mathbb{M}^{f_0\vec{E}}]\mathbf{E}^{n+1} + \mathbb{M}_g^{f_1\times\vec{B}}\mathbf{B}^{n+1} = -\mathbb{Q}_g^{\vec{f}_1}\mathbf{f}_1{}_g^{n+1}, \tag{215}$$

$$-\frac{1}{c^2}\mathbb{M}^{\vec{E}} D_t[\mathbf{E}] + \mathbb{C}\mathbf{B}^{n+1/2} = \mu_0 \mathbb{M}^{\vec{j}}\mathbf{j}^{n+1}, \tag{216}$$

$$\mathbb{M}^{\vec{B}} D_t[\mathbf{B}] + \mathbb{C}^T\mathbf{E}^{n+1/2} = -\mathbf{b}_{\vec{E}_\tau}^{\vec{B}}, \tag{217}$$

where the half-integer time levels symbolize the arithmetic mean between the consecutive levels. Likewise, the curly brackets represent the arithmetic mean between the adjacent velocity levels. Following the notation of chapter 6, the grid functions associated with the primary quantities are written in bold. The matrices and vectors can be identified with the corresponding terms in (208–211), but their definitions are not presented for brevity and can be found in [146]. Note that the referenced work uses an additional normalization of the quantities, which was skipped here for simplicity.

However, the newly appearing right-hand-side term $\mathbf{q}_{g+1/2}^{f_0}$ should be explained. It represents the contribution from the Fokker–Planck collision operator written in the mass-conserving form as a difference of two velocity-space fluxes [156]:

$$\mathbf{q}_{g+1/2}^{f_0} = \frac{1}{v_{g+1/2}^2}\frac{\mathbf{w}_{g+1}^{n+1} - \mathbf{w}_g^{n+1}}{\Delta v_{g+1/2}} \qquad \forall g \in \{0 \dots N_g - 1\}. \tag{218}$$

Though, the conservation of mass requires that the boundary fluxes in the velocity space to be zero, i.e. $\mathbf{w}_0^{n+1} = \mathbf{w}_{N_g}^{n+1} = 0$. Elsewhere, the velocity-space fluxes are defined as follows:

$$\mathbf{w}_{N_g-1}^{n+1} = \mathbb{F}_{N_g-1}^{+}\mathbf{f}_{0\,N_g-1/2}^{n+1} + \mathbb{F}_{N_g-1}^{-}\mathbf{f}_{0\,N_g-3/2}^{n+1} - \mathbb{G}_{N_g-1}\frac{1}{v_{N_g-1}\Delta v_{N_g-1}}\mathbf{f}_{0\,N_g-3/2}^{n+1}, \tag{219}$$

$$\mathbf{w}_g^{n+1} = \mathbb{F}_g^{+}\mathbf{f}_{0\,g+1/2}^{n+1} + \mathbb{F}_g^{-}\mathbf{f}_{0\,g-1/2}^{n+1} + \mathbb{G}_g\frac{1}{v_g\Delta v_g}(\mathbf{f}_{0\,g+1/2}^{n+1} - \mathbf{f}_{0\,g-1/2}^{n+1}). \tag{220}$$

The definitions of the matrices $\mathbb{F}_g^{+}, \mathbb{F}_g^{-}$ and $\mathbb{G}_g$ associated with the friction and diffusion coefficients (70–71) are not detailed here, but they are implicitly depending on $\mathbf{f}_0^{n+1}$, which requires iterations of the algorithm until convergence is reached. This approach is preferred over construction of the implicit matrix with implicit friction and diffusion terms, which would be (nearly) full due to the integral nature of the coefficients [157]. The splitting of the friction term $\mathbb{F}$ to the two parts is connected with Chang–Cooper weighting to stabilize the friction [156]. Conceptually, an upwinded differencing is favoured to stabilize the advection in friction-dominated areas, while the central difference is applied in the areas dominated by the dynamic diffusion to prevent negativity of f_0 and guarantee convergence to the equilibrium.

In addition to the non-linear iterations in the collision operator, also iterations in the non-linear terms of (214–215) must be performed. All terms are implicitly coupled, but the values in the matrices are retarded by one iteration. The construction of the matrix coupling electrons and the electric and magnetic fields is designed to keep symmetries between the equations and the resulting matrix in turn. Mainly, it is the symmetry between the electric field acceleration term in (215) and the electric current term in (216), which are essential for propagating plasma waves. The Hall term in (215) with the new magnetic field prevents asymmetry of the diagonal block corresponding to $\mathbf{f}_1$ and linearises the magnetic pressure contribution. Finally, the Joule heating term in (214) reduces the sparsity pattern by dependency on the electric field rather than $\mathbf{f}_1$, but its contribution is relatively small and slow compared to the others, since it can be considered a second-order term for transient resistive currents ($\sim \vec{f}_1 \cdot \vec{E} \sim (\nabla f_0)^2/\Delta t$). It should be also noted that this term does not guarantee positivity of f_0, hence not yet converged $\vec{f}_1$ could cause negativity of f_0 and destabilize the system.

Finally, the linear system (214–217) is solved numerically. Since the system is asymmetric, non-uniform and non-positive, preconditioning is necessary. It relies on construction of incomplete Schur complements, which approximate various coupled complexes and convey them to the solver. This includes potential thermodynamic diffusion, electric and magnetic resistive diffusion and the electromagnetic wave propagators. The preconditioning matrix is then structurally symmetric and its inverse is approximated by the ParaSails solver, designed for such purposes [158]. The whole system is solved by the FGMRES method, which provides robustness to the method even for considerably asymmetric matrices [159].

7.3 Example problems

To stress the strong points of the developed kinetic code and benchmark its performance, two example problems are presented. More test cases and convergence analyses can be found in [146]. To summarize, the code attains an arbitrary order of convergence in space proportional to the polynomial order of the elements, the second order in velocities and first order in time. Moreover, it conserves mass, charge and total energy.

7.3.1 Diffusion transport in magnetic field

The diffusion theory presented in chapter 3.1 was derived from the truncated Cartesian tensor expansion of chapter 1.3. Consequently, the reduced Vlasov–Fokker–Planck–Maxwell code numerically solving the governing equations (65–66) should converge to the identical result in the diffusion limit. In order to attain this limit, the electron Knudsen number must be small enough ($Kn_e \ll 1$) or the length-scales of the electron temperature and density perturbations should be significantly shorter that the mean free path in other words. Secondly, the simulation must be performed in the electrostatic regime ($\partial\vec{E}/\partial t = 0$) with stationary fluxes $\vec{f}_1$ ($\partial\vec{f}_1/\partial t = 0$). Although not required in principal, the transport is performed in the perturbative regime and the magnetic field is set also constant similarly to the isotropic part of the distribution

function f_0. This way, the transport is completely diffusive and linear.

The initial conditions for the problem are set in 2D as follows:

$$n_e(x,y) = 1 + \delta n_e(\cos(k_x x) + \cos(k_y y)), \tag{221}$$
$$T_e(x,y) = 1 + \delta T_e(\cos(k_x x) - \cos(k_y y)), \tag{222}$$
$$B(x,y) = \delta B \sin(k_x x)\sin(k_y y). \tag{223}$$

In an agreement with the perturbative regime of the transport, the parameters are set to $\delta n_e = \delta T_e = \delta B = 10^{-3}$ and $k_x = k_y = 10^{-4}\pi$. Note that the parameters (221–223) are normalized according to [146]. In order to relate the quantities, the ratio between the collisional and collective plasma behaviour must be fixed, which is $\omega_{pe} = 10^{-1}\nu_s$ in this case. This value favours the resistive current and Hall term contributions to $\vec{f_1}$ over the gradient ∇f_0 part. The normalized magnetic field is proportional to the magnetization, which would be $\chi = 3\sqrt{\pi/2}\,\delta B \doteq 3.76 \cdot 10^{-3}$ according to the classical definition [8]. Such field is not very strong from the point of view of the transport anisotropy according to chapter 3.1.1, but the induced electric current will dominate the transport. The boundary conditions are set isolating for $\vec{f_1}$ and free for the electric field, i.e. $\partial\vec{E}\cdot\vec{n}/\partial\vec{n}|_{\Gamma_{\text{free}}} = 0$. Due to the limit nature of the test, only a single time step was performed with the length $\Delta t = t_{fin} = 10^{-4}\nu_s^{-1}$. The domain has size $10^4 \times 10^4 \bar{\lambda}_e$.

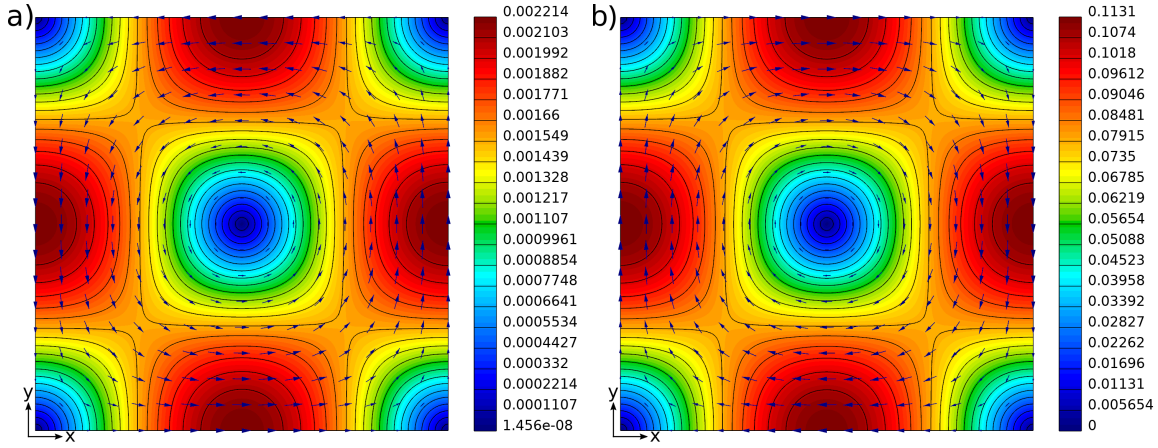

Figure 5: Numerical solution of the electron transport in magnetic field: a) electric field b) total heat flux. The values are normalized according to [146]. The false colours correspond to the magnitude, arrows show direction of the field/flux.

The solution for the heat flux and electric field is plotted in Figure 5. The simulation used 8×8 cubic elements and $N_g = 800$ velocity levels. As presumed, the electric field is dominated by the resistive current induced by the magnetic field. This can be clearly distinguished from the pressure term $\sim \nabla p_e$ or the thermoelectric term $\sim \nabla T_e$, which are proportional to the gradients of the temperature or density and which are maximal at the center of the domain. In contrast, the curl of the magnetic field is minimal there and in the corners, which agrees with the simulation. The profile of the heat flux is nearly identical and only oppositely oriented as it is dominated by the convective flux. However, also the term $T_e\underline{\underline{\beta}}\cdot\vec{j}$ significantly contributes by 37 %

approximately.

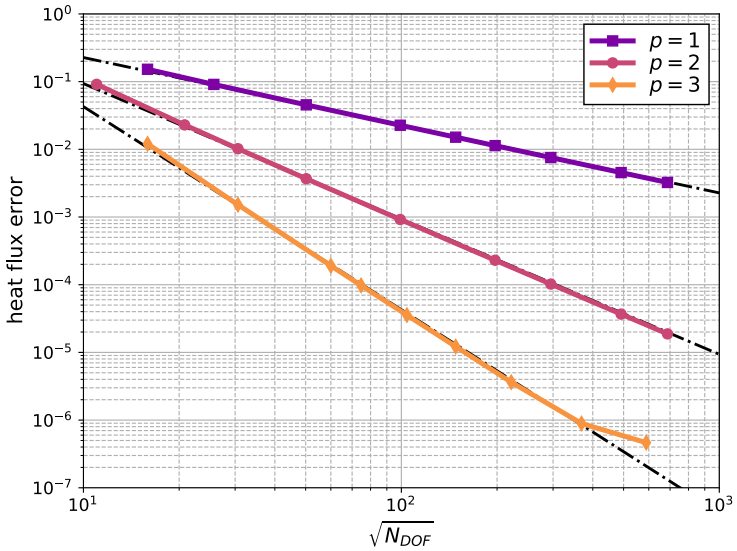

Figure 6: Convergence of the heat flux in the square root of the number of degrees of freedom. The resolution is $N_g = 800$ velocity levels. The legend denotes the orders of the elements. The black dash-dot lines indicate the first three orders of convergence.

The second goal of this test is benchmarking of the convergence in space and velocity. For reference, the classical diffusion solution is used [81], but it does not have a sufficient precision for the higher resolutions. Therefore, a reference numerical solution with 96×96 cubic elements was computed. The convergence analysis in Figure 6 shows the order of convergence is proportional to the order of the elements, which stresses the benefit of the high-order finite element methods. There is only a slight deviation near 10^{-7}, which can be attributed to the tolerance of the linear solver.

The velocity convergence is analysed in Figure 7. Approximately equal number of DOFs is used for all orders of the elements to not bias the results by this factor. The results confirm the second order of convergence, except the linear elements, where the error saturation onsets very early due to the slow convergence in space.

This test verified reproduction of the classical diffusive results by the kinetic model, where the high orders of convergence are attained thanks to the high-order finite elements in space. A strong steering of the heat flux by a magnetic field was observed.

7.3.2 Heat bath problem

The second problem considers a non-linear heat flux over a steep transition profile. This kind of problem is known as the heat bath in the literature [160, 27, 161]. Unlike the previous problem of heat diffusion, the non-local limit is explored with the Knudsen number $Kn_e \gtrsim 1$. The electrons are delocalized and a self-consistent electric field

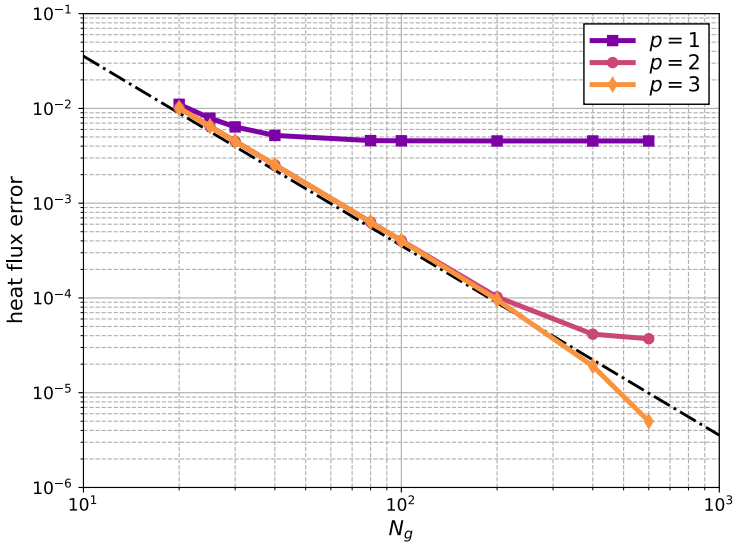

Figure 7: Convergence of the heat flux in the number of velocity levels N_g. The resolution is 200, 100 and 68 for the elements of the first, second and third order respectively. The legend denotes the orders of the elements. The black dash-dot lines indicates the second order of convergence.

emerges. The full transient electric field is modelled, despite that the simulation is run until the stationary limit is secured.

The transition profile is one-dimensional and only in the electron temperature, which is initially set as:

$$T_e(x) = 1 + \delta T_e \frac{2}{\pi} \arctan(x/\sigma_T). \tag{224}$$

The parameters are chosen as $\delta T_e = 0.9$ (in the relative units) and $\sigma_T = \delta T_e/(2Kn_e)$, where the Knudsen number is $Kn_e = 10^{-1}$. This setting presents already moderately strong non-locality [20]. The final time is $t_{fin} = 10\nu_s^{-1}$ to safely reach the desired stationary limit. Also the transient electrodynamic effects are minimized by the plasma frequency $\omega_{pe} = 10^2\nu_s$. The size of the domain is $200\bar{\lambda}_e$ to avoid boundary effects. The boundary conditions are set to the isolating for $\vec{f_1}$ and free for the electric field $(\partial\vec{E}\cdot\vec{n}/\partial\vec{n}|_{\Gamma_{\text{free}}} = 0)$.

The spatial profiles of the results are plotted in Figure 8. The simulation used 40 cubic elements, $N_g = 200$ velocity levels and the time step was set to $\Delta t = 10^{-3}\nu_s^{-1}$. The non-linearity of the flux is clearly visible from the strong asymmetry of the profiles. The flux is inhibited along the downstream, while it freely diffuses to the upstream.

A better insight is obtained from the plots of the distribution function in Figure 9. The energy-weighted isotropic part of the distribution function f_0v^4 is compared with the heat-flux-weighted anisotropic part $\vec{f_1}v^5$ at the three different point 80, 100 and 120 mean free paths from the left boundary (which are also indicated in Figure 8).

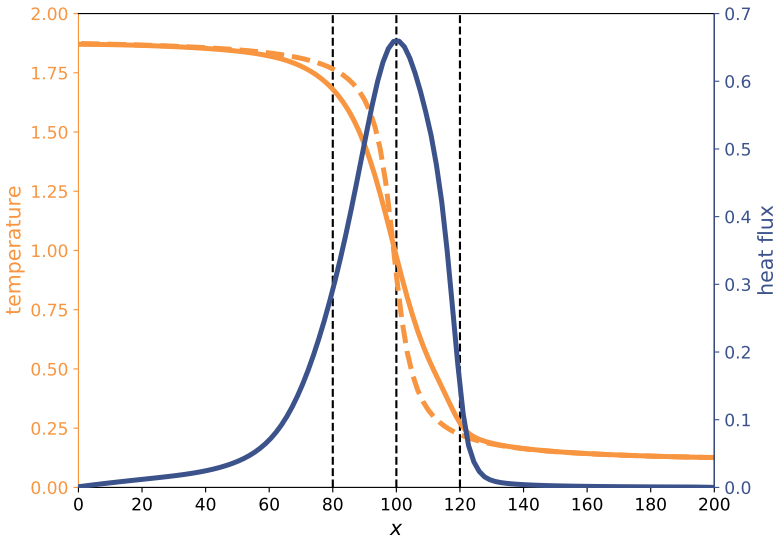

Figure 8: The numerical solution of electron transport across a transient profile. The electron temperatures are orange, heat fluxes blue. The dashed line shows the initial profile. The vertical lines indicate the points where the distribution function is investigated.

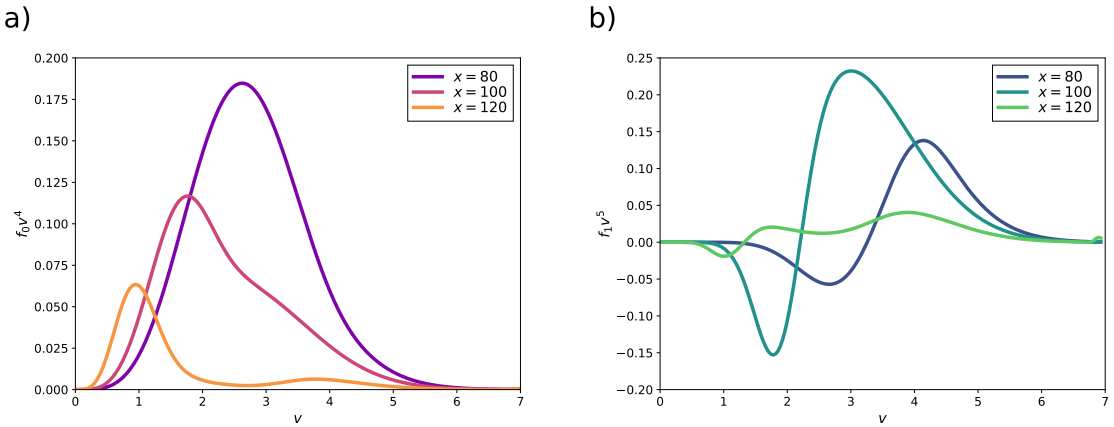

Figure 9: Spectral distribution of the electron internal energy (a) and total heat flux (b). The values are normalized according to [146]. The legend denotes the coordinates where distributions are observed along the transient profile.

The energy distribution has nearly the classical Maxwell–Boltzmann form at the first point in the upstream, but becomes gradually more non-equilibrium going further to the downstream. At the center of the domain ($x = 100\bar{\lambda}_e$), a significant deviation from the equilibrium is visible. The last point, deep in the downstream, shows a complete splitting of the distribution, where the left peak corresponds to the local temperature and the right to the temperature of the non-local electrons. The maximum is relatively small and distant, which can be attributed to the fact that only a small fraction of the high-velocity electrons is sufficiently collisionless to travel deep to the downstream. The rest is absorbed on shorter distances as the central point showed. The heat flux distributions confirm this observation. The classical profile, associated with the balance between the down-slope streaming electrons and the counter-streaming return current, appears in the upstream (compare with Figure 1). The situation changes at the central point, where the amount of the forward streaming electrons becomes relatively higher compared to the ones flowing in the opposite direction. However, the distribution of the heat flux is totally broken down in the downstream, where the return stream is strongly outbalanced by the non-local flux. Strong convective fluxes exist and the system is far from the charge and collisional equilibrium.

The problem showed an example of the non-linear, non-local heat transfer over a steep slope of temperature. The deviation of the distribution function from the Maxwell–Boltzmann distribution was observed, which points to the origins of the non-local behaviour and stresses importance of such modelling for the laser plasma physics.

8 Magneto-hydrodynamic models

The kinetic modelling of the previous chapter described electrons in a great detail, but was limited to the scale of the electron plasma frequency and approximation of motion-less ions. On the opposite side of the spectrum, magneto-hydrodynamic codes operate on longer scales, where ions and electrons move together in an approximately quasi-neutral flow (see chapter 2). Presumably, the best approach to modelling of laser plasma, where both aspects are important, is combination of the both. For this purpose, a multi-dimensional multi-physics code PETE2 has been developed [162, 163]. At the core, it relies on the resistive magneto-hydrodynamic description of the plasma, but enhances it by multiple closure models, which are subjects of the subsequent chapters.

8.1 Governing equations

The dynamics of the plasma is described in the Lagrangian framework, which was theoretically summarized in chapter 2.3. On top of the basic model, it applies the two-temperature description and contains additional terms. The governing equations are following [162, 164]:

$$\frac{\mathrm{D}\rho}{\mathrm{D}t} = -\rho\nabla\cdot\vec{u}, \tag{225}$$

$$\rho\frac{\mathrm{D}\vec{u}}{\mathrm{D}t} = -\nabla\cdot(\underline{\underline{P}}^e + \underline{\underline{P}}^i + \underline{\underline{P}}^B), \tag{226}$$

$$\vec{E}' = \frac{1}{\mu_0}\underline{\underline{\alpha}}\cdot\nabla\times\vec{B} - \frac{1}{en_e}\nabla\cdot\underline{\underline{P}}^e, \tag{227}$$

$$\frac{\mathrm{D}\vec{B}}{\mathrm{D}t} = -\nabla\times\vec{E}', \tag{228}$$

$$\rho\frac{\mathrm{D}\varepsilon_e}{\mathrm{D}t} = -\underline{\underline{P}}^e : \nabla\vec{u} + G(T_i - T_e) + \vec{j}\cdot\vec{E}' - \nabla\cdot(\vec{q}_e + \vec{S}_L) + g_R, \tag{229}$$

$$\rho\frac{\mathrm{D}\varepsilon_i}{\mathrm{D}t} = -\underline{\underline{P}}^i : \nabla\vec{u} + G(T_e - T_i) - \nabla\cdot\vec{q}_i, \tag{230}$$

$$\rho\frac{\mathrm{D}\varepsilon_B}{\mathrm{D}t} = -\underline{\underline{P}}^B : \nabla\vec{u} - \frac{1}{\mu_0}\vec{B}\cdot\nabla\times\vec{E}', \tag{231}$$

where $\vec{E}'$ is the fluid-frame electric field, which is a subject of the Lorentz transformation (97). The energy contributions are the electron heat flux $\vec{q}_e$, ion heat flux $\vec{q}_i$, radiation energy exchange rate g_R and the laser Poynting vector $\vec{S}_L$. It should be also noted that whole electric current $\vec{j}$ is inserted to the Joule heating term $\vec{j}\cdot\vec{E}'$, which is solely contributing to the electron energy equation (229). This procedure is justified by the domination of the electric and heat conduction by electrons due to their higher mobility. Though, ion heat transport is considered for the special when this assumption does not hold, but it is turned off in the most cases.

Lastly, a meaning must be given to (231). It presents the equation for the specific magnetic energy $\varepsilon_B = |\vec{B}|^2/(2\rho\mu_0)$, which can be derived similarly to the equation for the total electromagnetic energy (56). Consequently, the equation is redundant to the

equation for magnetic field (228) and mass density (225) in essence. However, it is one of the central ideas for construction of a conserving MHD scheme to keep this auxiliary equation [162, 53]. It has an identical structure to the other equations, where mechanical work of the pressure tensors matches the momentum gain in (226). Another symmetry appears between the electron energy equation (229) and the magnetic energy equation (231) when the Joule heating term in the former is rewritten as $\vec{j} \cdot \vec{E}' = 1/\mu_0 \nabla \times \vec{B} \cdot \vec{E}' = -\nabla \cdot \vec{S} + 1/\mu_0 \vec{B} \cdot \nabla \times \vec{E}'$. This symmetry leads to conservation of energy between the equations as the total contribution from the divergence of the Poynting vector vanishes globally for non-radiating boundary conditions ($(\vec{S} \cdot \vec{n})|_{\partial\Omega} = 0$).

8.1.1 Inversion of equation of state

The energy equations (229) and (230) are formally correct, but it must be realized that the temperatures are primarily used for calculation of the physical coefficients from the closure models. In order to obtain the temperatures, the equation of state must be inverted, which involves iterative algorithms and evaluations at multiple points in the thermodynamic space, which might be computationally expensive in the total. For this reason, the inversion is avoided by the following expansion, rewriting the internal derivatives as:

$$\frac{\mathrm{D}\varepsilon_e}{\mathrm{D}t} = \left(\frac{\partial \varepsilon_e}{\partial T_e}\right)_\rho \frac{\mathrm{D}T_e}{\mathrm{D}t} + \left(\frac{\partial \varepsilon_e}{\partial \rho}\right)_{T_e} \frac{\mathrm{D}\rho}{\mathrm{D}t} = c_{Ve} \frac{\mathrm{D}T_e}{\mathrm{D}t} - \rho \left(\frac{\partial \varepsilon_e}{\partial \rho}\right)_{T_e} \nabla \cdot \vec{u}, \tag{232}$$

$$\frac{\mathrm{D}\varepsilon_i}{\mathrm{D}t} = \left(\frac{\partial \varepsilon_i}{\partial T_i}\right)_\rho \frac{\mathrm{D}T_i}{\mathrm{D}t} + \left(\frac{\partial \varepsilon_i}{\partial \rho}\right)_{T_i} \frac{\mathrm{D}\rho}{\mathrm{D}t} = c_{Vi} \frac{\mathrm{D}T_i}{\mathrm{D}t} - \rho \left(\frac{\partial \varepsilon_i}{\partial \rho}\right)_{T_i} \nabla \cdot \vec{u}, \tag{233}$$

where c_{Ve} and c_{Vi} are the electron and ion specific heats. This means that substitution to (229) and (230) leads to only modification of the pressure work and no new term is necessary. For brevity, this is not explicitly written in the following chapters, but this substitution is always performed, so the primary variables are the temperatures instead of the internal energies. However, this relation holds only for the differential formulation and the discretization breaks it and the energy conservation consequently. Hence, the energy increments are integrated in parallel and the temperature is corrected in the sense of the symmetrical semi-implicit method (SSI) [165].

8.1.2 Temperature relaxation

The temperature relaxation is not linearized alongside the rest of the equations (225–231), since the relaxation operates on the time scales proportional to the local electron–ion energy collision frequency, which can be prohibitively short. For this reason, a semi-analytic approach is preferred, which may operate even on the longer time scales and preserves the correct limit behaviour. With the substitution according to chapter

8.1.1, the relaxation equations have the form:

$$\rho \left.\frac{\mathrm{D}\varepsilon_e}{\mathrm{D}t}\right|_{\text{relax}} = a_e \left.\frac{\mathrm{D}T_e}{\mathrm{D}t}\right|_{\text{relax}} = G(T_i - T_e), \tag{234}$$

$$\rho \left.\frac{\mathrm{D}\varepsilon_i}{\mathrm{D}t}\right|_{\text{relax}} = a_i \left.\frac{\mathrm{D}T_i}{\mathrm{D}t}\right|_{\text{relax}} = G(T_e - T_i), \tag{235}$$

where $a_e = \rho c_{Ve}$ and $a_i = \rho c_{Vi}$ are the heat capacities.

The semi-analytic solution approximates the equation of state as the ideal gas, i.e. considers the heat capacities constant. In fact, this is the approximation already applied in chapter 8.1.1. However, it is important that the method conserves the energy-like invariant $\epsilon_{relax} = a_e T_e + a_i T_i$ of the equations (234–235). With its help, the system can be reduced to a single equation:

$$a_{ei} \left.\frac{\mathrm{D}(T_e - T_i)}{\mathrm{D}t}\right|_{\text{relax}} = -G(T_e - T_i), \tag{236}$$

where $a_{ei} = 1/(1/a_e + 1/a_i)$ is the combined heat capacity. This equation can be solved analytically between the time levels n and $n+1$. After some manipulations, the solution can be written in the form of the differences as follows:

$$\rho\frac{\varepsilon_e^{n+1} - \varepsilon_e^n}{\Delta t} \approx a_e\frac{T_e^{n+1} - T_e^n}{\Delta t} = a_{ei}\frac{T_i^n - T_e^n}{\Delta t}\left(1 - \exp\left(-\frac{G}{a_{ei}}\Delta t\right)\right), \tag{237}$$

$$\rho\frac{\varepsilon_i^{n+1} - \varepsilon_i^n}{\Delta t} \approx a_i\frac{T_i^{n+1} - T_i^n}{\Delta t} = a_{ei}\frac{T_e^n - T_i^n}{\Delta t}\left(1 - \exp\left(-\frac{G}{a_{ei}}\Delta t\right)\right). \tag{238}$$

The equalities exactly hold only for the ideal gas, otherwise the conservative formulation with the internal energies is preferred. In this form, it is discretized analogously to the rest of the equations and the relaxation step is performed at the end of each time step.

8.2 Weak formulation

The weak formulation of the system (225–231) recognizes the thermodynamic space $\mathcal{T}$ for the scalar thermodynamic potentials $(T_e, T_i, \varepsilon_e, \varepsilon_i, \varepsilon_B)$, the kinematic space $\mathcal{K}$ for the kinematic vectors $(\vec{x}, \vec{u})$, the magnetic space $\mathcal{M}$ for the magnetic field $(\vec{B})$ and the electric space $\mathcal{E}$ for the electric field $(\vec{E})$. The energy flux terms $\vec{q}_e, \vec{q}_i, \vec{q}_R$ and $\vec{S}_L$ are not considered for the moment and are left for the subsequent chapters. The definitions of

the spaces in three dimensions are following:

$$\mathcal{T} = L_2(\Omega), \tag{239}$$
$$\mathcal{K} = \{\vec{\psi} \in (H^1(\Omega))^3 \mid \vec{\psi}(\vec{x}) \cdot \vec{n} = 0 \ \ \forall \vec{x} \in \Gamma_{\vec{u}_n}\}, \tag{240}$$
$$\mathcal{M} = H_{div}(\Omega), \tag{241}$$
$$\mathcal{E} = \{\vec{\xi} \in H_{curl}(\Omega) \mid \vec{\xi}(\vec{x}) \times \vec{n} \times \vec{n} = \vec{E}_\tau \ \ \forall \vec{x} \in \Gamma_{\vec{E}_\tau}\}. \tag{242}$$

The prescriptions already include the essential boundary conditions for non-moving boundary on $\Gamma_{\vec{u}_n}$ and tangential component of the electric field on $\Gamma_{\vec{E}_\tau}$.

The definitions in 2D are more involved, because both, the coplanar ($\|$) and transversal ($\perp$), components of the fields are modelled. The kinematic space has tensorial form and only the vector dimension is decreased ($\mathcal{K} \subset (H^1(\Omega))^2$). The definitions of the electric and magnetic spaces are:

$$\mathcal{M}_\| = H_{div}(\Omega), \tag{243}$$
$$\mathcal{M}_\perp = L_2(\Omega), \tag{244}$$
$$\mathcal{E}_\| = \{\vec{\xi} \in H_{curl}(\Omega) \mid \vec{\xi}(\vec{x}) \times \vec{n} \times \vec{n} = \vec{E}^\tau_\| \ \ \forall \vec{x} \in \Gamma_{\vec{E}_\tau}\}, \tag{245}$$
$$\mathcal{E}_\perp = \{\xi \in H^1(\Omega) \mid \xi(\vec{x}) = E^\tau_\perp \ \ \forall \vec{x} \in \Gamma_{\vec{E}_\tau}\}. \tag{246}$$

Returning back to the three-dimensional description, the procedure from chapter 6 is followed and the governing equations are multiplied by appropriate test functions. After some manipulations, the weak formulation is obtained ($\forall \varphi \in \mathcal{T}', \vec{\psi} \in \mathcal{K}', \vec{\Xi} \in \mathcal{M}'$):

$$\left(\rho \frac{\mathrm{D}\vec{u}}{\mathrm{D}t}, \vec{\psi}\right)_{\mathcal{K}\mathcal{K}} = \left((\underline{\underline{P}}^e + \underline{\underline{P}}^i + \underline{\underline{P}}^B) : \nabla\vec{\psi}\right)_{\mathcal{K}} - \left\langle \vec{P}_n \cdot \vec{\psi} \right\rangle_{\mathcal{K}}^{\Gamma_{\vec{P}_n}}, \tag{247}$$
$$\frac{\mathrm{D}\vec{B}}{\mathrm{D}t} = -\nabla \times \vec{E}', \tag{248}$$
$$\left(\underline{\underline{\alpha}}^{-1}\vec{E}', \vec{\xi}\right)_{\mathcal{E}\mathcal{E}} = \frac{1}{\mu_0}\left(\vec{B}, \nabla \times \vec{\xi}\right)_{\mathcal{M}\mathcal{E}} + \left(\underline{\underline{\alpha}}^{-1}\vec{E}_B, \vec{\xi}\right)_{\mathcal{E}\mathcal{E}} - \frac{1}{\mu_0}\left\langle \vec{B}_\tau \cdot \vec{\xi} \right\rangle_{\mathcal{E}}^{\Gamma_{\vec{B}_\tau}}, \tag{249}$$
$$\left(\rho \frac{\mathrm{D}\varepsilon_e}{\mathrm{D}t}, \varphi\right)_{\mathcal{T}\mathcal{T}} = -\left(\underline{\underline{P}}^e : \nabla\vec{u}, \varphi\right)_{\mathcal{K}\mathcal{T}} + \frac{1}{\mu_0}\left(\nabla \times \vec{E}', \vec{B}, \varphi\right)_{\mathcal{E}\mathcal{M}\mathcal{T}} + \left(\vec{E}', \vec{B}, \nabla\varphi\right)_{\mathcal{E}\times\mathcal{M}\mathcal{T}} + \\ - \frac{1}{\mu_0}\left\langle \vec{E}_\tau \times \mathrm{T}_\mathcal{M}\vec{B}, \mathrm{T}_\mathcal{T}\varphi \right\rangle_{\mathcal{M}\mathcal{T}}^{\Gamma_{\vec{E}_\tau}} - \frac{1}{\mu_0}\left\langle \vec{E}' \times \vec{B}_\tau, \mathrm{T}_\mathcal{T}\varphi \right\rangle_{\mathcal{E}\mathcal{T}}^{\Gamma_{\vec{B}_\tau}}, \tag{250}$$
$$\left(\rho \frac{\mathrm{D}\varepsilon_i}{\mathrm{D}t}, \varphi\right)_{\mathcal{T}\mathcal{T}} = -\left(\underline{\underline{P}}^i : \nabla\vec{u}, \varphi\right)_{\mathcal{K}\mathcal{T}}, \tag{251}$$
$$\left(\rho \frac{\mathrm{D}\varepsilon_B}{\mathrm{D}t}\varphi\right)_{\mathcal{T}\mathcal{T}} = -\left(\underline{\underline{P}}^B : \nabla\vec{u}, \varphi\right)_{\mathcal{K}\mathcal{T}} - \frac{1}{\mu_0}\left(\nabla \times \vec{E}', \vec{B}, \varphi\right)_{\mathcal{E}\mathcal{M}\mathcal{T}}. \tag{252}$$

The notation of the forms follows chapter 7.1, where the symbol $\times$ between the spaces denotes the cross product between the operands. The newly appearing vector $\vec{P}_n$ is the normal pressure at the boundary, which is a part of the natural boundary condition

for velocity on $\Gamma_{\vec{P}_n} \subset \partial\Omega$. Similarly, the boundary part $\Gamma_{\vec{B}_\tau} \subset \partial\Omega$ sets the natural boundary condition for the tangential magnetic field $\vec{B}_\tau$. The symbol $\mathrm{T}_{\mathcal{M}}$ represents trace of the tangential component in $\mathcal{M}$. Likewise, $\mathrm{T}_{\mathcal{T}}$ is trace in the thermodynamic space $\mathcal{T}$. Also, it can be noticed the equation of magnetic field (248) is written in the strong form, because the combination of the electric and magnetic fields respects the de Rham complex (195). In turn, the magnetic field remains always divergence-free, provided the initial condition satisfies the magnetic Gauss's law (37). Finally, it should be mentioned that the temperature relaxation terms are omitted, because they are treated separately as described in chapter 8.1.2. Also the definition of the Biermann battery term $\vec{E}_B$ is left for chapter 8.3.1. The construction in 2D and 1D is analogous, but more involved due to the splitting of the components, and the reader is navigated to [162] for more details.

8.3 Discrete model

The discretization procedure applies the conforming finite elements from subspaces of the functional spaces (239–246). The choices are similar to chapter 7.2, where discontinuous positive finite elements are used for the thermodynamic quantities. The numerical scheme can benefit from this construction in the vicinity of propagating discontinuities, for example [166]. The kinematic quantities rely on the (continuous) nodal Lagrange elements. Contrary to the kinetic model, the electric field uses the H_{curl}-conforming Nédélec finite elements and magnetic field the Raviart–Thomas H_{div}–conforming finite elements [149, 148]. These choices are made with respect to the de Rham complexes from chapter 6, so they are satisfied even on the discrete level for appropriately chosen spaces. Consequently, the (maximal) polynomial order of the discontinuous elements is lower by one than for the rest of the elements. Moreover, the thermodynamic part has the same order as the magnetic, which is denoted as $TpMp$ for the finite elements with the order of the thermodynamic space p [162]. The layout of the degrees of freedom on quadrilaterals/hexahedrals is depicted in Figure 10.

Unlike the kinetic model, where the computational mesh is static, the Lagrangian magnetohydrodynamics has a moving mesh, where the transformation properties of the elements are important. At the core, all finite elements utilize the isoparametric mapping, which ideally suits the Lagrangian description (see chapter 6). Essentially, it means the coordinates of the elements in the physical space are treated as the kinematic variable $\vec{x} \in \mathcal{K}$, which obeys the equation of motion $\mathrm{D}\vec{x}/\mathrm{D}t = \vec{u}$. The continuity equation (225) does not have to be solved at all. Due to the invariance of $|J|\rho$ according to chapter 2.3, density can be calculated at an arbitrary point as $\rho = |J_0|\rho_0/|J|$ from the initial values of density ρ_0 and Jacobian $|J_0|$. This property can be transferred to the discrete level and is known as the strong mass conservation [25]. It is also related to the fact that the matrices $\mathbb{M}_{\mathcal{K}}$ and $\mathbb{M}_{\mathcal{T}}$ are constant, since the invariant combination $\rho|J|$ is involved in their definitions. Secondly, it can be shown that the Piola transformation of the magnetic finite elements conserve their divergence and normal integrals, which implies a divergence-free structure for the field and conservation of the magnetic flux for arbitrarily deformed meshes. Similarly, the electric finite elements conserve their circulation [162, 167].

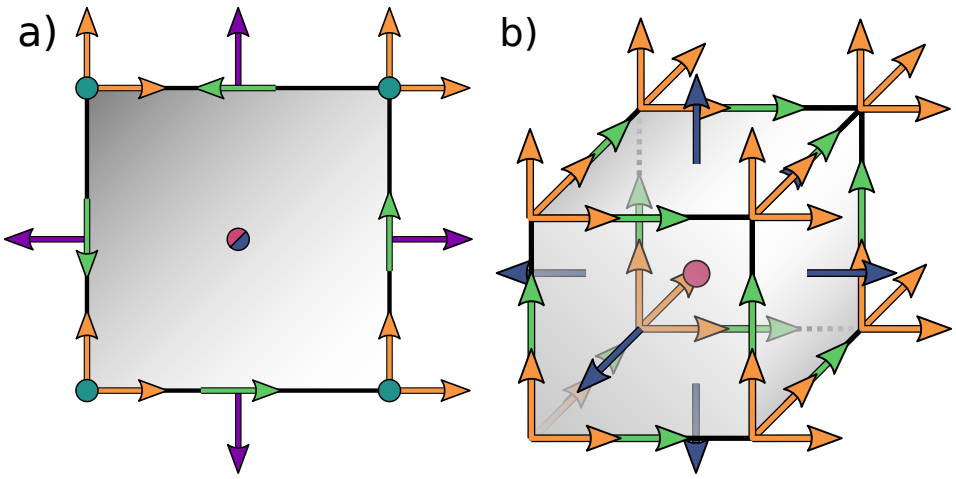

Figure 10: The spatial configuration of the magneto-hydrodynamic degrees of freedom on the reference quadrilateral/hexahedral element in 2D (a) and 3D (b). The piecewise-constant/linear finite elements $T0M0$ are presented. (red – thermodynamic, orange – kinematic, blue – (transverse) magnetic field, green – (coplanar) electric field, purple – coplanar magnetic field (only (a)), cyan – transverse electric field (only (a))).

The discretization procedure then follows chapter 6. After the discretization in space, the semi-discrete form of the system (247–252) becomes:

$$\frac{\mathrm{d}\mathbf{x}}{\mathrm{d}t} = \mathbf{u}, \tag{253}$$

$$\mathbb{M}_{\mathcal{K}} \frac{\mathrm{d}\mathbf{u}}{\mathrm{d}t} = -(\mathbb{F}_e + \mathbb{F}_i + \mathbb{F}_B)\mathbf{1} + \mathbf{b}_{\vec{P}_n}, \tag{254}$$

$$\frac{\mathrm{d}\mathbf{B}}{\mathrm{d}t} = -\mathbb{C}_D \mathbf{E}, \tag{255}$$

$$\mathbb{M}_{\mathcal{E}} \mathbf{E} = \frac{1}{\mu_0} \mathbb{C}_{.jk} \mathbf{B}_j \mathbf{1}_k + \mathbb{M}_{\mathcal{E}} \mathbf{E}_B + \mathbb{X}_B^T \mathbf{1}, \tag{256}$$

$$\mathbb{M}_{\mathcal{T}} \frac{\mathrm{d}\mathbf{e}_e}{\mathrm{d}t} = \mathbb{F}_e^T \mathbf{u} + \frac{1}{\mu_0} \mathbb{C}_{ij.} \mathbf{E}_i \mathbf{B}_j + \mathbb{S}_{ij.} \mathbf{E}_i \mathbf{B}_j + \mathbb{X}_E \mathbf{B} + \mathbb{X}_B \mathbf{E} + \mathbf{e}_B^c, \tag{257}$$

$$\mathbb{M}_{\mathcal{T}} \frac{\mathrm{d}\mathbf{e}_i}{\mathrm{d}t} = \mathbb{F}_i^T \mathbf{u}, \tag{258}$$

$$\mathbb{M}_{\mathcal{T}} \frac{\mathrm{d}\mathbf{e}_B}{\mathrm{d}t} = \mathbb{F}_B^T \mathbf{u} - \frac{1}{\mu_0} \mathbb{C}_{ij.} \mathbf{E}_i \mathbf{B}_j. \tag{259}$$

The terms can be identified with the corresponding forms in (247–252). The full definitions are not presented for brevity and can be found in [162]. The dot index means the tensors are contracted over the rest of the indices and the vectorial notation is used for the indicated one. As mentioned in the previous paragraph, the equation of motion (253) effectively replaces the continuity equation (225).

Important features of the scheme are its conservation properties. The mass and magnetic flux were discussed in the previous paragraph, while the momentum conservation is due to the definitions of the force matrices $\mathbb{F}_e, \mathbb{F}_i$ and $\mathbb{F}_B$. Provided the

boundary term $\mathbf{b}_{\vec{P}_n}$ is zero, the weak gradients appearing in the force matrices vanish when integrated over the whole domain [25]. The most intriguing is conservation of the total energy. The kinetic energy contribution is obtained by multiplication of the momentum equation (254) by $\mathbf{u}^T$ from the left. Apparently, the right hand side cancels out with the contributions from the energy equations (257–259) when integrated over the domain (multiplication by the unity vector of the thermodynamic space $\mathbf{1}^T$). As discussed already in connection with the weak form in chapter 8.2, the symmetry between (257) and (259) leads to cancellation of the exchange terms and the weak divergence of the Poynting vector also vanishes globally ($\mathbb{S} \cdot \mathbf{1} = \mathbb{O}$, where $\mathbb{O}$ is the zero matrix in the thermodynamic space). However, this is only true as long as the actual magnetic energy $\mathbf{B}^T\mathbb{M}_{\mathcal{M}}\mathbf{B}/(2\mu_0)$ is consistent with the auxiliary definition of the magnetic energy $\mathbf{1}^T\mathbb{M}_{\mathcal{T}}\mathbf{e}_B$. Without motion of the mesh, this is satisfied due to the consistency of the magnetic field equation (255) and the auxiliary magnetic energy equation (259), which can be recognized from the identity $\mathbb{C}\cdot\mathbf{1} = \mathbb{C}_D^T\mathbb{M}_{\mathcal{M}}$. Though, the consistency is broken for a moving mesh and the correction term $\mathbf{e}_B^c$ is evaluated after each time step to re-establish the total energy conservation [162]. It can be viewed as a subtle additional Joule heating term acting on the electrons.

8.3.1 Biermann battery

As straightforward integration of the Biermann term $\vec{E}_B = -\nabla p_e/(en_e)$ to the numerical scheme may seem as problematic it can be. It must be realized the term is non-linear in terms of the primary variables ρ and T_e, which predetermines it to be a subject of geometric errors. Moreover, the electron density appears in the denominator, where a direct discretization may result in the magnetic field update $\sim \nabla n_e \times \nabla T_e/n_e$ not vanishing for co-aligned gradients. Even worse, the term does not satisfy the magneto-hydrodynamic Rankine–Hugeniot conditions at shock waves. Consequently, strong, spatially oscillating localized magnetic fields might be generated at the shock fronts, which are further artificially self-amplified. This numerical instability is known as the Biermann catastrophe [168]. It was proposed to replace the term by $\vec{E}_B = k_B \ln p_e \nabla T_e/e$, which already satisfies the shock conditions and the involved temperature is typically continuous across a shock front. As long as the induced magnetic field is considered, both definitions are equivalent (for the ideal gas equation of state). Still, the full electric field is needed for the Poynting vector in the electron energy equation (257).

Another challenge is posed by generalization to the high-order finite elements [169, 170, 171]. The discontinuous temperature finite elements can be only differentiated in terms of the generalized functions, i.e. as sum of the jumps across the edges of the elements and gradients in their interiors. Due to the inherent non-linearity of the term, convergence cannot be expected for the solenoidal component especially. Secondly, the gradient part dominates the Biermann electric field with magnitude higher by multiple orders compared to the solenoidal typically, which leads to losses of precision when the components are calculated together. For these reasons, we propose a method treating the solenoidal and gradient components separately [164]. Fundamentally, it applies the Helmholtz decomposition $\vec{E}_B = \vec{E}_B^{sol} + \vec{E}_B^{grad}$. The solenoidal part $\vec{E}_B^{sol}$ and gradient

part $\vec{E}_B^{grad} = \nabla A$ are then calculated as follows:

$$\nabla \times \nabla \times \vec{E}_B^{sol} = \frac{k_B}{e} \nabla \times (\nabla \ln p_e \times \nabla T_e), \tag{260}$$

$$\Delta A = -\frac{1}{e} \nabla \cdot \frac{\nabla p_e}{n_e}. \tag{261}$$

The potential is discretized by H^1-conforming finite elements ($\mathcal{A} \subset H^1(\Omega)$), where the corresponding de Rham complexes (195), (196) can be utilized to obtain $\vec{E}_B^{grad}$ without interpolation errors. The gradients of the thermodynamic potentials in (260) are not calculated directly, but projections through weak gradients to the auxiliary variables $\vec{g}_{\ln p_e}, \vec{g}_{T_e} \in \mathcal{G} \subset H_{div}(\Omega)$ is made to avoid the problem with differentiation of discontinuous quantities. The resulting discrete system can be written as:

$$\mathbb{D}\bar{\mathbf{E}}_B = \mathbb{X}_{ij\cdot}(\mathbf{g}_{\ln p_e})_i(\mathbf{g}_{T_e})_j, \tag{262}$$

$$\mathbb{D}_{\mathcal{A}}\mathbf{A} = \mathbf{b}_A - \mathbb{G}^T\bar{\mathbf{E}}_B, \tag{263}$$

$$\mathbf{E}_B = \bar{\mathbf{E}}_B + \mathbb{G}_D\mathbf{A}, \tag{264}$$

where $\bar{\mathbf{E}}_B$ appears in the system instead of a grid function associated with $\vec{E}_B^{sol}$, because a numerical solution cannot guarantee that the undetermined gradient component of $\bar{\mathbf{E}}_B$ is not modified. Therefore, the weak gradient $\mathbb{G}^T$ then adds this spurious contribution to the potential $\mathbf{A}$. The discrete gradient $\mathbb{G}_D$ of the potential in turn eliminates this part from the electric field $\mathbf{E}_B$. The details about the procedure can be found in [164].

8.3.2 Magnetic diffusion

The semi-discrete model (253–259) involves not only the hyperbolic ideal magneto-hydrodynamic part, but also the parabolic magnetic diffusion due to the resistive eddy currents. This complex poses a computational challenge for traditional MHD codes, which apply an explicit time integration. Instead, the diffusive, magneto-dynamic part of the scheme is separated from the convective here, not stringently limiting the time step of the magnetohydrodynamics. In order to preserve the divergence-free structure of the magnetic field, the diffusion is solved for the electric field, where the new magnetic field $\mathbf{B}^{n+1}$ is inserted to the Ohm's law (256). This way, the implicit equations of magnetodynamics are obtained in the form:

$$\left(\mathbb{M}_{\mathcal{E}} + \frac{\alpha_m \Delta t}{\mu_0}\mathbb{D}\right)\mathbf{E}^{n+\alpha_m} = \frac{1}{\mu_0}\mathbb{C}_{\cdot jk}\mathbf{B}_j^n\mathbf{1}_k + \mathbb{X}_B^T\mathbf{1}, \tag{265}$$

$$\frac{1}{\Delta t}\mathbf{B}^{n+1} = \frac{1}{\Delta t}\mathbf{B}^n - \mathbb{C}_D\mathbf{E}^{n+\alpha_m}, \tag{266}$$

where the diffusion matrix $\mathbb{D} = (\mathbb{C}\cdot\mathbf{1})\mathbb{C}_D = \mathbb{C}_D^T\mathbb{M}_{\mathcal{M}}\mathbb{C}_D$ acts on the intermediate electric field $\mathbf{E}^{n+\alpha_m}$. The parameter α_m enables to chose between the explicit scheme ($\alpha_m = 0$), semi-implicit Crank-Nicolson scheme ($\alpha_m = 1/2$) and the fully implicit backward Euler scheme ($\alpha_m = 1$).

Numerically, the system (265–266) is solved by the preconditioned conjugate gradient method. In this case, the preconditioner is the Auxiliary-space Maxwell Solver (AMS) [172], which translates the problem to a nodal H^1-conforming space, where the algebraic multigrid method can be applied [173, 174].

The new values of the fields are inserted to the energy equations (257), (259), yielding the following explicit updates:

$$\left.\frac{\mathrm{d}\mathbf{e}_e}{\mathrm{d}t}\right|_{\text{Joule}} = \mathbb{M}_{\mathcal{T}}^{-1}\left(+\frac{1}{\mu_0}\mathbb{C}_{ij.}\mathbf{E}_i^{n+\alpha_m}\mathbf{B}_j^{n+1/2} + \mathbb{S}_{ij.}\mathbf{E}_i^{n+\alpha_m}\mathbf{B}_j^{n+1/2} + \mathbb{X}_E\mathbf{B}^{n+1/2} + \mathbb{X}_B\mathbf{E}^{n+\alpha_m}\right), \tag{267}$$

$$\left.\frac{\mathrm{d}\mathbf{e}_B}{\mathrm{d}t}\right|_{\text{Joule}} = \mathbb{M}_{\mathcal{T}}^{-1}\left(-\frac{1}{\mu_0}\mathbb{C}_{ij.}\mathbf{E}_i^{n+\alpha_m}\mathbf{B}_j^{n+1/2}\right). \tag{268}$$

Note that the time-centred magnetic field is used, which can be proved to guarantee exact energy conservation [162].

8.3.3 Time integration

Integration of the system (253–259) in time can be performed with multiple different methods. The Runge-Kutta methods of different orders present the basic option. However, this choice does not conserve the quadratic invariants, like the kinetic or magnetic energy. In this case, the operator splitting technique is applied and the magneto-dynamic part is solved as described in chapter 8.3.2. Another option is to employ the RK2-Average scheme derived from the classical Runge–Kutta method of the second order [25]. Although originally proposed for the classical hydrodynamics, the scheme can be extended for the resistive magnetohydrodynamics [162]. At the core, the state is split to the following three parts:

$$V = [\ \mathbf{u}\ ], \qquad B = [\ \mathbf{B}\ ], \qquad Y = [\ \mathbf{x},\ \mathbf{e}_e,\ \mathbf{e}_i,\ \mathbf{e}_B\ ]^T \tag{269}$$

$$\dot{V} = \dot{V}(t, Y), \qquad \dot{B} = \dot{B}(t, V, Y), \qquad \dot{Y} = \dot{Y}(t, V, B, Y), \tag{270}$$

where the upper dot designates the time derivatives. The updates $\dot{V}$ and $\dot{B}$ are implicit, while $\dot{Y}$ is explicit. However, the form of the momentum equation (254) does require an implicit solution, since the right hand side is independent of V. Thus, an explicit integration can be applied in fact, but it is important that the integration remains symplectic. Secondly, the magnetic field is solved within the update of B according to chapter 8.3.2, where the velocities are already known (which are needed in 2D and 1D, see [162]). Finally, the explicit step with $\dot{Y}$ is performed, where the time-centred velocity and magnetic field are known already. This way, the total energy is conserved. The outlined scheme presents a second-order implicit-explicit method (IMEX), which can be generalized for the hydrodynamics to the higher orders [175]. Unfortunately, this approach cannot be followed in the case of the magneto-hydrodynamic methods, where the negative time steps in the implicit part would draw the diffusion equation (265) ill posed. The high-order symplectic IMEX methods for this purpose remain a topic of the future research and the code is limited to the RK2-Average scheme.

The actual length of the time step controlled by the Courant–Fridrichs–Lewy (CFL) condition [176]. It limits the length of the time step with respect to the fastest propagating mode in the system. In the case of MHD, it is the fast mode with velocity $v_f^2 = c_s^2 + v_A^2$, where $c_s = c_s(\rho, T_e, T_i)$ is the speed of sound and $v_A = |B|/\sqrt{\mu_0 \rho}$ is the Alfvén velocity. The time step is then determined as the minimum of $C_{CFL} h / v_f$, where h is the inner radius of the element and $C_{CFL} < 1$ a chosen parameter. Though, the range of the permissible values of C_{CFL} is limited by the stability of the scheme, where $C_{CFL} \leq 1/2$ holds for the hydrodynamic scheme [25].

8.3.4 Artificial viscosity

Although the momentum equation (254) is deemed to be explicit within the time integration (chapter 8.3.3), the force matrices $\mathbb{F}_e$ and $\mathbb{F}_i$ depend on the internal energies $\mathbf{e}_e$ and $\mathbf{e}_i$, which in turn depend on their mechanical work. Similarly, the magnetic pressure term $\mathbb{F}_B$ depends on the magnetic field, which is compressed by motion of the fluid and computational mesh. Therefore, the numerical scheme must be stabilized to take into account this kind of non-linearity. The classical approach to this problem is integration of an artificial viscosity to the system. This viscosity is added to the physical pressure tensors and dissipates the kinetic energy to the internal through its mechanical work, which is typically added to the ion equation as ions are dominantly involved in the shocks in dense matter. In order to take into account directionality of the compression, the tensor viscosities are utilized, which depend on $\nabla \vec{u}$ [25, 177]. These are modified similarly to the CFL condition (chapter 8.3.3) to consider the magneto-hydrodynamic fast mode in plasma.

8.4 Example problems

Two example problems are presented here to test the features of the MHD model and benchmark its properties. The first problem (chapter 8.4.1) analyses convergence for smooth problems of ideal MHD on deformed meshes, while the second explores behaviour of the code for a physically relevant problem of a blast wave in a magnetic field. More test cases can be found in [162]. The results can be summarized in the way that an arbitrary order of convergence is achieved in space, proportional to the polynomial order of the elements. Similarly, convergence in time has an arbitrary order of convergence in the case of ideal MHD or uncoupled problems of resistive MHD, when the high-order IMEX methods are employed. The convergence for coupled problems of resistive MHD is limited to the second order for the RK2-Average scheme at the moment.

8.4.1 Taylor–Green vortex

The problem known as the Taylor–Green vortex presents a steady-state solution of incompressible, inviscid hydrodynamics. It was successfully applied to the high-order curvilinear finite element hydrodynamics [175, 25] and we extend its formulation to ideal magnetohydrodynamics in [162]. A specific magnetic field field $\vec{B} = \beta \sqrt{\mu_0} \vec{u}$ co-aligned with the velocity is chosen, where β is a free parameter. This construction

guarantees a divergence-free structure of the magnetic field similarly to the velocity. The stationary solution takes the following form in 2D:

$$\vec{u}_x(x,y) = \sin(\pi x)\cos(\pi y), \tag{271}$$
$$\vec{u}_y(x,y) = -\cos(\pi x)\sin(\pi y), \tag{272}$$
$$p(x,y) = 1 + \frac{1-\beta^2}{4}(\cos(2\pi x) + \cos(2\pi y)) - \frac{\beta^2}{2}(\sin^2(\pi x)\cos^2(\pi y) + \cos^2(\pi x)\sin^2(\pi y)). \tag{273}$$

The classical hydrodynamic problem is obtained for $\beta = 0$, but the magnetic pressure contributes to the momentum equation in other cases, which is compensated by the definition of the scalar pressure p (one-temperature model is used). The method of fabricated solution is then followed to keep the system stationary, which entails an additional source of energy in the energy equation. It has the identical form with the original problem due to the compensation of the pressures [162, 25]:

$$S_e = \frac{3}{8}\pi(\cos(3\pi x)\cos(\pi y) - \cos(\pi x)\cos(3\pi y)). \tag{274}$$

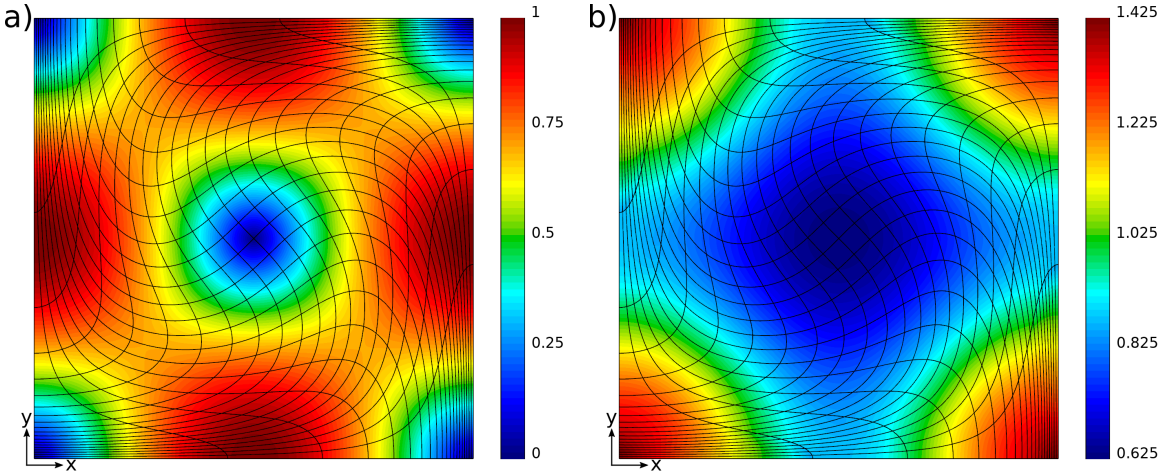

Figure 11: Numerical solution of the Taylor–Green vortex at the final time $t = 0.75$: a) velocity magnitude, b) thermal pressure. All values are in relative units.

The ideal gas equation of state is used throughout the simulations, where proton number and ionization are set to $A = Z = 1$ and the Poisson constant is $\gamma = 5/3$. The initial density is uniformly set as $\rho = 1$ and remains (approximately) constant due to the incompressibility, hence it is not a part of the solution. The artificial viscosity is not applied, because the problem is smooth as full consistency with the ideal model is desired. The coefficient of the magnetic field is chosen as $\beta = 1/2$, which effectively means the dynamic pressure is four times stronger than the magnetic. The numerical solution in visualized in Figure 11 for quadratic/cubic finite elements $T2M2$ and the third-order IMEX time integrator with $C_{CFL} = 0.5$. A strong torsion of the computational mesh is apparent, but the quantities remain mostly unaffected, which

highlights advantages of high-order methods.

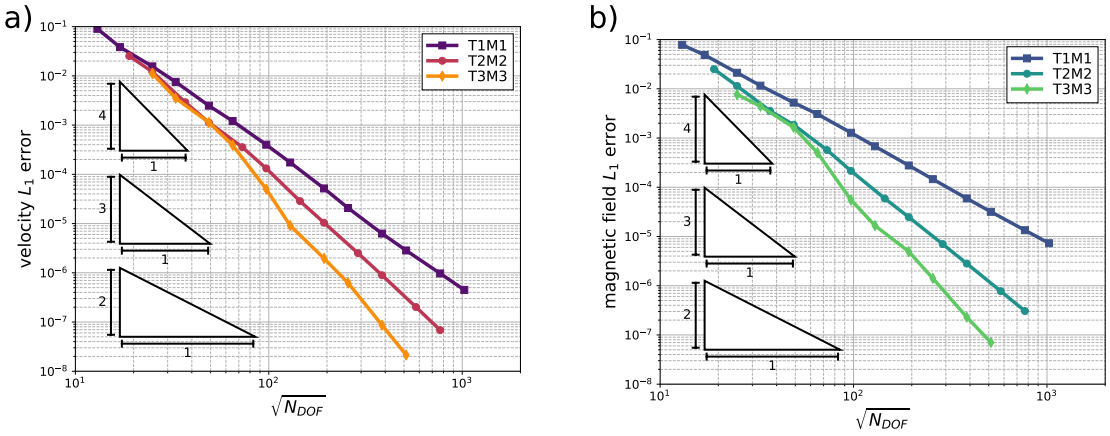

Figure 12: Convergence rates for the Taylor–Green problem in the number of degrees of freedom N_{DOF}: a) velocity, b) magnetic field. The legend designates the finite elements used. See the accompanying text for more details.

The convergence analysis of the problem is plotted in Figure 12. Finite elements of different orders are compared ($T1M1$, $T2M2$ and $T3M3$), where the orders of the conservative IMEX integrators are chosen adequately. Due to the fixed CFL condition, the time step decreases with increasing resolution, implying the total convergences are measured. The convergence rates proportional to the polynomial order of the elements are apparent. However, the velocity rate is noticeably higher. This phenomenon can be explained by the magnetic pressure contributing to the momentum equation, which has a higher order than the thermal pressure. The effect vanishes with decreasing coefficient β as the Alfvén velocity slows down compared to the fluid velocity.

The problem of the Taylor–Green vortex showed the high orders of convergence of the curvilinear finite element MHD for smooth problems. The high-order finite elements in space were combined with high-order time integration methods. The presence of a magnetic field was not jeopardizing the convergence, but rather improving it.

8.4.2 Blast wave in magnetic field

The problem of a propagating blast wave in a magnetic field is one of the classical test cases for magneto-hydrodynamic codes [178], but already presents a simplified model of magnetized cosmic jets [179]. Although, it has a relevance to the inertial confinement fusion too [180]. In principal, it holds a strong resemblance to the (purely) hydrodynamic problem of Sedov blast wave [181]. A high amount of energy is deposited at the center of the domain and the symmetric blast wave propagating from this point is simulated. The imposed magnetic field then adds the effect of collimation and along the field lines and generation of magneto-hydrodynamic blasts in the transverse direction. Still, the symmetry along the field is preserved, where the effects of mesh imprinting can be studied, i.e. effect of the mesh geometry on the dispersion relations and the numerical results in the end.

The simulation runs on the simulation domain $(-1, 1)^3$ in three dimensions. The energy $E = 1$ is deposited at the origin of the coordinates system, while the background medium has density $\rho = 1$ and negligible pressure. The ideal gas equation of state is used with the Poisson constant $\gamma = 5/3$, atomic mass number $A = 1$ and ionization $Z = 0$. The magnetic field is imposed along the x axis with magnitude $B_x = \sqrt{4/3\mu_0}$. The evolution is tracked till the final time $t_{fin} = 0.25$ with the CFL constant $C_{CFL} = 0.5$. The tensor artificial viscosity based on eigenvector decomposition is used with the linear coefficient 0.5 and quadratic 2 [25, 177].

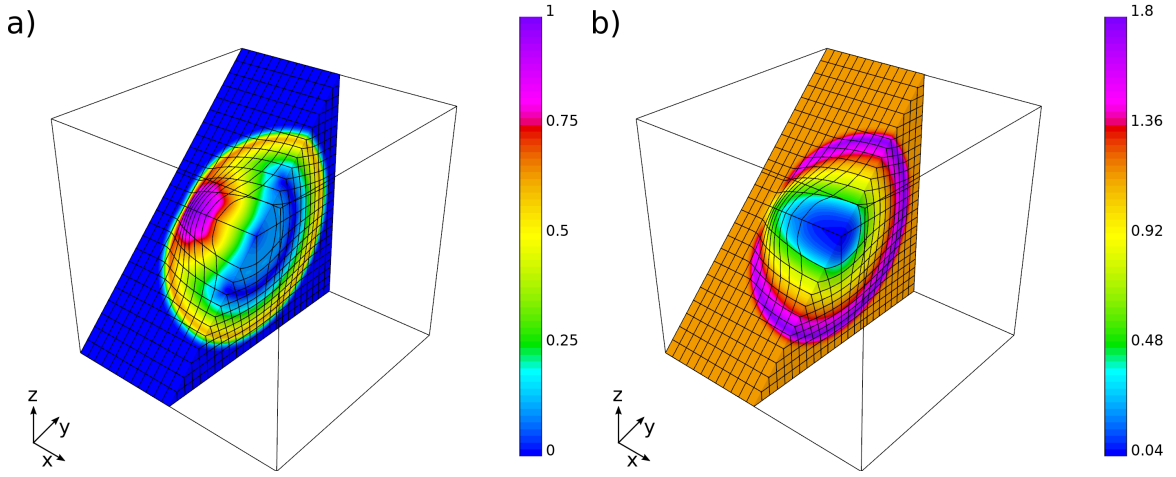

Figure 13: The numerical solution of the blast wave in magnetic field: a) velocity magnitude, b) magnetic field magnitude. The values are in the relative units. The resolution is $24 \times 24 \times 24$ finite elements of the $T2M2$ type.

The numerical profiles of the velocity and magnetic field are plotted at the final time in Figure 13. The quadratic/cubic finite elements $T2M2$ are employed with the third-order IMEX time integrator. The results confirm the high resiliency of the numerical scheme with respect to deformation of the computational mesh. The propagation of the wave remains mostly unaffected by the geometry and the Lagrangian nature of the model leads to an increased resolution near the tips of the collimated jet in x axis. The natural compression of the magnetic field in the transverse plane can be also observed, which is not modelled explicitly, but given by the transformation properties of the magnetic elements (see chapter 8.3).

The problem of a strong blast wave in a magnetic field showed capabilities of the MHD code under physically-relevant conditions. The symmetry of the problem was maintained to a great extend thanks to the high-order curvilinear finite elements. The magnetic field was compressed and convected along the blast fronts correctly without its explicit calculation, highlighting another benefit of the finite element Lagrangian magnetohydrodynamics.

9 Diffusion models

The diffusion modelling is the most common approach for the heat fluxes and radiation fluxes as described in chapters 3.1 and 4.1. From the theoretical point of view, the parabolic nature of the equations is advantageous in the way that entropy is produced and the minimal value theorem holds. Therefore, stable convergent numerical methods can be constructed with a relative ease. An implicit treatment of the time integration is favoured to avoid explicit time-stepping with $\Delta t \sim \Delta x/\eta$, where Δx is the resolved spatial scale and η the diffusivity. This approach was already followed in the chapter about the magnetodynamics 8.3.2.

9.1 Governing equations

The equations of heat diffusion and radiation diffusion hold many similarities, but there are subtle, yet important differences in the formulations and the accustomed types of the boundary conditions. Typically, it is the isolating boundary condition for zero normal boundary heat flux in the case of heat diffusion, while free streaming to open space is used for the radiation.

9.1.1 Heat diffusion

The electron/ion heat diffusion contribution to the electron/ion energy equations (229), (230) has the form:

$$a_{e/i} \left.\frac{\mathrm{D}T_{e/i}}{\mathrm{D}t}\right|_{\text{heat}} = -\nabla \cdot \vec{q}_{e/i}, \tag{275}$$

$$\vec{q}_{e/i} = -\underline{\underline{\kappa_{e/i}}} \cdot \nabla T_{e/i}, \tag{276}$$

where symbols $\underline{\underline{\kappa_e}}$ and $\underline{\underline{\kappa_i}}$ represent the tensor heat conductivities. However, the conductivities are strongly temperature-dependent as derived in chapter 3.1. Hence, it is beneficial to non-linearly transform the equations to obtain the normalized form:

$$\bar{a}_{e/i} \left.\frac{\mathrm{D}\bar{T}_{e/i}}{\mathrm{D}t}\right|_{\text{heat}} = -\nabla \cdot \vec{q}_{e/i}, \tag{277}$$

$$\vec{q}_{e/i} = -\underline{\underline{\bar{\kappa}_{e/i}}} \cdot \nabla \bar{T}_{e/i}, \tag{278}$$

where the quantities are transformed as follows:

$$\bar{T}_{e/i} = T^{\alpha_T+1}, \qquad \bar{a}_{e/i} = \frac{a_{e/i}}{\alpha_T+1} T_{e/i}^{-\alpha_T}, \qquad \underline{\underline{\bar{\kappa}_{e/i}}} = \frac{\underline{\underline{\kappa_{e/i}}}}{\alpha_T+1} T_{e/i}^{-\alpha_T}. \tag{279}$$

The parameter α_T is the exponent of the nominal dependency of the heat conductivity $\kappa \sim T_{e/i}^{\alpha_T}$ on temperature. In the case of the Spitzer-Härm conductivity it is $\alpha_T = 5/2$. This way, the equations is approximately linear and suitable for discretization.

9.1.2 Radiation diffusion

The radiation non-equilibrium diffusion in the gray-body approximation (152) has nearly the identical structure to the heat diffusion equations (275–276) and read:

$$\frac{\mathrm{D}\epsilon_R}{\mathrm{D}t} = -\nabla \cdot \vec{q}_R + \mu_R(a_R T_e^4 - \epsilon_R), \tag{280}$$

$$a_e \left.\frac{\mathrm{D}T_e}{\mathrm{D}t}\right|_{\mathrm{rad}} = \mu_R(\epsilon_R - a_R T_e^4), \tag{281}$$

$$\vec{q}_R = -D_R \nabla \epsilon_R, \tag{282}$$

where $D_R = f_R^{lim} c/(3\rho\kappa_R)$ is the radiation diffusion coefficient and $\mu_R = c\rho\kappa_P$ is the relaxation coefficient. The difference is given by the coupling to another quantity. In principle, a similar linear coupling appears between the electron and ion temperatures, but the temperature relaxation is treated separately by the procedure outlined in chapter 8.1.2. In the case of radiation, the coupling can be very strong and compete with the transport within the radiative shock waves. Therefore, the coupling is implicitly included, following the methodology of [182]. The system (280–281) is rewritten as:

$$\frac{\mathrm{D}\epsilon_R}{\mathrm{D}t} = -\nabla \cdot \vec{q}_R + \mu_R(\theta_e - \epsilon_R), \tag{283}$$

$$\left.\frac{\mathrm{D}\theta_e}{\mathrm{D}t}\right|_{\mathrm{rad}} = \frac{1}{\tau_R}(\epsilon_R - \theta_e), \tag{284}$$

where $\theta_e = a_R T_e^4$ is the material source function and $\tau_R = a_e T_e^{-3}/(4 a_R \mu_R)$ is the relaxation time of θ_e. The material equation (284) can be implicitly solved either numerically or semi-analytically and inserted to the radiation equation (283). The implicit temperature is expressed as a mere linear combination $\theta_e = \beta_R \theta_e^n + (1-\beta_R)\epsilon_R$, reducing the system to a single equation:

$$\frac{\mathrm{D}\epsilon_R}{\mathrm{D}t} = -\nabla \cdot \vec{q}_R + \mu_R \beta_R(\theta_e^n - \epsilon_R). \tag{285}$$

The numerical approach is based on the backward Euler scheme for (281). It is straightforward to derive $\beta_R = 1/(1+\Delta t/\tau_R)$ in this case. Principally, the result is only correct for $\Delta t/\tau_R \ll 1$, but an advantage of the approach is the symmetry between the equations when the radiation equation (283) is discretized implicitly.

Another choice is the semi-analytic approach when ϵ_R is assumed fixed. Integration of the linear equation yields the result $\beta_R = \exp(1 - \Delta t/\tau_R)$. It is valid even for $\Delta t/\tau_R \gg 1$, but breaks the symmetry between the equations, because a numerical solution of (283) does not respect this limit.

In any case, time-stepping with a time step significantly longer than the relaxation time τ_R is not advisable, because propagation of the non-linear radiation waves can be affected [108]. Therefore, time sub-steps with length equal to a fraction of τ_R are performed. Note the non-linear transformation from chapter 9.1.1 is not possible here unless the model is reduced to the equilibrium diffusion.

9.2 Weak formulation

The diffusion equations for heat transport (277–278) or radiation diffusion (285), (282) present a classical mixed problem. Instead of reducing the system to the primary form for the temperatures/energies, it is intentionally left in the mixed form. The reason can be seen from the choices of the functional spaces, which follow the MHD code construction (chapter 8):

$$\mathcal{T} = L_2(\Omega), \tag{286}$$

$$\mathcal{G} = \{\vec{\zeta} \in H_{div}(\Omega) \mid \vec{\zeta}(\vec{x}) \cdot \vec{n} = \vec{q}_n \;\; \forall \vec{x} \in \Gamma_{\vec{q}_n}\}. \tag{287}$$

Note the definitions are applicable only in 2D and 3D, while $H^1(\Omega)$ space is used for $\mathcal{G}$ in 1D instead. The essential boundary condition for the normal flux on $\Gamma_{\vec{q}_n} \subset \partial\Omega$ is included. The discontinuous nature of the thermodynamic space would lead to the methods of discontinuous diffusion in the primary form, where treatment of the double discontinuities in the Laplace operator is a subject of research [183]. Instead, the mixed form is preferred here, which respects the de Rham complex (195) in 3D and (197) in 2D and yields a locally conserving scheme as becomes clear from the weak formulation.

The transformed system of heat diffusion (277–278) in the weak form becomes ($\forall \varphi \in \mathcal{T}', \vec{\zeta} \in \mathcal{G}'$):

$$\left(\bar{a}_{e/i}\frac{\mathrm{D}\bar{T}_{e/i}}{\mathrm{D}t}, \varphi\right)_{\mathcal{T}\mathcal{T}} + \left(\nabla \cdot \vec{q}_{e/i}, \varphi\right)_{\mathcal{G}\mathcal{T}} = 0, \tag{288}$$

$$-\left(\bar{T}_{e/i}, \nabla \cdot \vec{\zeta}\right)_{\mathcal{T}\mathcal{G}} + \left(\underline{\underline{\bar{\kappa}_{e/i}}}^{-1}\vec{q}_{ei/i}, \vec{\zeta}\right)_{\mathcal{G}\mathcal{G}} = -\left\langle \bar{T}^{\Gamma}_{e/i}\vec{\zeta} \cdot \vec{n}\right\rangle^{\Gamma_{T_{e/i}}}_{\mathcal{G}}. \tag{289}$$

The newly appearing boundary term corresponds to the natural boundary condition for the outer temperature $\bar{T}^{\Gamma}_{e/i}$ on $\Gamma_{T_{e/i}} \subset \partial\Omega$. Conveniently, the temperature equation (288) has conserving form and is consistent with Gauss's theorem. Indeed, choosing an arbitrary sub-domain $V \subset \Omega$ and inserting its characteristic function $\chi_V \in L_2(\Omega)$ as the test function ($\varphi \leftarrow \chi_V$) to (288) enables to use Gauss's theorem and state conservation of the energy on V, which is only exchanged by the obtained boundary fluxes.

The weak formulation of the radiation transport is mostly analogous and can be written as ($\forall \varphi \in \mathcal{T}', \vec{\zeta} \in \mathcal{G}'$):

$$\left(\frac{\mathrm{D}\epsilon_R}{\mathrm{D}t} + \mu_R\beta_R\epsilon_R, \varphi\right)_{\mathcal{T}\mathcal{T}} + (\nabla \cdot \vec{q}_R, \varphi)_{\mathcal{G}\mathcal{T}} = (\mu_R\beta_R\theta_e^n\varphi)_{\mathcal{T}}, \tag{290}$$

$$-\left(\epsilon_R, \nabla \cdot \vec{\zeta}\right)_{\mathcal{T}\mathcal{G}} + \left(D_R^{-1}\vec{q}_R, \vec{\zeta}\right)_{\mathcal{G}\mathcal{G}} = -\left\langle \frac{1}{k_R}\vec{q}_R \cdot \vec{n}, \vec{\zeta} \cdot \vec{n}\right\rangle^{\Gamma_{k_R}}_{\mathcal{G}\mathcal{G}} - \left\langle \epsilon^{\Gamma}_R\vec{\zeta} \cdot \vec{n}\right\rangle^{\Gamma_{\epsilon_R}}_{\mathcal{G}}. \tag{291}$$

The main distinction points are the additional relaxation terms in the energy equation (290) and the new natural boundary condition in the flux equation (291). The Newton boundary condition $\vec{q}_R \cdot \vec{n} = k_R(\epsilon_R - \epsilon^{\Gamma}_R)$ on $\Gamma_{\epsilon_R} \cap \Gamma_{k_R} \subset \partial\Omega$ enables to set the boundary radiation conduction factor $k_R \neq 0$. This general construction allows to impose the

very common Milne-like boundary condition $\vec{q}_R \cdot \vec{n} = 1/2c\epsilon_R$ on $\Gamma_{k_R} \subset \Omega, \Gamma_{k_R} \cap \Gamma_{\epsilon_R} = \emptyset$ for the value of the conductivity $k_R = 1/2c$, which can be understood as free streaming of radiation to an empty half-space [102].

9.3 Discrete model

The discretization procedure follows the general pattern of chapter 6. The finite elements are chosen from the H_{div}-conforming Raviart–Thomas spaces [148, 149] for the fluxes from $\mathcal{G}$ and the positive discontinuous L_2 finite elements for the temperatures/energies. This setting keeps compatibility with the MHD model from chapter 8, so no reinterpolations are needed for transition between the models.

After the discretization in space, the semi-discrete formulation of the mixed heat diffusion (277–278) has the form:

$$\mathbb{M}_{\bar{T}_{e/i}} \frac{\mathrm{D}\bar{\mathbf{T}}_{e/i}}{\mathrm{D}t} - \mathbb{G}_{\mathcal{T}}^T \mathbf{q}_{e/i} = \mathbf{0}, \tag{292}$$

$$\mathbb{G}_{\mathcal{T}} \bar{\mathbf{T}}_{e/i} + \mathbb{M}_{\vec{q}_{e/i}} \mathbf{q}_{e/i} = \mathbf{b}_{\bar{T}_{e/i}}. \tag{293}$$

The definitions of the matrices are not detailed here for brevity and the reader is navigated to [164]. Although the model applies the local approximation by the ideal gas and the non-linear transformation of temperature (see chapter 9.1.1), the energy equation (257) or (258) can be directly used after the sought heat flux $\mathbf{q}_{e/i}$ is obtained, as it is invariant of the transformation. The model maintains the local conservation property on the discrete level, which can be seen from multiplication of the temperature equation (292) by the grid function $\mathbf{1}_\chi$ equal to one on the support of a selected element and zero elsewhere. The product $\mathbf{1}_\chi^T \mathbb{G}_{\mathcal{T}}^T \mathbf{q}_{e/i}$ is equal to the integral of normal fluxes over the faces of the element due to the construction of the Raviart–Thomas finite elements [148, 149]. The global conservation of energy is then a mere consequence of the local one, since the elements are normally-continuous, so the inter-element fluxes cancel each other out exactly.

The spatial discretization of the radiation diffusion governed by the weak formulation (285), (282) is similar and reads:

$$\left(\mathbb{M}_{\epsilon_R} \frac{\mathrm{D}}{\mathrm{D}t} + \mathbb{M}_{\beta_R \mu_R} \right) \boldsymbol{\epsilon}_R - \mathbb{G}_{\mathcal{T}}^T \mathbf{q}_R = \mathbb{M}_{\beta_R \mu_R} \boldsymbol{\theta}_e^n, \tag{294}$$

$$\mathbb{G}_{\mathcal{T}} \boldsymbol{\epsilon}_R + \mathbb{M}_{\vec{q}_R} \mathbf{q}_R = \mathbf{b}_{\epsilon_R}. \tag{295}$$

Note the conductivity boundary contribution is absorbed in the definition of $\mathbb{M}_{\vec{q}_R}$. The local conservation properties are satisfied also in this case for the radiation energy, but the exchange of energy between material and radiation must be checked. In order to conserve energy, it must have the symmetric form:

$$\mathbb{M}_{\mathcal{T}} \frac{\mathrm{D}\mathbf{e}_e}{\mathrm{D}t} = \mathbb{M}_{\beta_R \mu_R} (\boldsymbol{\epsilon}_R - \boldsymbol{\theta}_e^n). \tag{296}$$

Apparently, the sum of the material equation (296) and the radiation equation (294)

cancels out in the exchange terms and the (local) conservation of the total energy $\mathbf{1}^T(\mathbb{M}_{\epsilon_R}\boldsymbol{\epsilon}_R + \mathbb{M}_{\mathcal{T}}\mathbf{e}_e)$ is attained.

The time discretization of the systems (292–293) and (294–295) is implicit. The fully implicit, L-stable backward Euler method can be used or the semi-implicit, A-stable Crank-Nicolson scheme can be applied. Alternatively, the singly diagonally implicit Runge–Kutta (SDIRK) methods can be employed, which do not require more than an implicit solution for a certain fractional time step.

Numerically, the heat and radiation systems are solved in the mixed forms or the dual form for the heat fluxes, i.e. the temperature/energy is expressed from the corresponding equation and substituted to the flux equation. The latter has the following form for the heat diffusion system (292–293):

$$\left(\mathbb{M}_{\vec{q}_{e/i}} + \alpha_h \Delta t \mathbb{G}_{\mathcal{T}} \mathbb{M}^{-1}_{\bar{T}_{e/i}} \mathbb{G}^T_{\mathcal{T}}\right) \mathbf{q}^{n+\alpha_h}_{e/i} = \mathbf{b}_{\bar{T}_{e/i}} - \mathbb{G}_{\mathcal{T}} \bar{\mathbf{T}}^n_{e/i}, \tag{297}$$

where the fractional time index is meant in the sense of linear interpolation and the parameter α_h allows to chose between the Crank-Nicolson scheme ($\alpha_h = 1/2$) and backward Euler scheme ($\alpha_h = 1$) similarly to chapter 8.3.2. Returning to the mixed system, it is indefinite and the generalized minimal residual method (GMRES) is employed. However, the discontinuous nature of the temperature/energy elements favours the dual form (297) (and the analogous for the radiation diffusion), where the mass matrix of the discontinuous elements has a block-diagonal structure and its inverse can be calculated on the element level. The dual form has a positively-definite matrix and can be solved by the preconditioned conjugate gradient (PCG) method. The preconditioner in this case is the Auxiliary-space Divergence Solver (ADS) [184], which converts the problem to an auxiliary H^1-conforming space to apply the algebraic multigrid method (AMG) [173, 174]. Still, the high-order elements are not efficiently treated, because many DOFs are inner and do not contribute to diffusion of the solution globally. Hence, the hybridization technique is implemented, which can be understood in simple terms as enforcing of the continuity between the flux elements weakly, through Lagrange multipliers. Only the constraint equation for the multipliers is then solved globally, where the flux equation is locally eliminated [185]. This approach greatly reduces the number of DOFs, but requires inversion of the local dense matrices. In this case, the AMG preconditioner can be applied directly to the system.

Lastly, a problem associated with the high-order elements for parabolic equations should be mentioned. The Laplace operator formed for the flux in (297) does not respect the minimal value theorem, i.e. local extrema can be created by its application [186]. The problem stems from the inverse of the temperature mass matrix, which involves anti-diffusive contributions for high-order elements. When lumped (i.e. sums of the rows/columns form a diagonal matrix), the Laplace operator $\sim \mathbb{G}_{\mathcal{T}}\mathbb{G}^T_{\mathcal{T}}$ would be obtained with only diffusive contributions, but the high-order order interpolation of the temperature elements would not be respected, degrading the convergence. A corrective (conservative) post-processing of the fluxes can be performed when the energy update is calculated through (257), (258) or (294), but stability of the implicit method can be hazarded already. Truly monotonous operators for the high-order positive elements are needed in this case [187], which remain a topic of the future development.

9.4 Example problems

The purpose of this chapter is to validate and benchmark the numerical methods of radiation and heat diffusion. Since the equations of radiation and heat diffusion presented in this chapter have nearly an identical structure, also the numerical implementation is shared among them. Therefore, the tests devised for one of the models can be reinterpreted for the other only by redefinition of the variables. The first test in chapter 9.4.1 measures convergence of the schemes on the problem of diffusion over a transition profile. The second problem presents the results for a non-equilibrium radiation wave in chapter 9.4.2.

9.4.1 Heat bath

The first test concerns heat diffusion over a transition profile. In essence, it strongly resembles the heat bath problem from chapter 7.3.2, but the transport is linear independently of the initial conditions as long as heat flux limiters are not used (see chapter 3.1.2). Another difference is given by the fact the initial profile is chosen as a step function, highlighting the benefits of the discontinuous temperature finite elements and the weak formulation avoiding differentiation of the temperature.

In particular, the initial profile is a step function in temperature centred around $x = 0.5$ with the left temperature $T_l = 13$ and the right $T_r = 3$. The analytic solution of the one-temperature heat diffusion is:

$$T(x,t) = \frac{T_r + T_l}{2} + \frac{T_r - T_l}{2}\mathrm{erf}\left(\frac{x - x_0}{\sqrt{4\kappa t/a}}\right), \tag{298}$$

$$q(x,t) = -(T_r - T_l)\sqrt{\frac{\kappa a}{4\pi t}}\exp\left(-\frac{(x-x_0)^2}{4\kappa t/a}\right). \tag{299}$$

Note the relative units are applied for all quantities. The heat conductivity is set to $\kappa = 0.1$ and the heat capacity $a = 10$, yielding the diffusivity $\eta_h = k/a = 10^{-2}$. The final time of the simulation is $t_{fin} = 0.4$ and it runs on the domain $(0, 1)$ in one dimension, as the construction of the schemes is completely analogous in all dimensions. However, the results were checked in multiple dimensions that they agree almost perfectly. The solution and the initial profile are depicted in Figure 14. It can be compared with similar Figure 8. The ideal symmetry of the linear diffusive heat flux is apparent.

An analysis of the spatial convergence can be found in Figure 15. Different orders of the finite elements are compared, where the semi-implicit scheme ($\alpha_h = 1/2$) is used in all cases. The time step is fixed at the relatively small value $\Delta t = 10^{-4}$ in order to not limit the convergence by the time integration error. The order of the convergence proportional to the polynomial order of the elements is confirmed, where it should be noted the heat flux elements have the order higher by one compared to the thermodynamic. The only deviation from the trend occurs for the heat fluxes, where the error saturates at about the value 10^{-8}, which can be attributed to the tolerance of the linear solver. Fortunately, the error does not propagate to the temperatures thanks to the symmetry of the problem.

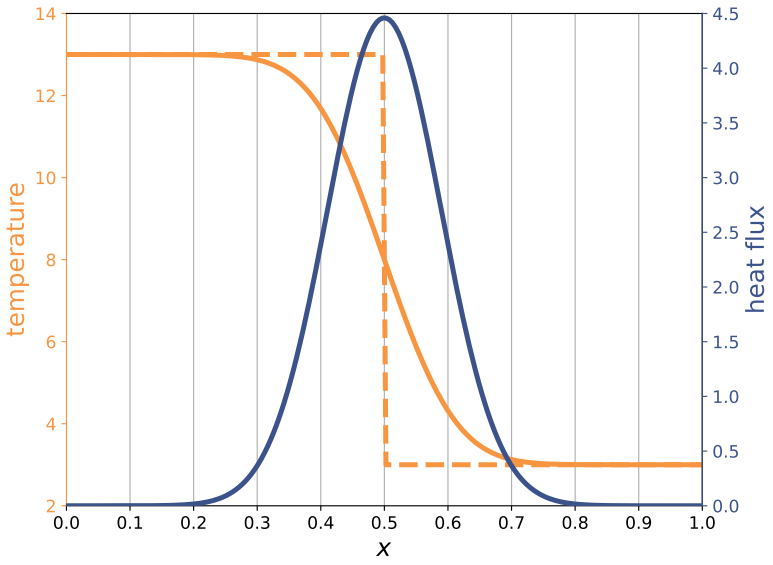

Figure 14: The analytic solution of the heat bath problem at the final time $t_{fin} = 0.4$: temperature (orange), heat flux (blue). The initial profile is designated by the dashed line. The values are in the relative units.

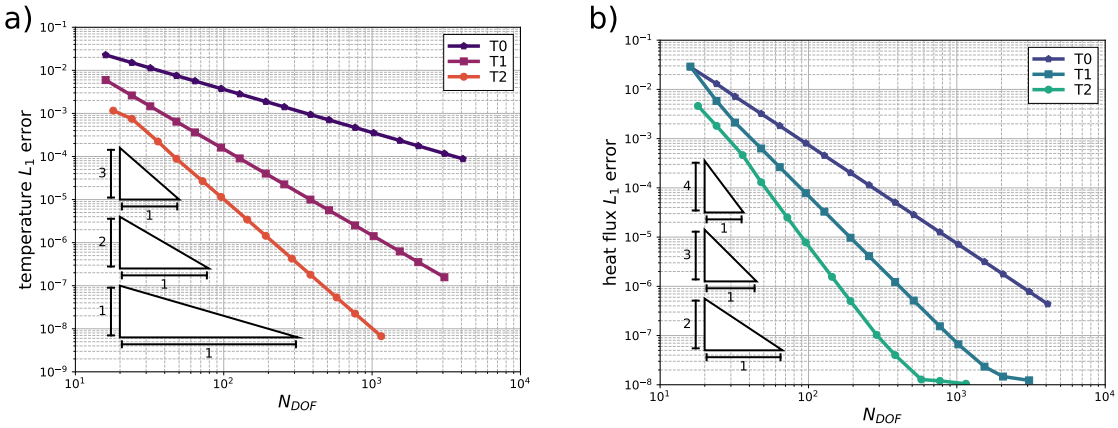

Figure 15: Spatial convergence of the heat diffusion in the heat bath problem: a) temperature, b) heat flux. The integral L_1 errors are plotted as functions of the number of degrees of freedom N_{DOF}. The legend denotes the polynomial orders of the thermodynamic elements.

The problem of heat conduction over a step function of temperature with an analytic solution was used for testing of the diffusion model. The discontinuity was resolved perfectly and the orders of convergence proportional to the polynomial orders of the elements were measured, showing benefits of the high-order finite elements.

9.4.2 Marshak wave

The second problem concentrates on a classical test for non-equilibrium radiation diffusion, which is known as the Su–Olson problem in the literature [188]. We concentrate on its original form for the grey-body diffusion, even though a solution was found even for more complicated cases later [189, 190]. The essence of the problem is a non-equilibrium radiative Marshak wave propagating to the domain from a radiating boundary condition. No hydrodynamic motion is considered and only the radiation diffusion and relaxation processes lead to heating of the material inside the domain.

The initial conditions are trivial in this case, setting the density to $\rho \equiv 1\,\mathrm{g/cm^3}$ radiation temperature T_R and material T_m to zero, where $\epsilon_R = a_R T_R^4$. The radiating boundary condition sets the outer radiation temperature to $T_R^\Gamma = 1\,\mathrm{keV}$ and the (single) opacity to $\kappa_P = \kappa_R = 1\,\mathrm{cm^2/g}$. The opposite boundary condition is then for zero outer radiation temperature. However, the cornerstone of the semi-analytic solution is a special form of the dependency of the heat capacity on temperature $a = 4a_R T_m^3$, which was proposed by Pomraning originally [191]. It can be noticed it cancels out with the temperature dependency of the relaxation coefficient τ_R, making it constant, which greatly simplifies the problem.

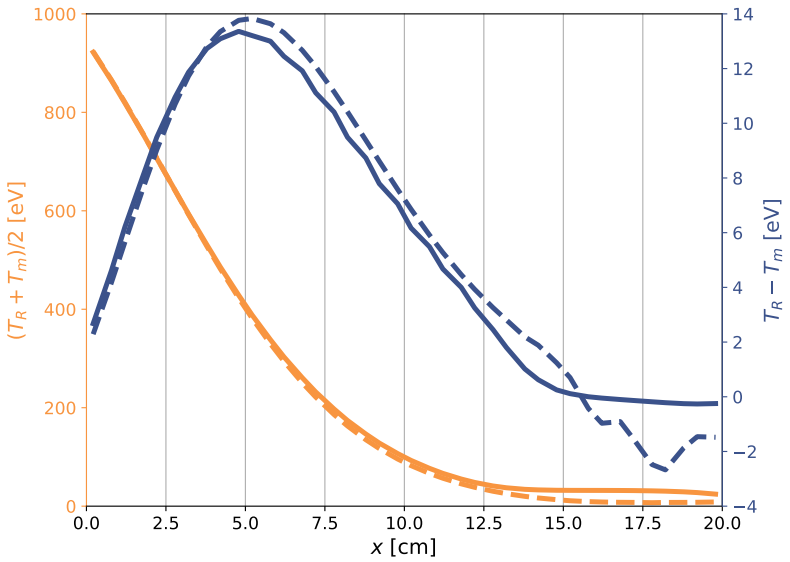

Figure 16: The numerical (solid) and semi-analytic (dashed) solution of the non-equilibrium Marshak wave problem: average of the radiation and material temperatures (left) and their difference (right).

The numerical simulation is performed on the domain $(0, 20\,\mathrm{cm})$ from the time

$t_0 = 0.1\,\mathrm{ns}$ to the final time $t_{fin} = 0.6\,\mathrm{ns}$. The computational mesh consists of 20 quadratic/cubic finite elements of $T2$ type in 1D. The time integration is implicit (backward Euler) with the semi-analytic approximation of the relaxation. The time step is kept as small as $\Delta t = 10\,\mathrm{ps}$, but it must be considered the relaxation time is only $\tau_R \doteq 33.4\,\mathrm{ps}$. Therefore, the time step is still smaller, but numerical errors originating from the integration of the radiation relaxation can be expected. The results are presented in Figure 16. The numerical solution shows a very good performance on the left, near the radiating boundary condition, and only slightly underestimates the relaxation in the central area. Though, a more noticeable deviation can be seen on the right side, but it can be attributed to the semi-analytic initial condition already. As can be observed on the difference curve, the semi-analytic solution based on ExactPack [192] exhibits an oscillative behaviour for more distant areas from the radiation source. In the case of the initial condition, the semi-analytic profiles are non-monotonous and the temperatures are not lower than $\approx 30\,\mathrm{eV}$. Therefore, the numerical results seem to be adequate and smoother than the reference solution in fact.

In summary, the capabilities of the non-equilibrium radiation diffusion code were demonstrated on the problem of a radiative Marshak wave. The strong coupling between the radiation and material tested the implicit radiation energy relaxation and diffusion. Relatively accurate results were obtained even with a low number of the finite elements, pointing to the rapid convergence of the method and its robustness.

10 Non-local models

There exists various models of non-local energy transport, where the most popular approaches were reviewed in chapters 3 and 4 for the electron heat transport and radiation transfer respectively. The methods greatly vary in their formulations and so do their numerical implementations, but the fundamental difference from the diffusive methods of chapter 9 is given by the fact that the transport is not governed by a parabolic equation, but contain also a hyperbolic contribution. This distinction point then must be reflected also on the side of the numerical methods applied. The major influence in the field of non-local electron heat transport comes from the well-established methods of radiation transfer. This resemblance is highlighted in the following chapter, but important differences between them must be recognized as well. Photons are charge-free quanta, which do not experience the Lorentz force. In contrast, numerical treatment of the electric and magnetic fields must be then an inherent part of the methods of the electron transport. Though, we have mainly concentrated on the BGK model of transport (chapter 3.3), which considers the electric effect only through an explicit correction, where a full parallel to the discrete ordinates method for radiation transfer (chapter 4.3) can be made. The methods of angular moments (chapters 3.2 and 4.2) with self-consistent electric (and magnetic) fields are then topics of the future research.

10.1 Governing equations

As mentioned in the introduction, an analogy between the methods of radiation transfer and the BGK model from chapter 3.3 can be found. In particular, the equations of transfer (135) and (144) for the electron heat intensity I_e and total radiation intensity I_R can be unified into a single system together with the electron energy equation (229). The resulting governing equations take the form:

$$\frac{1}{c_{e/R}}\frac{\mathrm{D}I_{e/R}}{\mathrm{D}t} + \vec{\Omega}\cdot\nabla I_{e/R} = \frac{1}{\bar{\lambda}_{e/R}}\left(S_{e/R} - I_{e/R}\right), \tag{300}$$

$$\rho c_{Ve}\left.\frac{\mathrm{D}T_e}{\mathrm{D}t}\right|_{\mathrm{heat/rad}} + \int_{4\pi}\left(\frac{1}{c_{e/R}}\frac{\mathrm{D}I_{e/R}}{\mathrm{D}t} + \vec{\Omega}\cdot\nabla I_{e/R}\right)\mathrm{d}\vec{\Omega} = 0, \tag{301}$$

where the velocities are $c_e = +\infty$ and $c_R = c$, the mean free paths $\bar{\lambda}_e = \alpha\lambda_{SH}$ and $\bar{\lambda}_R = 1/(\rho\kappa_P)$, and the source functions $S_e = \sqrt{2}n_e v_{Te}^3/\pi^{3/2}$ and $S_R = \sigma_{SB}/\pi T_e^4$. It can be noticed the velocity of the electrons is higher than that of radiation paradoxically. The reason can be seen from the construction of the BGK model in chapter 3.3, where the averaging procedure for the inverse electron velocity yields a dependency on a different velocity moment, which cannot be easily modelled, in contrast to the radiation with an approximately constant velocity. The inertial term for the radiation could be neglected similarly to the electron under the same assumptions, but its integration does not pose any problem and rather stabilizes the simulation, as explained later. Also note that transition to the fluid-frame is made without transformation of the transfer equations, because the velocities of the species are significantly higher than the velocity of the fluid ($c_e, c_R \gg |\vec{u}|$). Though, the contributions to the energy equation involve

only the non-convective terms, as it was the case with the diffusion models in chapter 9. It should be also noted the scattering terms are omitted for simplicity, even though the uniform isotropization according to the equation (144) or the Laplace–Beltrami operator $\sim \partial^2 I_{e/R}/\partial\vec{\Omega}^2$ are implemented, but the electron model in the presented form does not consider them and scattering effects for the radiation are of a lesser importance in laser plasma typically [100, 106]. Finally, it should be recognized the temperature dependencies are considerably different, where the source function depends on $\sim T_e^{3/2}$ for electrons and $\sim T_e^4$ for radiation and similarly the mean free paths differ. This fact has a significant effect on the global profiles and dynamics during the laser–target interaction [95].

In any case, the procedure of the source function linearisation is performed. As already mentioned in chapter 4.3, the method consists in expansion of the source functions to the Taylor series $S_{e/R} = S^A_{e/R} T_e + S^b_{e/R}$ [113]. Both terms are still strongly temperature dependent due to the non-linearity of the system, but it can be solved implicitly in temperatures already. It implies the incoming flux is balanced with the outgoing and the expensive iterations in the source function are avoided or reduced from the numerical point of view.

For brevity, we limit the discussion to the 1D Cartesian geometry and the construction of the numerical scheme in multiple dimensions and coordinate systems is not reviewed here, but all details can be found in [94]. For convenience, the single spatial coordinate z, polar angle $\phi \in [0, \pi)$ and azimuthal angle $\theta \in [0, 2\pi)$ (not to be confused with θ_e in chapter 9.1.2) are used instead of the spatial vector $\vec{x}$ and the direction vector $\vec{\Omega}$. In this 1D cylindrical geometry, the system (301–300) can be rewritten as:

$$\frac{1}{c_{e/R}} \frac{\mathrm{D}I_{e/R}}{\mathrm{D}t} + \cos\phi \partial_z I_{e/R} = \frac{1}{\bar{\lambda}_{e/R}} \left(S^A_{e/R} T_e + S^b_{e/R} - I_{e/R} \right), \tag{302}$$

$$\rho c_{Ve} \frac{\mathrm{D}T_e}{\mathrm{D}t} + \int_{2\pi} \int_{\pi} \left(\frac{1}{c_{e/R}} \frac{\mathrm{D}I_{e/R}}{\mathrm{D}t} + \cos\phi \partial_z I_{e/R} \right) \sin\phi \, \mathrm{d}\phi \, \mathrm{d}\theta = 0. \tag{303}$$

Note the equations are independent of the azimuthal angle θ, which could be removed from the integration, but the terms are retained for a formal correspondence with other geometries.

10.2 Weak formulation

The weak formulation of the non-local transport system (300–301) relies on discontinuous functions in space. This choice matches the numerical magnetohydrodynamics described in chapter 8.2 and is suitable for hyperbolic systems, where discontinuities may appear in the solution and dissipative processes are not desired. The angular space is approximated by the discontinuous functions, which are suitable for strongly anisotropic transport, but may lead to considerable ray effects [116, 117]. Also only the uniform isotropization is implemented, as the angular diffusion is not straightforward to employ. On the other hand, a space of continuous functions offers a direct way

towards implementation of the Laplace–Beltrami operator (in addition to the uniform isotropization), but an artificial diffusion in angles can be expected [118]. Hence, it better suits more diffusive conditions.

In order to proceed according to the finite element method apparatus from chapter 6, the problem is considered on the multi-dimensional domain $\Omega_I = \Omega \times \Omega_{\vec{\Omega}} = \Omega \times \Omega_\phi \times \Omega_\theta$, where the latter is the decomposition for the cylindrical geometry. The spatial and angular spaces then read:

$$\mathcal{T} = \mathcal{I}_z = L_2(\Omega), \tag{304}$$
$$\mathcal{I}_\phi = L_2(\Omega_\phi) \qquad \text{or} \qquad H^1(\Omega_\phi), \tag{305}$$
$$\mathcal{I}_\theta = L_2(\Omega_\theta) \qquad \text{or} \qquad H^1(\Omega_\theta), \tag{306}$$

where the temperatures are taken from the thermodynamic space ($T_e \in \mathcal{T}$) and the intensities are taken from the combination of the spatial, polar and azimuthal spaces ($I_{e/R} \in \mathcal{I} = \mathcal{I}_z \times \mathcal{I}_\phi \times \mathcal{I}_\theta$). As mentioned in chapter 10.1, the 1D formulation is independent of the azimuthal angle, so only the space of constant functions $\mathrm{span}(1) \subset L_2(\Omega_\theta)$ is considered there.

Afterwards, the variational formulation of the non-local transport system in the cylindrical coordinates can be obtained in the following form ($\forall \varphi \in \mathcal{T}', \omega_z \in \mathcal{I}_z', \omega_\phi \in \mathcal{I}_\phi', \omega_\theta \in \mathcal{I}_\theta'$):

$$\left(\frac{1}{c_{e/R}}\frac{\mathrm{D}I_{e/R}}{\mathrm{D}t} + \cos\phi\partial_z I_{e/R} + \bar{\lambda}_{e/R}^{-1} I_{e/R}, \omega_z\omega_\phi\omega_\theta\right)_{\mathcal{I}\mathcal{I}} + \left\langle (\vec{\Omega}\cdot\vec{n})\mathrm{T}_{\mathcal{I}_z}^{\vec{\Omega}\cdot\vec{n}} I_{e/R}, \mathrm{T}_{\mathcal{I}_z}\omega_z\omega_\phi\omega_\theta\right\rangle_{\mathcal{I}\mathcal{I}} +$$
$$+ \left\langle (\vec{\Omega}\cdot\vec{n})\mathrm{T}_{\mathcal{I}_z} I_{e/R}, \mathrm{T}_{\mathcal{I}_z}\omega_z\omega_\phi\omega_\theta\right\rangle_{\mathcal{I}\mathcal{I}}^{-} = 4\pi\left(\bar{\lambda}_{e/R}^{-1} S_{e/R}^A T_e, \omega_z\right)_{\mathcal{T}\mathcal{I}_z} + 4\pi\left(\bar{\lambda}_{e/R}^{-1} S_{e/R}^b \omega_z\right)_{\mathcal{I}_z} +$$
$$+ \left\langle (\vec{q}_{e/R}^{\,\Gamma}\cdot\vec{n})\mathrm{T}_{\mathcal{I}_z}\omega_z\right\rangle_{\mathcal{I}_z}^{\Gamma_{\vec{q}}^+}, \tag{307}$$

$$\left(\rho c_{Ve}\frac{\mathrm{D}T_e}{\mathrm{D}t}, \varphi\right)_{\mathcal{T}\mathcal{T}} + \left(\frac{1}{c_{e/R}}\frac{\mathrm{D}I_{e/R}}{\mathrm{D}t} + \cos\phi\partial_z I_{e/R}, \varphi\right)_{\mathcal{I}\mathcal{I}} = 0. \tag{308}$$

Note the identity of the thermodynamic and spatial intensity spaces is utilized and contraction by constant functions is made in (308). The transformation of the sphere differential $\mathrm{d}\vec{\Omega} = \sin(\phi)\,\mathrm{d}\phi\,\mathrm{d}\theta$ is included in the definitions of the forms. Finally, a meaning must be given the plus and minus signs in the superscript. They symbolize the outflow ($-$) and inflow ($+$) parts of the boundary, i.e. the parts with $\vec{\Omega}\cdot\vec{n} \geq 0$ or $\vec{\Omega}\cdot\vec{n} < 0$ respectively. The boundary inflow is then determined by the boundary flux $\vec{q}_{e/R}^{\,\Gamma}$ defined on $\Gamma_{\vec{q}} \subset \partial\Omega$, where only the part $\Gamma_{\vec{q}}^+ \subset \Gamma_{\vec{q}}$ is considered with the flow opposing the outer normal. The identical upwinding is applied anywhere discontinuities appear inside the domain. The surface integrals of the sub-domains are evaluated, where $\mathrm{T}_{\mathcal{I}_z}$ represents the trace of the space $\mathcal{I}_z$ on the integrated sub-domain and $\mathrm{T}_{\mathcal{I}_z}^{\vec{\Omega}\cdot\vec{n}}$ the trace from the upstream sub-domain. The idea behind the procedure is to naturally follow the characteristics of the hyperbolic system along $\vec{\Omega}$ and stabilize the method.

Furthermore, it should be mentioned the boundary conditions are not limited

to the influx only, but there exits also the reflective boundary condition, which is not detailed for its formal complexity. Though, it is important for thermodynamic isolation of the system, similarly to the heat diffusion in chapter 9.

It is also worth a note the divergence term is formulated in the strong way, which does not guarantee conservation of energy for the discrete scheme. The weak form would solve this problem and remains a topic of the future development. This point is also related to the simplification given by absence of the normal jumps at the discontinuities in (308), which is justified by convergence of the intensity to a continuous solution, as only volumetric losses are involved.

10.3 Discrete model

The discretization of the non-local transport employs discontinuous elements in space, while classical nodal continuous or discontinuous elements are used in angles, following the choices in chapter 10.2. The design with discontinuous elements has another advantage of an increased sparsity of the resulting discrete system. Also the assembly process is greatly simplified, when the matrices are constructed from separate blocks corresponding to the spatial, polar and azimuthal coordinates. In this connection, it must be noted only the spatial matrices must be recomputed every time step, but the angular tessellation is not changing in time and the element matrices are constant.

The time integration is fully implicit to treat correctly the coupling through the temperature. The first order backward Euler scheme is employed, where a higher order time stepping could be devised with the SDIRK methods similarly to chapter 9, but non-linearity of the system must be considered. All coefficients in the equations are temperature-dependent and must be updated, so an improved convergence only of the linearised system would not yield the desired overall results.

The discretized system (307–308) takes the form:

$$\underbrace{\mathbb{M}_\theta \otimes \left(\mathbb{M}_\phi \otimes \left(\frac{1}{c_{e/R}\Delta t}\mathbb{M}_z + \mathbb{M}_{\lambda_{e/R}} \right) + \mathbb{M}_{\cos\phi} \otimes \mathbb{D}_z \right)}_{\mathbb{A}_{I_{e/R}}} \mathbf{I}^{n+1} =$$

$$= \underbrace{\mathbb{M}_{\theta 0} \otimes \mathbb{M}_{\phi 0} \otimes \mathbb{M}_{S^A_{e/R}}}_{\mathbb{A}_{I_{e/R}T_e}} \mathbf{T}_e^{n+1} + \underbrace{\mathbb{M}_{\theta 0} \otimes \mathbb{M}_{\phi 0} \otimes \mathbf{b}_{S^b_{e/R}} + \mathbf{b}_{\vec{q}_{e/R}} + \frac{1}{c_{e/R}\Delta t}\mathbb{M}_\theta \otimes \mathbb{M}_\phi \otimes \mathbb{M}_z \mathbf{I}^n}_{\mathbf{b}_{I_{e/R}}}, \tag{309}$$

$$\frac{1}{\Delta t}\mathbb{M}_{T_e}\mathbf{T}_e^{n+1} + \underbrace{\mathbb{M}_{\theta 0}\otimes\left(\mathbb{M}_{\phi 0}\otimes\frac{1}{c_{e/R}\Delta t}\mathbb{M}_z^{T_eI} + \mathbb{M}_{\cos\phi 0}\otimes\mathbb{D}_z^{T_eI}\right)}_{\mathbb{A}_{T_eI_{e/R}}}\mathbf{I}^{n+1} = \\ = \frac{1}{\Delta t}\mathbb{M}_{T_e}\mathbf{T}_e^{n} + \underbrace{\frac{1}{c_{e/R}\Delta t}\mathbb{M}_\theta\otimes\mathbb{M}_\phi\otimes\mathbb{M}_z^{T_eI}\mathbf{I}^n}_{\mathbf{b}_{T_eI_{e/R}}}. \quad (310)$$

The zeros in the subscripts designate the contracted matrices. The matrices and vectors correspond to chapter 10.2, but more details with exact definitions of the terms can be found in [94]. Note the spatial matrices in the temperature equation (310) are distinguished from those in the intensity equation (309). This points to the fact the discrete spaces can be different. Typically, the intensity spatial polynomial order is chosen higher by one than the temperature, which correlates with the divergence gradient terms.

The implicit system (309–310) is not solved in the mixed form, but reduced to the temperature or intensity equation. To see this, the system is rewritten as:

$$\mathbb{A}_{I_{e/R}}\mathbf{I}^{n+1} - \mathbb{A}_{I_{e/R}T_e}\mathbf{T}_e^{n+1} = \mathbf{b}_{I_{e/R}}, \quad (311)$$

$$\mathbb{A}_{T_eI_{e/R}}\mathbf{I}^{n+1} + \frac{1}{\Delta t}\mathbb{M}_{T_e}\mathbf{T}_e^{n+1} = \frac{1}{\Delta t}\mathbb{M}_{T_e}\mathbf{T}_e^{n} + \mathbf{b}_{T_eI_{e/R}}. \quad (312)$$

The elimination of the intensity leads to a banded system for the temperature, which was originally solved by an iterative sweeping of the domain with in-time construction of the element matrices [82, 113]. However, this approach is not transferable to multiple dimensions, where an optimal explicit ordering of the elements is not known. Therefore, an alternative approach is devised, where a global system of intensity is formed with the upwinding procedure determining the sparsity pattern. Eventually, the hybridization technique is applied for high-order elements to decrease the size of the linear system, similarly to chapter 9.3. The system can be then efficiently solved by the block incomplete LU preconditioner and generalized minimal residual method or a direct solver. Thus, the second method better suits the anisotropic and non-local regime of the transport, while a tight coupling with the material temperature and rather local, isotropic transport favours the original method.

Another related problem is the possible poor regularity of $\mathbb{A}_{I_{e/R}}$. Especially for the electrons, the inertial term is absent (or weak in the case of radiation) and the absorption part might be in the non-local regime relatively weak as well. A slight regularization of the system by an additional diagonal matrix scaled by a factor proportional to the Frobenius norm is applied and iterated until convergence in the intensities is reached. Note the procedure is completely local and executed on the element level due to discontinuity of the intensity elements.

10.4 Example problems

This chapter presents numerical tests and examples of the non-local transport. Due to the identical construction of the scheme for radiation and electron heat, both can be validated by a single test. In particular, it is the steady cosines test in chapter 10.4.1, which serves for this purpose and offers measurement of the convergence too. The hotspot problem covered in chapter 10.4.2 is more realistic and compares the results with reference models of the transport.

10.4.1 Steady cosines

The first problem validates and analyses convergence of the numerical methods of non-local transport to a stationary solution. In order to simplify the conditions, the test is considered in 1D with a constant absorptivity k_λ and a prescribed source function $S = S(z)$. The transport equation (302) reduces to an ordinary differential equation of the form:

$$\mu \partial_z I(z, \mu) = k_\lambda (S(z) - I(z, \mu)), \tag{313}$$

where the single intensity $I = I(z, \mu)$ and the polar cosine $\mu = \cos \phi$ appear. It can be noticed the system is dependent only on the single parameter of the effective inverse mean free path $k_\mu = k_\lambda / \mu$. The source function is chosen as $S(z) = \sin(\pi z)$ and the boundary condition for zero influx is applied at z_0. The opposite boundary condition is free, i.e. setting zero normal jump of the intensity. Under these conditions, the transport equation (313) has an analytic solution, which reads [94]:

$$I(z, \mu) = \exp(-k_\mu (z - z_0)) \frac{k_\mu \pi \cos(\pi z_0) - k_\mu^2 \sin(\pi z_0)}{\pi^2 + k_\mu^2} - \frac{k_\mu \pi \cos(\pi z) - k_\mu^2 \sin(\pi z)}{\pi^2 + k_\mu^2}. \tag{314}$$

The solution for different polar angles is depicted in Figure 314. The domain spans from 0 to 1 and the left boundary has the zero inflow condition ($z_0 = 0$). The absorptivity is set to $k_\lambda = 4$ in the relative units. The intensity originating from the source is gradually attenuated with the travelled distance, but the intensity closer to the axis penetrates further due to the contribution of the relatively stronger cosine terms, which represent the advection in the solution.

The convergence analysis is performed in Figure 18 for different polynomial orders of the spatial elements. The polar angle is specifically chosen as $\phi = \pi/4$, which matches the central DOF of the polar second-order element when two segments are used. This segmentation is minimal to safely separate the forward and backward propagating intensity, but the specific combination of the angle with the polar element implies no interpolation is needed, resembling the discrete ordinate method, and the convergence is independent of the angular resolution. For different angles, the angular resolution would have to be increased proportionally to the spatial to decrease the overall error. The results show the order of convergence is proportional to the spatial order of the elements. Though, the combination of the linear thermodynamic elements with the quadratic intensity elements exhibits only the first order convergence after a steeper start. This phenomenon can be explained by the fact that the asymmetric

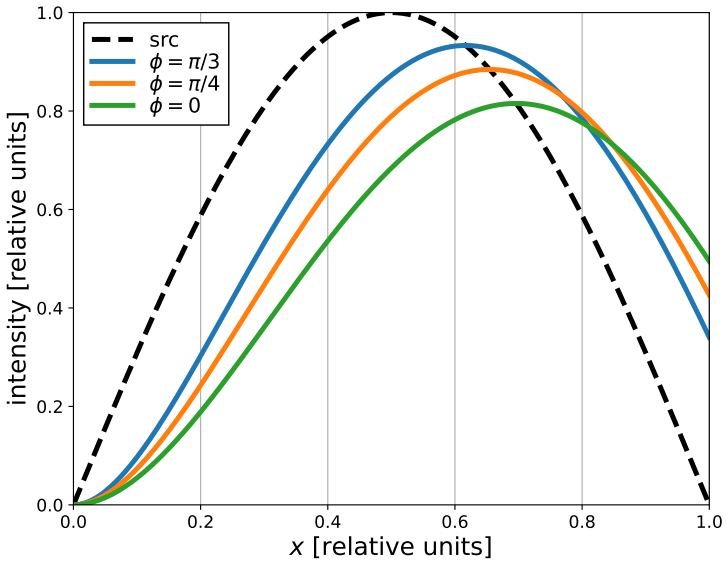

Figure 17: Solution of the steady cosines problem. The dashed curve corresponds to the source function and the full lines show the solution for different polar angles denoted in the legend.

shape functions mediate the advection to the neighbouring elements rather than the symmetric, so the convergence improves only with the odd orders of the intensity elements. Ultimately, this behaviour is confirmed even by the fourth order elements.

The steady cosines test was designed to verify the stationary non-local transport. The comparison with the analytic solution confirmed convergence rates proportional to the polynomial orders of the intensity elements. Though, an irregularity of this relation was recognized, where the convergence was improving only with the odd orders.

10.4.2 Hotspot relaxation

The second test concentrates on a more realistic problem, which can be relevant to the ICF or other areas of research. It is known as the hotspot relaxation problem and consists in dissipation of a compact initial profile of temperature by means of (non-local) heat transport to the surrounding cold medium [160]. In fact, it closely resembles the heat bath problem from chapters 7.3.2 and 9.4.1, but the upstream reservoir is considered finite in this case and the evolution is tracked until (partial) depletion of the source. The highly non-homogeneous conditions and substantial variations in the temperature lead to combination of different regimes of the non-local transport. Consequently, no analytic solution is known for the problem, but multiple models of transport can be compared instead.

The hotspot is modelled as a Gaussian profile with the peak temperature 5 keV and the base 1 keV with the initial Gaussian half-width $8.44\bar{\lambda}^0_{ei}$. All values are then normalized to this mean free path, which is calculated for fully ionized hydrogen with the initial density $n_e = 1.5 \cdot 10^{21}\,\mathrm{cm}^{-3}$ and the base temperature to be $\bar{\lambda}^0_{ei} = 15\,\mu\mathrm{m}$. Simi-

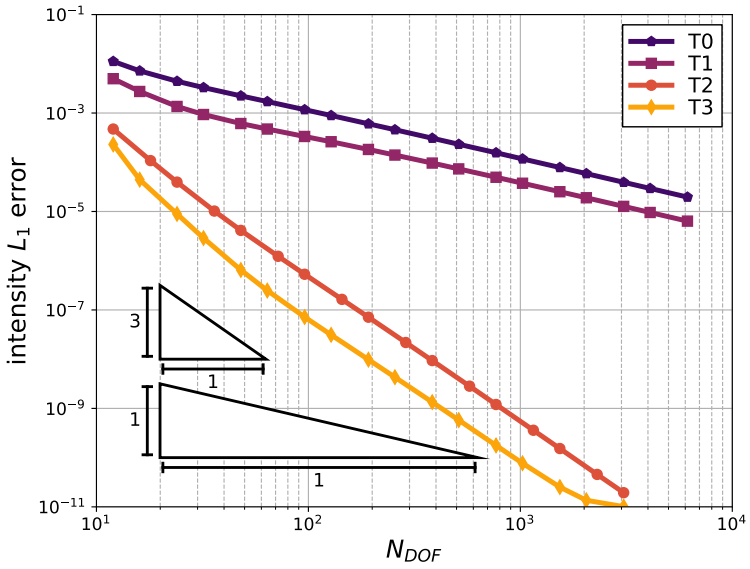

Figure 18: Convergence of the intensity under the polar angle $\phi = \pi/4$. The integral L_1 error of the intensity is plotted as a function of the number of thermodynamic degrees of freedom. The legend designates the thermodynamic polynomial orders of the elements.

larly, the time scale is normalized to the collision time $\tau_{ei}^0 = 1.11\,\mathrm{ps}$. The simulations are performed on the domain $(-80\bar{\lambda}_{ei}^0, +80\bar{\lambda}_{ei}^0)$ till the final time $t_{fin} = 30\tau_{ei}^0$.

The results for the hotspot problem are summarized in Figure 19. The heat diffusion with and without a flux limiter is compared with the BGK non-local transport and kinetic simulations from [160]. At the earliest time, the transport is in the non-local regime to a large extend and the unlimited diffusion clearly overestimates the fluxes and the relaxation in turn. By coincidence, the absolute values of the heat fluxes are similar for the unlimited diffusion and the kinetic simulations, but they must be related to the temperatures, which are substantially higher for the kinetic model. In contrast, the non-local closure model shows excessive flux inhibition in this regime, as already revealed in chapter 3.3. Still, the flux-limited diffusion inhibits the heat flux even stronger. It becomes more clear for the later times, where the non-physical limitation of the heat flux leads to the effect of "heat flux starvation". The artefacts appear in the solution near the edges of the hotspot, presenting bottlenecks for the transport, and the central area cannot relax due to the locality of the diffusion model. Oppositely, the unlimited diffusion continues to excessively dissipate the hotspot, but the process naturally slows down for the later times. The heat transport gets under milder conditions and the BGK model starts to show a very good agreement with the kinetic model.

In conclusion, the hotspot problem showed behaviour of the non-local model under realistic conditions, which was relatively close to the reference kinetic simulations for the mildly non-local regime. The comparison with the diffusion model stressed importance of the non-local models for the laser plasma modelling.

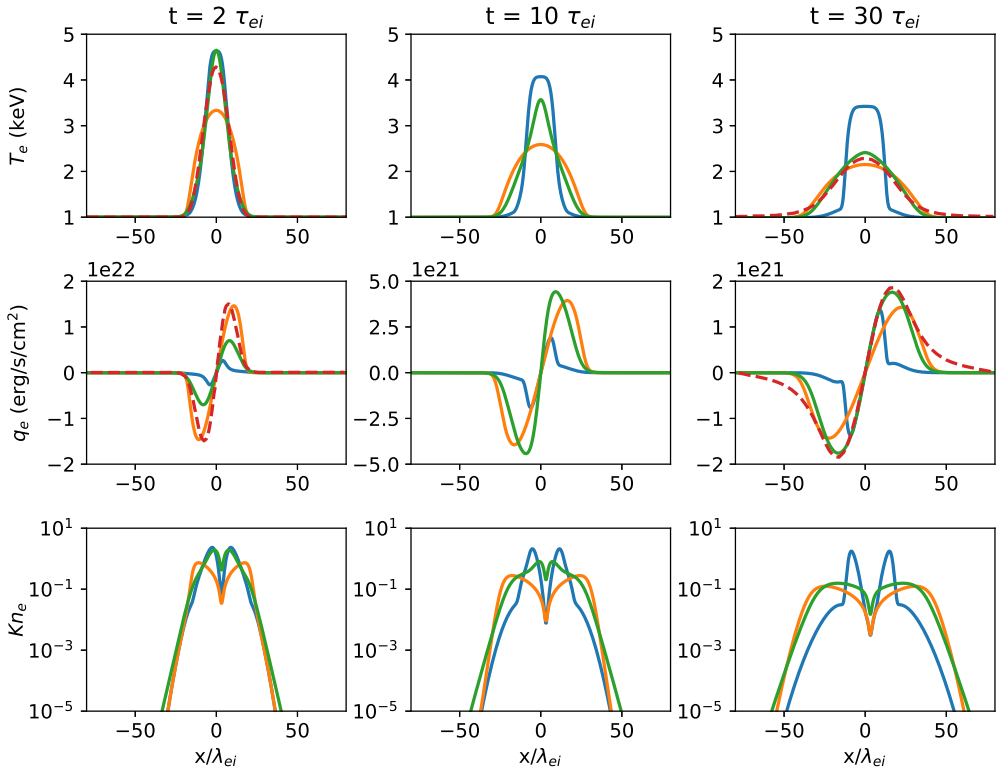

Figure 19: The spatial profiles for the hotspot relaxation problem at different times (columns): the electron temperature (top row), heat flux (middle row), and Knudsen number (bottom row). The models of heat transport are compared: flux-limited diffusion (blue), unlimited diffusion (orange), non-local BGK model (green), reference kinetic simulation (dashed red). The spatial coordinates and time are normalized to the initial mean free path and collision time respectively. Adopted from [20] with modifications.

11 Laser absorption models

The models of laser absorption are absolutely essential for modelling of laser plasma, as the laser presents the main source of energy in the simulations. Moreover, the vicinity of the critical plane is also the place of origin for most of the non-local electrons due to the steep profile of temperature located in this zone typically [95]. Therefore, an increased physical realism and numerical precision of the methods for laser absorption is needed. For this purpose, the code PETE2 implements multiple physical models reviewed in chapter 5.

First, it is the WKB model, which benefits from the high-order finite element treatment, but no refraction of the rays is considered nor reflection from the critical plane. The simplicity of the physical model allows its implementation in multiple dimensions straightforwardly, despite that the model remains only single-dimensional from the physical point of view, i.e. the propagation follows a single predetermined direction.

The second model is based on the stationary Maxwell's equations (SME), as described in chapter 5.2. It offers a full self-consistency in the vicinity of the critical plane, but it is also single-directional and cannot be extended to multiple dimensions directly. An effort has been done to apply the model on parallel rows/columns of a regular multi-dimensional mesh, but remapping from the Lagrangian mesh was necessary [82]. This approach is ruled out with the curvilinear finite elements due to the geometrical complexity of the possible intersection. Therefore, the model remains limited to the single dimension.

Finally, a ray-tracing code has been developed by M. Šach [128], which was interconnected with the code PETE2. At its core, it follows the general description of such methods presented in chapter 5.1, but ray equation is solved only in the approximation of a piecewise-constant medium. The rays then propagate along straight lines and refraction occurs only at the element edges. The connection to the high-order curvilinear meshes is enabled by the transfer to a low-order refined mesh and back again. Furthermore, the ray-tracing is enhanced by additional laser absorption mechanism, as described in chapter 11.3.

In conclusion, there is no model clearly surpassing the other and different models better suit different conditions. (Ultra-)short pulses can be modelled realistically by the SME model in 1D. The absorption on a large focal spot with dominance of the inverse Bremsstrahlung can be efficiently simulated by the WKB approach in 2D or 3D, while the cases with more pronounced geometrical effects in 2D and eventually contribution from the resonant absorption or reflection on the critical plane better suit the ray-tracing method.

11.1 WKB model

The Wentzel–Kramers–Brillouin (WKB) model presents one of the simplest physical descriptions for propagation and absorption of the laser. Following the optical approximation reviewed in chapter 5.1, the magnitude of the wave envelope is separated from the direction of propagation. The refraction of the rays is not modelled anyhow in this

case and they propagate along straight lines. The power of the laser is the attenuated according to the Beer–Lambert law (179). Together with its contribution to the energy equation (229), the governing equations read:

$$\vec{\Omega}_L \cdot \nabla I_L = -\alpha_L I_L, \tag{315}$$

$$\rho \left.\frac{\mathrm{D}\varepsilon_e}{\mathrm{D}t}\right|_{\text{laser}} + \vec{\Omega}_L \cdot \nabla I_L = 0. \tag{316}$$

In essence, the equations strongly resemble the non-local transport of chapter 10.1, but the single, predetermined direction of propagation $\vec{\Omega}_L$ appears in the system. Another distinction point is absence of the sources in the domain and only a Dirichlet boundary condition for I_L. Moreover, the propagation of the laser is limited to the under-dense region of the plasma. This phenomenon can be introduced to the model by promotion of the propagation coefficient to a function ($\vec{\Omega}_L = \vec{\Omega}_L(\vec{x})$). It is defined as follows:

$$\vec{\Omega}_L(\vec{x}) = \begin{cases} \vec{d}_L & n_e(\vec{x}) < n_c, \\ \vec{0} & n_e(\vec{x}) \geq n_c, \end{cases} \tag{317}$$

where $\vec{d}_L$ is the (unit) direction vector of the laser. The unitary value in the under-dense part of the domain allows free propagation and the zero value in the over-dense forces the intensity to zero there effectively. This means no reflection of the intensity is modelled and the full power is absorbed there. From the physical point of view, anomalous processes are assumed to operate there and lead to absorption on the distances of a few mean free paths from the critical plane [43]. Though, a fraction of the intensity should be reflected back, which cannot be simulated by the means of the simplified model. However, the input intensity of the laser can be downscaled to match the absorbed power thanks to the linearity of the model.

11.1.1 Weak formulation

The finite element method is applied also to the WKB model governed by the equations (315–316). Similarly to the non-local transport in chapter 10.2, discontinuous functions are used for the intensity. The thermodynamic and intensity spaces then coincide in the definition $\mathcal{T} = \mathcal{I}_L = L_2(\Omega)$. The variational formulation of the laser absorption then reads ($\forall \varphi \in \mathcal{T}', \varpi \in \mathcal{I}_L'$):

$$\begin{aligned}(\alpha_L I_L, \varpi)_{\mathcal{I}_L\mathcal{I}_L} + \left(\vec{\Omega}_L \cdot \nabla I_L, \varpi\right)_{\mathcal{I}_L\mathcal{I}_L} + \left\langle (\vec{\Omega}_L \cdot \vec{n}) \mathrm{T}_{\mathcal{I}_L}^{\vec{\Omega}_L \cdot \vec{n}} I_L, \mathrm{T}_{\mathcal{I}_L} \varpi \right\rangle_{\mathcal{I}_L\mathcal{I}_L} + \\ + \left\langle (\vec{\Omega}_L \cdot \vec{n}) \mathrm{T}_{\mathcal{I}_L} I_L, \mathrm{T}_{\mathcal{I}_L} \varpi \right\rangle_{\mathcal{I}_L\mathcal{I}_L}^{-} = \left\langle (\vec{S}_L^{\Gamma} \cdot \vec{n}) \mathrm{T}_{\mathcal{I}_L} \varpi \right\rangle_{\mathcal{I}_L}^{\Gamma^+_{\vec{S}_L}}, \end{aligned} \tag{318}$$

$$\left(\rho\frac{\mathrm{D}\varepsilon_e}{\mathrm{D}t},\varphi\right)_{\mathcal{T}\mathcal{T}}+\left(\vec{d}_L\cdot\nabla I_L,\varphi\right)_{\mathcal{I}_L\mathcal{T}}+\left\langle(\vec{d}_L\cdot\vec{n})\mathrm{T}^{\vec{d}_L\cdot\vec{n}}_{\mathcal{I}_L}I_L,\mathrm{T}_{\mathcal{I}_L}\varpi\right\rangle_{\mathcal{I}_L\mathcal{I}_L}+$$
$$+\left\langle(\vec{d}_L\cdot\vec{n})\mathrm{T}_{\mathcal{T}_L}I_L,\mathrm{T}_{\mathcal{T}}\varphi\right\rangle^{-}_{\mathcal{I}_L\mathcal{T}}=\left\langle(\vec{S}^{\mathrm{T}}_L\cdot\vec{n})\mathrm{T}_{\mathcal{T}}\varphi\right\rangle^{\Gamma^+_{\vec{S}_L}}_{\mathcal{T}}. \quad (319)$$

The equations have nearly identical form as the non-local transport in space, where upwinding is employed in the domain to stabilize the advection. Also an influx boundary condition is applied for the incoming laser irradiation characterized by the Poynting vector $\vec{S}^{\mathrm{T}}_L$ on the inflow boundary $\Gamma^+_{\vec{S}_L}$. The main difference appears in the energy equation (319). The strong divergence involves also the normal jumps at the discontinuities, which are upwinded to maintain consistence with the intensity equation, but the direction vector $\vec{d}_L$ is used directly. The reason is that the critical plane can be reached and the intensity is discontinuous there due to the propagation coefficient $\vec{\Omega}_L$. In this case, the whole power should be deposited in the first over-dense element. It implies the solution cannot be assumed continuous even in the limit unlike the non-local transport and the surface integrals must be evaluated precisely.

11.1.2 Discrete model

The discretization procedure chooses the discontinuous positive finite elements for both spaces, the thermodynamic and intensity. Due to the strong gradient applied on the intensities in the energy equation (319), the intensity elements are chosen with the polynomial order higher by one normally. The resulting semi-discrete model reads:

$$\left(\mathbb{M}_{\alpha_L}+\mathbb{D}_{\vec{\Omega}_L}\right)\mathbf{I}_L=\mathbf{b}_{\vec{S}_L}, \quad (320)$$

$$\mathbb{M}_{\mathcal{T}}\frac{\mathrm{D}\mathbf{e}_e}{\mathrm{D}t}+\mathbb{D}^{T_eI}_{\vec{d}_L}\mathbf{I}_L=\mathbf{b}^{T_e}_{\vec{S}_L}. \quad (321)$$

The notation follows the chapter about the non-local models (10.3). The system is solved for the intensity, which is then utilized for an explicit update of the internal energy. The power of the laser is not conserved exactly, similarly to the non-local transport. The weak formulation would solve the situation in principle, but mismatch of the polynomial orders in the definitional integrals can be expected. A more severe problem is violation of monotonicity during the inversion of $\mathbb{M}_{\mathcal{T}}$. The possible discontinuity at the critical plane may cause oscillations and undershoots of the intensity behind it due to Runge's phenomenon. This effect is then manifested by a non-physical negative laser absorption at that place. In order to prevent this behaviour, the method of flux corrected transport (FCT) for L_2 elements is utilized [193]. The high-order anti-diffusive contributions are rescaled to keep the intensity values positive, although the order of the method is locally decreased effectively.

Also in this case, the combination of block incomplete LU decomposition (ILU) and generalized minimal residual method (GMRES) is employed or the UMFPACK direct solver for serial builds of the code [194].

11.1.3 Example problem

The functioning of the WKB laser absorption model is demonstrated on a simple problem of normal target irradiation. A step profile of the density and temperature is tailored to provide conditions for propagation and continuous absorption of the laser on the right side, while the left side is over-dense, disabling any propagation and localized absorption of the laser at the critical plane is expected.

The computational domain is defined as $(0, 60\,\mu\text{m}) \times (-40\,\mu\text{m}, +40\,\mu\text{m})$ in 2D. The mesh consists of 20×20 linear thermodynamic and quadratic intensity elements. Moreover, the nodes of the mesh are randomly displaced by the factor of 20 % to validate behaviour of the method under non-ideal conditions. The critical plane is placed at the coordinate $x = 10\,\mu\text{m}$ and the over-dense part has the density $n_e^l = 1.1 n_c$ and temperature $T_e^l = 1\,\text{eV}$, while the under-dense plateau has the density $n_e^r = (1 - 10^{-5}) n_c$ and temperature $T_e^r = 1\,\text{keV}$. The laser impinges the profile from the right with the intensity 10^{12} W/cm^2 and the Gaussian spatial profile with the full-width-half-maximum (FWHM) of $40\,\mu\text{m}$. The wavelength of the laser is set to $1\,\mu\text{m}$ for simplicity.

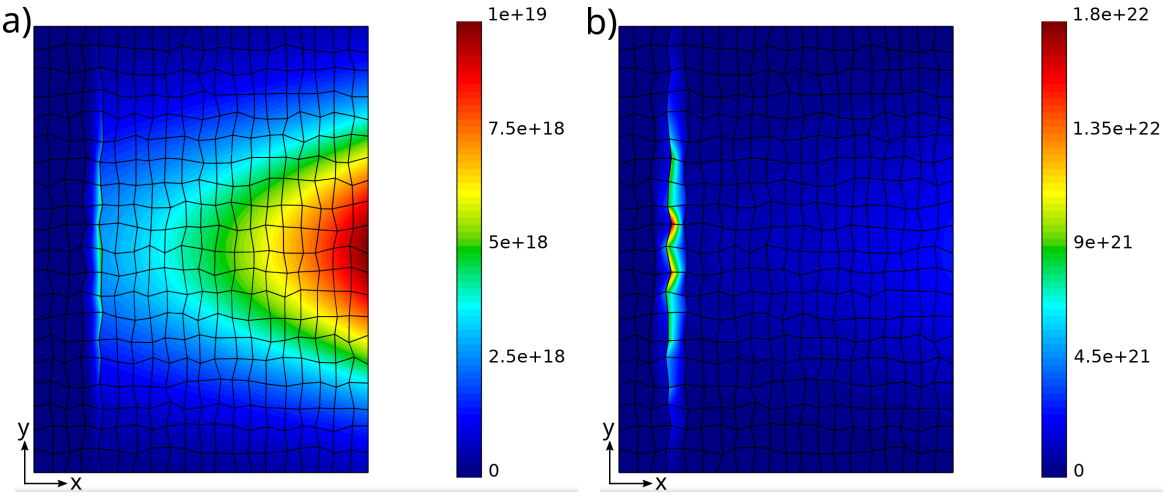

Figure 20: Laser propagation and absorption by the WKB method on the step profile: a) laser intensity [erg/cm^2/s], b) absorbed power density [erg/cm^3].

The results of the numerical simulation are visualized in Figure 20. The gradual attenuation of the laser intensity can be seen in the under-dense area until the critical plane (in the fourth column of cells from the left) is reached. The intensity locally overshoots the previous values due to discontinuity of the elements and the rapid decline of the values as approaching critical plane. The absorption plot shows an intense localized absorption at the place, which is deposited rather to the back side of the cells, into the over-dense part, due to the upwinding technique. A slight permeation to the next column of the cells is visible due to interpolation of the intensity elements, but without any undershoots and negative absorption thanks to the FCT correction of the projection to the thermodynamic space.

Concluding this chapter, the WKB method of laser absorption was checked to operate correctly in under-dense media and provide a smooth numerical solution for the

collisional absorption. Moreover, it was able to capture the critical plane and deposit the power in a strongly localized manner without numerical artefacts.

11.2 Stationary wave model

The physical model based on the stationary Maxwell's equations was presented in chapter 5.2. It provides a full stationary wave solution, which remains valid and fully self-consistent even in the vicinity of the critical plain unlike the WKB or ray-tracing models. In other words it is not limited to the slow variations of permittivity compared to the local wavelength of the laser ($|\nabla\hat{\varepsilon}|/|\hat{\varepsilon}| \ll \hat{n}_r/\lambda_L$). The decomposition of the waves to the incoming characterized by the vector field P and the reflection coefficient V reduced the problem to the pair of equations (188–189), which has properly determined boundary conditions. On the side of vacuum, it is the intensity of the laser imposing the value of P and zero value of the reflection coefficient V a few skin depths behind the critical plane. Unfortunately, this decomposition is possible only in 1D for transversal waves. Still, the method can be applied in the normal direction to the target if the interaction is sufficiently planar, but remapping to a regular mesh is necessary [82] or application of the parallel rays method [135], which become cumbersome due to the complex geometry of the high-order curvilinear finite elements, as mentioned in the introduction of this chapter. Another approach is limitation of the model to the vicinity of the critical plane, where it is mostly needed, and solve the laser propagation on larger scales by a ray-tracing code [138]. This methodology can be viable and remains a topic of the future development.

In any case, the underlying stationary Maxwell's equations must be solved efficiently and robustly on the hydrodynamic scales to present a feasible option for the codes. In [132], we devised a method combining a semi-analytic approach with a differential. The semi-analytic method is applied on the longer scales when the wavelength of the laser cannot be resolved or the absorption is rapid. Though, the method is limited only to the second order of convergence. In contrast, the differential approach can attain virtually an arbitrary order of convergence on a sufficiently resolved domain due the finite element method applied.

In order to proceed with the description of the methods, it must be realized the equation for V (189) presents a complex ordinary differential equation (ODE) of Riccati type. In order to solve it efficiently, it can be reformulated to a pair of linear ODEs by choosing $V = K/L$ (assuming $L \neq 0$), where $K = K(x)$ and $L = L(x)$ are auxiliary functions. The decomposition is not unique and it can be realized that the original pair of wave vectors P and R was related to V in the same way, i.e. $V = R/P$. Though, this procedure enables to transit to a simpler system of equations:

$$L' = \frac{\hat{n}'}{2\hat{n}} K, \tag{322}$$

$$K' = -2ik_0\hat{n}K + \frac{\hat{n}'}{2\hat{n}} L. \tag{323}$$

The system forms a symmetric matrix and reduces to a single equation effectively in absence of gradients of the refractive index.

11.2.1 Semi-analytic method

The first approach to solution of the equations for L and K (322–323) is the semi-analytic method. It is formally given by the matrix exponential of the integral of the system matrix $\mathbb{A}$, i.e. $(L \quad K)^T \sim \exp(\int \mathbb{A}\,\mathrm{d}x)$. The derivation of the solution is detailed not here and can be found in [132]. The resulting propagator matrix, relating the vector of unknowns at one point (x_0) with another (x), depends only on integrals of the refractive index and its boundary values. Consequently, a semi-analytic method can be directly constructed by numerical evaluation of these underlying integrals and their insertion to the analytic solution. The discontinuity of the refractive index calculated from the thermodynamic quantities can be encompassed by matching conditions at the interfaces. When the values of L and K are known, the solutions for P or A are reconstructed in the form:

$$P(x) = P(x_0)\frac{L(x)}{L(x_0)}\sqrt{\frac{\hat{n}(x_0)}{\hat{n}(x)}}\exp\left(ik_0\int_{x_0}^{x}\hat{n}\,\mathrm{d}x\right), \tag{324}$$

$$A(x) = A(x_0)\left|\frac{L(x)}{L(x_0)}\sqrt{\frac{\hat{n}(x_0)}{\hat{n}(x)}}\right|^2\exp\left(-2k_0\int_{x_0}^{x}\mathrm{Im}\ \hat{n}\,\mathrm{d}x\right). \tag{325}$$

It can be noticed the solutions simplify to the classical form of exponential attenuation (and harmonic oscillation in the case of P) in a homogeneous medium when L is constant according to (322). The solution is then evaluated on a quadrature and projected onto appropriate high-order finite elements. In particular, the continuous Lagrange finite elements are used for the Poynting vector, which is of the primary interest. Fundamentally, this energy flux must be continuous and it can be proved the matching conditions at interfaces for the auxiliary variables satisfy this condition, meaning no averaging has to be done [132].

11.2.2 Differential method

The differential approach relies on the finite element method. The spaces of discontinuous Galerkin elements are used for the quantities L, K and P or A. The system (322–323) is solved variationally, where the matching conditions at the inter-element interfaces couple the system. Due to the single-dimensional construction and the aforementioned discontinuity, a sweep can be performed from one boundary to the other, where the element matrices are inverted locally. The boundary condition for $V = 0$ behind the critical plain can be translated to $K = 0$ and $L = 1$, for example. Indeed, the system is invariant to mutual scaling of both variables. Moreover, the algorithm can be switched to the semi-analytic regime any time the resolution criterion is not met [132]. When L and K are known, the original equation for P (189) or A (190) can be solved in the identical manner from the opposite boundary. Finally, a quadrature values of the Poynting vector are calculated according to (191) and projected to the continuous finite elements.

11.2.3 Example problem

There are not many known problems in the literature with a full numerical analytic solution for the stationary Maxwell's equations. An exception are Epstein profiles, which were first studied in the context of propagation of radio waves in Earth's atmosphere [195]. However, they represent simple transition profiles, which are not asimilar from the partially expanded profiles of laser plasma that are smooth in the vicinity of the critical plane due to various transport mechanisms. The wave nature of the absorption can manifest under such conditions. It can be also the environment of foams, which have low densities and the skin depth can be considerably long [196]. The evanescent waves, which are not modelled by the classical WKB model, can penetrate the target to a notable depth.

The Epstein profiles defined for the complex refraction index and permittivity as follows:

$$\hat{n}^2 = \hat{\varepsilon} = \hat{\varepsilon}_l + (\hat{\varepsilon}_r - \hat{\varepsilon}_l)\frac{1}{\exp(-\varsigma)}, \qquad \varsigma = \frac{k_0 x}{\Delta\xi} = \frac{\xi}{\Delta\xi}, \tag{326}$$

where ξ is (vacuum) phase coordinate and $\Delta\xi$ is the width of the transition profile in these units. For convenience, the width is normalized as $\Delta\xi = (\xi_{max} - \xi_{min})\sigma$, where the $\xi_{min} = -400\pi$ and $\xi_{max} = +400\pi$ are the boundaries of the domain. The profiles of the refractive index are plotted in Figure 21 for three different values of the parameter σ. The parameters of the transition layer are chosen as $\hat{\varepsilon}_l = (10^{-2} + 10^{-6}i)^2$ and $\hat{\varepsilon}_r = (5 \cdot 10^{-4} + 10^{-2}i)^2$.

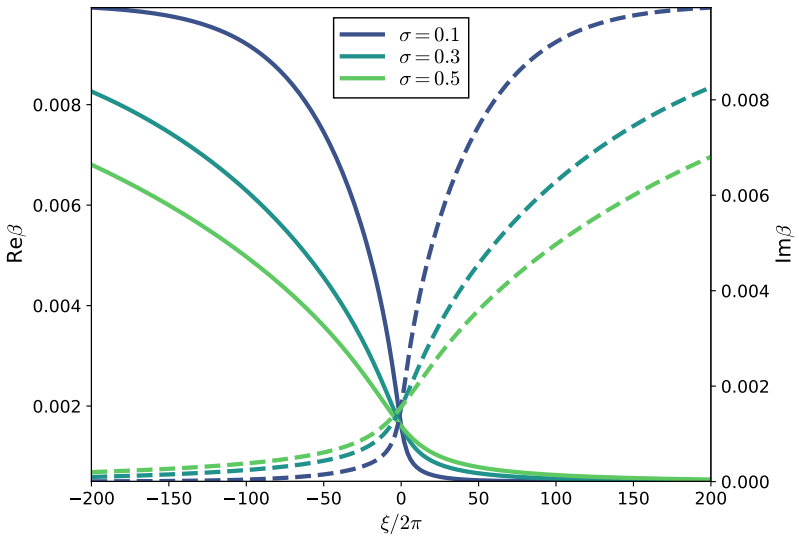

Figure 21: Complex refractive index for the Epstein profiles: real part (full), imaginary part (dashed). The legend designates the steepness parameter σ. Reprinted from [132].

The problem of Epstein transition layers has an analytic solution in terms of hypergeometric functions [195], which can be translated to the variables of the SME model [132]. The electromagnetic wave approaches the profile from the left, i.e. the

left boundary condition for A is set. The resulting Poynting vector and its divergence are plotted in Figure 22. The wave nature of the interaction is clearly manifested. The steepest profile shows a single peak in absorption around of the critical plane, which is located near $\xi \approx 0$. In essence, it is very close to the step function and most of the energy is reflected as can be seen from the Poyinting vector value. Though, considerable penetration to the target by means of the evanescent wave can be recognized. This result justifies the technique of absorption at the critical point in the WKB model, but it must be realized the real problem is inter-coupled and the steep plasma profiles may not exist without a simplified absorption model and self-consistence of the modelling is needed. In contrast, the moderate gradients show gradual reflection and a smaller absorption peak at the critical point. The solution remains significantly oscillating even about 200 wavelengths from the critical plane, stressing importance of the wave modelling. Under real conditions, such extreme distances cannot be expected, but the wave modelling is still important at least multiple wavelengths from the critical plane [138]. The wave mechanism of the cross-beam energy transfer (CBET) is also strongest in the vicinity of the caustics with severe implications to the ICF dynamics [197, 198].

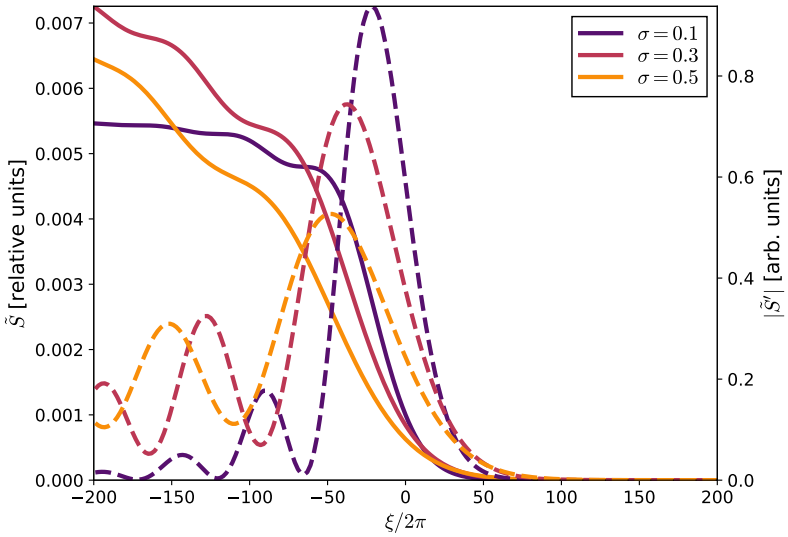

Figure 22: Solution of the interaction of an electromagnetic wave with the Epstein profile: normalized Poynting vector (full), normalized divergence of the Poynting vector (dashed). The legend designates the steepness parameter σ. Reprinted from [132].

In [132], we show the numerical solution converges to the analytic with the first order for a piecewise constant approximation of the refractive indices and the semi-analytic method. This improves up to the second order for a quadratic representation of the refractive index, but the convergence does not scale further. On the other hand, the differential solution scales with the polynomial order of the elements, but is strictly limited in the lowest possible resolution, otherwise poorer results than with the analytic approach are obtained. The optimal strategy is then combination of both methods based on a local criterion, as we proposed in [132].

In summary, the problem of an electromagnetic wave interacting with the Epstein transition profiles showed complexity of the wave optics and its importance in the laser plasma modelling. The numerical treatment combining the semi-analytic and high-order finite element approaches can benefit from the positive features of both and attain robustness as well as a rapid convergence.

11.3 Ray-tracing model

The ray-tracing model relies on the optical approximation of the laser, which was theoretically summarized in chapter 5.1. From this point of view, it is fundamentally close to the WKB model presented in chapter 11.1 and shares the differential description of the collisional absorption through the Beer–Lambert law (315) with it. The main distinction between the models is refraction, which is naturally included in the ray-tracing models. The influx of the laser radiation is split to numerous rays, which are traced throughout the domain, governed by the ray equation (175) or the equation of motion (177) in the Hamilton–Jacobi formalism.

It can be immediately seen the equations reduce to propagation along straight lines in absence of gradients of the complex refractive index. In the case of a piecewise-constant medium, the rays obey Snell's law at the interfaces:

$$\vec{n} \times \vec{k}_1 = \vec{n} \times \vec{k}_2, \tag{327}$$

where $\vec{n}$ is the normal to the interface and $\vec{k}_1$ and $\vec{k}_2$ are the wave vectors in the half-spaces separated by the interface. In fact, it can be seen as the mere discontinuous limit of the aforementioned ray equation with a matching condition for the tangential wave number. A simple analytic solution also exists for a (piecewise-)linear medium, where the rays follow parabolas, giving rise to the methods of parabolic ray-tracing [121].

The method of straight-line ray-tracing was implemented by M. Šach primarily for the purposes of X-rays amplification, but with functionality of the laser absorption as well [128]. In addition to the classical model of inverse Bremsstrahlung, it offers a simplified model of resonant absorption near the turning point of the rays for p-polarized laser beams [123]. Even though the rays are typically totally reflected before reaching the critical plane, the initial interaction with the laser may lead to their interaction with the bare critical plane. Therefore, a condition stopping the rays is integrated. Unlike most of the codes of this kind, which deposit the full power of the rays at that point similarly to the WKB method, the described ray-tracing code is equipped with the Fresnel equations to determine the fraction of power crossing the interface. With an appropriately calibrated collision frequency closure model [82], the reflectivity of a solid target can be simulated correctly.

11.3.1 High-order mapping

The described model of ray-tracing considered only a piecewise-constant medium. When integrated with the high-order finite element magnetohydrodynamics of chapter 8, the construction would be limited only to the $T0$ elements, losing most of the benefits offered by the method. Therefore, a procedure mapping the high-order finite

elements to the low-order refined finite elements and back is devised. In fact, the ray-tracing requires only three quantities to operate: the electron density n_e, real refraction index $\hat{n}_r$ and absorption coefficient $\alpha_L = -2k_0\hat{n}_i$. These grid functions must be mapped to the refined mesh, so the tracing of the rays can be performed and the absorbed power of the laser is obtained. This power is then mapped back to the coarse high-order mesh.

In particular, the computational mesh is uniformly refined by the factor equal to the number of DOFs per element multiplied by an additional coefficient greater or equal to one. The additional refinement is useful for the ray-tracing algorithm, which can be strongly non-linear when the rays are totally reflected in the vicinity of the critical plane. It enables to capture spatial variations of the quantities in the domain and deformation of the computational mesh.

The interpolation of the quantities is performed by the L_2 integral projection in the direction from the coarse mesh to the fine. The associated operator F is defined in the discrete form as follows:

$$\mathbb{F}_{ij} = (\mathbb{M}^{LOR}_{ik})^{-1} \int_{\Omega_h} \varphi^{LOR}_k \varphi^{HO}_j \,\mathrm{d}V \qquad \forall i, j, \tag{328}$$

where φ^{HO}_j are the basis functions of the high-order elements from the thermodynamic space and φ^{LOR}_j correspond to the low-order refined elements. The term $\mathbb{M}^{LOR}_{ik}$ is the mass matrix of the thermodynamic elements on the fine mesh. It must be noted these elements are discontinuous, so the operation can be performed locally including the inversion of the mass matrix, which is diagonal for the piece-wise constant elements.

The reverse procedure of mapping the absorbed power onto the high-order elements also utilizes an L_2 projection. At the core, it performs the operation $(\mathbb{M}^{HO})^{-1}\mathbb{F}^T$, but such operator does not respect local extremes of the functions. Thus, overshoots to negative values can be expected behind the critical plane, where the intensity of the laser rapidly drops. Therefore, the L_2 FCT is employed to correct the inversion of the mass matrix [193], similarly to the WKB method (see chapter 11.1.2). Though, a difference exists in the procedure, where not only positivity of the function is of a concern, but also the local extrema, which are determined over the sub-cells of the refined mesh and the edge neighbourhood. Finally, it should be mentioned an alternative to the high-order mass matrix $\mathbb{M}^{HO}$ is construction of $\mathbb{F}^T\mathbb{M}^{LOR}\mathbb{F}$, which has an advantage of a potentially less diffusive action on the grid functions and also providing the left inverse of the forward operator within the backward projection ($(\mathbb{F}^T\mathbb{M}^{LOR}\mathbb{F})^{-1}\mathbb{F}^T\mathbb{M}^{LOR}\mathbb{F} = \mathbb{I}$) [199]. However, this alternative approach remains a topic of the future development.

11.3.2 Parallelization

A difficulty inherently connected with the ray-tracing methods is their parallelization. As they do not operate on grid functions, but a set of independently propagating rays, they do not conform to the domain decomposition paradigm. Though, the magneto-hydrodynamic code PETE2 is primarily parallelized in this way. Therefore, the ray-tracing code has to communicate the rays on the distributed computational mesh, while load-balancing is nearly ruled out by the fact the trajectory on the mesh is not

known beforehand and is a part of the solution. This point presents a considerable disadvantage compared to the simpler, but grid-based WKB method.

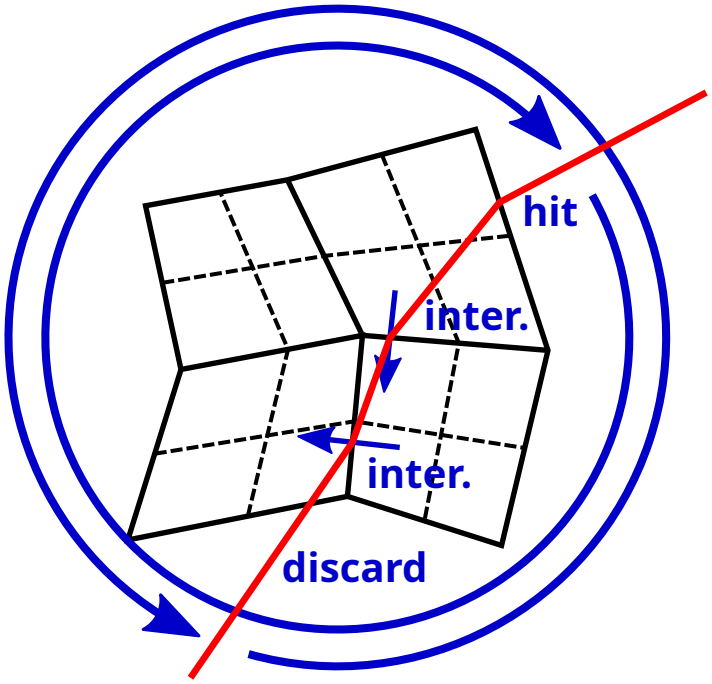

Figure 23: Diagram of the parallel ray tracing: computational cells (dashed black), distributed sub-zones (full black), laser (red) and communication (blue). Types of the messages are denoted (hit/intersection/discard). The refraction of the ray is indicated only at the sub-zone interfaces for simplicity.

The actual parallelization relies on a global pool of the rays, which are being traced. A schematic view of the communication is illustrated in Figure 23. The first type of event that must be communicated is a hit of the target. As the computational domain can be non-convex, multiple boundary intersections with the axis of an incoming ray may exist. The initial intersection is determined based on the distance from the source. The globally closest intersection to the source is chosen using chain communication between the peers. The tracing starts only after this notice loops around the cluster, guaranteeing consistence between the processes . Oppositely, the ray may not hit the target at all. This piece of information must be communicated as well, so all peers can safely remove the ray from the pool. The final decision is made by the root process, which sends out another type of message, the discard notice, when informed about the ray by the rest of the processes though a chain message. The discarding process is initiated not only when the target is missed, but also when it leaves the domain or is completely absorbed. The discard notice is also relayed by all peers and loops around until it reaches the originator and only then it is removed from its pool, guaranteeing consistence of the global pool again. Finally, it is the exchange of the intersections and powers of the rays transiting from one sub-domain to another. Unlike the other messages, these are addressed only to the peers sharing the involved face of an element. All communication is performed in the asynchronous regime with a timely

garbage collection of the completed transactions to regulate the memory consumption.

11.3.3 Example problem

The test problem for the ray-tracing code is nearly identical to the problem for the WKB method in chapter 11.1.3. The main difference is given by the angle incidence, which is fixed to 45° in this case to show reflection of the rays, which was not possible to model within the WKB method. The setting of the test is not fully physical as the laser is totally reflected at the critical plane, otherwise the results would be very similar to the WKB approximation with maximal absorption at the plane, only corrected by the Fresnel coefficients for the given angle of incidence. The coefficients of reflection are set equal to the unity, in order to make the reflected laser light more visible.

The simulation domain spreads over $(0, 60\,\mu\text{m}) \times (-60\,\mu\text{m}, +60\,\mu\text{m})$. The resolution is 20×20 linear thermodynamic finite elements. The nodes of the uniform computational mesh are randomly dislocated by 10 %. The parameters of the laser are identical to chapter 11.1.3, i.e. wavelength 1 µm, Gaussian spatial profile with the peak intensity 10^{12} W/cm^2 and FWHM 40 µm. Likewise, the step is located at $x = 10\,\mu\text{m}$ and the left values of the temperature and electron density are $T_e^l = 1\,\text{eV}$ and $n_e^l = 1.1 n_c$. The opposite side has the relatively high temperature $T_e^r = 1\,\text{keV}$ to reduce the absorptivity of the plasma, while the density is very close to the critical value $n_e^r = (1 - 10^{-5}) n_c$.

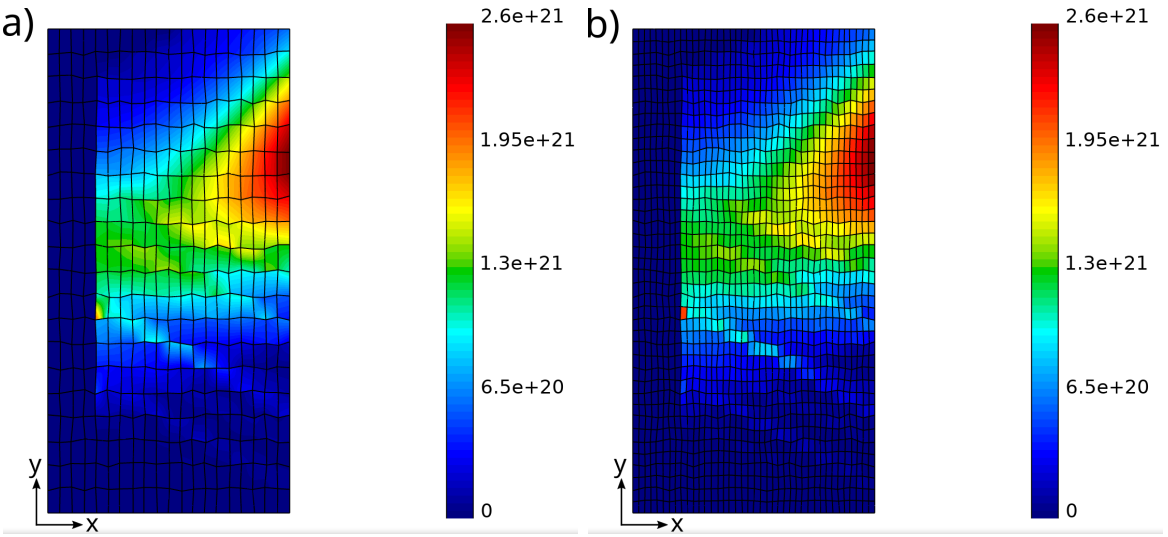

Figure 24: Total reflection of the laser on the step function simulated by the ray-tracing method: a) projected absorption on the linear finite elements, b) absorption on the refined piecewise-constant elements. The values are in erg/cm^3/s.

The results of the numerical simulation are visualized in Figure 24. The actual absorption is performed on the low-order refined mesh and mapped to the high-order finite elements, as described in chapter 11.3.1. In total, 400 rays are traced from the emitting line wide 80 µm towards the origin of the coordinate system. The plots of the absorbed power show a smooth reconstructed profile further from the step, where

only the incoming laser is gradually attenuated. These results are on par with the those obtained by the WKB method. The situation becomes more involved closer to the interface, which is not perfectly flat due to the random displacement of the mesh nodes. Most of the rays are reflected in an approximately correct direction, giving the bulk shape to the reflected beam. Though, some of the rays are reflected from the more uneven segments of the interface. It shows sensitivity of the method to the underlying geometry of the computational mesh, which must be always kept in mind. However, it must be mentioned the code relies on the gradients of electron density obtained by the least squares reconstruction from the local neighbourhood instead of the normals to the edges when determining refraction and reflection [128]. Thus, relatively stable results can be expected in continuous media even for disturbed meshes. Furthermore, the interfaces in discontinuous media can be smoother resolved by the curvilinear finite elements, which was not investigated in this test, since only the nodes of the mesh were dislocated.

The test problem confirmed the ability of the ray-tracing method to model reflection from an internal interface. The combination of the refinement and the integral projection offers smooth results in a continuous medium. The actual reflection was afflicted by geometrical errors, which presents a difficulty for all methods of this kind, but the curvilinear finite elements may help to reduce these errors under real conditions.

Part III
Simulations

12 One-dimensional simulations

This chapter presents one dimensional simulations of laser–target interactions under realistic conditions. Different contributions to the energy transport are investigated. Primarily, it is the radiation transport (chapter 12.1) and electron heat transport (chapter 12.2). In both cases, the diffusive approximation and the non-local discrete ordinates methods are compared, highlighting the salient distinct features. From this point of view, the 1D modelling has the undeniable advantage of a better detail and more straightforward analysis of the involved physical phenomena.

12.1 Radiation transport

The notion of non-locality is inherently connected with radiation transport, as photons can travel vast distances between their point of origin and their final destination. Though, it was already reasoned in chapter 4 that the minuscule dimensions of the laser plasmas and the high densities favour rather subsequent absorption and re-emission processes [100]. The measure distinguishing between the diffusive and free streaming regimes of transport is the radiation Knudsen number $Kn_R = |\vec{q}_R|/(c\epsilon_R)$, which simplifies in the context of the diffusion to $Kn_R = |\nabla\epsilon_R|/(\rho\kappa_R\epsilon_R)$ (see chapter 4.1). Small values ($\lesssim 10^{-2}$) indicate mostly diffusive and isotropic transport, while high values ($\gtrsim 1$) correspond to the non-local regime accompanied by a strong anisotropy typically.

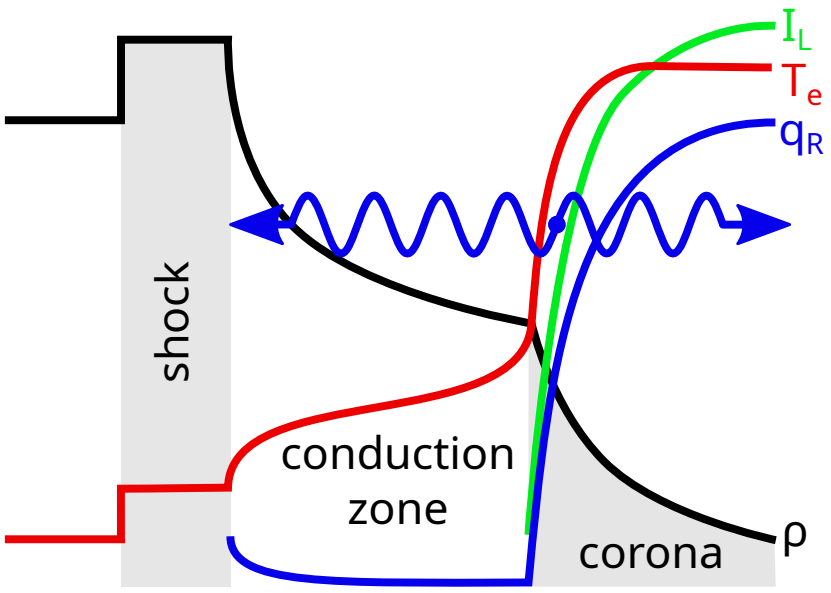

Figure 25: Schematic view of the laser–target interaction: mass density (black), electron temperature (red), laser intensity (green) and radiation flux (blue).

The typical situation in laser plasma is illustrated in Figure 25. The interaction of a laser beam with a solid target leads to ablative removal of the material and formation of a plasma plume. The laser propagates only up to the point of the critical density, which separates the coronal part and the conduction zone. The corona is partially

transparent for the laser, which is gradually attenuated until it reaches the critical plane (consult chapter 5). The deposition of the laser power heats up the plasma and generates an intense thermal radiation, which almost freely escapes the plume through the low-density corona, where the Knudsen number is highest normally. On the other side, radiation propagates to the over-dense region of the so-called conduction zone, which is established based on the balance between the fluxes. Provided the radiation transfer is the dominant transport mechanism in the area, which is the case for high-Z materials typically, it is the balance of the outward hydrodynamic flux $\sim p\vec{u}$ and the radiation flux $\vec{q}_R$ into the target. For this reason, this zone is very sensitive to the magnitudes of the fluxes and the underlying transport modelling, strongly affecting the shape of the so-called double ablation front (DAF) structure [200]. A comparative study under different physical conditions and the implied regimes of transport was made in [95]. The Knudsen numbers are moderate in this area, depending on the particular conditions, making the modelling cumbersome. Returning to the description of the typical scenario, the efficient transport through the conduction zone induces the ablation pressure on the target, driving a shock wave inwards. The Knudsen numbers are very low in the area as the radiation cannot penetrate the compressed material, but the compression itself mildly heats the matter.

In order to demonstrate the plasma processes and effects of different models, a numerical simulation under typical conditions is performed. A solid aluminium target at the approximately room temperature (0.03 eV) is considered. A laser with wavelength $\lambda_L = 351\,\mathrm{nm}$ (corresponding to the third harmonic frequency of a Nd:glass laser system) impinges the target from the right side. The laser pulse has the peak intensity $I_L = 1 \cdot 10^{14}\,\mathrm{W/cm^2}$ and Gaussian time profile with FWHM 2.5 ns and an equal temporal offset. The computational domain spans from $-200\,\mu\mathrm{m}$ to 0. In total, 40 quadratic/cubic finite elements $T2$ are geometrically distributed with the factor 0.88. The geometric factor determines the ratio between the sizes of every two successive elements. The time stepping employs the RK2-Average scheme with the CFL constant $C_{CFL} = 0.25$. The tensor viscosity based on the full eigenvector decomposition is used with the linear factor $C_{lin} = 0.5$ and quadratic $C_{quad} = 2.0$ [25, 177]. As the equation of state, QEOS is chosen with interpolation provided by the HerEOS library (see chapter 2.4). The simulation runs in the two-temperature regime with either the model of non-equilibrium gray-body radiation diffusion or the gray-body non-local radiation transport. The diffusion model relies on the backward Euler relaxation and the limiter by Levermore & Pomraning (see chapters 4.1 and 9.1). The boundary conditions for zero flux and Milne-like free streaming are set on the left and right boundaries respectively. In the case of the non-local approach, the cubic discontinuous elements are applied in space and polar angle, which is divided to two $\pi/2$ segments. This setting is sufficient for separation of the forward and backward propagating radiation in 1D and smooth interpolation in both directions. The combination of the boundary condition for zero intensity derivative and free propagation is set. The mean Planck and Rosseland opacities are calculated from scaling laws according to [201].

The comparison of the diffusive and non-local modelling is made in Figure 26. Both approaches exhibit a strong radiation cooling effect, where over 60 % is radiated away. Though, distribution of the radiation flux on the opposite side is notably differ-

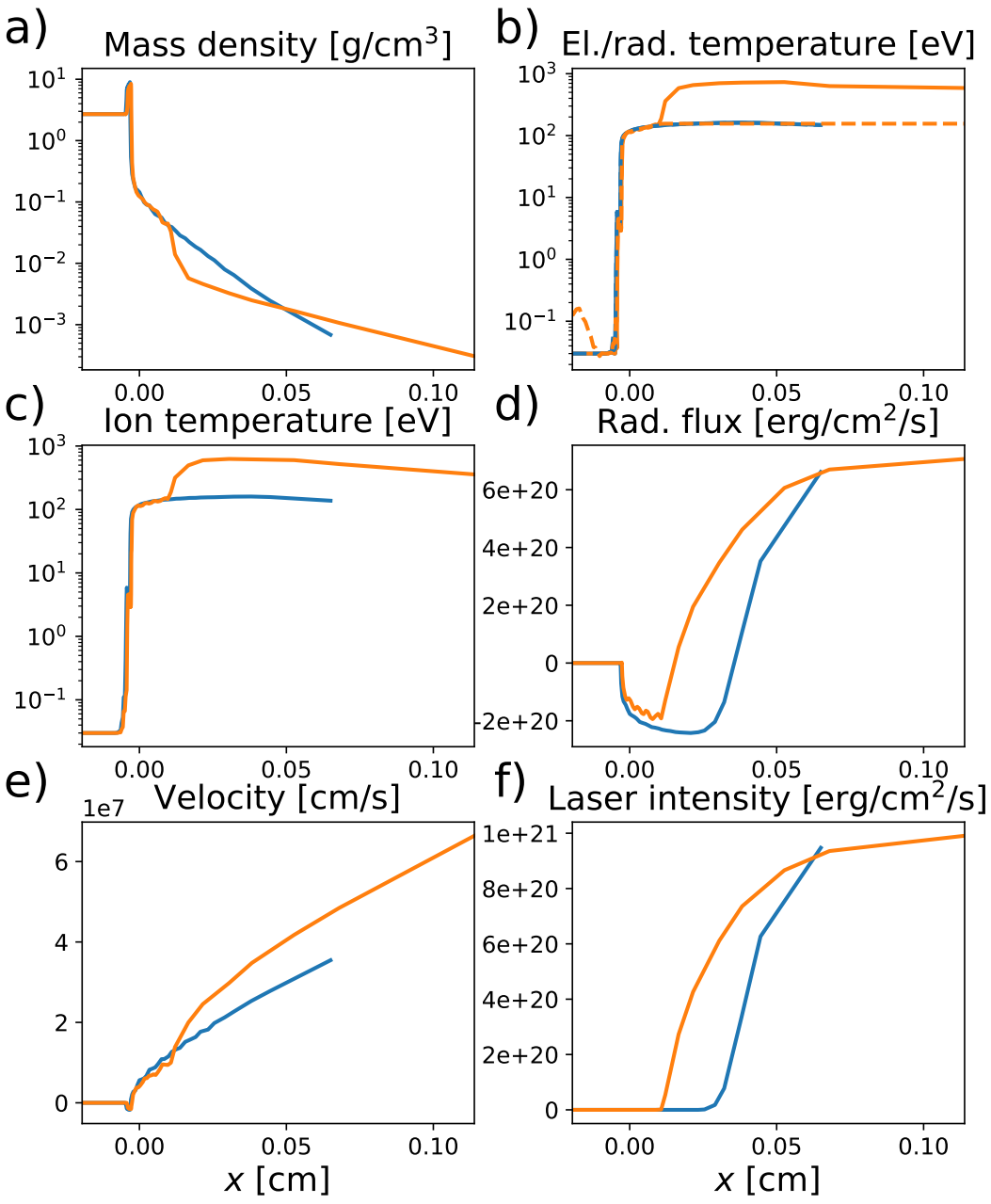

Figure 26: Comparison of the non-equilibrium radiation diffusion (blue) and non-local transport (orange) at time $t = 2.5\,\mathrm{ns}$: a) mass density, b) electron (full) and radiation (dashed) temperatures, c) ion temperature, d) radiation flux, e) velocity and f) laser intensity.

ent. Although the temperatures are very similar in the conduction zone, the radiation diffusion does not limit the flux significantly due to the maximal Knudsen number ≈ 2, which results in an elongated profile of the zone and a continuous temperature and density profile. In contrast, the non-local model limits the radiation flux strongly, which is manifested by the laser absorption closer to the target and the bent temperature and density profiles. The electron temperature then departs from the radiation temperature given by the conditions at the critical point predominantly. Consequently, the velocity is higher in the corona and the density decreases to lower values, but with a smaller slope, since the radiation cooling mechanism is effectively lost due to decoupling of the electron temperature. In both cases, the temperatures are relatively low and the simulation remains in the equilibrium between the ions and electrons. Also an effect of the left non-local transport boundary condition is visible, which causes radiation temperature accumulation, but without any consequences for the electron and/or ion temperature.

The problem demonstrated important differences between the radiation transport modelling and the non-local radiation transfer. However, the peripheral regions of corona and conduction zone were mainly affected, without any significant effects on the shock wave propagation.

12.2 Electron heat transport

The electron transport holds many similarities with the radiation transport, as already recognized in chapters 3 and 10. Also in this case, the regime of transport can be characterized by the Knudsen number $Kn_e = \bar{\lambda}_e|\nabla T_e|/T_e$ for dominant variations of the temperature or $Kn_e = \bar{\lambda}_e|\nabla n_e|/n_e$ in the case of the density. Alternatively, these definitions can be related through the transport equation (300), which offers the expression for the mixed case $Kn_e = \bar{\lambda}_e|\nabla S_e|/S_e = \bar{\lambda}_e(|\nabla n_e|/n_e + 3/2|\nabla T_e|/T_e)$. The electrons with high values of Kn_e are strongly delocalized and can cross spatial variations of temperature density before being absorbed. Contrary, the low values of the parameter indicate transport by means of many collisional events under the conditions dictated by the local values of the thermodynamic potentials. However, important differences must be recognized, as the significantly different temperature dependencies of the coefficients and the collective interaction through the self-consistent electric field maintaining quasi-neutrality of the plasma. These distinction points lead to overall different behaviour and operation on different scales traditionally [95].

The typical profiles during a laser–target interaction are schematically depicted in Figure 27. Similarly to chapter 12.1, the laser is gradually absorbed before reaching the critical plane. This driver induces localized heating of the plasma and produces the super-thermal electrons. These electrons can also freely stream through the coronal low-density plasma, as the mean free paths are comparable with or exceed the size of the plume, but they cannot escape the expanding plasma due to the conservation of the total charge. Physically, some separation of the charge is possible, as the Debye length increases ($\lambda_{De} = \sqrt{\epsilon_0 k_B T_e/(n_e e^2)}$), but the approximation of the plasma as a quasi-neutral fluid does not allow this behaviour in its simplicity. Therefore, the heat flux must vanish at the outer boundary of the plume, directing most of the energy towards

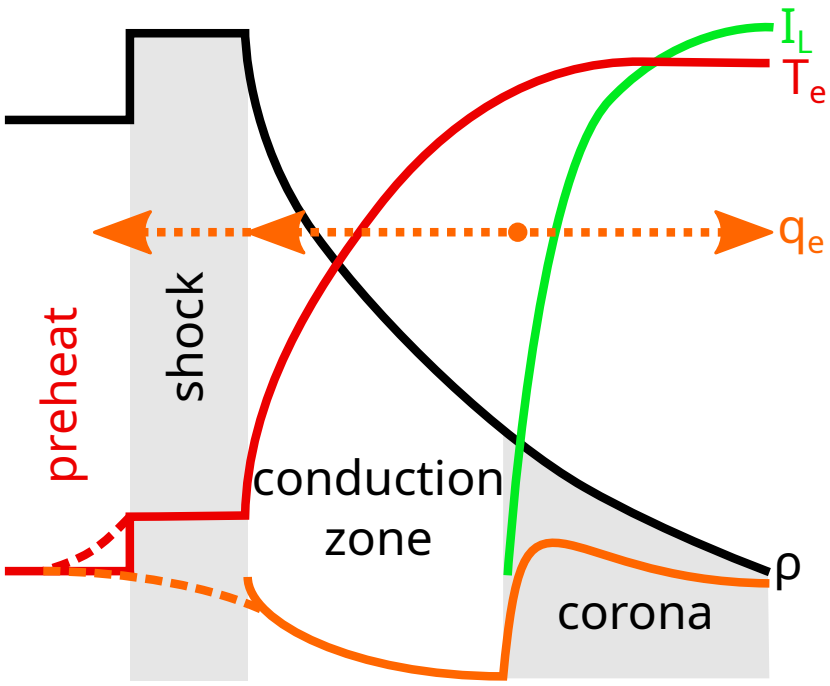

Figure 27: Schematic view of the laser–target interaction: mass density (black), electron temperature (red), laser intensity (green) and electron heat flux (orange). The preheating effect due to the non-local electrons is distinguished by the dashed line.

the target. Provided the electron transport is dominant in the conduction zone, which is the case for low-Z materials, its shape is also governed by its balance with other fluxes, although the spatial scales are typically smaller than for the thermal radiation. Also the flux limitation may not be as dramatic, not breaking the temperature profile visibly. However, a small fraction of the highly non-local electrons can penetrate even the shock wave and get deposited in the area of the hydrodynamically unperturbed target, degrading the compression ratio, which is critical for ICF applications [31]. Although the preheat is undesirable, the coupling between the laser and the driven shock wave can be improved by the non-local species [33], which is especially important for the shock ignition schemes [32]. For this reason, it is worthwhile to compare estimates of different electron transport models.

12.2.1 Hydrodynamic closure models

First, the hydrodynamic closure models of heat diffusion and the BGK non-local transport are compared. The physical conditions and numerical settings are identical with those of chapter 12.1, i.e. an aluminium target is irradiated by a defined laser pulse. The only difference is the resolution of the computational mesh, where only 30 elements with the geometric factor 0.9 were taken for the BGK electron transport. The reason are stability issues connected to the method, as commented later. The heat diffusion model uses the heat flux limiter rescaling the conductivity by the harmonic mean (see chapter 3.1.2). The limiting fraction of the heat flux versus the free-streaming flux is $f_{lim} = 0.05$.

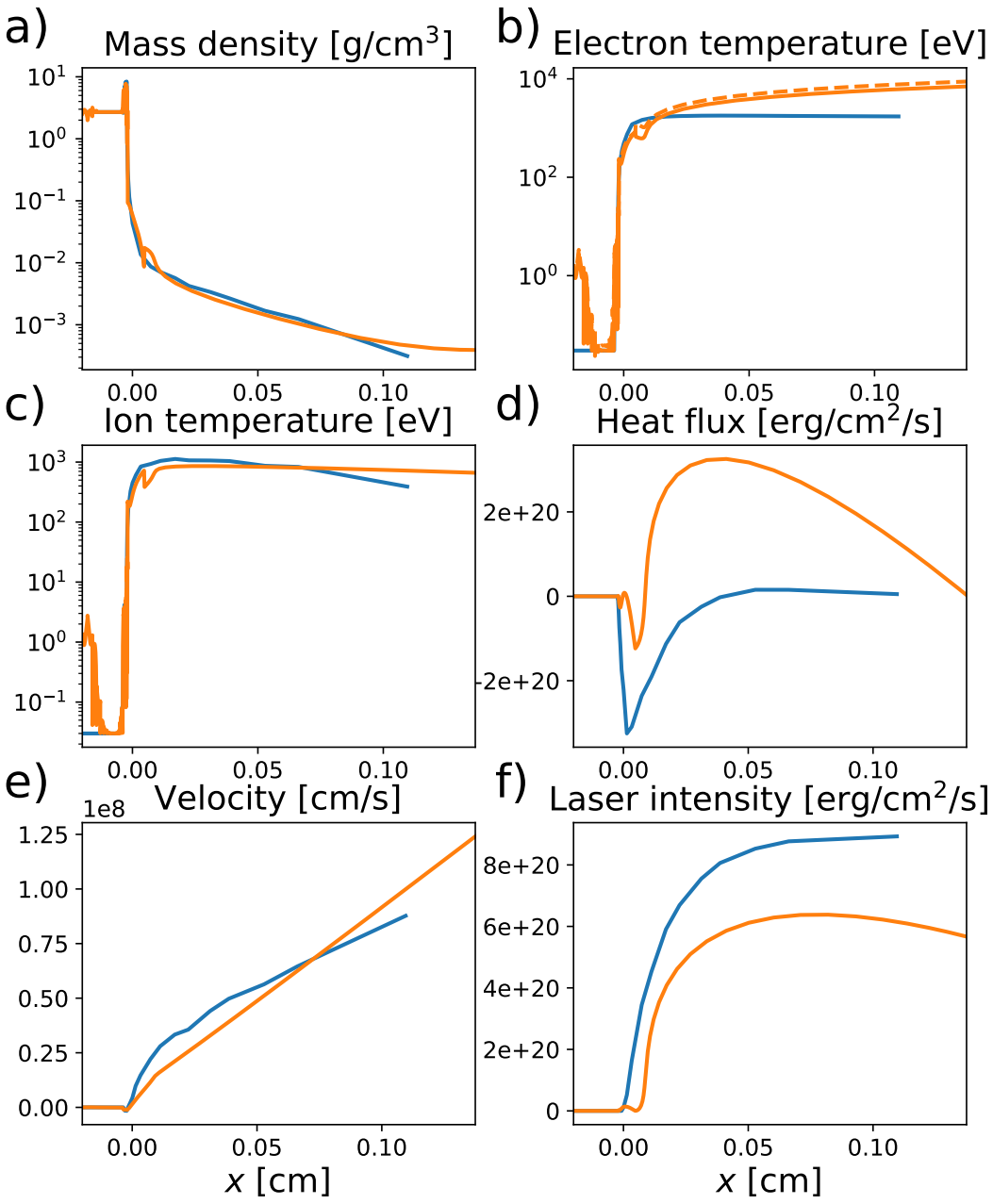

Figure 28: Comparison of the electron heat diffusion (blue) and non-local transport (orange) at time $t = 2\,\text{ns}$: a) mass density, b) electron temperature (non-local temperature is dashed), c) ion temperature, d) heat flux, e) velocity and f) laser intensity.

The numerical results obtained with the two models are compared in Figure 28. Very similar density profiles appear in both cases, but with flatter tail for the non-local transport. This feature corresponds to the ever increasing velocity and temperature, which are caused by the strong heat flux to the corona and rather weak towards the target. Contrary, the diffusion model shows only marginal deposition of energy in the under-dense region, but intense to the target. The flux limitation is potentially underestimated there as the moderately non-local regime emerges with the Knudsen number $Kn_e \sim 10^{-3} - 10^{-2}$ in the vicinity of the critical plane, which stresses importance of a self-consistent treatment. The reason for the peculiar behaviour of the non-local transport in the corona can be seen in the plot of the non-local electron temperature, which accompanies the (local) electron temperature, but is always slightly higher. This phenomenon is implicated by the fact the source function of electrons is density-dependent. When only the heat intensity is transported without any notion of the spectral distribution, the non-local electron temperature and the the contribution to the local temperature must be calculated from the local densities, which continuously decrease. This effect leads to overheating of the corona and issues with stability of the simulations. The multi-group treatment can potentially cure the problem (similarly to the SNB model from chapter 3.1.3), but the lack of a self-consistent electric field implies inability to couple different velocity groups correctly, as discussed in chapter 3.3 already.

Also a minor problem appears near the left boundary condition, where the accumulated electron heat intensity causes minor heating of the material. A similar artefact appeared in the radiation transport simulations in the previous chapter (12.1), but had no implications for the material temperature. The exact mechanism of this anomaly must be studied, but it has a negligible impact on the overall dynamics of the simulation.

Finally, the laser intensity profile has its maximum distanced from the emitting boundary, but this peculiar feature can be attributed to the low resolution and discontinuity of the elements. The inflow boundary condition then integrally acts this way, but the resulting divergence of the Poynting vector includes the boundary contribution according to chapter 11.1 and remains negative, i.e. the absorbed power is positive. Unfortunately, this is not true for the non-local transport based on the original design [113, 94], which does not include the contributions from the discontinuities in the discrete divergence (see chapter 10.2) and exhibits small ditches between the temperature elements for these reasons most probably.

In summary, the simulations with the diffusion and non-local transport highlighted differences between the approaches, where the technique of flux limitation cannot reflect the actual changing conditions. However, the comparison also revealed numerical issues connected to the BGK model of non-local transport, which can be partially attributed to its physical design already. This point motivates future development of better models for the non-local electron transport.

12.2.2 Kinetic model

The kinetic reduced Vlasov–Fokker–Planck–Maxwell model from chapter 7 presents an alternative to the hydrodynamic closure models of heat diffusion and non-local BGK transport. However, it does not account for the ion motion and its temporal scale is tied to the plasma frequency and other microscopic scales. Even though the implicit construction and the reduced nature of the model offer less expensive computation, simulations on the hydrodynamic scales are still demanding and the full coupling with a hydrodynamic code is non-trivial [202] and remains a possible topic of the future development. Therefore, a single time frame from the previous hydrodynamic simulation with the diffusion model is used as the initial condition for the kinetic code. In order to attain the quasi-static regime of the hydrodynamic scales, the calculation is performed without the transient fluxes and electric fields, i.e. only the isotropic part of the electron distribution function f_0 is non-stationary to self-adjust to the physical conditions.

In particular, the starting point is the time $t = 2\,\mathrm{ns}$ investigated in the previous chapter (12.2.1). The reduced VFP simulation then runs with the time step $\Delta t = 2.5 \cdot 10^{-22}\,\mathrm{s}$ for the time $6.75 \cdot 10^{-19}\,\mathrm{s}$. Such a short time step correlates with the extremely short collision time in the compressed area, which is as short as $\approx 3.2 \cdot 10^{-22}\,\mathrm{s}$ for the electron–electron interaction based on the classic formula (72). The combination of the quadratic f_0 and cubic $\vec{f}_1$ and $\vec{E}$ is used to directly match the hydrodynamic simulation. In total, 400 velocity levels are considered uniformly distributed from 0 to $7v_{Te}$ for the maximal temperature 1800 eV.

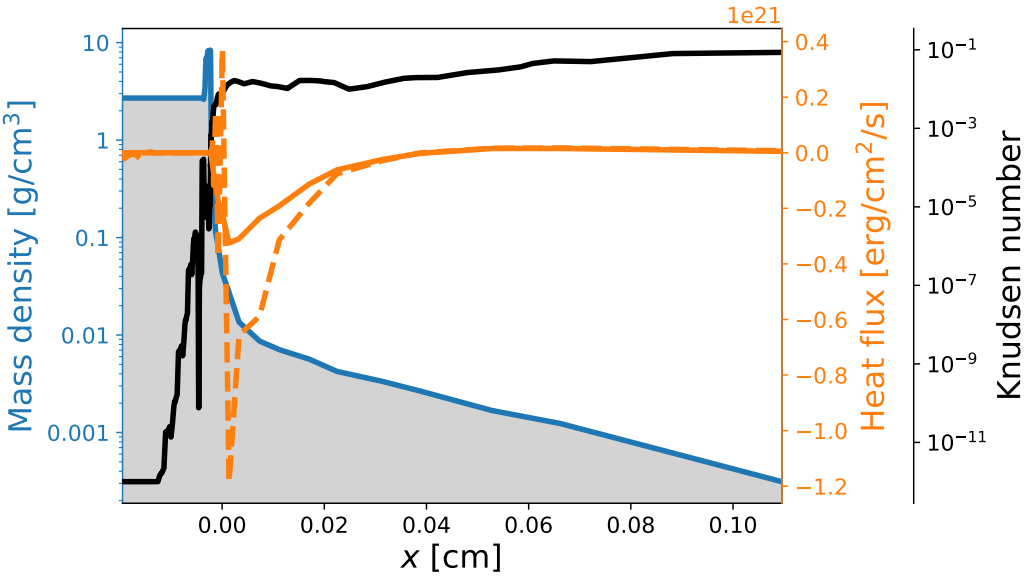

Figure 29: Heat transport modelled by the diffusion (full) and kinetic model (dashed): mass density (blue), heat flux (orange) and the Knudsen number (black).

A comparison of the diffusive and kinetic results is made in Figure 29. The plot of the Knudsen number confirms the previous analysis and indicates that differences between the approaches can be expected only in the conduction zone and corona. The

very low values in the solid target push both models towards the diffusive regime, where they were confirmed to agree in chapter 7.3.1. However, it must be mentioned the hydrodynamic model includes correction of the heat conductivity for solid densities [82], while the classical Spitzer-Härm conductivity, to which the kinetic model converges, declines to extremely small values. Replacement of the Fokker–Planck collision operator by a dedicated model for solid matter is a possible topic of the future research, which would enable simulations of the preheat effect. The most significant difference appears in the vicinity of the critical plane. The heat flux towards the target is approximately four times stronger for the kinetic model than for the diffusive one. Some corrugation of the profile is visible further away from the plane, which can be attributed to the transition from the hydrodynamic to the kinetic code. Inversion of the f_0 mass matrix is necessary during the process, which entails deformation of the profile. Also the short convection zone can be affected by this numerical phenomenon partially. However, there is also the effect of the non-local electrons reflected from the dense part. On the hydrodynamic scale, these fluxes would elongate the conduction zone and normalize over time, similarly to the BGK model in the previous chapter (12.2.1). This argument is supported by the still relatively high values of the Knudsen number of the order 10^{-2}, which permits moderately non-local transport.

The kinetic modelling of a snapshot from the diffusion simulation showed an excessive heat flux limiting in the latter, but also indicated non-locality of the transport, which cannot be adequately modelled diffusively. This non-locality was qualitatively encompassed by the BGK model to some extend, but significant quantitative differences could be found. This supports the direction of research towards non-local closure models closer to their kinetic foundation.

13 Two-dimensional simulations

The two-dimensional simulations focus on problems, where the geometric effects can be important. Conceptually, they present a trade-off between the enormously demanding 3D simulations on one side and the oversimplified 1D models on the other. In particular, the problems of laser absorption (chapter 13.1) and spontaneous magnetic fields generation (chapter 13.2) are presented. The laser absorption involves reflections and refraction on transverse gradients of the plasma profiles. Moreover, with an oblique incidence of the laser rays, also the mechanism of resonant laser absorption can be included. While the laser absorption can be modelled 1D approximately, the simulations of spontaneous magnetic fields generation are completely impossible there, since the mechanism of Biermann battery relies on misalignment of the density and temperature gradients. The 2D dynamics of both quantities must be simulated precisely, as the gradients naturally tend to align again due to convective and conductive processes.

13.1 Laser absorption

The process of laser absorption is determining for ablation of material from a solid target and production of the super-thermal electrons and radiation. Depending on the parameters of the laser and target, the deposition of the laser power can be more localized to the vicinity of the critical plane, where it resonantly excites electrons, which is the case for longer wavelengths typically. Or it can be gradually attenuated in the corona by the collisional absorption, which occurs for shorter wavelengths usually, as they penetrate to the more dense regions due to the higher values of the critical density (consult chapter 5). Moreover, the beam can be partially reflected or refracted in the plasma, as described in chapter 5.1. Therefore, multiple numerical methods for solution of the laser absorption were offered in chapter 11. Although the most physically accurate description is provided by the wave-based model theoretically, it is limited to a single dimension and differences from the optical limit can be observed mainly on small spatial and/or temporal scales. For the simulations of longer pulses in multiple dimensions, the ray-tracing code or the WKB model are more suitable. Despite the fact the models stem from the identical optical approximation in principle, their performance under realistic conditions is worthwhile to compare.

The simulated problem is taken from [128, 135], where it served for demonstration of the developed ray-tracing codes on low order computational meshes. It involves a laser with wavelength $\lambda_L = 1.315\,\mu\text{m}$, corresponding the fundamental frequency of an iodine laser, which impinges a solid aluminium target from the right. The spatial and temporal profiles are idealized as Gaussian with FWHM 400 ps in time with an identical offset and focal spot size 100 µm. The peak intensity is $1.2 \cdot 10^{15}\,\text{W/cm}^2$ at the central axis and p polarization of the laser is assumed. The simulated part of the target has size $40\,\mu\text{m} \times 30\,\mu\text{m}$ and the frontal surface is aligned with the coordinate $x = 0$. It is covered by the computational mesh with 30×20 elements with geometric factor 0.88 along the x axis. The main difference from the original problem is given by usage of the quadratic/cubic finite elements, where the mapping to the low-order refined mesh for the ray-tracing is performed according to chapter 11.3.1. The additional refinement

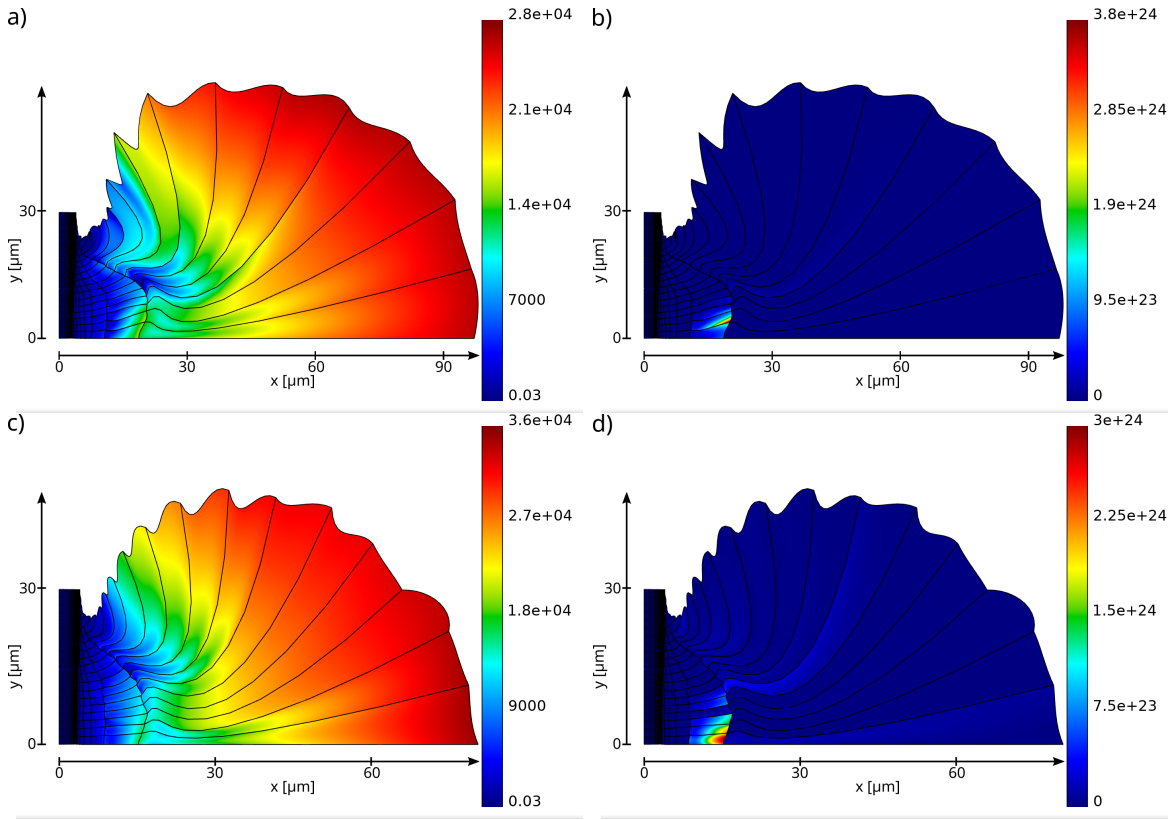

Figure 30: Comparison of the ray-tracing (a,b) and WKB method (c,d) at time $t = 320\,\mathrm{ps}$: a,c) temperature [eV] and b,d) absorbed laser power [erg/cm^3/s].

factor is set to 4, meaning that 12×12 piecewise-constant finite elements are used for a single high-order element. The rays are distributed uniformly over the transverse distance of 1.5 FWHM with 10 rays per each frontal surface edge, giving 2400 rays in total. For simplicity, the ideal gas equation of state with the full ionization is used as in the references. The hydrodynamic scheme employs the RK2-Average scheme with the CFL constant $C_{CFL} = 0.25$ and the full eigenvector decomposition tensor viscosity with the coefficients $C_{lin} = 0.5$ and $C_{quad} = 2.0$. In addition, the heat diffusion model is used with the harmonic heat flux limitation and the limiting fraction $f_{lim} = 0.05$. Unlike other problems presented here, only the single-temperature approach is followed.

The numerical results obtained with the ray-tracing model and the WKB method are compared in Figure 30. The overall shapes and distributions of the temperature are very similar in both cases. Though, certain differences exist between the models. Mainly, the ray-tracing expands the plasma more than the WKB model does. The reason can be seen in the plots of the absorbed power, which show that the dominant mechanism of laser absorption is absorption at the critical plane, as expected from the infra-red laser wavelength and the low associated critical density ($n_c = 6.45{\cdot}10^{20}\,\mathrm{cm}^{-3}$). In other words, the beam crosses the low-density plasma and reaches the critical point before being attenuated by the inverse Bremsstrahlung. The ray-tracing reduces the absorbed fraction by the Fresnel coefficient of reflection, but it is insignificant for the normal incidence and a continuous medium. A difference could appear at the very

beginning of the simulation, when the frontal cell is over-dense and all power is absorbed at the interface with vacuum. It should be noted such sharp vacuum boundary is only a numerical idealization due to finite sizes of the cells and absence of a pre-pulse, which justifies the technique. After the first low-order mesh cell is burned through, the interaction is very similar within both methods. Though, the internal reflections and refraction tends to deposit the energy slightly more to the outer cells, which leads to the more expanded corona. However, the temperatures are higher in the case of the WKB method, which indicates approximately same absorbed energy over time in both simulations, which is only confined in different volumes. Also the peaks of the absorbed power differ in their maxima and sizes, but the shapes vary dynamically and the total power is again approximately identical in both cases.

The simulation of the interaction between an iodine laser and a solid target confirmed viability of the method remapping between high-order and low-order refined finite elements for purposes of the ray-tracing. Moreover, it showed convergence of both methods to a single solution, where only subtle differences exist, which can be primarily attributed to the richer physical model of laser propagation and absorption in the case of the ray-tracing method.

13.2 Spontaneous magnetic fields

Even without an external magnetic field, strong magnetic fields may emerge in plasma. Chapter 3.1 described the Biermann battery process from the physical perspective, while its numerical modelling within the MHD code was summarized in chapter 8.3.1. In essence, the process is responsible for generation of localized magnetic fields even in quasi-neutral plasmas. The only physical condition is misalignment of the density and temperature gradients in the plasma, which can occur due to non-convective transport mechanisms. Even in the context of a laser–target interaction, mega-gauss magnetic fields can be achieved [76, 203]. Approximately toroidal fields are formed above the target surface in the cusp of the plasma plume or at the front of the shock wave propagating into the target [204]. Though, other mechanisms can be equally important, like the generation of the spontaneous fields by a stream of fast electrons generated by the interaction of the laser with the plasma [205]. These species are highly non-collisional, penetrating deep through the plasma column, and induce the resistive return current. The resulting circulation of the currents generates the strong magnetic field. Ideally, the former contribution could be included in the non-local transport models for a self-consistent and predictive modelling of the problem, but the generation processes of the fast electrons on the hydrodynamic scales are poorly understood and the models of non-local transport from chapter 10 were designed rather for an efficient treatment of the super-thermal electrons, not far from the collisional equilibrium. However, a simplified approach was proposed, modelling the species as an external electric current scaled with the laser intensity [206]. Implementation of this model remains a topic of the future work, but early results of the Biermann battery mechanism modelled with the new numerical scheme (chapter 8.3.1) were presented at [207].

A solid aluminium target is considered at the room temperature approximately (0.03 eV). For purposes of demonstration, a laser with wavelength 1 µm irradiates the

target from the right hand side. The spatial and temporal profiles of the laser pulse are Gaussian functions with the spatial FWHM 7.5 µm and temporal FWHM 500 ps. The pulse reaches its peak intensity $1 \cdot 10^{12}$ W/cm^2 at time 500 ps. The narrow focusing implies strong geometric effects, which in turn lead to the circulation of the current and magnetic field generation. Though, it gets to the limit of the optical approximation, as the WKB model of absorption is applied, which presents a certain simplification and the real situation can be more involved, but generation of the spontaneous magnetic field is the main merit of the problem. The computational domain spans over $(0, 2\,\mu\text{m}) \times (0, 10\,\mu\text{m})$ and the central symmetry is assumed. Since the modelling of the Biermann battery with high-order finite elements is under development, only piecewise-constant thermodynamic and magnetic finite elements are used. The elements are not uniformly distributed, but 120 elements with the geometric factors 0.99 are placed along the horizontal axis and 75 with the factor 1.01 vertically. The geometric factors determine the ratio between the size of the next cell compared to the previous. The aim is to refine the mesh at the front surface, where the laser interacts with the target. The simulation is performed in the two-temperature regime, where the models of (isotropic) resistive MHD and electron heat diffusion (with the flux limiter $f_{lim} = 0.1$) are present. The equation of state based on the SESAME tables was used [63, 64].

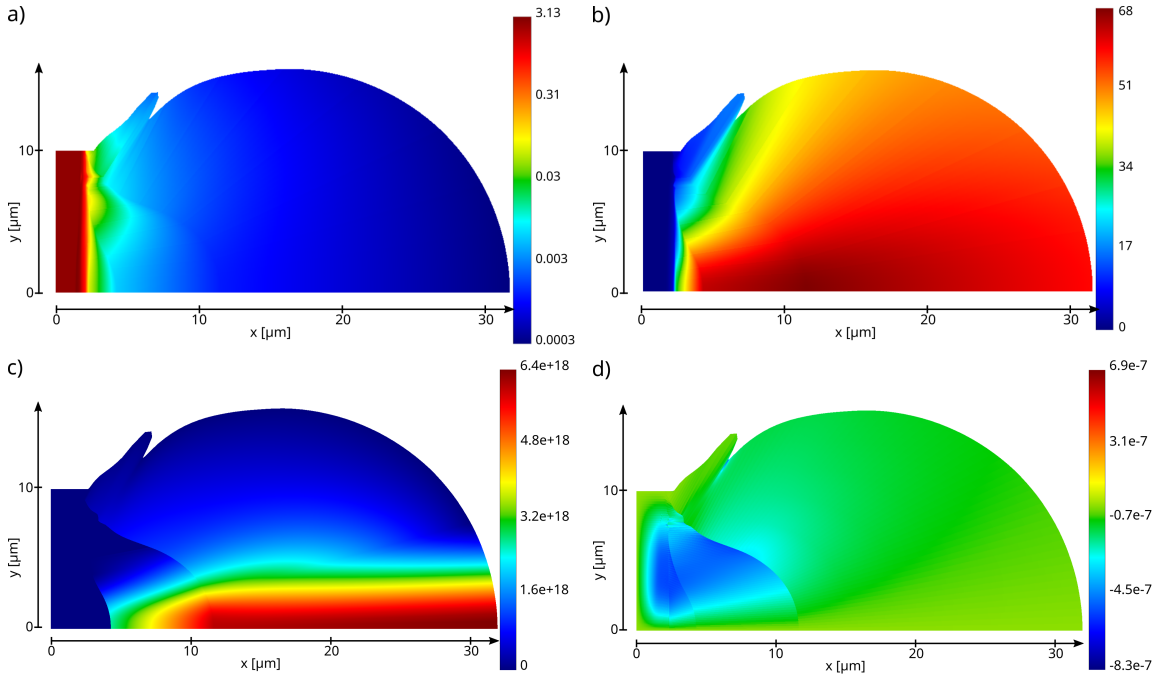

Figure 31: The spatial profiles with active magnetic field generation at time $t = 300$ ps: a) mass density (interpolated) [g/cm^3], b) electron temperature (interpolated) [eV], c) laser intensity [erg/cm^2/s] and d) magnetic field [statT].

The numerical results are presented in Figure 31 for time $t = 300$ ps. The plasma expands in a nearly spherical manner due to the small focal spot. The prevalent density gradient is directed from the target, while the temperature decreases in the direction from the central axis, where the laser is being absorbed. This misalignment

of the gradients generates the magnetic field by the effect of Biermann battery. It is strongest near the surface of the target, but extends in both directions. In the corona, the gradients naturally align as the flow is driven by the pressure gradient, combining both quantities. On the other hand, the high densities in the solid target limit expansion of the fields in that direction, but magnetic diffusion mediated by eddy currents spreads them considerably. Consequently, the fields produced by the shock wave propagating into the target are not visible. Due to the relatively weak power of the laser, the fields do not have the potential to affect the dynamics of the system, as the magnetic pressure $\approx 2.5 \cdot 10^7\,\mathrm{erg/cm^3} \doteq 25\,\mathrm{bar}$ is significantly smaller than the thermal one. Also the magnetization ($\chi \lesssim 10^{-3}$) is not sufficiently high to affect the thermal transport noticeably, which justifies the applied isotropic approximation (see chapter 3.1.1).

The problem demonstrates that even a relatively weak laser can generate notably strong magnetic fields. In this case, the maximal field is $8.3 \cdot 10^{-7}\,\mathrm{statT} \doteq 25\,\mathrm{kG}$, which is in line with the expectations for the given parameters. The fields are not intense enough to affect the dynamics of the system nor the thermal transport to a greater extend, but they have been experimentally measured even for longer laser pulses [208]. Such configurations are relevant, among other applications, to the deposition of thin films studied before [209], where knowledge of the detailed plasma conditions is crucial.

14 Three-dimensional simulations

The multi-dimensional design of most of the numerical methods presented in this work allows even 3D simulations of laser–target interaction. Though, such simulations are demanding in terms of the computational resources required. Therefore, the use is typically limited to the most complex scenarios of the interaction, where the spatial symmetries are broken. In the context of ICF, it can be inhomogeneity of the laser irradiation or of the capsule itself, which in turn generates swirls of the self-generated magnetic field, further degrading the symmetry [210]. However, the pre-pulse physics is simulated with idealized conditions of absolutely flat targets usually and it is rather the effect of spatial confinement of the laser energy for narrow focusing, which plays a role in the interaction. Still, if the laser has an approximately axially symmetric intensity profile, the simulations can be performed in the cylindrical coordinates in 2D. The hydrodynamic scheme based on the high-order curvilinear finite elements can be formulated axisymmetrically [211], but the implementation and extension to the rest of the physical models remains a prospect of the future work.

For the computational demands of 3D simulations, a single problem is presented, designed for demonstration of the code capabilities under typical conditions. An aluminium target at the solid density $\rho_0 = 2.7\,\mathrm{g/cm^3}$ and near room temperature $T_0 = 0.03\,\mathrm{eV}$ is irradiated by a constant laser pulse with the intensity $1 \cdot 10^{14}\,\mathrm{W/cm^2}$, which can be considered as an approximation of the pedestal of an ultra-relativistic laser pulse, for example [34]. The focal spot size is $r_f = 5\,\mu\mathrm{m}$ for the Gaussian radial profile of the laser. For simplicity, the ideal gas equation of state is employed with the full ionization. In addition, the heat diffusion is applied with the flux limiter $f_{lim} = 0.05$. Finally, the computational mesh consists of $4 \times 4 \times 20$ elements from the $T2$ family, which are distributed over the domain $(0, 8\,\mu\mathrm{m}) \times (0, 8\,\mu\mathrm{m}) \times (0, 10\,\mu\mathrm{m})$ with the geometric factor 0.96 in the z direction, i.e. axis of the laser.

The numerical results from the early stage of the interaction are visualized in Figure 32, which were also presented in [163]. The process of laser ablation is clearly visible there, including the launched shock wave, the laser absorption at the critical density and a strong heat transport in its vicinity. Even relatively low number of the interacting finite elements is able to capture the spatial details of the plasma profiles and curvature of the expanding plasma plume. Thanks to the high-order representation of the quantities, a smooth interpolation is performed inside the elements. Also the mesh imprint is relatively small as far as the cylindrical symmetry is considered.

The problem of a laser–target interaction demonstrated the capabilities of the multi-dimensional multi-physics code PETE2 in 3D. Moreover, it showed benefits of the high-order curvilinear finite element treatment of the Lagrangian hydrodynamics for simulations of ablative processes.

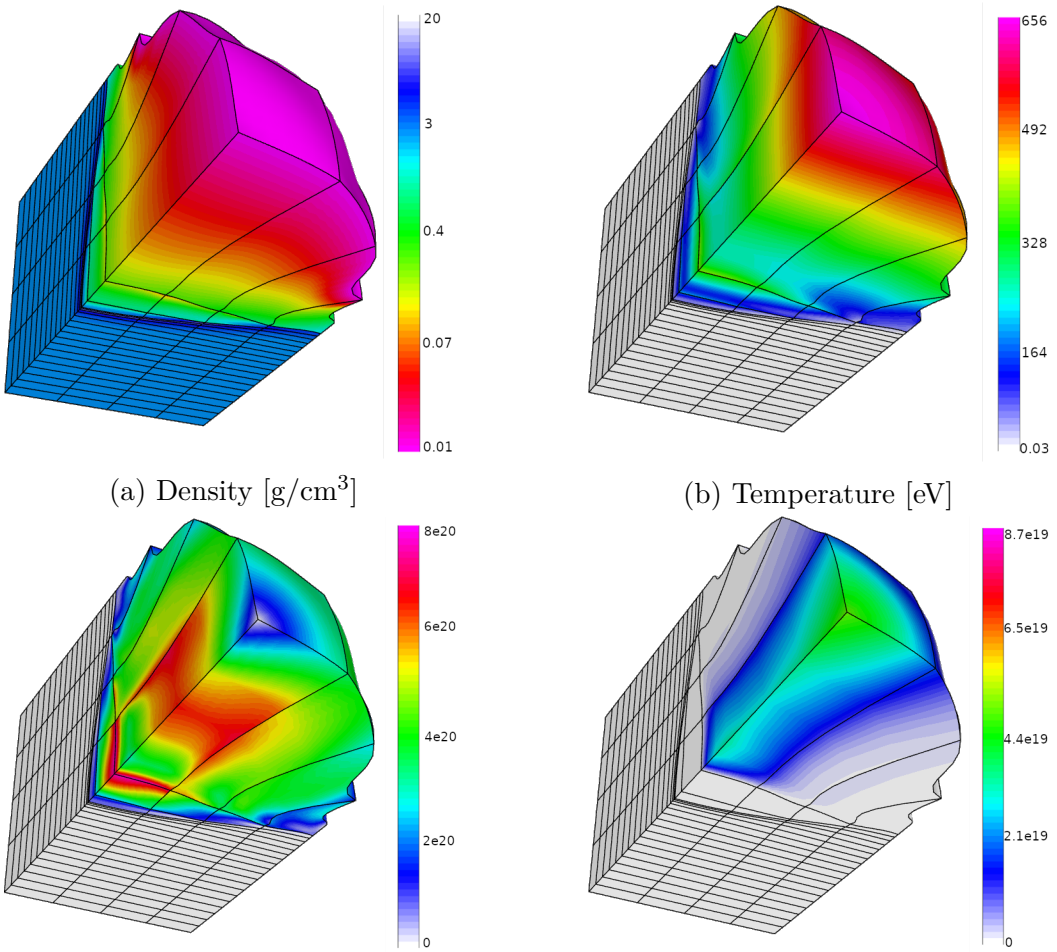

(a) Density [g/cm^3]

(b) Temperature [eV]

(c) Heat flux magnitude [erg/s/cm^2]

(d) Laser intensity [erg/s/cm^2]

Figure 32: Plasma profiles in the 3D simulation of laser–target interaction at time 30 ps. The combination of the quadratic thermodynamic and cubic kinematic finite elements is used. Reprinted from [163].

Conclusions

The non-local transport of energy in laser plasma is a complex phenomenon, which is not limited only to electrons, but also entails coherent and incoherent radiation, for example. The species can be called non-local whenever their mean free path exceeds the characteristic length of the local variations. Freed of the collisions/absorption events, they can transport energy from the point of their origin on vast distances relatively to the local conditions. Various attempts have been made to accurately, yet efficiently capture the behaviour of the non-local species over the course of the past decades. Though, the challenges associated with the description of non-locality are not only on the side of the physical description, but also arise in the numerical modelling of the transport. The non-locality changes the fundamental structure of the equations from the parabolic diffusion to hyperbolic advection, which renders the efficient and stable convection solvers honed over time completely inapplicable or inefficient at least. It is also the increasing anisotropy and non-linearity of the models associated with the non-locality, which foils the efforts for straightforward integration of this kind of transport to the existing methods. Therefore, a change of the paradigm is unavoidable from the theoretical basis to the numerical solution.

The first part of this work laid the theoretical groundwork for the particular methods presented later on. The fundamental principles of the kinetic theory were covered in chapter 1, describing plasma in an unmatched detail. However, solution in the full phase space is infeasible, as it poses a 7D problem in general. Hence, the model was reduced to the hydrodynamic framework described in chapter 2, where the simplifying assumption of the kinetic equilibrium was made. This procedure eliminated the notion of non-locality from the description completely, as only the convective processes are present in the ideal hydrodynamics. The topic of chapter 3 was then to reintroduce the heat transport processes. At first, it was achieved by allowing only infinitesimal deviations from the equilibrium in the classical diffusive paradigm of chapter 3.1. The additional models of non-local electron transport in chapters 3.2–3.3 partially borrowed from the kinetic description again, but only in a limited extent to retain feasibility of the methods. Along the same lines, also the radiation transport description continued and a good analogy between the descriptions of both species, electrons and photons, was recognized, which underpinned construction of some of the methods at hand. The laser absorption modelling described in chapter 5 circumvented the problem of the unresolved high-frequency fields by formulation of the closure models for the electromagnetic energy flux vector (Poynting vector), which reduced the laser model to a mere energy source from the hydrodynamical point of view. The optical approximation in chapter 5.1 separated the envelope from the phase completely. However, the assumptions of the slowly varying envelope break down in the vicinity of the resonant points like the critical density in the context of laser plasma. This was addressed by the wave-based method of chapter 5.2, but only in a single dimension, making the methods complementary in essence.

The second part presented the design and construction of the numerical methods devised for solution of the physical models from the part first. Chapter 6 established the framework of the finite element method, which is applied in most of the cases thanks to

its versatility and scalability to high orders of convergence. Chapter 7 returned to the kinetic modelling, but the description was reduced to the Cartesian tensor expansion up to the first order, making the approach feasible even in multiple dimensions. The implicit formulation provided the method overall robustness and stability. The finite element construction then offered an arbitrary order of convergence in space, while maintaining conservation of mass and energy. Despite the undoubted detail of the Vlasov–Fokker–Planck–Maxwell method in description of electrons, motion of ions was not encompassed anyhow, limiting the use cases to those dominated by thermal transport. In contrast, chapter 8 summarized construction of the magneto-hydrodynamic code PETE2, which models the flows of matter in a magnetic field. The Lagrangian nature of the method was ideally matched by the curvilinear finite elements, providing also an arbitrary order of convergence in space, while conserving mass, momentum, magnetic flux and total energy at the same time. Since the idealized MHD does not include any transport processes other than convection, complementary closure models are needed. Therefore, the diffusion of electron heat and non-equilibrium radiation diffusion closures were constructed in chapter 9. As already accustomed, high orders of convergence were attained with the finite elements, while maintaining (local) energy conservation. The notion of non-locality was then introduced to the transport in chapter 10, where the discrete ordinates method for electrons and photons is numerically solved by finite elements in space and angles. This combination offered smooth interpolation in both domains and provided the method high rates of convergence, but exact conservation of energy was not respected by the original design and remains a prospect of the future work. In any case, the implicit treatment of the coupling with matter reduced the need of the source iterations, making the methods more feasible in the context of hydrodynamic simulations. Finally, the techniques of laser absorption, which fuel all the transport mechanisms essentially, were briefly summarized in chapter 11. The most accurate physical picture was provided by the method based on the stationary Maxwell's equations, which can self-consistently describe the reflection and absorption in the vicinity of the critical point in terms of the wave optics with up to the second order of convergence semi-analytically or with even higher orders differentially, but resolution of the laser wavelength was required. Unfortunately, the underlying decomposition of the waves was possible only in 1D, leaving the laser absorption in multiple dimensions on the WKB and ray-tracing methods. Both rely on the optical approximation, but a grid-based formulation was retained in the case of the WKB method due to absence of refraction, where the high-order discontinuous finite elements could be employed. Oppositely, the ray-tracing solved the propagation with internal refractions along the characteristics, which are the trajectories of the rays essentially. The coupling with the curvilinear finite element MHD code was then enabled by the mapping between the high-order elements and low-order refined ones.

The last, third part was dedicated to simulations under realistic conditions. The single-dimensional problems in chapter 12 allowed to study the processes of radiation transfer and electron heat transport in detail. The former showed an agreement between the methods to certain extent, but the distribution of the fluxes is not fully self-consistent as long as the flux-limited diffusion approach is applied. Even the slight difference in the fluxes in the case of the non-local model notably affected the conduc-

tion zone and corona. A similar effect was observed for the electron heat transport on a substantially smaller scale more typical for electrons. However, the non-physical behaviour of the BGK model in the corona afflicted the simulations, which is given by the loss of the information about the spectral distribution of the species. This analysis was confirmed by the kinetic model, resolving fully velocities of the transported species. No such spurious fluxes to the corona were observed and rather a stronger flux towards the target appeared in the results with an indication the non-local species contributing to it. This conclusion underpins efforts in construction of a non-local transport method more closely related to the kinetic foundations, while remaining efficient and feasible for large-scale hydrodynamic simulations. The P1/M1 model from chapter 3.2 represents such approach, which can be seen as the quasi-neutral limit of the reduced VFPM model enhanced by the entropy maximizing closure. Though, the truncation of the distribution function expansion is related to a destabilizing effect of the electric field [212]. Therefore, a careful numerical treatment must be devised, which remains a topic of the future research.

The two-dimensional simulations in chapter 13 focused on problems involving geometric effects, mainly related to the laser absorption and generation of the spontaneous magnetic fields. The importance of the laser absorption is given by the fact it drives the formation of the plasma and most of the non-local species are produced by a direct laser–plasma interaction or by the steep slope of temperature in the vicinity of the critical plane, where the power of the laser is deposited. A comparison of the methods for laser propagation and absorption is then desirable. The WKB and the mapped ray-tracing methods were examined, where only minor differences were found between the two, confirming their common basis. The latter slightly more favoured absorption further away from target, which can be attributed to the reflections and refraction in the plasma. Even such a minor detail can have consequences for the non-local transport of energy by means of super-thermal electrons or radiation, which may not penetrate deep enough to the target to preheat it in front of the shock wave, for example. Experimental monitoring of such internal interfaces is challenging, but the method of resonant small-angle X-ray scattering can reveal these effects [213]. The second problem under consideration was generation of spontaneous magnetic fields by the Biermann battery effect. The simulation showed this inherently non-linear and numerically cumbersome process can be modelled and relatively strong magnetic fields are generated even for weaker laser pulses. For higher laser intensities, even stronger magnetic fields on the megagauss level can be expected with implications for the thermal transport in ICF targets [77, 78]. The induced anisotropy inhibits the transport across the field lines classically or collimates the hot species [214].

Finally, the three-dimensional simulation in chapter 14 demonstrated capabilities of the Lagrangian code in more dimensions, including the diffusion transport. Though, such simulations are the most expensive computationally and their usage is designated to the most complex geometries typically. Such situations may appear in the context of ICF or narrow focusing in the interaction of a laser with a planar target and effects of the polarization. Even when the process remains mostly axisymmetric within the hydrodynamic modelling, our earlier studies pointed to emergence of a strong filamentation in particle-in-cell simulations of an ultra-relativistic laser pulse interacting with

the macroscopically modelled density plateau formed by the laser pedestal, where the non-local transport is important due to sensitivity of the process to the exact plasma conditions [34, 35]. Later, we proposed the concept of a plasma shutter preventing the detrimental interaction of the pedestal with the main target. Not only the contrast is enhanced, but also a narrower focusing is achieved by means of linear and non-linear plasma optics [215], improving the laser ion acceleration as one of the major applications [216, 217, 218].

In conclusion, our research contributed to investigation of various aspects of the non-local transport of energy in laser plasma, which cannot be narrowed to a single simplistic model. Moreover, an increased physical realism and resolution is needed from other involved methods to capture the delicate nature of the kinetic effects. For this reason, new numerical tools have been developed for high-order modelling of the underlying magnetohydrodynamics, driving laser absorption and the actual radiation and thermal transports with a dedicated kinetic code serving as a reference. Shifting the frontiers of the numerical modelling in multiple ways, the final goal of a robust, yet efficient description of the non-locality manifested in all its aspects is closer than ever before.

Being this said, more directions of the future work are opened rather than definitely closed. The kinetic r-VFPM model would benefit from a high-order treatment in the velocity domain, while maintaining the conservation of energy. The simulations in a solid material then pointed to the need of a modification of the collision operator for such environments. Also ion motion could be introduced to the model through coupling with a hydrodynamic code. Finally, the modelling of the electrons could be enhanced by a particle code to treat highly-energetic and nearly collision-less species. Also the magneto-hydrodynamic code can be further extended in multiple ways. The modelling of laser–target interaction would definitely benefit from the axisymmetric formulation, as most lasers in the laboratories posses this symmetry, except dedicated applications, like X-ray plasma sources or ICF. An Arbitrary Eulerian-Lagrangian (ALE) extension would then provide robustness to the Lagrangian simulations [193], smoothing the computational mesh when needed, similarly to the other codes we contributed to [170, 171, 219]. However, the Eulerian flows open the problem of mixing multiple materials, which must be addressed specifically [220]. Finally, the model of the Biermann battery effect for high-order elements is one of the nearest goals. However, such strong magnetic fields are also associated with anisotropy of the transport, where the diffusion models must be revised. Also the radiation diffusion and non-local radiation transfer can be extended to the multi-group model and integrated with an opacity code. The non-local models can further benefit from the conserving weak formulation for the discontinuous finite elements. In the case of the electron heat transport, the aforementioned direction of the P1/M1 model is especially promising. However, the full non-local magnetohydrodynamics must face the same challenges associated with the increasing anisotropy in magnetic fields as the diffusive approximation. Finally, the methods of laser absorption can be improved. The WKB model can be formulated in a conserving way and the wave-based method could enhance the ray-tracing model in the vicinity of the critical plane.

List of publications

Journal papers

[1] M. Matys, S. V. Bulanov, M. Kucharik, M. Jirka, **J. Nikl**, M. Kecova, J. Proska, J. Psikal, G. Korn and O. Klimo. Plasma shutter for improved heavy ion acceleration by ultra-intense laser pulses. *New Journal of Physics*, 2022. Submitted.

[2] **J. Nikl**, M. Kuchařík and S. Weber. High-order curvilinear finite element magneto-hydrodynamics I: A conservative Lagrangian scheme. *Journal of Computational Physics*, page 111158, 2022. doi:10.1016/j.jcp.2022.111158. In press.

[3] L. Gaus, L. Bischoff, M. Bussmann, E. Cunningham, C. B. Curry, J. E, E. Galtier, M. Gauthier, A. L. García, M. Garten, S. Glenzer, J. Grenzer, C. Gutt, N. J. Hartley, L. Huang, U. Hübner, D. Kraus, H. J. Lee, E. E. McBride, J. Metzkes-Ng, B. Nagler, M. Nakatsutsumi, **J. Nikl**, M. Ota, A. Pelka, I. Prencipe, L. Randolph, M. Rödel, Y. Sakawa, H.-P. Schlenvoigt, M. Šmíd, F. Treffert, K. Voigt, K. Zeil, T. E. Cowan, U. Schramm and T. Kluge. Probing ultrafast laser plasma processes inside solids with resonant small-angle x-ray scattering. *Physical Review Research*, 3(4):043194, 2021. doi:10.1103/PhysRevResearch.3.043194.

[4] **J. Nikl**, I. Göthel, M. Kuchařík, S. Weber and M. Bussmann. Implicit reduced Vlasov–Fokker–Planck–Maxwell model based on high-order mixed elements. *Journal of Computational Physics*, 434:110214, 2021. doi:10.1016/j.jcp.2021.110214.

[5] J. Limpouch, V. Tikhonchuk, J. Dostal, R. Dudzak, M. Krupka, N. Borisenko, **J. Nikl**, A. Akunets, L. Borisenko and V. Pimenov. Characterization of the homogenization time of a plasma created by laser ionization of a low-density foam. *Plasma Physics and Controlled Fusion*, 62(3):035013, 2020. doi:10.1088/1361-6587/ab6b4d.

[6] **J. Nikl**, M. Kuchařík, J. Limpouch, R. Liska and S. Weber. Wave-based laser absorption method for high-order transport–hydrodynamic codes. *Advances in Computational Mathematics*, 45(4):1953–1976, 2019. doi:10.1007/s10444-019-09671-3.

[7] R. Lokasani, H. Kawasaki, Y. Shimada, M. Shoji, K. Anraku, T. Ejima, T. Hatano, W. Jiang, S. Namba, **J. Nikl**, M. Zeman, G. O'Soullivan, T. Higashiguchi and J. Limpouch. Soft X-ray spectral analysis of laser produced molybdenum plasmas using fundamental and second harmonics of a Nd:YAG laser. *Optics Express*, 27(23):33351–33358, 2019. doi:10.1364/OE.27.033351.

[8] **J. Nikl**, M. Holec, M. Zeman, M. Kuchařík, J. Limpouch and S. Weber. Macroscopic laser-plasma interaction under strong non-local transport conditions for coupled matter and radiation. *Matter and Radiation at Extremes*, 3:110–126, 2018. doi:10.1016/j.mre.2018.03.001.

[9] M. Holec, **J. Nikl** and S. Weber. Nonlocal transport hydrodynamic model for laser heated plasmas. *Physics of Plasmas*, 25(3):032704, 2018. doi:10.1063/1.5011818.

[10] M. Holec, **J. Nikl**, M. Vranic and S. Weber. The effect of pre-plasma formation under nonlocal transport conditions for ultra-relativistic laser-plasma interaction. *Plasma Physics and Controlled Fusion*, 60(4):044019, 2018. doi: 10.1088/1361-6587/aab05a.

Proceedings

[1] M. Kucharik, **J. Nikl** and J. Limpouch. Second-order magnetic field generation model for Lagrangian and ALE plasma simulations. In *International Conference of Numerical Analysis and Applied Mathematics ICNAAM 2021*, AIP Conference Proceedings. 2021. Accepted.

[2] **J. Nikl**, M. Kuchařík and S. Weber. Self-generated magnetic fields modelling within high-order Lagrangian magneto-hydrodynamics. In *Europhysics Conference Abstracts – 47th EPS Conference on Plasma Physics*, page P1.2022. European Physical Society, 2021.

[3] M. Kucharik, J. Limpouch and **J. Nikl**. Development of ALE hydrodynamic code for laser-plasma interactions with self-generated magnetic fields. In *Europhysics Conference Abstracts – 47th EPS Conference on Plasma Physics*, page P1.2020. European Physical Society, 2021.

[4] M. Matys, M. Kecova, M. Kucharik, **J. Nikl**, S. V. Bulanov, M. Jirka, P. Janecka, J. Psikal, G. Korn, J. Grosz and O. Klimo. Laser-driven ion acceleration enhancementusing silicon nitride plasma shutter. In *Europhysics Conference Abstracts – 47th EPS Conference on Plasma Physics*, page P3.2026. European Physical Society, 2021.

[5] **J. Nikl**, M. Jirka, M. Matys, M. Kuchařík and O. Klimo. Contrast enhancement of ultra-intense laser pulses by relativistic plasma shutter. In J. Hein, T. J. Butcher, P. Bakule, C. L. Haefner, G. Korn and L. O. Silva, editors, *High Power Lasers and Applications*, volume 11777 of *Proc. of SPIE*, page 117770X. 2021. doi:10.1117/12.2589245.

[6] M. Matys, S. V. Bulanov, M. Kecova, M. Kucharik, M. Jirka, P. Janecka, J. Psikal, **J. Nikl**, J. Grosz, G. Korn and O. Klimo. Ion acceleration enhancement by laser-pulse shaping via plasma shutter. In S. S. Bulanov, J. Schreiber and C. B. Schroeder, editors, *Laser Acceleration of Electrons, Protons, and Ions VI*, volume 11779 of *Proc. of SPIE*, page 117790Q. 2021. doi:10.1117/12.2589096.

[7] **J. Nikl**, M. Kuchařík and S. Weber. Lagrangian magneto-hydrodynamics based on curvilinear finite elements. In *14th WCCM-ECCOMAS Congress*. CIMNE, 2021. doi:10.23967/wccm-eccomas.2020.186.

[8] **J. Nikl**, M. Jirka, M. Kuchařík, M. Holec, M. Vranic and S. Weber. The effect of pre-plasma formed under the non-local transport conditions on the interaction of the ultra-high intensity laser with a solid target. In *Research using Extreme Light:*

Entering New Frontiers with Petawatt-Class Lasers IV, volume 11039 of *Proc. of SPIE*, page 110391E. 2019. doi:10.1117/12.2522450.

[9] **J. Nikl**, M. Kuchařík and S. Weber. Modelling of the non-local transport of energy in laser plasmas with high-order numerical methods. In *Europhysics Conference Abstracts – 46th EPS Conference on Plasma Physics*, volume 43C, page P5.2010. European Physical Society, 2019. ISBN 979-10-96389-11-7.

[10] M. Kuchařík, J. Limpouch, R. Liska and **J. Nikl**. Hydrodynamic simulations of laser/plasma interactions via ALE methods. In *Europhysics Conference Abstracts – 46th EPS Conference on Plasma Physics*, volume 43C, page P5.2009. European Physical Society, 2019. ISBN 979-10-96389-11-7.

[11] **J. Nikl**, M. Kuchařík, M. Holec and S. Weber. Curvilinear high-order Lagrangian hydrodynamic code for the laser-target interaction. In S. Coda, J. Berndt, G. Lapenta, M. Mantsinen, C. Michaut and S. Weber, editors, *Europhysics Conference Abstracts – 45th EPS Conference on Plasma Physics*, volume 42A, page P1.2019. European Physical Society, 2018. ISBN 979-10-96389-08-7.

References

[1] H. Lorentz. The motion of electrons in metallic bodies I. *KNAW, Proceedings*, 7:438, 1905.

[2] S. Chapman. VI. On the law of distribution of molecular velocities, and on the theory of viscosity and thermal conduction, in a non-uniform simple monatomic gas. *Philosophical Transactions of the Royal Society of London. Series A, Containing Papers of a Mathematical or Physical Character*, 216(538-548):279–348, 1916. doi:10.1098/rsta.1916.0006.

[3] L. D. Landau. Kinetic equation for the Coulomb effect. *Physikalische Zeitschrift der Sowjetunion*, 10:154, 1936.

[4] S. Chandrasekhar. Dynamical friction I. General considerations: the coefficient of dynamical friction. *Astrophysical Journal*, 97:255, 1943. doi:10.1086/144517.

[5] T. G. Cowling. The electrical conductivity of an ionized gas in a magnetic field, with applications to the solar atmosphere and the ionosphere. *Proceedings of the Royal Society of London. Series A. Mathematical and Physical Sciences*, 183(995):453–479, 1945. doi:10.1098/rspa.1945.0013.

[6] R. S. Cohen, L. Spitzer and P. M. Routly. The electrical conductivity of an ionized gas. *Physical Review*, 80(2):230–238, 1950. doi:10.1103/PhysRev.80.230.

[7] L. Spitzer and R. Härm. Transport phenomena in a completely ionized gas. *Physical Review*, 89(5):977–981, 1953. doi:10.1103/PhysRev.89.977.

[8] S. I. Braginskii. Transport processes in a plasma. *Reviews of Plasma Physics*, 1:205–311, 1965.

[9] M. N. Rosenbluth, W. M. MacDonald and D. L. Judd. Fokker-planck equation for an inverse-square force. *Physical Review*, 107(1):1–6, 1957. doi:10.1103/PhysRev.107.1.

[10] J. M. Dawson. On the production of plasma by giant pulse lasers. *Physics of Fluids*, 7(7):981, 1964. doi:10.1063/1.1711346.

[11] R. C. Malone, R. L. McCrory and R. L. Morse. Indications of strongly flux-limited electron thermal conduction in laser-target experiments. *Physical Review Letters*, 34(12):721–724, 1975. doi:10.1103/PhysRevLett.34.721.

[12] D. Gray and J. D. Kilkenny. The measurement of ion acoustic turbulence and reduced thermal conductivity caused by a large temperature gradient in a laser heated plasma. *Plasma Physics*, 22:81–111, 1980. doi:10.1088/0032-1028/22/2/001.

[13] T. H. Kho and D. J. Bond. Application of a moment method to calculation of heat flow in a plasma with a Fokker-Planck collision term. *Journal of Physics D: Applied Physics*, 14(8):L117–L119, 1981. doi:10.1088/0022-3727/14/8/001.

[14] J. P. Matte and J. Virmont. Electron heat transport down steep temperature gradients. *Physical Review Letters*, 49(26):1936–1939, 1982. doi:10.1103/PhysRevLett.49.1936.

[15] J. F. Luciani, P. Mora and J. Virmont. Nonlocal heat transport due to steep temperature gradients. *Physical Review Letters*, 51(18):1664–1667, 1983. doi:10.1103/PhysRevLett.51.1664.

[16] A. Bendib, J. F. Luciani and J. P. Matte. An improvement of the nonlocal heat flux formula. *Physics of Fluids*, 31(4):711, 1988. doi:10.1063/1.866806.

[17] M. K. Prasad and D. S. Kershaw. Nonviability of some nonlocal electron heat transport modeling. *Physics of Fluids B: Plasma Physics (1989-1993)*, 1(12):2430–2436, 1989. doi:10.1063/1.859178.

[18] G. P. Schurtz, P. D. Nicolaï and M. Busquet. A nonlocal electron conduction model for multidimensional radiation hydrodynamics codes. *Physics of Plasmas*, 7(10):4238, 2000. doi:10.1063/1.1289512.

[19] D. Del Sorbo, J.-L. Feugeas, P. Nicolaï, M. Olazabal-Loumé, B. Dubroca, S. Guisset, M. Touati and V. Tikhonchuk. Reduced entropic model for studies of multidimensional nonlocal transport in high-energy-density plasmas. *Physics of Plasmas*, 22(8):082706, 2015. doi:10.1063/1.4926824.

[20] M. Holec, J. Nikl and S. Weber. Nonlocal transport hydrodynamic model for laser heated plasmas. *Physics of Plasmas*, 25(3):032704, 2018. doi:10.1063/1.5011818.

[21] D. Fridrich, R. Liska and B. Wendroff. Cell-centered Lagrangian Lax–Wendroff HLL hybrid method for elasto-plastic flows. *Computers & Fluids*, 157:164–174, 2017. doi:https://doi.org/10.1016/j.compfluid.2017.08.030.

[22] M. L. Wilkins. *Methods in Computational Physics*, volume 3, chapter Calculation of Elastic-Plastic Flow. Academic Press, 1964.

[23] E. Caramana, D. Burton, M. Shashkov and P. Whalen. The construction of compatible hydrodynamics algorithms utilizing conservation of total energy. *Journal of Computational Physics*, 146(1):227–262, 1998. doi:10.1006/jcph.1998.6029.

[24] D. E. Burton. Conservation of energy, momentum, and angular momentum in Lagrangian staggered-grid hydrodynamics. Technical Report UCRL-JC-105926, Lawrence Livermore National Laboratory, Livermore, CA, 1990.

[25] V. Dobrev, Tz. Kolev and R. Rieben. High-order curvilinear finite element methods for lagrangian hydrodynamics. *SIAM Journal on Scientific Computing*, 34(5):B606–B641, 2012. doi:10.1137/120864672.

[26] R. Abgrall and S. Tokareva. Staggered grid residual distribution scheme for Lagrangian hydrodynamics. *SIAM Journal on Scientific Computing*, 39(5):A2317–A2344, 2017. doi:10.1137/16M1078781.

[27] J. P. Brodrick, R. J. Kingham, M. M. Marinak, M. V. Patel, A. V. Chankin, J. T. Omotani, M. V. Umansky, D. Del Sorbo, B. Dudson, J. T. Parker, G. D. Kerbel, M. Sherlock and C. P. Ridgers. Testing nonlocal models of electron thermal conduction for magnetic and inertial confinement fusion applications. *Physics of Plasmas*, 24(9), 2017. doi:10.1063/1.5001079.

[28] T. Z. Esirkepov, J. K. Koga, A. Sunahara, T. Morita, M. Nishikino, K. Kageyama, H. Nagatomo, K. Nishihara, A. Sagisaka, H. Kotaki, T. Nakamura, Y. Fukuda, H. Okada, A. S. Pirozhkov, A. Yogo, M. Nishiuchi, H. Kiriyama, K. Kondo, M. Kando and S. V. Bulanov. Prepulse and amplified spontaneous emission effects on the interaction of a petawatt class laser with thin solid targets. *Nuclear Instruments and Methods in Physics Research, Section A: Accelerators, Spectrometers, Detectors and Associated Equipment*, 745:150–163, 2014. doi: 10.1016/j.nima.2014.01.056.

[29] M. Zhao, A. Chankin and D. Coster. Kinetic simulations of electron heat flux in the scrape-off layer. *Nuclear Materials and Energy*, 12:819–824, 2017. doi: 10.1016/j.nme.2017.01.025.

[30] K. Falk, M. Holec, C. J. Fontes, C. L. Fryer, C. W. Greeff, H. M. Johns, D. S. Montgomery, D. W. Schmidt and M. Šmíd. Measurement of preheat due to nonlocal electron transport in warm dense matter. *Physical Review Letters*, 120(2):1–5, 2018. doi:10.1103/PhysRevLett.120.025002.

[31] V. Tikhonchuk. Physics of laser plasma interaction and particle transport in the context of inertial confinement fusion. *Nuclear Fusion*, 59(3):032001, 2019. doi:10.1088/1741-4326/aab21a.

[32] D. Batani, S. Baton, A. Casner, S. Depierreux, M. Hohenberger, O. Klimo, M. Koenig, C. Labaune, X. Ribeyre, C. Rousseaux, G. Schurtz, W. Theobald and V. Tikhonchuk. Physics issues for shock ignition. *Nuclear Fusion*, 54(5):054009, 2014. doi:10.1088/0029-5515/54/5/054009.

[33] P. Nicolaï, J. L. Feugeas, T. Nguyen-Bui, V. Tikhonchuk, L. Antonelli, D. Batani and Y. Maheut. Effect of nonthermal electrons on the shock formation in a laser driven plasma. *Physics of Plasmas*, 22(4), 2015. doi:10.1063/1.4917472.

[34] M. Holec, J. Nikl, M. Vranic and S. Weber. The effect of pre-plasma formation under nonlocal transport conditions for ultra-relativistic laser-plasma interaction. *Plasma Physics and Controlled Fusion*, 60(4):044019, 2018. doi: 10.1088/1361-6587/aab05a.

[35] J. Nikl, M. Jirka, M. Kuchařík, M. Holec, M. Vranic and S. Weber. The effect of pre-plasma formed under the non-local transport conditions on the interaction of the ultra-high intensity laser with a solid target. In *Research using Extreme Light: Entering New Frontiers with Petawatt-Class Lasers IV*, volume 11039 of *Proceedings of SPIE*, page 110391E. 2019. doi:10.1117/12.2522450.

[36] P. Velarde, D. García-Senz, E. Bravo, F. Ogando, A. Relaño, C. García and E. Oliva. Interaction of supernova remnants: From the circumstellar medium to the terrestrial laboratory. *Physics of Plasmas*, 13:092901, 2006. doi:10.1063/1.2338281.

[37] R. L. Liboff, R. S. Berry, J. L. Birman and H. E. Stanley. *Kinetic Theory: Classical, Quantum, and Relativistic Descriptions*. Graduate Texts in Contemporary Physics. Springer-Verlag, third edition edition, 2003. ISBN 0-387-95551-8. doi:10.1007/b97467.

[38] N. N. Bogoliubov. Problems of a dynamical theory in a statistical physics. In J. DeBoer and G. E. Uhlenbeck, editors, *Studies in Statistical Mechanics*. North-Holland, 1962.

[39] I. P. Shkarofsky, T. W. Johnston and M. P. Bachynski. *The particle kinetics of plasmas*. Addison-Wesley, London, 1966.

[40] P. Kulhánek. *Úvod do teorie plazmatu*. AGA, 2011.

[41] P. Degond and B. Lucquin-Desreux. The Fokker-Planck asymptotics of the Boltzmann collision operator in the Coulomb case. *Mathematical Models and Methods in Applied Sciences*, 02(02):167–182, 1992. doi:10.1142/S0218202592000119.

[42] T. J. Boyd, T. J. M. Boyd and J. J. Sanderson. *The physics of plasmas*. Cambridge University Press, 2003. ISBN 0521452902.

[43] P. Mulser and D. Bauer. *High Power Laser-Matter Interaction*, volume 238 of *Springer Tracts in Modern Physics*. Springer Berlin Heidelberg, 2010. ISBN 978-3-540-50669-0. doi:10.1007/978-3-540-46065-7.

[44] Y. T. Lee and R. M. More. An electron conductivity model for dense plasmas. *Physics of Fluids*, 27(5):1273, 1984. doi:10.1063/1.864744.

[45] N. J. Fisch. Theory of current drive in plasmas. *Reviews of Modern Physics*, 59:175–234, 1987. doi:10.1103/RevModPhys.59.175.

[46] J. R. Albritton, E. A. Williams, I. B. Bernstein and K. P. Swartz. Nonlocal electron heat transport by not quite Maxwell-Boltzmann distributions. *Physical Review Letters*, 57(15):1887–1890, 1986. doi:10.1103/PhysRevLett.57.1887.

[47] P. L. Bhatnagar, E. P. Gross and M. Krook. A model for collision processes in gases. I. Small amplitude processes in charged and neutral one-component systems. *Physical Review*, 94(3):511–525, 1954. doi:10.1103/PhysRev.94.511.

[48] W. Manheimer, D. Colombant and A. Schmitt. Analytic insights into nonlocal energy transport. I. Krook models. *Physics of Plasmas*, 25(8):082711, 2018. doi:10.1063/1.5039530.

[49] W. Manheimer, D. Colombant and V. Goncharov. The development of a Krook model for nonlocal transport in laser produced plasmas. I. Basic theory. *Physics of Plasmas*, 15(8):1–10, 2008. doi:10.1063/1.2963078.

[50] T. W. Johnston. Cartesian tensor scalar product and spherical harmonic expansions in Boltzmann's equation. *Physical Review*, 120(4):1103–1111, 1960. doi:10.1103/PhysRev.120.1103.

[51] S. Chandrasekhar. Brownian motion, dynamical friction, and stellar dynamics. *Reviews of Modern Physics*, 21(3):383–388, 1949. doi:10.1103/RevModPhys.21.383.

[52] S. Childress. *An introduction to theoretical fluid mechanics*, volume 19. American Mathematical Society, 2009.

[53] F. Wu, R. Ramis and Z. Li. A conservative MHD scheme on unstructured Lagrangian grids for Z-pinch hydrodynamic simulations. *Journal of Computational Physics*, 357:206–229, 2018. doi:10.1016/j.jcp.2017.12.014.

[54] M. Lax and D. F. Nelson. Maxwell equations in material form. *Physical Review B*, 13:1777–1784, 1976. doi:10.1103/PhysRevB.13.1777.

[55] R. M. More, K. H. Warren, D. A. Young and G. B. Zimmerman. A new quotidian equation of state (QEOS) for hot dense matter. *Physics of Fluids*, 31(10):3059, 1988. doi:10.1063/1.866963.

[56] C. Cranfill and R. M. More. IONEOS: A fast, analytic ion equation-of-state routine. Technical Report LA–7313–MS, Los ALamos Scientific Laboratory, 1978.

[57] J. F. Barnes. Statistical atom theory and the equation of state of solids. *Physical Review*, 153(1):269–275, 1967. doi:10.1103/PhysRev.153.269.

[58] R. Feynman, N. Metropolis and E. Teller. Equations of state of elements based on the generalized Fermi-Thomas theory. *Physical Review*, 75(10), 1949.

[59] A. J. Kemp and J. Meyer-ter-Vehn. An equation of state code for hot dense matter, based on the QEOS description. *Nuclear Instruments and Methods in Physics Research, Section A: Accelerators, Spectrometers, Detectors and Associated Equipment*, 415(3):674–676, 1998. doi:10.1016/S0168-9002(98)00446-X.

[60] S. Faik, M. M. Basko, A. Tauschwitz, I. Iosilevskiy and J. A. Maruhn. Dynamics of volumetrically heated matter passing through the liquid–vapor metastable states. *High Energy Density Physics*, 8(4):349–359, 2012. doi:10.1016/j.hedp.2012.08.003.

[61] T. A. Heltemes and G. A. Moses. BADGER v1.0: A Fortran equation of state library. *Computer Physics Communications*, 183(12):2629–2646, 2012. doi:10.1016/j.cpc.2012.07.010.

[62] J. Abdallah Jr, G. Kerley, B. Bennett, J. Johnson, R. Albers and W. Huebner. HYDSES: a subroutine package for using Sesame in hydrodynamic codes. Technical Report LA-8209, Los Alamos Scientific Lab., NM (USA), 1980.

[63] Group T. SESAME report on the Los Alamos equation-of-state library. Technical Report LALP-83-4, Los Alamos National Laboratory, Los Alamos, 1983.

[64] S. P. Lyon and J. D. Johnson. Sesame: the Los Alamos National Laboratory equation of state database. Technical Report LA-UR-92-3407, Los Alamos National Laboratory, Los Alamos, NM, 1992.

[65] M. Zeman, M. Holec and P. Váchal. HerEOS: A framework for consistent treatment of the equation of state in ALE hydrodynamics. *Computers and Mathematics with Applications*, 2018. doi:10.1016/j.camwa.2018.10.014.

[66] M. Zeman. *Thermodynamically Consistent Interpolation of the Equation of State for Hydrodynamic Calculations*. Bachelor's project, FJFI ČVUT v Praze, 2016.

[67] R. Courant and D. Hilbert. *Methods of mathematical physics*. Wiley, 1953.

[68] D. Enskog. The numerical calculation of phenomena in fairly dense gases. *Arkiv för matematik, astronomi och fysik*, 16(1):1–60, 1921.

[69] S. Chapman, T. G. Cowling and D. Burnett. *The mathematical theory of non-uniform gases*. Cambridge University Press, third edition edition, 1990. ISBN 052140844X.

[70] E. M. Epperlein and R. W. Short. A practical nonlocal model for electron heat transport in laser plasma. *Physics of Fluids B: Plasma Physics (1989-1993)*, 3(1991):3092–3098, 1991. doi:10.1063/1.859789.

[71] J. J. Bissell, C. P. Ridgers and R. J. Kingham. Super-Gaussian transport theory and the field-generating thermal instability in laser–plasmas. *New Journal of Physics*, 15(2):025017, 2013. doi:10.1088/1367-2630/15/2/025017.

[72] A. V. Brantov and V. Y. Bychenkov. Nonlocal transport in hot plasma. part I. *Plasma Physics Reports*, 39(9):698–744, 2013. doi:10.1134/S1063780x13090018.

[73] C. P. Ridgers, R. J. Kingham and A. G. R. Thomas. Magnetic cavitation and the reemergence of nonlocal transport in laser plasmas. *Physical Review Letters*, 100(7):075003, 2008. doi:10.1103/PhysRevLett.100.075003.

[74] L. Biermann. Über den Ursprung der Magnetfelder auf Sternen und im interstellaren Raum (miteinem Anhang von A. Schlüter). *Zeitschrift Naturforschung Teil A*, 5:65, 1950.

[75] R. M. Kulsrud, R. Cen, J. P. Ostriker and D. Ryu. The protogalactic origin for cosmic magnetic fields. *The Astrophysical Journal*, 480:481–491, 1997. doi: 10.1086/303987.

[76] J. A. Stamper, E. A. McLean and B. H. Ripin. Studies of spontaneous magnetic fields in laser-produced plasmas by Faraday rotation. *Physical Review Letters*, 40:1177–1181, 1978. doi:10.1103/PhysRevLett.40.1177.

[77] I. V. Igumenshchev, A. B. Zylstra, C. K. Li, P. M. Nilson, V. N. Goncharov and R. D. Petrasso. Self-generated magnetic fields in direct-drive implosion experiments. *Physics of Plasmas*, 21(6):062707, 2014. doi:10.1063/1.4883226.

[78] M. Sherlock and J. J. Bissell. Suppression of the Biermann battery and stabilization of the thermomagnetic instability in laser fusion conditions. *Physical Review Letters*, 124:055001, 2020. doi:10.1103/PhysRevLett.124.055001.

[79] J. D. Sadler, C. A. Walsh and H. Li. Symmetric set of transport coefficients for collisional magnetized plasma. *Physical Review Letters*, 126:075001, 2021. doi:10.1103/PhysRevLett.126.075001.

[80] C. A. Walsh, J. P. Chittenden, D. W. Hill and C. Ridgers. Extended-magnetohydrodynamics in under-dense plasmas. *Physics of Plasmas*, 27:022103, 2020. doi:10.1063/1.5124144.

[81] E. M. Epperlein and M. G. Haines. Plasma transport coefficients in a magnetic field by direct numerical solution of the Fokker–Planck equation. *Physics of Fluids*, 29:1029, 1986. doi:10.1063/1.865901.

[82] J. Nikl. *Some aspects of numerical methods for laser plasma hydrodynamics*. Master's thesis, FJFI ČVUT v Praze, 2017.

[83] M. D. Rosen, D. W. Phillion, V. C. Rupert, W. C. Mead, W. L. Kruer, J. J. Thomson, H. N. Kornblum, V. W. Slivinsky, G. J. Caporaso, M. J. Boyle and K. G. Tirsell. The interaction of 1.06 μm laser radiation with high Z disk targets. *Physics of Fluids*, 22(10):2020, 1979. doi:10.1063/1.862501.

[84] A. Sunahara, J. A. Delettrez, C. Stoeckl, R. W. Short and S. Skupsky. Time-dependent electron thermal flux inhibition in direct-drive laser implosions. *Physical Review Letters*, 91(9):950031–950034, 2003. doi:10.1103/PhysRevLett.91.095003.

[85] A. R. Bell, R. G. Evans and D. J. Nicholas. Elecron energy transport in steep temperature gradients in laser-produced plasmas. *Physical Review Letters*, 46(4):243–246, 1981. doi:10.1103/PhysRevLett.46.243.

[86] T. H. Kho and M. G. Haines. Nonlinear kinetic transport of electrons and magnetic field in laser-produced plasmas. *Physical Review Letters*, 55(8):825–828, 1985. doi:10.1103/PhysRevLett.55.825.

[87] L. Drska, J. Limpouch and R. Liska. Fokker-Planck simulations of ultrashort-pulse laser-plasma interactions. *Laser and Particle Beams*, 10(3):461–471, 1992. doi:10.1017/S0263034600006704.

[88] M. K. Prasad and D. S. Kershaw. Stable solutions of nonlocal electron heat transport equations. *Physics of Fluids B: Plasma Physics (1989-1993)*, 3(11):3087–3091, 1991. doi:10.1063/1.859995.

[89] G. Schurtz, S. Gary, S. Hulin, C. Chenais-Popovics, J. C. Gauthier, F. Thais, J. Breil, F. Durut, J. L. Feugeas, P. H. Maire, P. Nicolaï, O. Peyrusse, C. Reverdin, G. Soullié, V. Tikhonchuk, B. Villette and C. Fourment. Revisiting nonlocal electron-energy transport in inertial-fusion conditions. *Physical Review Letters*, 98(9):3–6, 2007. doi:10.1103/PhysRevLett.98.095002.

[90] P. D. Nicolaï, J. L. A. Feugeas and G. P. Schurtz. A practical nonlocal model for heat transport in magnetized laser plasmas. *Physics of Plasmas*, 13(3):1–14, 2006. doi:10.1063/1.2179392.

[91] V. Y. Bychenkov, W. Rozmus, V. T. Tikhonchuk and A. V. Brantov. Nonlocal electron transport in a plasma. *Physical Review Letters*, 75(24):4405–4408, 1995. doi:10.1103/PhysRevLett.75.4405.

[92] D. Del Sorbo, J.-L. Feugeas, P. Nicolaï, M. Olazabal-Loumé, B. Dubroca and V. Tikhonchuk. Extension of a reduced entropic model of electron transport to magnetized nonlocal regimes of high-energy-density plasmas. *Laser and Particle Beams*, 34(03):412–425, 2016. doi:10.1017/S0263034616000252.

[93] A. Colaïtis. *Multiscale Description of the Laser-Plasma Interaction, Application to the Physics of Shock Ignition in Inertial Confinement Fusion*. Ph.D. thesis, Université de Bordeaux, France, 2015.

[94] M. Holec. *Nonlocal Transport Hydrodynamic Modeling of Laser Heated Plasmas*. Doctoral thesis, FJFI ČVUT v Praze, 2016.

[95] J. Nikl, M. Holec, M. Zeman, M. Kuchařík, J. Limpouch and S. Weber. Macroscopic laser-plasma interaction under strong non-local transport conditions for coupled matter and radiation. *Matter and Radiation at Extremes*, 3:110–126, 2018. doi:10.1016/j.mre.2018.03.001.

[96] E. M. Epperlein. Effect of electron collisions on ion-acoustic waves and heat flow. *Physics of Plasmas*, 1(1):109, 1994.

[97] D. Mihalas and B. W. Mihalas. *Foundations of Radiation Hydrodynamics*. Oxford University Press, 1984. ISBN 0195034376.

[98] G. Pomraning. *Equations of Radiation Hydrodynamics*. Pergamon Press, 1973.

[99] R. Lokasani, H. Kawasaki, Y. Shimada, M. Shoji, K. Anraku, T. Ejima, T. Hatano, W. Jiang, S. Namba, J. Nikl, M. Zeman, G. O'Soullivan, T. Higashiguchi and J. Limpouch. Soft X-ray spectral analysis of laser produced molybdenum plasmas using fundamental and second harmonics of a Nd:YAG laser. *Optics Express*, 27(23):33351–33358, 2019. doi:10.1364/OE.27.033351.

[100] R. Sigel, K. Eidmann, F. Lavarenne and R. F. Schmalz. Conversion of laser light into soft x rays. Part I: Dimensional analysis. *Physics of Fluids B: Plasma Physics*, 2(1):199–207, 1990. doi:10.1063/1.859528.

[101] N. Vaytet, M. González, E. Audit and G. Chabrier. The influence of frequency-dependent radiative transfer on the structures of radiative shocks. *Journal of Quantitative Spectroscopy and Radiative Transfer*, 125:105–122, 2013. doi:10.1016/j.jqsrt.2013.03.003.

[102] J. Castor. *Radiation hydrodynamics*. Cambridge University Press, New York, 2004. ISBN 0511231334.

[103] G. L. Olson, L. H. Auer and M. L. Hall. Diffusion, P1, and other approximate forms of radiation transport. *Journal of Quantitative Spectroscopy and Radiative Transfer*, 64(6):619–634, 1999. doi:10.1016/S0022-4073(99)00150-8.

[104] C. D. Levermore and G. C. Pomraning. A flux-limited diffusion theory. *Astrophysical Journal*, 248:321, 1981. doi:10.1086/159157.

[105] G. N. Minerbo. Maximum entropy Eddington factors. *Journal of Quantitative Spectroscopy and Radiative Transfer*, 20(6):541–545, 1978. doi:10.1016/0022-4073(78)90024-9.

[106] Y. Raizer and Y. Zeldovich. *Physics of Shock Waves and High-Temperature Hydrodynamic Phenomena*. Dover Publications, New York, 2002.

[107] N. J. Turner and J. M. Stone. A module for radiation hydrodynamic calculations with ZEUS-2D using flux-limited diffusion. *The Astrophysical Journal Supplement Series*, 135(1):30, 2001. doi:10.1086/321779.

[108] C. C. Ober and J. N. Shadid. Studies on the accuracy of time-integration methods for the radiation-diffusion equations. *Journal of Computational Physics*, 195(2):743–772, 2004. doi:10.1016/j.jcp.2003.10.036.

[109] J. Morel. Diffusion-limit asymptotics of the transport equation, the P1/3 equations, and two flux-limited diffusion theories. *Journal of Quantitative Spectroscopy and Radiative Transfer*, 65(5):769–778, 2000. doi:10.1016/S0022-4073(99)00148-X.

[110] D. S. Kershaw. Flux limiting nature's own way: A new method for numerical solution of the transport equation. *Lawrence Livermore National Laboratory, UCRL-78378*, 1976. doi:10.2172/104974.

[111] C. Levermore. Relating Eddington factors to flux limiters. *Journal of Quantitative Spectroscopy and Radiative Transfer*, 31(2):149–160, 1984. doi:10.1016/0022-4073(84)90112-2.

[112] S. Chandrasekhar. *Radiative transfer*. Dover Publications, New York, 1960.

[113] M. Holec, J. Limpouch, R. Liska and S. Weber. High-order discontinuous Galerkin nonlocal transport and energy equations scheme for radiation hydrodynamics. *International Journal for Numerical Methods in Fluids*, 83(10):779–797, 2017. doi:10.1002/fld.4288.

[114] I. Babuška and M. Suri. On locking and robustness in the finite element method. *SIAM Journal on Numerical Analysis*, 29(5):1261–1293, 1992. doi:10.1137/0729075.

[115] J. C. Ragusa, J. L. Guermond and G. Kanschat. A robust SN-DG-approximation for radiation transport in optically thick and diffusive regimes. *Journal of Computational Physics*, 231(4):1947–1962, 2012. doi:10.1016/j.jcp.2011.11.017.

[116] J. C. Chai, H. S. Lee and S. V. Patankar. Ray effect and false scattering in the discrete ordinates method. *Numerical Heat Transfer, Part B: Fundamentals*, 24(4):373–389, 1993. doi:10.1080/10407799308955899.

[117] B. Hunter and Z. Guo. Numerical smearing, ray effect, and angular false scattering in radiation transfer computation. *International Journal of Heat and Mass Transfer*, 81:63–74, 2015. doi:10.1016/j.ijheatmasstransfer.2014.10.014.

[118] R. O. Castro and J. P. Trelles. Spatial and angular finite element method for radiative transfer in participating media. *Journal of Quantitative Spectroscopy and Radiative Transfer*, 157:81–105, 2015. doi:10.1016/j.jqsrt.2015.02.008.

[119] S. Eliezer. *The interaction of high-power lasers with plasmas*. IOP Publishing Ltd, 2002. ISBN 0750307471.

[120] M. Born and E. Wolf. *Principles of optics: Electromagnetic Theory of Propagation, Interference and Diffraction of Light*. Cambridge University Press, 7th edition, 1999. ISBN 0521642221. doi:10.1016/S0030-3992(00)00061-X.

[121] T. B. Kaiser. Laser ray tracing and power deposition on an unstructured three-dimensional grid. *Physical Review E*, 61(1):895–905, 2000. doi:10.1103/PhysRevE.61.895.

[122] A. Colaïtis, G. Duchateau, P. Nicolaï and V. Tikhonchuk. Towards modeling of nonlinear laser-plasma interactions with hydrocodes : The thick-ray approach. *Physical Review E*, 89(3):033101, 2014. doi:10.1103/PhysRevE.89.033101.

[123] J. Velechovský. *Numerické metody modelování laserového plazmatu*. Master's thesis, FJFI ČVUT v Praze, 2011.

[124] Y. A. Kravtsov. Complex rays and complex caustics. *Radiophysics and Quantum Electronics*, 10(9-10):719–730, 1971. doi:10.1007/BF01031601.

[125] Y. A. Kravtsov and P. Berczynski. Gaussian beams in inhomogeneous media: A review. *Studia Geophysica et Geodaetica*, 51(1):1–36, 2007. doi:10.1007/s11200-007-0002-y.

[126] A. Colaïtis, J. P. Palastro, R. K. Follett, I. V. Igumenschev and V. Goncharov. Real and complex valued geometrical optics inverse ray-tracing for inline field calculations. *Physics of Plasmas*, 26:032301, 2019. doi:10.1063/1.5082951.

[127] A. Colaïtis, R. K. Follett, J. P. Palastro, I. Igumenschev and V. Goncharov. Adaptive inverse ray-tracing for accurate and efficient modeling of cross beam energy transfer in hydrodynamics simulations. *Physics of Plasmas*, 26:072706, 2019. doi:10.1063/1.5108777.

[128] M. Šach. *Hydrodynamic simulations of X-ray generation and propagation in laser-produced plasmas.* Master's thesis, FJFI ČVUT v Praze, 2021.

[129] M. Šach. *Hydrodynamické simulace plazmatu pro realizaci rentgenového laseru.* Bachelor project, FJFI ČVUT v Praze, 2019.

[130] R. Ramis, K. Eidmann, J. Meyer-Ter-Vehn and S. Hüller. MULTI-fs - A computer code for laser-plasma interaction in the femtosecond regime. *Computer Physics Communications*, 183(3):637–655, 2012. doi:10.1016/j.cpc.2011.10.016.

[131] Y. V. Afanas'ev, N. N. Demchenko, O. N. Krokhin, V. B. Rosanov, Y. V. Afanas, N. N. Demchenko, O. N. Krokhin and V. B. Rosanov. Absorption and reflection of laser radiation by a dispersing high-temperature plasma. *Soviet Physics - JETP*, 45:90–94, 1977.

[132] J. Nikl, M. Kuchařík, J. Limpouch, R. Liska and S. Weber. Wave-based laser absorption method for high-order transport–hydrodynamic codes. *Advances in Computational Mathematics*, 45(4):1953–1976, 2019. doi:10.1007/s10444-019-09671-3.

[133] Y. V. Afanas'ev, E. G. Gamalii, N. N. Demchenko, O. N. Krokhin and V. B. Rozanov. Theoretical study of the hydrodynamics of spherical targets taking the refraction of the laser radiation into account. *Soviet Physics - JETP*, 52(3):425–431, 1980.

[134] T. Kapin, M. Kuchařík, J. Limpouch and R. Liska. Hydrodynamic simulations of laser interactions with low-density foams. *Czechoslovak Journal of Physics*, 56:B493–B499, 2006. doi:10.1007/s10582-006-0243-y.

[135] J. Velechovský. *Modelování absorpce laserového záření v plazmatu (Modelling of laser radiation absorption in plasma).* Bachelor project, FJFI ČVUT v Praze, 2009.

[136] A. Colaïtis, G. Duchateau, X. Ribeyre, Y. Maheut, G. Boutoux, L. Antonelli, P. Nicolaï, D. Batani and V. Tikhonchuk. Coupled hydrodynamic model for laser-plasma interaction and hot electron generation. *Physical Review E - Statistical, Nonlinear, and Soft Matter Physics*, 92(4):1–5, 2015. doi:10.1103/PhysRevE.92.041101.

[137] I. G. Lebo, N. N. Demchenko, A. B. Iskakov, J. Limpouch, V. B. Rozanov and V. F. Tishkin. Simulation of high-intensity laser-plasma interactions by use of the 2D Lagrangian code "ATLANT-HE". *Laser and Particle Beams*, 22(3):267–273, 2004. doi:10.1017/S0263034604223096.

[138] M. M. Basko and I. P. Tsygvintsev. A hybrid model of laser energy deposition for multi-dimensional simulations of plasmas and metals. *Computer Physics Communications*, 214(6):59–70, 2017. doi:10.1016/j.cpc.2017.01.010.

[139] O. C. Zienkiewicz, R. L. Taylor and J. Z. Zhu. *The Finite Element Method: Its Basis and Fundamentals*. Butterworth-Heinemann, Elsevier Ltd., 7 edition, 2013. ISBN 9781856176330.

[140] P. Šolín, K. Segeth and I. Doležel. *High-Order Finite Element Methods*. Chapman & Hall/CRC, 2004. ISBN 1-58488-438-X.

[141] D. N. Arnold, R. S. Falk and R. Winther. *Compatible Spatial Discretizations*, chapter Differential Complexes and Stability of Finite Element Methods I. The de Rham Complex, pages 23–46. Springer New York, 2006. doi:10.1007/0-387-38034-5_2.

[142] MFEM: Modular finite element methods library. `<https://mfem.org>`. doi:10.11578/dc.20171025.1248.

[143] R. Anderson, J. Andrej, A. Barker, J. Bramwell, J.-S. Camier, J. Cerveny, V. Dobrev, Y. Dudouit, A. Fisher, Tz. Kolev, W. Pazner, M. Stowell, V. Tomov, I. Akkerman, J. Dahm, D. Medina and S. Zampini. MFEM: A modular finite element methods library. *Computers & Mathematics with Applications*, 2020. doi:10.1016/j.camwa.2020.06.009.

[144] R. D. Falgout, J. E. Jones and U. M. Yang. *Numerical Solution of Partial Differential Equations on Parallel Computers*, volume 51, chapter The Design and Implementation of hypre, a Library of Parallel High Performance Preconditioners, pages 267–294. Springer-Verlag, 2006. ISBN 9783540290766. doi:10.1007/3-540-31619-1_8.

[145] GLVis: OpenGL finite element visualization tool. `<https://glvis.org>`. doi:10.11578/dc.20171025.1249.

[146] J. Nikl, I. Göthel, M. Kuchařík, S. Weber and M. Bussmann. Implicit reduced Vlasov–Fokker–Planck–Maxwell model based on high-order mixed elements. *Journal of Computational Physics*, 434:110214, 2021. doi:10.1016/j.jcp.2021.110214.

[147] R. Rieben, D. White and G. Rodrigue. Improved conditioning of finite element matrices using new high-order interpolatory bases. *IEEE Transactions on Antennas and Propagation*, 52(10):2675–2683, 2004. doi:10.1109/TAP.2004.834387.

[148] P. Lesaint and P. A. Raviart. On a finite element method for solving the neutron transport equation. *Mathematical aspects of finite elements in partial differential equations*, 33:89–123, 1974.

[149] J. C. Nedelec. Mixed finite elements in R3. *Numerische Mathematik*, 35(3):315–341, 1980. doi:10.1007/BF01396415.

[150] A. B. Langdon. Conservative differencing of the electron Fokker–Planck transport equation. In *CECAM Report of Workshop on The Flux Limiter and Heat Flow Instabilities in Laser-Fusion Plasmas, Universite Paris Sud, France*, page 69. 1981.

[151] E. M. Epperlein. Implicit and conservative difference scheme for the Fokker-Planck equation. *Journal of Computational Physics*, 112(2):291–297, 1994. doi: 10.1006/jcph.1994.1101.

[152] W. T. Taitano, L. Chacón and A. N. Simakov. An adaptive, implicit, conservative, 1D-2V multi-species Vlasov–Fokker–Planck multi-scale solver in planar geometry. *Journal of Computational Physics*, 365:173–205, 2018. doi: 10.1016/j.jcp.2018.03.007.

[153] R. J. Kingham and A. R. Bell. An implicit Vlasov–Fokker–Planck code to model non-local electron transport in 2-D with magnetic fields. *Journal of Computational Physics*, 194(1):1–34, 2004. doi:10.1016/j.jcp.2003.08.017.

[154] W. T. Taitano and L. Chacón. Charge-and-energy conserving moment-based accelerator for a multi-species Vlasov–Fokker–Planck–Ampère system, part I: Collisionless aspects. *Journal of Computational Physics*, 284:718–736, 2015. doi: 10.1016/j.jcp.2014.12.038.

[155] R. Rieben, D. White and G. Rodrigue. High-order symplectic integration methods for finite element solutions to time dependent Maxwell equations. *IEEE Transactions on Antennas and Propagation*, 52(8):2190–2195, 2004. doi: 10.1109/TAP.2004.832356.

[156] J. S. Chang and G. Cooper. A practical difference scheme for Fokker-Planck equations. *Journal of Computational Physics*, 6(1):1–16, 1970. doi:10.1016/0021-9991(70)90001-X.

[157] E. M. Epperlein and R. W. Short. Nonlocal electron transport in the presence of high-intensity laser irradiation. *Physical Review E*, 50(2):1697–1699, 1994. doi:10.1103/PhysRevE.50.1697.

[158] E. Chow. A priori sparsity patterns for parallel sparse approximate inverse preconditioners. *SIAM Journal on Scientific Computing*, 21(5):1804–1822, 2000. doi:10.1137/S106482759833913X.

[159] Y. Saad. A flexible inner-outer preconditioned GMRES algorithm. *SIAM Journal on Scientific Computing*, 14(2):461–469, 1993. doi:10.1137/0914028.

[160] A. Marocchino, M. Tzoufras, S. Atzeni, A. Schiavi, P. D. Nicolaï, J. Mallet, V. Tikhonchuk and J.-L. Feugeas. Comparison for non-local hydrodynamic thermal conduction models. *Physics of Plasmas*, 20(2):022702, 2013. doi: 10.1063/1.4789878.

[161] M. Sherlock, J. P. Brodrick and C. P. Ridgers. A comparison of non-local electron transport models for laser-plasmas relevant to inertial confinement fusion. *Physics of Plasmas*, 24(8):082706, 2017. doi:10.1063/1.4986095.

[162] J. Nikl, M. Kuchařík and S. Weber. High-order curvilinear finite element magneto-hydrodynamics I: A conservative Lagrangian scheme. *Journal of Computational Physics*, page 111158, 2022. doi:10.1016/j.jcp.2022.111158. In press.

[163] J. Nikl, M. Kuchařík, M. Holec and S. Weber. Curvilinear high-order Lagrangian hydrodynamic code for the laser-target interaction. In S. Coda, J. Berndt, G. Lapenta, M. Mantsinen, C. Michaut and S. Weber, editors, *Europhysics Conference Abstracts – 45th EPS Conference on Plasma Physics*, volume 42A, page P1.2019. European Physical Society, 2018. ISBN 979-10-96389-08-7.

[164] J. Nikl, M. Kuchařík and S. Weber. High-order curvilinear finite element magneto-hydrodynamics II: The Biermann battery, 2022. In preparation.

[165] E. Livne and A. Glasner. A finite difference scheme for the heat conduction equation. *Journal of Computational Physics*, 66(1):59–66, 1985. doi:10.1016/0021-9991(85)90156-1.

[166] J. Glaubitz. Shock capturing by Bernstein polynomials for scalar conservation laws. *Applied Mathematics and Computation*, 363:124593, 2019. doi:10.1016/j.amc.2019.124593.

[167] R. N. Rieben, D. A. White, B. K. Wallin and J. M. Solberg. An arbitrary Lagrangian–Eulerian discretization of MHD on 3D unstructured grids. *Journal of Computational Physics*, 226(1):534–570, 2007. doi:10.1016/j.jcp.2007.04.031.

[168] C. Graziani, P. Tzeferacos, D. Lee, D. Q. Lamb, K. Weide, M. Fatenejad and J. Miller. The Biermann catastrophe in numerical magnetohydrodynamics. *The Astrophysical Journal*, 802(1):43, 2015. doi:10.1088/0004-637X/802/1/43.

[169] J. Nikl, M. Kuchařík and S. Weber. Self-generated magnetic fields modelling within high-order Lagrangian magneto-hydrodynamics. In *Europhysics Conference Abstracts – 47th EPS Conference on Plasma Physics*, page P1.2022. European Physical Society, 2021.

[170] M. Kucharik, J. Nikl and J. Limpouch. Second-order magnetic field generation model for Lagrangian and ALE plasma simulations. In *International Conference of Numerical Analysis and Applied Mathematics ICNAAM 2021*, AIP Conference Proceedings. 2021. Accepted.

[171] M. Kucharik, J. Limpouch and J. Nikl. Development of ALE hydrodynamic code for laser-plasma interactions with self-generated magnetic fields. In *Europhysics Conference Abstracts – 47th EPS Conference on Plasma Physics*, page P1.2020. European Physical Society, 2021.

[172] Tz. V. Kolev and P. S. Vassilevski. Parallel auxiliary space AMG for H(Curl) problems. *Journal of Computational Mathematics*, 27(5):604–623, 2009. doi: 10.4208/jcm.2009.27.5.013.

[173] V. E. Henson and U. M. Yang. BoomerAMG: A parallel algebraic multigrid solver and preconditioner. *Applied Numerical Mathematics*, 41(1):155–177, 2002. doi:10.1016/S0168-9274(01)00115-5.

[174] J. W. Ruge and K. Stüben. *Algebraic multigrid (AMG)*, chapter 4, pages 73–130. SIAM, 1987. doi:10.1137/1.9781611971057.ch4.

[175] A. Sandu, V. Tomov, L. Cervena and Tz. Kolev. Conservative high-order time integration for Lagrangian hydrodynamics. *SIAM Journal on Scientific Computing*, 43(1):A221–A241, 2021. doi:10.1137/20M1314495.

[176] R. Courant, K. Friedrichs and H. Lewy. Über die partiellen Differenzengleichungen der mathematischen Physik. *Mathematische Annalen*, 100(1):32–74, 1928. doi:10.1007/BF01448839.

[177] Tz. V. Kolev and R. N. Rieben. A tensor artificial viscosity using a finite element approach. *Journal of Computational Physics*, 228(22):8336–8366, 2009. doi: 10.1016/j.jcp.2009.08.010.

[178] A. L. Zachary, A. Malagoli and P. Colella. A higher-order Godunov method for multidimensional ideal magnetohydrodynamics. *SIAM Journal on Scientific Computing*, 15(2):263–284, 1994. doi:10.1137/0915019.

[179] D. Kössl, E. Müller and W. Hilldebrandt. Numerical simulations of axially symmetric magnetized jets. I : The influence of equipartition magnetic fields. *Astronomy and astrophysics*, 229(2):378–396, 1990.

[180] L. J. Perkins, D. D. Ho, B. G. Logan, G. B. Zimmerman, M. A. Rhodes, D. J. Strozzi, D. T. Blackfield and S. A. Hawkins. The potential of imposed magnetic fields for enhancing ignition probability and fusion energy yield in indirect-drive inertial confinement fusion. *Physics of Plasmas*, 24(6):062708, 2017. doi:10.1063/1.4985150.

[181] L. I. Sedov. *Similarity and dimensional methods in mechanics*. CRC press, 1993.

[182] M. Gittings, R. Weaver, M. Clover, T. Betlach, N. Byrne, R. Coker, E. Dendy, R. Hueckstaedt, K. New, W. R. Oakes, D. Ranta and R. Stefan. The RAGE radiation-hydrodynamic code. *Computational Science & Discovery*, 1:015005, 2008. doi:10.1088/1749-4699/08/015005.

[183] M. Alhawwary and Z. Wang. A combined-mode Fourier analysis of DG methods for linear parabolic problems. *SIAM Journal on Scientific Computing*, 42(6):A3825–A3858, 2020. doi:10.1137/20M1316962.

[184] R. Hiptmair and J. Xu. Nodal auxiliary space preconditioning in H(curl) and H(div) spaces. *SIAM Journal on Numerical Analysis*, 45(6):2483–2509, 2007. doi:10.1137/060660588.

[185] F. Brezzi and M. Fortin. *Mixed and Hybrid Finite Element Method*. Springer, New York, 1991.

[186] H. Hoteit, R. Mosé, B. Philippe, P. Ackerer and J. Erhel. The maximum principle violations of the mixed-hybrid finite-element method applied to diffusion equations. *International Journal for Numerical Methods in Engineering*, 55:1373–1390, 2002. doi:10.1002/nme.531.

[187] H. Hajduk, D. Kuzmin, Tz. Kolev, V. Tomov, I. Tomas and J. N. Shadid. Matrix-free subcell residual distribution for Bernstein finite elements: Monolithic limiting. *Computers & Fluids*, 200:104451, 2020. doi:10.1016/j.compfluid.2020.104451.

[188] B. Su and G. L. Olson. Benchmark results for the non-equilibrium Marshak diffusion problem. *Journal of Quantitative Spectroscopy and Radiative Transfer*, 56:337–351, 1996. doi:10.1016/0022-4073(96)84524-9.

[189] B. Su and G. L. Olson. An analytical benchmark for non-equilibrium radiative transfer in anisotropically scattering medium. *Annals of Nuclear Energy*, 24:1035–1055, 1997. doi:10.1016/S0306-4549(96)00100-4.

[190] B. Su and G. L. Olson. Non-grey benchmark results for two temperature non-equilibrium radiative transfer. *Journal of Quantitative Spectroscopy and Radiative Transfer*, 62:279–302, 1999. doi:10.1016/S0022-4073(98)00105-8.

[191] G. Pomraning. The non-equilibrium Marshak wave problem. *Journal of Quantitative Spectroscopy and Radiative Transfer*, 21(3):249–261, 1979. doi:10.1016/0022-4073(79)90016-5.

[192] R. Singleton Jr, D. M. Israel, S. W. Doebling, C. N. Woods, A. Kaul, J. W. Walter Jr and M. L. Rogers. Exactpack documentation. Technical Report LA-UR-16-23260, Los Alamos National Lab.(LANL), Los Alamos, NM (United States), 2016. doi:10.2172/1253491.

[193] R. W. Anderson, V. A. Dobrev, Tz. V. Kolev, R. N. Rieben and V. Z. Tomov. High-order multi-material ALE hydrodynamics. *SIAM Journal on Scientific Computing*, 40:B32–B58, 2018. doi:10.1137/17M1116453.

[194] T. A. Davis. Algorithm 832: UMFPACK V4.3—an unsymmetric-pattern multifrontal method. *ACM Transactions on Mathematical Software*, 30(2):196–199, 2004. doi:10.1145/992200.992206.

[195] P. S. Epstein. Reflection of waves in an inhomogeneous absorbing medium. *Proceedings of the National Academy of Sciences of the United States of America*, 16(10):627, 1930. doi:10.1073/pnas.16.10.627.

[196] J. Limpouch, V. Tikhonchuk, J. Dostal, R. Dudzak, M. Krupka, N. Borisenko, J. Nikl, A. Akunets, L. Borisenko and V. Pimenov. Characterization of the homogenization time of a plasma created by laser ionization of a low-density foam. *Plasma Physics and Controlled Fusion*, 62(3):035013, 2020. doi:10.1088/1361-6587/ab6b4d.

[197] R. K. Follett, D. H. Edgell, D. H. Froula, V. N. Goncharov, I. V. Igumenshchev, J. G. Shaw and J. F. Myatt. Full-wave and ray-based modeling of cross-beam energy transfer between laser beams with distributed phase plates and polarization smoothing. *Physics of Plasmas*, 24:103128, 2017. doi:10.1063/1.4998713.

[198] A. Colaïtis, G. Duchateau, X. Ribeyre and V. Tikhonchuk. Modeling of the cross-beam energy transfer with realistic inertial-confinement-fusion beams in a large-scale hydrocode. *Physical Review E - Statistical, Nonlinear, and Soft Matter Physics*, 91:013102, 2015. doi:10.1103/PhysRevE.91.013102.

[199] Tz. Kolev and W. Pazner. Conservative and accurate solution transfer between high-order and low-order refined finite element spaces. *SIAM Journal on Scientific Computing*, 44(1):A1–A27, 2022. doi:10.1137/21M1403916.

[200] J. Sanz, R. Betti, V. A. Smalyuk, M. Olazabal-Loume, V. Drean, V. Tikhonchuk, X. Ribeyre and J. Feugeas. Radiation hydrodynamic theory of double ablation fronts in direct-drive inertial confinement fusion. *Physics of Plasmas*, 16(8), 2009. doi:10.1063/1.3202697.

[201] G. Tsakiris and K. Eidmann. An approximate method for calculating Planck and Rosseland mean opacities in hot, dense plasmas. *Journal of Quantitative Spectroscopy and Radiative Transfer*, 38(5):353–368, 1987. doi:10.1016/0022-4073(87)90030-6.

[202] C. P. Ridgers. *Magnetic Fields and Non-Local Transport in Laser Plasmas*. Doctoral thesis, Imperial College London, 2008.

[203] P. M. Nilson, L. Willingale, M. C. Kaluza, C. Kamperidis, S. Minardi, M. S. Wei, P. Fernandes, M. Notley, S. Bandyopadhyay, M. Sherlock, R. J. Kingham, M. Tatarakis, Z. Najmudin, W. Rozmus, R. G. Evans, M. G. Haines, A. E. Dangor and K. Krushelnick. Magnetic reconnection and plasma dynamics in two-beam laser-solid interactions. *Physical Review Letters*, 97:255001, 2006. doi:10.1103/PhysRevLett.97.255001.

[204] G. Gregori, A. Ravasio, C. D. Murphy, K. Schaar, A. Baird, A. R. Bell, A. Benuzzi-Mounaix, R. Bingham, C. Constantin, R. P. Drake, M. Edwards, E. T. Everson, C. D. Gregory, Y. Kuramitsu, W. Lau, J. Mithen, C. Niemann, H. S. Park, B. A. Remington, B. Reville, A. P. Robinson, D. D. Ryutov, Y. Sakawa,

S. Yang, N. C. Woolsey, M. Koenig and F. Miniati. Generation of scaled protogalactic seed magnetic fields in laser-produced shock waves. *Nature*, 481:480–483, 2012. doi:10.1038/nature10747.

[205] T. Pisarczyk, S. Y. Gus'Kov, T. Chodukowski, R. Dudzak, P. Korneev, N. N. Demchenko, Z. Kalinowska, J. Dostal, A. Zaras-Szydlowska, S. Borodziuk, L. Juha, J. Cikhardt, J. Krasa, D. Klir, B. Cikhardtova, P. Kubes, E. Krousky, M. Krus, J. Ullschmied, K. Jungwirth, J. Hrebicek, T. Medrik, J. Golasowski, M. Pfeifer, O. Renner, S. Singh, S. Kar, H. Ahmed, J. Skala and P. Pisarczyk. Kinetic magnetization by fast electrons in laser-produced plasmas at sub-relativistic intensities. *Physics of Plasmas*, 24:1–11, 2017. doi:10.1063/1.4995044.

[206] K. Jach, T. Pisarczyk, W. Stępniewski, R. Świerczyński, J. Krasa, T. Chodukowski, Z. Rusiniak, A. Zaraś-Szydłowska, J. Dostal, R. Dudzak, L. Juha, I. Kochetkov, M. Krupka and S. Borodziuk. 2D MHD simulation of spontaneous magnetic fields generated during interaction of 1315.2-nm laser radiation with copper slabs at 10^{16} W/cm^2. *Physics of Plasmas*, 28:092704, 2021. doi:10.1063/5.0054283.

[207] J. Nikl, M. Kuchařík and S. Weber. Modelling of spontaneous magnetic fields generation in laser-produced plasmas. Poster at MECMATPLA (Matter in Extreme Conditions : from MATerial science to Plasmas for Laboratory Astrophysics) International School and Workshop 2022, 2022.

[208] F. Hussain, S. Bashir, M. Akram, S. H. Butt, K. Mahmood, M. Javed and H. Ahmad. Measurement of characteristic parameters and self-generated electric and magnetic fields (SGEMFs) of laser-induced aluminum plasma. *Applied Physics B: Lasers & Optics*, 127(5):1 – 11, 2021.

[209] J. Nikl. *Hydrodynamické simulace ablace a expanze plazmatu při pulzní laserové depozici*. Bachelor project, FJFI ČVUT v Praze, 2015.

[210] C. A. Walsh, J. P. Chittenden, K. McGlinchey, N. P. L. Niasse and B. D. Appelbe. Self-generated magnetic fields in the stagnation phase of indirect-drive implosions on the National Ignition Facility. *Physical Review Letters*, 118(15):155001, 2017. doi:10.1103/PhysRevLett.118.155001.

[211] V. A. Dobrev, T. E. Ellis, Tz. V. Kolev and R. N. Rieben. High-order curvilinear finite elements for axisymmetric Lagrangian hydrodynamics. *Computers and Fluids*, 83:58–69, 2013. doi:10.1016/j.compfluid.2012.06.004.

[212] J. Nikl, M. Kuchařík and S. Weber. Modelling of the non-local transport of energy in laser plasmas with high-order numerical methods. In *Europhysics Conference Abstracts – 46th EPS Conference on Plasma Physics*, volume 43C, page P5.2010. European Physical Society, 2019. ISBN 979-10-96389-11-7.

[213] L. Gaus, L. Bischoff, M. Bussmann, E. Cunningham, C. B. Curry, J. E, E. Galtier, M. Gauthier, A. L. García, M. Garten, S. Glenzer, J. Grenzer, C. Gutt, N. J.

Hartley, L. Huang, U. Hübner, D. Kraus, H. J. Lee, E. E. McBride, J. Metzkes-Ng, B. Nagler, M. Nakatsutsumi, J. Nikl, M. Ota, A. Pelka, I. Prencipe, L. Randolph, M. Rödel, Y. Sakawa, H.-P. Schlenvoigt, M. Šmíd, F. Treffert, K. Voigt, K. Zeil, T. E. Cowan, U. Schramm and T. Kluge. Probing ultrafast laser plasma processes inside solids with resonant small-angle x-ray scattering. *Physical Review Research*, 3(4):043194, 2021. doi:10.1103/PhysRevResearch.3.043194.

[214] B. E. R. Williams and R. J. Kingham. Hybrid simulations of fast electron propagation including magnetized transport and non-local effects in the background plasma. *Plasma Physics and Controlled Fusion*, 55:124009, 2013. doi: 10.1088/0741-3335/55/12/124009.

[215] M. Jirka, O. Klimo and M. Matys. Relativistic plasma aperture for laser intensity enhancement. *Physical Review Research*, 3(3):033175, 2021. doi: 10.1103/PhysRevResearch.3.033175.

[216] M. Matys, S. V. Bulanov, M. Kucharik, M. Jirka, J. Nikl, M. Kecova, J. Proska, J. Psikal, G. Korn and O. Klimo. Plasma shutter for improved heavy ion acceleration by ultra-intense laser pulses. *New Journal of Physics*, 2022. Submitted.

[217] M. Matys, M. Kecova, M. Kucharik, J. Nikl, S. V. Bulanov, M. Jirka, P. Janecka, J. Psikal, G. Korn, J. Grosz and O. Klimo. Laser-driven ion acceleration enhancementusing silicon nitride plasma shutter. In *Europhysics Conference Abstracts – 47th EPS Conference on Plasma Physics*, page P3.2026. European Physical Society, 2021.

[218] M. Matys, S. V. Bulanov, M. Kecova, M. Kucharik, M. Jirka, P. Janecka, J. Psikal, J. Nikl, J. Grosz, G. Korn and O. Klimo. Ion acceleration enhancement by laser-pulse shaping via plasma shutter. In S. S. Bulanov, J. Schreiber and C. B. Schroeder, editors, *Laser Acceleration of Electrons, Protons, and Ions VI*, volume 11779 of *Proeedings of SPIE*, page 117790Q. 2021. doi:10.1117/12.2589096.

[219] M. Kuchařík, J. Limpouch, R. Liska and J. Nikl. Hydrodynamic simulations of laser/plasma interactions via ALE methods. In *Europhysics Conference Abstracts – 46th EPS Conference on Plasma Physics*, volume 43C, page P5.2009. European Physical Society, 2019. ISBN 979-10-96389-11-7.

[220] V. A. Dobrev, Tz. V. Kolev, R. N. Rieben and V. Z. Tomov. Multi-material closure model for high-order finite element Lagrangian hydrodynamics. *International Journal for Numerical Methods in Fluids*, 82:689–706, 2016. doi: 10.1002/fld.4236.